TRANSFORMATION OF IRON AND TRACE ELEMENTS DURING COAL COMBUSTION

by

Taofang Zeng

Submitted to the Department of Mechanical Engineering
in Partial Fulfillment of the Requirements for the Degree of

DOCTOR OF SCIENCE

IN MECHANICAL ENGINEERING

at the

MASSACHUSETTS INSTITUTE OF TECHNOLOGY

June, 1998

Signature of Author _____
Department of Mechanical Engineering
May 17, 1998

Certified by _____
Adel F. Sarofim
Professor Emeritus of Chemical Engineering
Thesis Supervisor

Accepted by _____
Ain A. Sonin
Chairman, Committee on Graduate Students
Department of Mechanical Engineering

Transformation of Iron and Trace Elements during Coal Combustion

by

Taofang Zeng

Submitted to the Department of Mechanical Engineering
on May 17, 1998 in partial fulfillment of the
requirements for the degree of Doctor of Science in
Mechanical Engineering

ABSTRACT

Pulverized Pittsburgh, Elkhorn/Hazard, Illinois and Wyodak coals were classified into size and density segregation fractions using a small fluidized-bed separator. The occurrences of elements were determined using selective leaching method and XAFS. It was found that: nearly all arsenic is associated with pyrite except for Wyodak coal; selenium is mainly associated with pyrite; chromium is probably presented in the form of -COOCr; and iron is mostly in the form of pyrites, except for Elkhorn/Hazard coal which has a significant amount of jarosite.

Experiments by ASTM standard pyrolysis and rapid heat up in a drop tube furnace show that: Iron cannot be devolatilized like other trace elements in the ASTM standard pyrolysis procedure, but iron can be found in submicron char particles under the high heating rates in the drop tube furnace, which is due to the fragmentation of pyrrhotite. During coal combustion, a small part of pyrrhotite was fragmented into fine particles (iron fume), which was verified by direct characterizing the iron state of submicron ash particles. Most of iron is in glassy state in the submicron ash particles, which shows that most iron was from vaporization, and the vaporized iron reacted with the vaporized silicates to produce glassy iron.

Vaporization was enhanced by char combustion, thus controlled by the reducing reaction with CO. The vaporization rate was estimated using a modified Quann/Sarofim equilibrium-diffusion model.

The experimental results show that the vaporization rate of trace elements is approximately proportional to concentrations, and more elements were vaporized at higher pyrolysis temperatures and at higher oxygen concentration. Calculation shows that the thermodynamic properties for the elements concerned are very different, while the fraction vaporized is in the same order of magnitude.

For those elements(As, Se, Sb) associated with pyrite in coal, the release processes are composed by three series steps: diffusion through the pyrrhotite melt, vaporization at the interface of melt and gas, and transport through the pores of the char. The kinetics of those steps were estimated. The elements organically bounded to the coal can be devolatilized during pyrolysis, and their release rate was approximated using the semi-empirical Arrhenius law for volatile devolatilization.

Thesis Supervisor: Professor Adel F. Sarofim
Title: Professor Emeritus of Chemical Engineering

ACKNOWLEDGEMENTS

First, I would like to express my gratitude to my advisor Adel, F. Sarofim for his advising and supporting during my study at MIT.

Thanks also goes to Profs. John Lienhard and János Beér for their input and time.

Special thanks to Dr. Ilhan Olmez and his assistants: Jianmei Che and Jac Gone. They spent so much time and money on analyzing my samples. Without their help, there would never be such a thesis!

Many thanks to Dr. Connie Senior at PSI for her stimulating discussion and strong leadership on this project.

Thanks to Profs. G. Huffman and F. Huggins at the University of Kentucky, and Dr. R. Finkelman for their characterizing the coal and mineral samples.

Thanks to Prof. J. Helble at the University of Connecticut for his help and suggestion on iron research. Thanks to Prof. M. Wornat at Princeton University for her helpful discussions.

Thanks to Prof. Y. Levendis and Dr. A. Atal at Northeastern University for measuring the coal combustion temperatures. Also thanks to Prof. R. Hurt at Brown University for advising me on using the code for predicting coal combustion temperature. Thanks to Prof. J. Fang and Tony Modestino for their help on preparing coal samples and maintaining experimental facility. Thanks to Prof. J. Howard for revising my paper to Combustion and Flame.

Thanks to my office mate, Angelo Kandas and Jonathan Allen for sharing the office.

Special thanks to Emmi Snyder who helped me in any way she could!

Many thanks to my wife Jennifer for her love, help and patience.

Thanks to US DoE Pittsburgh Energy Technology Center(PETC) for sponsoring the research projects of this thesis.

Tables of Contents

List of Figures

List of Tables

SUMMARY OF WORK

S.1 Summary of Results for Coal Characterization

The coals used in this study include: Illinois No. 6; Pittsburgh seam (washed); A low sulfur bituminous coal, a mixture of the Elkhorn and Hazard seams from eastern Kentucky; and Wyodak subbituminous coal. The coals were first segregated into two narrow size ranges: 45 -63 microns and 90 - 106 microns, and then segregated into three density ranges by using a smaller fluidized-bed reactor(separator). As part of a large project sponsored by the US Department of Energy and EPRI, the compositon and the mineralogy of the coals (both segregated and raw coal) were analyzed using Neutron Activation Analyzer (NAA) at MIT, Computer Controlled Scanning Electron Microscopy (CCSEM), Mossbauer spectroscopy, microprobe, leaching, and X-ray absorption fine structure(XAFS) spectroscopy at University of Kentucky and US Geological Survey (USGS).The main results from this study and from the University of Kentucky and USGS are:

(1) Ash is concentrated in the large dense coal particles;

(2) Nearly all As is associated with pyrites except for Wyodak coal which has very low arsenic content and very low content of pyrites;

(3) Selenium is mainly associated with pyrites, and some of it is organically bound in coal;

(4) Chromium is mainly present tied to the carboxyl ion;

(5) Zinc is mostly in the form of ZnS in Illinois coal, while it may be associated with other minerals in other coals;

(6) Iron is present in the form of pyrites or jarosite.

S.2 Summary of Experimental Studies

S.2.1 Experimental apparatus

Combustion experiments were performed in a laboratory scale laminar flow furnace-the so called drop-tube furnace. And the pyrolysis experiments were performed in the high temperature pyrolysis furnace, which has a very similar structure as the drop-tube furnace. Here a brief description of the drop-tube furnace is presented. The detailed description will be given in Chapter 2. The drop-tube furnace (Figure S-1) is composed of three major parts: the electrically-heated reactor chamber; the feeding system; and the collection probe.

The reaction zone was heated by an externally controlled graphite heating element surrounding the 50 mm inner diameter alumina tube. The total length of the heated section was 430 mm, with the first 120mm used for preheating and distributing uniformly the reacting gases.

In the coal feeder, the nitrogen carrier gas flowing over the surface of the particle bed at the rate of 80 std ml/min. Sample particles were entrained by the carrier gas and were fed into the center of the cylindrical combustion zone in the coaxial direction. The feed rate was kept about 1 gram-coal/hour. Therefore it can be taken as a single particle combustion.

Upon completion of the reaction in the chamber, the gaseous product laden with particulate were pulled through the water-cooled collection probe out of the chamber. A cascade impactor, a Mark II 20-800 non-viable ambient particle sizing sampler manufactured by Andersen 200, Inc., combined with an impactor preseparator, was used to collect and classify the particles.

S.2.2 Experimental results for iron (Fe) transformation

Ash samples were obtained at a fixed gas temperature of 1700K, with different oxygen concentrations of 30%, 40% 60% and 100% oxygen for the Pittsburgh No.8 washed coal. The chemical states of iron was analyzed using Mossbauer spectroscopy,

and some results for the submicron ash particle are presented in Table S-1. It shows that the major compound of iron is glassy iron: for 40% O_2, there is 70% glassy iron, and 30% magnetite, haematite and pyrrhotite; for 100% O_2, there is about 65% glassy iron, and 35% magnetite, haematite, and pyrrhotite. Since silicates can not be devolatilized, the glassy iron can only be formed from the vaporization of silicates, which coagulates with the vaporized iron in the boundary layer surrounding the burning coal particles. This shows that most of the iron in submicron ash particles is from vaporization. The presence of pyrrhotite is solid evidence of fragmentation of pyrrhotite. And magnetite and haematite in submicron ash particles also comes from fragmentation. Since the combustion temperature with 100% O_2 is higher than that with 40% O_2, it can be concluded that at higher combustion temperature, more pyrrhotite will be fragmented, while vaporization is still the main source responsible for submicron iron fume.

In order to further test the conclusions above, another experiment was carefully performed under the conditions to yield a combustion temperature of a coal particle equal to (or almost the same as) the devolatilization temperature using the same coal samples. A result is presented in Table S-2.

Table S-2 Fraction of iron in submicron ash or char particles

Coal type	conditions	temperature (K)	Fraction in submicron particles
PTH90106	**combustion at 10% O_2**	**1950**	**5.1 %**
	pyrolysis	**2040**	**4.1 %**
WY90106	**combustion at 5% O_2**	**1995**	**19.8 %**
	pyrolysis	**2050**	**13.2 %**

From this table it can be seen that the fraction of iron in submicron particles for combustion is always higher than that at pyrolysis condition for the same reaction temperature. The differences between the two reaction conditions for the same coal samples are their chemical compositions at the coal surface: for combustion condition,

the coal particle is under reducing condition since the primary combustion product of carbon is carbon monoxide - CO (Zeng and Fu, 1996); and for the pure pyrolysis condition, the chemical atmosphere is neutral - under argon(Ar). Therefore the vaporization is enhanced by CO. The controlling reaction for the iron vaporization is thus:

$$FeS + CO \leftrightarrow Fe + COS$$

S.2.3 Experimental results for trace elements transformation

In this thesis work, an extensive data base was generated for selected coals under well-controlled conditions in order to delineate the physical processes for trace element vaporization. These data were compared to Quann et al.'s results (1990). And under the same condition, they agreed with each other. A typical result for Arsenic is shown in Figure S-2. From this figure, it can be seen that, the vaporization rate is proportional to the As concentration, because while the of As in samples tested were different, the fractions in the submicron ash particles are nearly the same. The particle size has a small effect on vaporization. The effect of coal type may be attributed to their different combustion temperature under the same conditions.

In order to quantitatively find the effects of combustion temperature on vaporization, a coal, PTH90106, was burned at the same furnace temperature of 1700 K and with different bulk oxygen concentrations of 10%, 20%, 35%, 50%. The result for Arsenic is presented in Figure S-3. It can be seen that, as the oxygen concentrations increases, and the combustion temperature which will be calculated, less As is retained in coarse particles. The higher combustion temperatures facilitate the vaporization in two ways: the diffusivity within the melt is enhanced, and the vapor pressure for the element increases.

S.3 Summary of Results for Modeling

To generalize the experimental data, a model for the physicochemical processes during trace element vaporization was set up for the first time. The model, in turn, further justifies the arguments from the experimental data.

S.3.1 Modeling for iron vaporization

As has been shown, the fraction of iron in submicron particles comes from two sources: iron fume, and vaporization of pyrrhotite under reducing condition. The mechanism for formation of iron fume is very complicated and unclear. The possible explanations are they may be expelled by S_2, or by fragmentation of pyrrhotite during particle heat up. It was discovered that the amount of iron fume is determined by the heat up rate: only at high heat up rate can iron fume be produced. Since the melting point of pyrrhotite is 1356K, pyrrhotite particle can only be fragmented before the temperature reaches 1356K. Therefore, for a fixed heat up rate, the amount of iron fume produced by fragmentation will be negligible after the pyrrhotite is melted.

The amount of iron fume produced by fragmentation can then be found from the devolatilization experiment with the same bulk gas temperature. After subtracting this amount, the remainder of the submicron iron is that produced by vaporization by reduction. This amount can be calculated using Quann's model as shown in Figure S-4 incorporating the CO calculation by Zeng and Fu (1996). A typical result is shown in Figure S-5.

S.3.2 Modeling for trace element devolatilization and vaporization

The vapor pressure for an element is an important factor determining the vaporization properties. In this thesis, the vapor pressures for the selected elements under specified temperature were calculated using the Clausius-Clapeyron equation and the basic data from the JANAF Thermochemical Tables(1985). The calculated results are given in Table S-3.

$$\frac{\ln P_1 - \ln P_2}{\left(\frac{1}{T}\right)_1 - \left(\frac{1}{T}\right)_2} = -\frac{\Delta H}{R}$$

where, the subscripts denote any two different states 1 and 2, P is the vapor pressure.

Table S-3 Equilibrium vapor pressure for pure substances

	Fe	Na	Cr	Co	As	Se
melting point(K)	1808	371	1173	1765	1089	490
boiling point(K)	3023	1154	2963	3373	888	958
vapor pressure at 1473 K(atm)	8.3e-8	1.038	3.31e-7	3e-8	500	68
vapor pressure at 2040K(atm)	6.5e-4	1.435	1.94e-3	3.2e-4	4725	771
total fraction vaporized*	4.1%	32%	35%	26%	36%	>90% (estimated)

*Values for Cr, Co, As are from subtraction of fraction in coarse particle

From the table, it can be seen that, while the equilibrium vapor pressures for the pure substances differ by several orders of magnitude, the fractions of the elements found in the submicron particles are of the same order of magnitude. This shows that, in addition to its physical property, the chemical state - chemical bounding with other elements is also very important.

Characterization of the coal shows that trace elements in coal can be basically categorized into two classes: associated with minerals such as pyrite or weakly bound to the coal matrix. For those elements associated with pyrite, a diffusion-kinetics model was proposed as discussed in the following section. For those elements weakly bound in the coal, the same argument as the volatile devolatilization was made for the devolatilization of trace element. And the fraction by pyrolysis is calculated. For the type of element

presented both in pyrite and in weakly bound state, the fractions from the two processes were calculated respectively.

Those elements associated with pyrite are actually embedded in a liquid melt during coal combustion, because pyrrhotite is at liquid state at a temperature above 1356K, which is well within the range of coal combustion temperature.

Based upon the analyses above, it is proposed here that vaporization of trace element associated with pyrite is composed by four consecutive steps:

(i) transport of molecules or atoms or ions through the bulk liquid melt to the melt surface;

(ii) vaporization at the melt surface/interface;

(iii) transport of vapor through the char pores to the char surface;

(iv) transport through the boundary layer surrounding the char particle, whose resistance is negligible.

Therefore, the overall mass transport coefficient, K, is a function of the liquid phase mass transport, K_L, the vaporization rate, K_E, and the gas mass transport coefficient through the pore, K_U.

$$\frac{1}{K} = \frac{1}{K_L} + \frac{1}{K_E} + \frac{1}{K_U}$$

where K_E can be calculated using Knudsen-Langmuir equation, K_U can be calculated using the Quann's model on transport in pore. K_L can be found using the vaporization rate under different combustion temperature. The model was used to predict vaporization of trace element for other types of coal with different combustion condition. The predicted extent of vaporization agrees well with the experiment.

These elements organically bounded to the coal matrix can be released during devolatilization, which was proved using the ASTM standard pyrolysis procedure and the rapid heat up pyrolysis in drop-tube furnace. Therefore, their release rate was predicted using the semi-empirical Arrhenius law for volatile devolatilization.

Table S-1 Iron distribution on submicron ash particles produced under 40% O_2

Stage	Size range	Compositions	Percentage
8	0.65-1.1	Fe^{++}(glass)	0
		Fe^{+++}(glass)	73
		Fe_3O_4 + -Fe_2O_3	19
		Fe-metal	2
		$Fe_{1-x}S$	6
9	0.43-0.65	Fe^{++}(glass)	0
		Fe^{+++}(glass)	67
		Fe_3O_4 + -Fe_2O_3	22
		Fe-metal	0
		$Fe_{1-x}S$	11
10	<0.43	Fe^{++}(glass)	2
		Fe^{+++}(glass)	73
		Fe_3O_4 + -Fe_2O_3	14
		Fe-metal	2
		$Fe_{1-x}S$	9

Iron distribution on submicron ash particles under 100% O_2

8	0.65-1.1	Fe^{++}(glass)	2
		Fe^{+++}(glass)	58
		Fe_3O_4 + -Fe_2O_3	31
		Fe-metal	5
		$Fe_{1-x}S$	4
9	0.43-0.65	Fe^{++}(glass)	3
		Fe^{+++}(glass)	60
		Fe_3O_4 + -Fe_2O_3	28
		Fe-metal	5
		$Fe_{1-x}S$	4
10	<0.43	Fe^{++}(glass)	2
		Fe^{+++}(glass)	66
		Fe_3O_4 + -Fe_2O_3	20
		Fe-metal	5
		$Fe_{1-x}S$	7

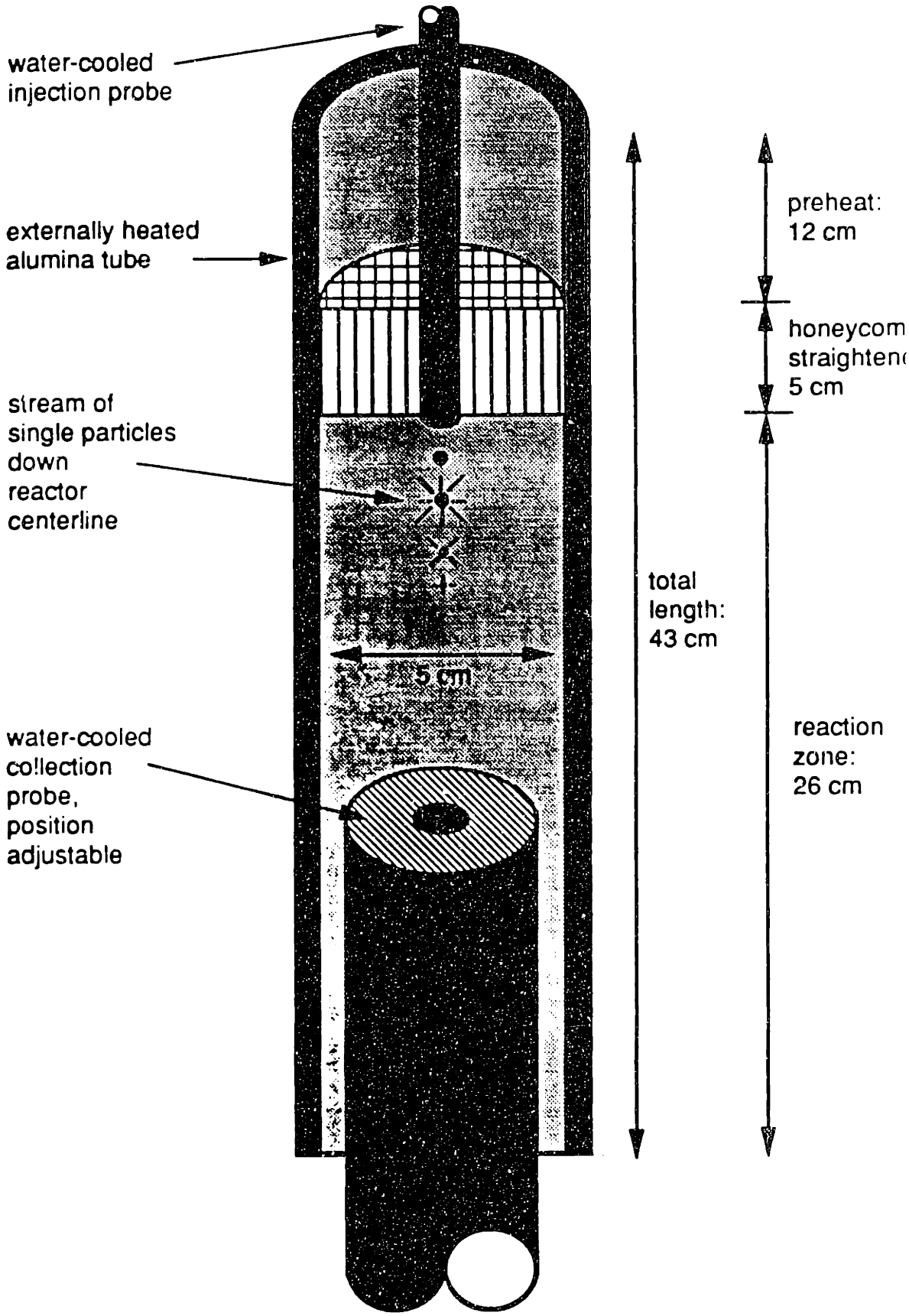

Figure S-1 Laminar flow reactor

Figure S-2 Effects of As concentration in the coal on the total As collected in submicron ash particles

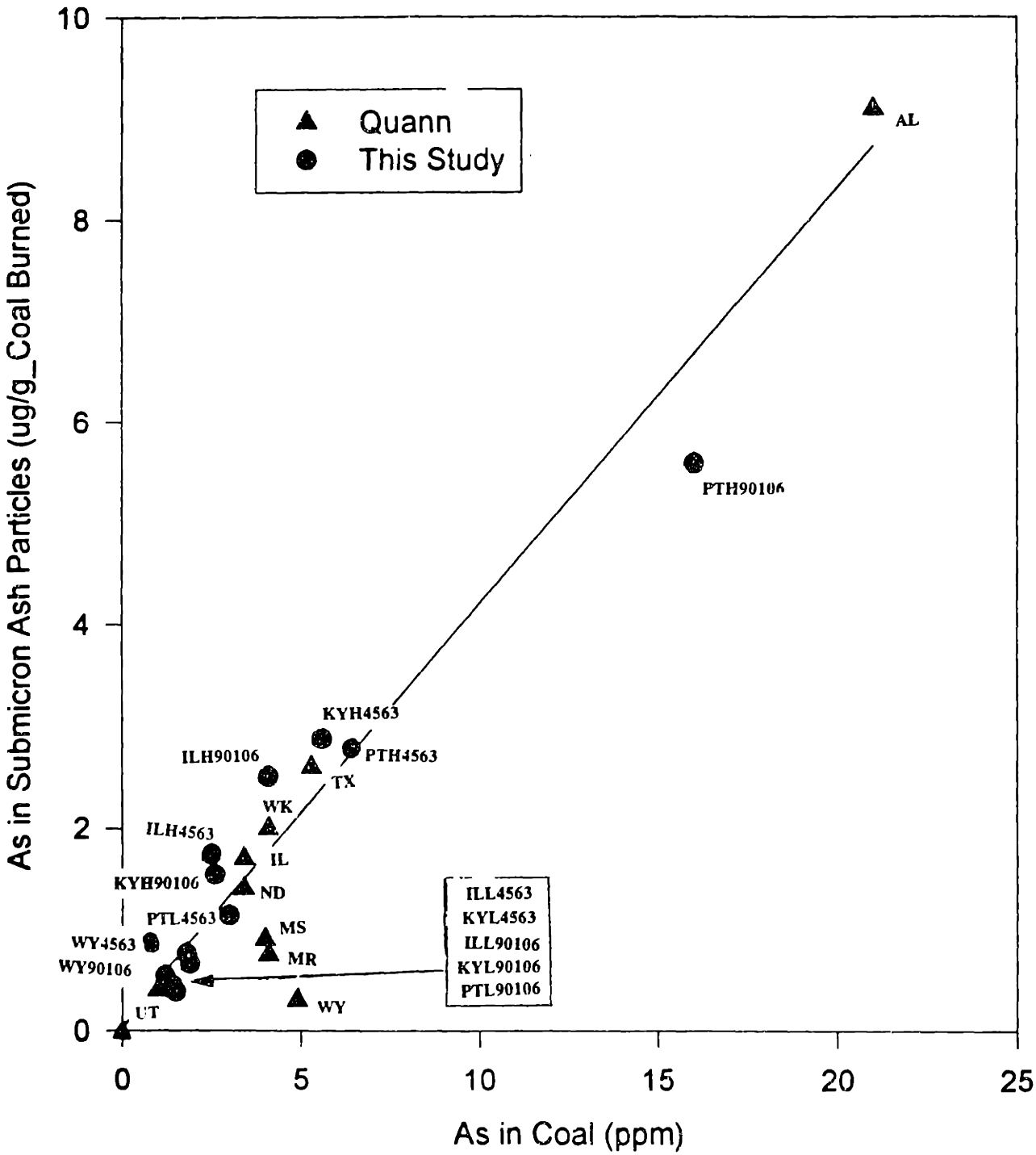

Figure S-3 Effects of pyrolysis temperature and CO2 concentration on the fractions of As retained in the coarse particles (%)

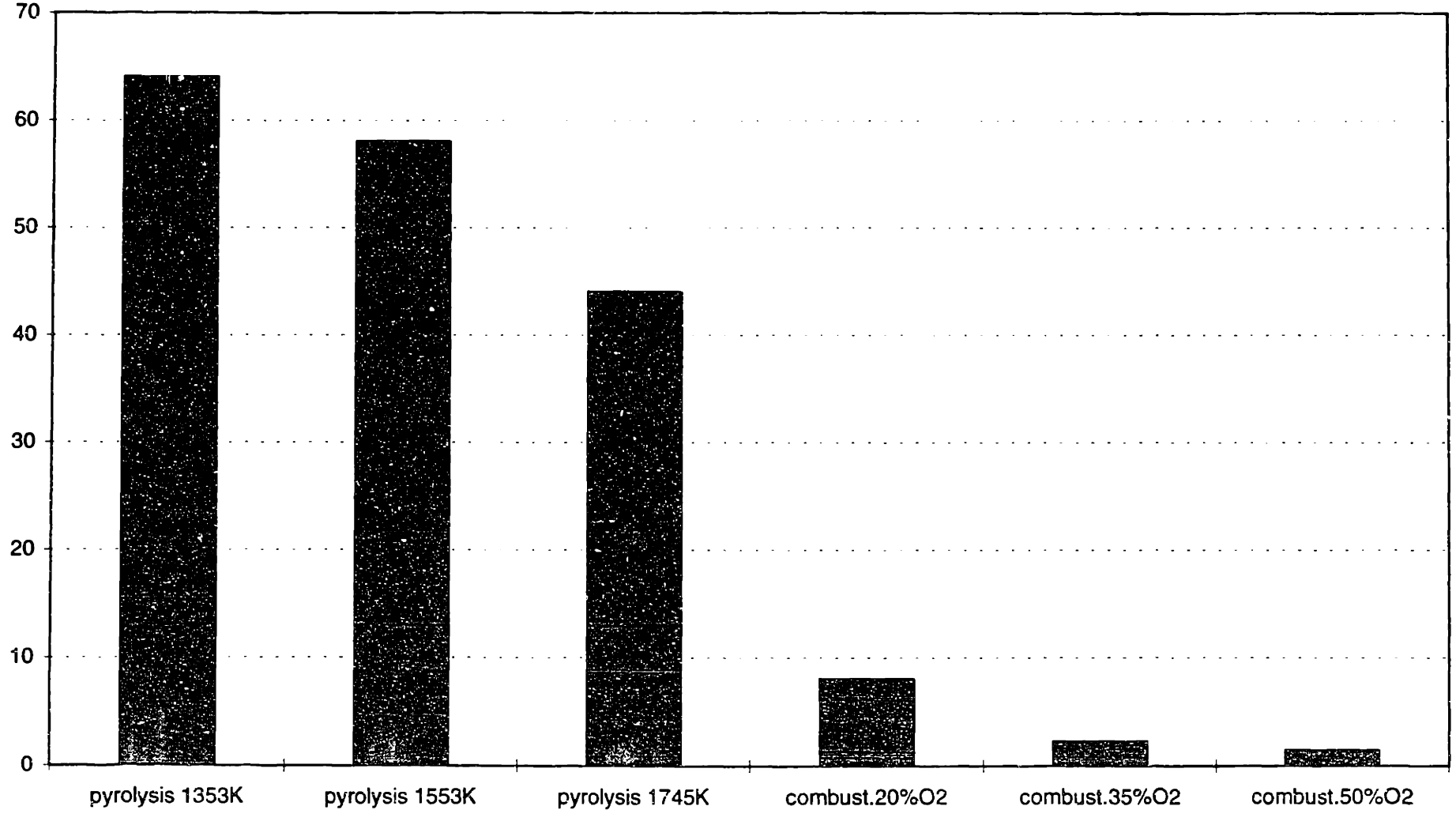

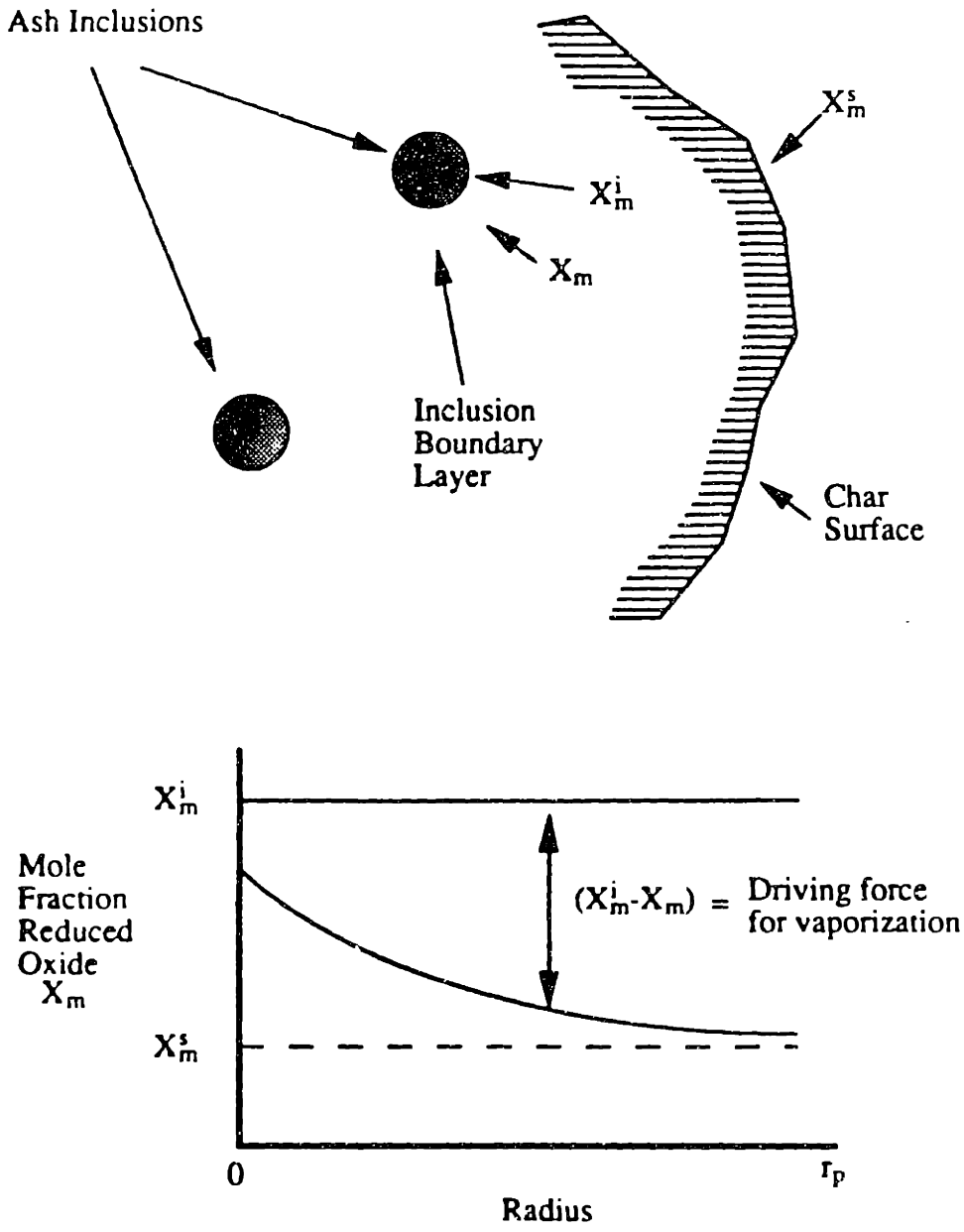

Where:

X_m = mean field mole fraction metal vapor species

X_m^i = mole fraction metal vapor species at inclusion surface

X_m^s = mole fraction metal vapor species at char surface

Figure S-4 Vaporization model

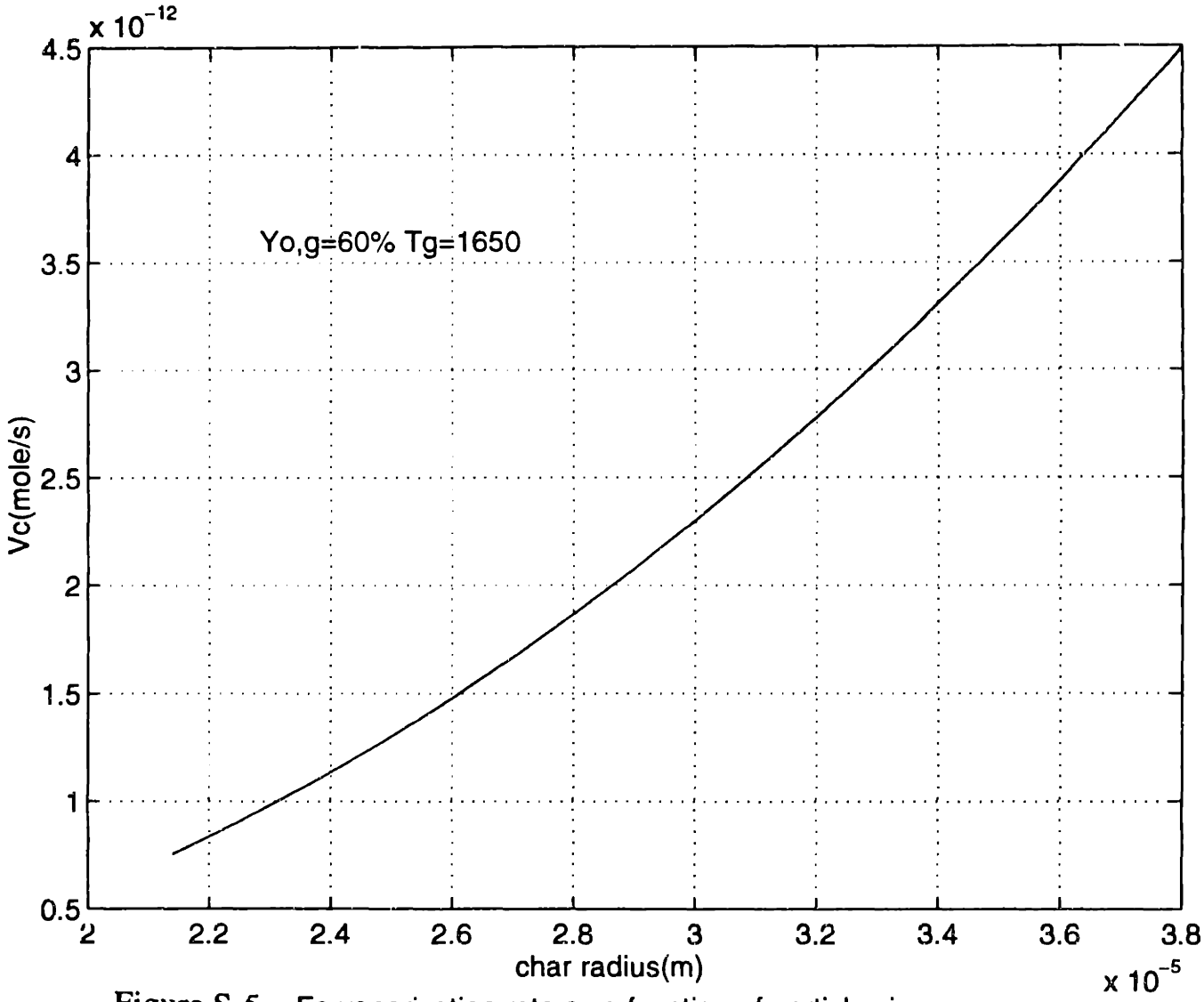

Figure S-5 Fe vaporization rate as a function of particle size

Chapter 1 INTRODUCTION

During the past two decades, coal consumption in the United States has been continually increasing, to the point where it represents 22% of the energy consumed in this country, and more than 50% of the electrical power (Helble, 1987). Compared to natural gas and oil, coal is a "dirtier" resource, because it contains minerals and can release pollutants during combustion such as CO_2 and toxic substances such as NO_x, SO_x, and hazardous air pollutants such as As, Se, Hg et al. To reduce the negative impacts by fossil fuel combustion, one way is to improve the combustion efficiency, the other way is to find a method to reduce and remove the pollutants from the combustion products. Knowledge of the behavior of mineral matter during combustion is important because it determines the distribution of elements as a function of particle size, which is needed for evaluation of collection efficiency in the air pollution control.

1.1 Mineral matter transformation

Pulverized coal combustion is the most widely used method of coal utilization in coal-fired power stations. In pulverized coal combustion, coal is pulverized to small particles with size less than 120 microns, and is injected into a furnace where it is burned in preheated air. Combustion of pulverized coal in the combustion chamber generates heat and the particulate-laden flue gas. The highest gas temperature in the chamber is between 1500 to 2000C dependent upon the combustion intensity chosen. After losing about 40% of the heat generated to the surrounding evaporator tubes mainly by radiation, the flue gas passes over various stages of superheater, reheater and ecomomizer surfaces, to which it loses another 40% heat by a combination of radiation and convection. Finally, a further 10% is transferred to the preheater air. About 10% is lost to the atmosphere through the chimney as sensible and latent heat.

The fly ash particles generated during combustion are carried through different stages of the furnace and some of them deposit on each possible surface of the system.

The result of ash deposition on walls is either called "slagging" or "fouling". The term "slagging" refers to liquid layer deposit generally on furnace walls in proximity to the flame, and the term "fouling" refers to a dry, powdery deposition of ash on convective heat transfer surfaces. This slagging and fouling behavior, which is closely related to the fly ash particle size and chemical compositon, lowers heat transfer efficiency and necessitates periodic cleaning.

Researchers have developed various fundamentally-based boiler performance models incorporating coal particle combustion, boiler aerodynamics and heat transfer, ash formation and ash properties. It is found that the propensities of slagging and fouling are generally determined by the ash particle size and the chemical compositions of the ash particles.

It was shown by many researchers (see Figure 1-1) that there are two major, distinct types of fly ash during combustion. One type has a particle size around 0.1 microns in aerodynamic diameter (submicron ash), and the other type ranges from 1 to 50 microns (residual ash). There two types of fly ash are produced through two different mechanisms. The submicron ash is from the vaporization and recondensation of mineral matter as suggested by some researchers, or from the fume by fragmentation of mineral matter as suggested by other researchers, which will be discussed in the next section. The larger, residual ash is formed by coalescence and shedding of mineral matter included in the coal particles.

Submicron ash formation

Previous studies on the submicron ash formation (Schmidt et al,. 1976; Flagan, 1978; Neville et al., 1981; Linak and Peterson, 1986) suggest the following scenario as a submicron ash formation mechanism. During combustion, a certain fraction of the mineral matter in coal particles vaporizes under reducing atmosphere. The inorganic vapor nucleates homogeneously thus yielding a lot of fine particles with diameter less

than 0.01 microns. These particles coagulate with each other to generate bigger particles with sizes up to about 0.05 microns for the typical conditions (fraction of ash vaporized, residence time). Heterogeneous condensation also take place in addition to the homogeneous nucleation.

Studies were performed in Sarofim 's group to testify the important question on this scenario. And it was confirmed that the vaporization and condensation mechanism as a convincing submicron ash formation mechanism for some selected inorganic (Quann and Sarofim, 1982; Neville and Sarofim, 1982; Neville and Sarofim, 1985; Graham, 1991). Single-particle experiment and ash samples collected from power station show that the submicron ash particles produced are enriched in iron, magnesium, potassium and sodium while they are depleted in aluminum and calcium. This enrichment is believed to be from the vaporization of the more volatile species and their condensation on very fine ash particles which provides most of the surface area.

Based upon the experimental results, and by neglecting the interaction between minerals in coal, Quann and Sarofim (1982) proposed a mechanism to explain the vaporization of refractory oxides. By assuming that the reducing reaction

$$MO_n + CO = MO_{n-1} + CO_2$$

is at equilibrium at the surface of a mineral inclusion, the vaporization rate and amount of refractory vaporization were predicted to vary with the inclusion size. This model has been successfully applied to the oxides of CaO, MgO and SiO_2.

Fragmentation is also an important source for submicron ash particles (Baxter, 1992; Raask, 1984). For example, during the heat up of pyrite particle the pressure of the sulfur vapor within the particle is high enough to fragment the pyrite grain into some 0.1 - 0.5 microns(Raask, 1984).

Residual ash formation

During combustion at typical pulverized coal-fired boiler conditions, about 99% mineral is presented in coarse ash particles with size greater than 1 micron. It was observed that the bulk of the mineral matter coalesces to form spherical ash droplets on the char surface. If the char particle remains intact throughout combustion, one fly ash particle will be generated by each coal particle. The ash droplet on the surface usually grows in size as the char surface recedes. Growth of ash droplets occur by either the drawing together and coalescence of smaller mineral inclusions, or by the addition of the atomically dispersed elements to existing ash particles. The number of ash particles and the size of an ash particle generated by one coal particles are therefore determined by the competition between the coalescence of ash particles on the char surface and the shedding and fragmentation from char particle.

Fragmentation of char generally is believed to be from the formation of cenosphere (Wibberley and Wall, 1986). This was confirmed by Kang , Sarofim and Beer (1992). They found that increased macroporosity can result in a reduction in the coalescence of smaller mineral inclusions with an attendant decrease in the size of the maximum of the intermediate fraction from 4 to 2.5 microns.

1.2 Transformation of Iron During Combustion

Iron, predominately in the form of minerals as pyrite(FeS_2), siderite($FeCO_3$), and jarosite ($KFe_3(SO_4)_2(OH)_6$), is generally believed to be the major mineral in determining the stickiness or viscosity of a ash particle(Wall, 1992; Srinivasachar, et al., 1992). Wall (1992) and Raask (1985) outlined the association of iron with deposition from four sources:

(a) An oxide fume from organically associated iron;

(b) Larger oxide ash particles;

(c) Molten sulfide and oxide particles from partially oxidized pyrite;

(d) Fused silicates with dissolved iron;

Iron can be categorized into the so-called inherent part, which is closely associated with pulverized coal and is not separated from a coal particle before combustion, and the extraneous part, which is essentially carbon-free mineral matter. The decomposition and oxidation of pure pyrite particle have been studied(Jorgensen, 1981;Srinivasachar and Boni, 1989). It was proposed that the reaction proceeded through the following four stages: heating to the ignition temperature, decomposition to pyrrhotite - $Fe_{1-x}S$ (970K), formation of Fe-S-O melt, and subsequent oxidation to magnetite(Fe_3O_4) and haematite(Fe_2O_3). The steps requiring the greatest time were predicted to be pyrrhotite oxidation, which is determined by the diffusion of oxygen through the melt, and magnetite crystallization. The reaction time in the molten state was found to be approximately proportional to the square of the particle size.

Transformation of inherent pyrite is rather complicated. It was believed that when inherent pyrite was heated up, a significant of pyrite fume was produced(Baxter and Mitchell, 1992; Groves et al., 1987; Raask, 1985). Furthermore, Baxter and Mitchell found that iron was released within a 25 ms period immediately following or during coal devolatilization. If this is true, then the iron state in the submicron ash particles will be pyrrhotite, magnetite and haematite. In those studies, the interaction or sintering of pyrite with other minerals, especially alumina silicates was overlooked. A good study performed by Bool et al. (1995) combined the formation of silicate iron and the crystallization of pyrrhotite melt. However, the formation of submicron ash particles was not included in this study.

In summary, much of the mechanism governing the transformation of iron has been revealed. The formation of iron silicates can be well explained and predicted using Bool's model. The formation of iron in submicron ash particle is still not very clear. Whether it is from the direct devolatilization or from the reduction of pyrrhotite melt is not resolved. The interest of this thesis study is to: (1) provide direct evidence on how submicron iron ash is produced; (2) to predict the formation rate of iron fume.

1.3 Transformation of Toxic Elements During Coal Combustion

Of the 189 substances identified as hazardous pollutants by Title of the 1990 Clean Air Act Amendments (CAAA), 37 species, including 11 metals, have been detected by the Electric Power Research Institute (EPRI) in the flue gases of pulverized coal-fired boilers. Over the past decade, a large database identifying the partitioning and emitted concentrations of several of these species has been developed. Laboratory data have also been generated to help define the general behavior of several elements in combustion systems. These data have been used to develop empirical and probabilistic models to predict species emissions. While useful for providing average emissions of toxic species, these empirically based models fail when extrapolated beyond their supporting database.

Behavior of toxic species in combustion system - field studies

Several studies have been conducted to measure the partitioning of trace and toxic species in the effluent stream of coal fired utility boilers. One of the major efforts is the current Power Plant Integrated Systems Chemical Emissions Study (PISCES) led by EPRI. Within PISCES, EPRI performed an extensive literature search on the partitioning of toxic and trace species into the various output streams of power plants. Extensive field testing was also conducted to measure the concentrations of 22 species in the outputs of selected power plants(Chow and Torrens, 1994).This effort has resulted in the development of a large database on the emissions of toxic and trace elements(Wetherhold and Chow, 1991) Meserole and Chou(1991) used these data to describe the average volatilization and condensation behavior of several species. They found that several elements, including As, Cd, Hg and Se, typically volatilize in utility boilers. Some of these elements condense on fly ash and are removed by pollution control devices. Others, such as Hg, F, and Cl, typically are emitted as vapors. However, significant variations in trace element behavior were noted, possibly caused by interaction with other minerals or differences in mode of occurrence. This was emphasized by Meij(1994), who observed

large differences in As and Hg partitioning as coal type was varied in one utility boiler unit. These differences were attributed to differences in the mode of occurrence and the combustion transformations (speciation) of these metals. If the fundamental mechanisms that govern the behavior of these species were understood, the utility industry could better predict emission rates. This need increases in importance when unique fuels, equipment configurations, and operation conditions are considered.

Other investigators have studied the behavior of trace and toxic species in laboratory coal combustion systems. Much of this work has been discussed in several recent review papers (Brooks, 1989; Linak and Wendt, 1993; Clarke and Sloss, 1992). Despite these efforts, mechanistic information is generally lacking. For example, Linak and Wendt presented the results from several laboratory and field studies on the enrichment of trace elements in the submicron ash. Although the data set is not entirely consistent for all species, it does show enrichment of several elements in the submicron ash (which is most likely to escape particulate control devices). These elements include Sb, As, Cd, Cr, Pb, Hg, Ni, and Se. Other elements, such as Cl, were found to remain in the vapor phase.

Meij et al., and others have suggested grouping elements with similar observed combustion behavior in utility power boilers. A typical categorization of elements is reproduced in Figure 1-2. Volatile species are generally grouped into one set, species with limited volatility are placed in a second group, and the elements that show little or no volatility are placed into a third group. Low volatility species(Group 1) tend to be easily captured with the bottom ash and fly ash. Group 2 elements may go through a vaporization-condensation mechanism but are typically removed with the fly ash. These elements will therefore not contribute to air emissions, but may contribute to water or soil contamination when the fly ash is landfilled if toxic species are present as a surface coating or in water-soluble form. Group 3 elements typically escape the particulate control devices as either a vapor or a submicron aerosol. This last group is of critical importance for air toxic emissions from coal combustion systems.

Organic toxins may also be emitted from coal fired systems. Field studies have suggested that the emission of organic species from coal-fired power plants is tied to the combustion efficiency but is typically very low (Sage and Williamson, 1993; Miller et al. 1994). During EPRI's PISCES field testing project, Chu et al. (1993) found that the emissions of volatile organic compounds were consistently very low - from 0.5 to 10 micrograms/m^3. Poly-aromatic hydrocarbons were typically in the ng/m^3 range, while aldehydes and dioxins were generally at or below their detection limits of 5 to 10 micrograms/m^3 and picograms/m^3, respectively, during steady state operation. Based on these results, organic toxic species emissions, while they do occur, are typically much less than the emissions of inorganic toxic species. This suggest that under normal operating conditions, the organic hazardous air pollutant emissions from pulverized coal are not likely to be excessive relative to Title III requirements, provided good furnace combustion conditions are maintained (Miller et al. 1994).

Prior laboratory results on toxic partitioning

Previous mineral matter transformation work has demonstrated the critical importance of the form or modes of occurrence of species in coal on their behavior during combustion(Helble, et al., 1992; Zygarlicke et al. 1991). For example, organically associated metals such as sodium typically vaporize during combustion as do many alkali salts. Metals contained in clays typically do not vaporize. This dependence of combustion behavior on the form of the species in the coal also holds true for many trace elements. Helble(1994) suggested that the volatility of Cr and Mn is dependent on elemental form. Quann et al.(1990) noted the importance of form in an earlier systematic 20-coal study conducted at MIT. The coals were all burned at a furnace temperature of 1750K in air so that the effect of coal type could be separated from that of furnace type and combustion conditions. For some metals, coal rank (and presumably elemental form) affected vaporization. In the case of zinc, the vaporization fraction was different for the lignite and the bituminous coals. The explanation for this is likely a difference in the form of zinc in

the bituminous coals and the lignite. The zinc was thought to be present in extraneous sphalerite (ZnS) for the lignite and to be included in the organic matter for the bituminous coals. The zinc in the bituminous coals will vaporize to a large extent because it is subjected to a higher temperatures and locally reducing conditions during combustion. The vanadium and chromium in the fume were interesting as they correlated with the amount of silicon in the fume (Figure 1-3). This is believed to be a result of the association of the chromium and vanadium with the alumino-silicates in the coals. These results underline the importance of characterizing the distribution of the trace elements in the coals in order to understand their combustion behavior.

Another important issue that must be addressed in describing the behavior of toxic species is the important combustion mechanisms that govern behavior. For example it is unknown whether trace element behavior differ under staged, initially reducing (low-NO_x) conditions, It s unknown whether the use of low ash beneficiated fuels increases the volatile fraction of trace toxic elements by decreasing the probability of trace/mineral coalescence.

Concentration and modes of occurrence of trace species in coal

In his book on trace elements, Swaine (1990) considered 22 trace elements in coal to be of possible significance in environmental issues arising from coal utilization. These 22 elements include all the elements to be studied in this thesis : specifically , the 11 trace elements(Sb, As, Be, Cd, Cr, Co, Hg, Mn, Ni, Pb and Se) explicitly identified in the 1990 CAAA, two radionuclides(U and Th), as well as a number of other elements(B, Cu, Mo, Sn, Tl, V, and Zn) of environmental concern only in coals of unusually high abundance of the given element. These elements are listed in Table 1-1, and the range for their concentration in U.S. coals is shown. There is a great deal of variation, not only in the concentrations of the different elements, but also in the range (typically>100 fold) of concentration exhibited by each element. However, the concentration of the element is

one important factor that must be considered in order to assess the environmental impact of a specific element in coal utilization; mode of occurrence is another.

The mode of occurrence of an element is important because of the tremendous diversity in which an element can be found in coal. As indicated in Figure 1-4, an element may be completely dispersed throughout the coal macerals or can exist within a discrete mineral phase. Such differences in mode of occurrence will greatly influence the behavior of an element in many coal utilization processes, notably its partitioning during coal cleaning by conventional processes, its susceptibility to oxidation upon exposure to air, as well as physical properties upon heating. A preliminary laboratory study (Huggins et al. 1994) has suggested that the behavior of arsenic during combustion, will be determined by whether arsenic is present as a substitutional element for sulfur in pyrite or is present in oxidized form as arsenate minerals. The former mode undergoes explosive volatilization, in which most of the arsenic will be volatilized, either as arsenic vapor or as fine particle arsenic oxide, the latter mode will fuse, react, and be assimilated as arsenate the aluminosilicate fly ash particles. Therefore, arsenic associated with pyrite will be much more likely to escape in flue gases.

There is much that we do not know regarding the modes of occurrence of many elements, as is indicated by the frequent question marks in Table 1-1. The F.R.I. values, suggested by Finkelman, indicate the degree of confidence (0 lowest, 8 highest) in the reported modes of occurrence for a given element. Furthermore, relatively little is known about how an element's mode of occurrence varies with coal rank, depositional environment, etc., making it difficult to generalize about how a given element occurs in different coals. Most of the direct evidence for element modes of occurrence comes from observations using optical or scanning electron microscopy (Finkelman and Stanton, 1978) or microprobe analysis methods(Ruppert, et al., 1992; Finkelman, et al., 1984; Morelli, et al. 1988). Furthermore, because discrete mineral occurrences have the highest concentrations of the element of interest, there is likely to be a bias to find such element modes of occurrence. Recently, X-ray absorption fine structure (XAFS) spectroscopy has

been shown (Huggins, et al., 1993) to be useful for the identification of modes of occurrence for various trace elements, down to concentrations as low as 5ppm.

Mechanisms for transformation of trace element during coal combustion

As discussed above, most of the trace elements are more or less associated with the major minerals. For those trace elements closely associated with major minerals, their transformations are basically determined by the transformation of major minerals. For example, if arsenic is embedded in pyrite, then the fate of arsenic is dependent upon the properties and transformation of pyrites. In last section, it is found that, during ash formation, mineral form and combustion conditions are both of critical importance in shaping ash size and composition distribution. At fixed combustion conditions, the mineral type, size, abundance, and degree of association with the organic matter in coal were the primary factors affecting ash formation. This held true regardless of the scale of combustion facility over the range of facilities from drop-tube furnace (1 gram/hour) to industrial boiler. Helble et al.(1994) showed that mineral effects are of primary importance in fly ash formation from ash samples from utility boiler, while combustion conditions also plays a significant role in submicron ash formation.

Figure 1-1 provides the transformation pathways for major mineral matter. Non-volatile mineral species fragment, oxide, and/or coalesce with other minerals during the combustion process. Certain elements vaporize during the combustion processes. The vaporized species then oxidize, heterogeneously condense or react with existing ash particle, or coagulate with other elements in the boundary layer surrounding the particle, or nucleate to form submicron particles. Particle growth occurred by condensation and coagulation.

These same mechanisms that were found to control major species behavior will control the formation and partitioning of toxic species during combustion. In order to better understand how each of these mechanisms affects the behavior of toxic species

during combustion it is important to perform carefully controlled combustion tests under various combustion conditions. These tests, in conjunction with careful analysis for form and concentration of the trace metals in the coals, are necessary to determine the effect of "real-world" combustion environments on trace element behavior. This is especially important for identifying those species where equilibrium analysis is inappropriate. Specifically, these tests are necessary to develop a better understanding of the parameters that control trace element behavior and to develop fundamentally based models to predict this behavior.

1.4 Objective and Approaches of Study

The objective of this thesis is to find out the mechanism governing the transformation of iron and trace elements during coal combustion: specifically, (a) to experimentally determine whether the formation of iron on submicron ash particles is by vaporization or by devolatilization or both, and the governing processes for these mechanism; (b) to experimentally determine the vaporization rates for trace elements and, based upon the analyses of the data, to find out the mechanisms on how trace elements is released from coal, and then to propose a quantitative model for the transformation processes. The specific approaches are:

(a) To use some advanced instruments to characterize the mineral composition and chemical states of iron and trace elements in coals and in ash samples(most of the work was done at the University of Kentucky and the USGS);
(b) To experimentally investigate the effect of ash size on the chemical states of iron in ash samples;
(c) To study the mechanisms governing the vaporization of iron;
(d) To experimentally study the vaporization rates of trace element under well controlled conditions for well classified coal samples;
(e) To investigate the influences of various factors such as combustion temperatures, inclusion size, the associations between different elements on the vaporization of trace

element; and finally to develop a model to quantitatively explain and predict the vaporization processes.

1.5 Thesis Outline

In the following chapter (Chapter 2), the experimental apparatus and procedure is described. Chapter 3 summarizes the results on coal characterization. Iron transformation is studied in chapter 4, which includes both experimental results and modeling. Chapter 5 contains studies on trace element transformation. Conclusions from this thesis are given in chapter 6.

References

Baxter, L. L., Char Fragmentation and Fly Ash Formation During Pulverized-Coal Combustion, Combust. Flame 90:174-184, 1992

Baxter, L. L., and Mitchell, R. E., The Release of Iron during the Combustion of Illinois No. 6 Coal, Combust. Flame 88: 1-14, 1992

Bool, L. E., Peterson, T. W., and Wendt, J. O. L., The Partitioning of Iron during the Combustion of Pulverized Coal, Combust. Flame 100: 262-270, 1995

Brooks, G., Estimating Air Toxics Emissions from Coal and Oil Combustion Sources, Report to US EPA, NO. PB89-194229, 1989

Chow, W., and Torrens, I. M., American Power Conference, Chicago, IL, 1994

Chu, P., Nott, B., and Chow, W., 2nd International Conf. On Managing Hazardous Air Pollutants, 1993

Clarke, L. B., and Sloss, L. L., Trace Elements - Emissions from Coal Combustion and Gasification, IEA Coal Research , Report IEACR/49, London, United Kingdom, 1992

Flagan, R.C., Seventeenth Symposium (International) on Combustion, The Combustion Institute, p.97, 1978

Finkelman, R. B., Simons, D. S., Dulong, F. T. and Steel, E. B., Int. J. Coal Geol. 3:279, 1984

Finkelman, R. B., and Stanton, R. W., Fuel 57:763-768, 1978

Graham, K. A., Submicron Ash Formation and Interaction with Sulful Oxides During Pulverized Coal Combustion, MIT PhD thesis, 1991

Groves, S. J., Williamson, J., and Sanyal, A., Fuel 66:461, 1987

Helble, J. J., Bool, L. E., Senior, C. L., Sarofim, A. F., Zeng, T., Huffman, G. P., Huggins, F. E., and Shah, N., Fundamental Study of Ash Formation and Deposition, Quarterly Report to DoE/PETC (Contract No. DE-AC22-93PC92190), May, 1994

Helble, J. J., Srinivasachar, S., Wilemski, J., Boni, A. A., Kang, S. G., et al., Transformation of Inorganic Coal Constituents in Combustion Systems, PSI Final Report to DoE/PETC (contract No. DE-AC22-86PC90751, Nov. 1992

Helble, J.J. Mechanisms of Particle Formation and Growth During Pulverized Coal Combustion, MIT PhD thesis, 1987

Huggins, F. E., Huffman, G. P., and Helble, J. J., 2nd International Conf. On Managing Hazardous Air Pollutants, 1994

Huggins, F.E., Shah, N., Zhao, J., Lu, F., and Huffman, G. P., Energy and Fuels 7: 482-489, 1993

Jorgensen, F. R. A., Combustion of Pyrite Concentrate Under Simulated Flash-Smelting Conditions, Trans. Instn. Min. Metall. 90: C1-C9, 1981

Kang, S. G., Sarofim, A. F., and Beer, J. M., Effect of Char Structure on Residual Ash Formation during Pulverized Coal Combustion, Twenty-fourth Symposium (International) on Combustion, The Combustion Institute, pp.1153-1160, 1992

Linak, W. P., and Wendt, J. O. L., Prog. Energy Comb. Sci. 19:145-185, 1993

Linak, W. P. and Peterson, T. W., Twenty-first Symposium (International) on Combustion, The Combustion Institute, p.399, 1986

Meij, R. American Power Conference, Chicago, IL, 1994

Meserole, F. B., and Chow, International Conf. On Managing Hazard Air Pollutants: State of the Art, Palo Alto, 1991

Miller, C. A., Sravistava, R. K., and Ryan, J. V., Environ. Sci. Tech. 28 : 5, 1994

Morelli, J. J., Hercules, D. M., Lyons, P. C., Palmer, C. A., and Fletcher, J. D., Mikrochim. Acta (wien) 111:105, 1988

Neville, M., Quann, R. J., Haynes, B. S., and Sarofim, A. F., Eighteenth Symposium (International) on Combustion, The Combustion Institute, p.1267, 1981

Neville, M., and Sarofim, A. F., Nineteenth Symposium (International) on Combustion, The Combustion Institute, The Combustion Institute, p. 1441, 1982

Neville, M., and Sarofim, A. F., The Fate of Sodium During Pulverized Coal Combustion, Fuel 64: 384-390, 1985

Quann, R. J. and Sarofim, A. F., Nineteenth Symposium (International) on Combustion, The Combustion Institute, The Combustion Institute, p. 1429, 1982

Quann, R. J., Neville, M. and Sarofim, A. F., A Laboratory Study or the Effect of Coal Selection on the Amount and Composition of Combustion Generated Submicron Particles, Combust. Sci. Tech. 71: 245-265, 1990

Raask, E., Mineral Impurities in Coal Combustion, Behavior Problems and remedial Measures, Hemisphere Publishing, 1985

Raask, E. J. Inst. Energy 57:231, 1984

Ruppert, L. F., Minkin, J. A., Mcgee, J. J., and Celil, C. B., Energy and Fuels 6: 120-126, 1992

Sage, P.W. and Williamson, F., 2nd International Conf. On Managing Hazardous Air Pollutants, 1993

Schmidt, E.W., Gieseke, J. A. and Allen, J. M., Atmospheric Environment 10:1065, 1976

Srinivasachar, S., Senior, C. L., Helble, J. J., and Moore, J. W., A Fundamental Approach to the Prediction of Coal Ash Deposit Formation in Combustion Systems, Twenty-fourth Symposium (International) on Combustion, The Combustion Institute, pp.1179-1188, 1992

Srinivasachar, S., and Boni, A., A Kinetic Model for Pyrite Transformations in a Combustion Environment, Fuel 68:829-836, 1989

Swaine, D. J., Trace Elements in Coal, Butterworths, London, 1990

Wall, T. F., Mineral Matter Transformations and Deposition in Pulverized Coal Combustion, Twenty-fourth Symposium (International) on Combustion, The Combustion Institute, pp. 1119-1126, 1992

Wibberley, L.J. and Wall, T. F., Comb. Sci. Tech. 48:177, 1986

Wetherhold, R. G., and Chow, W., International Conf. On Managing Hazard Air Pollutants: State of the Art, Palo Alto, 1991

Zeng, T. and Fu, W. B., The Ratio CO/CO_2 of Oxidation on a Burning Carbon Surface, Combust. Flame 107:197-210, 1996

Zygarlicke, C. J., Toman, D. L., Erickson, T. A., Ramanathan, M. and Folkedahl, B. S., Combustion Inorganic Transformations, UND EERC Final Report to DoE/PETC (Contract No. De-FC21-86MC10637), 1991

Table 1-1 Elemental modes of occurrence in coal after Swaine, Finkelman, and others

Element	Abundance (ppm)	Modes of Occurrence	F.R.I.
Antimony	<0.1 - 40	Sulfides, pyrite	4
Arsenic	<1 - 250	As for S in pyrite	8
Beryllium	<1 - 30	Clays?, org. assoc.?	4
Boron	<1 - 500	Clays, org. assoc.	—
Cadmium	<0.1 - 10	ZnS, clays?, carbonates?	8
Chlorine	100 - 8000	Maceral moisture, NaCl?	—
Chromium	1 - 100	Clays?, $FeCr_2O_4$?, CrOOH?	2
Cobalt	<1 - 50	Sulfides?, clays?	4
Copper	<1 - 200	Sulfides?, org. assoc.?	—
Fluorine	<20 - 1000	Fluorapatite, clays	—
Lead	<1 - 100	PbS, pyrite, PbSe	8
Manganese	5 - 1000	Org. assoc., carbonate, other	8
Mercury	0.01 - 10	Sulfides?, Hg?, org. assoc.?	6
Molybdenum	0.5 - 50	Pyrite, MoS_2?, org. assoc.?	—
Nickel	<1 - 100	Sulfides, org. assoc.?	2
Selenium	0.1 - 20	Org. Se, sulfides, etc.	8
Tin	0.1 - 20	Oxides, sulfides, org. assoc.	—
Thallium	0.1 - 3	Sulfides	—
Thorium	<0.1 - 50	Monazite, zircon	—
Uranium	0.1 - 50	Org. assoc., var. minerals	—
Vanadium	<1 - 300	Clays, org. assoc.?	—
Zinc	1 - 300	ZnS, org. assoc.?	—

*F.R.I. - Finkelman Reliability Index [18]

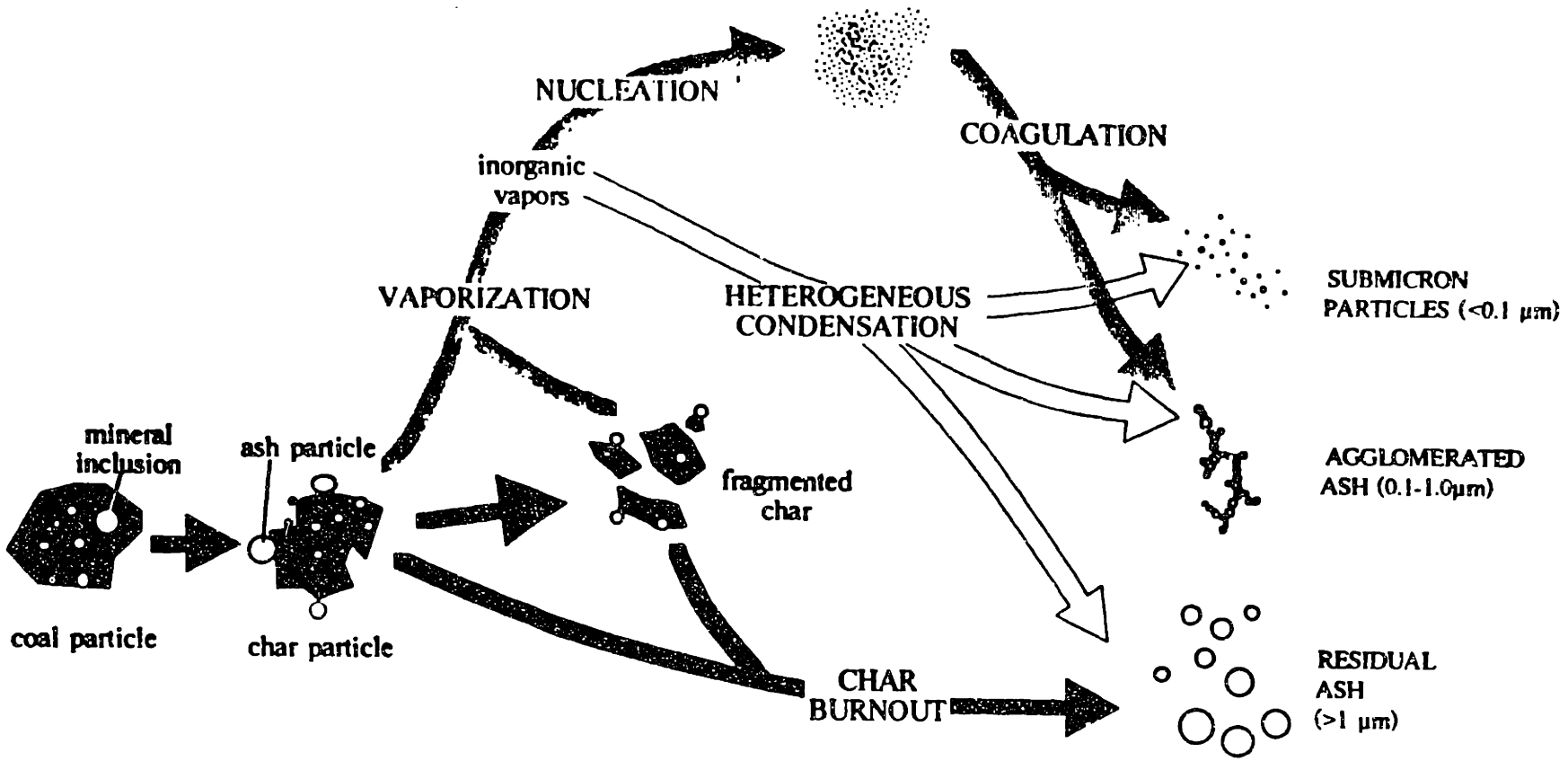

Figure 1-1 A schematic diagram of ash formation processes: submicron ash and residual ash formation processes are shown in the diagram (Helble, 1987).

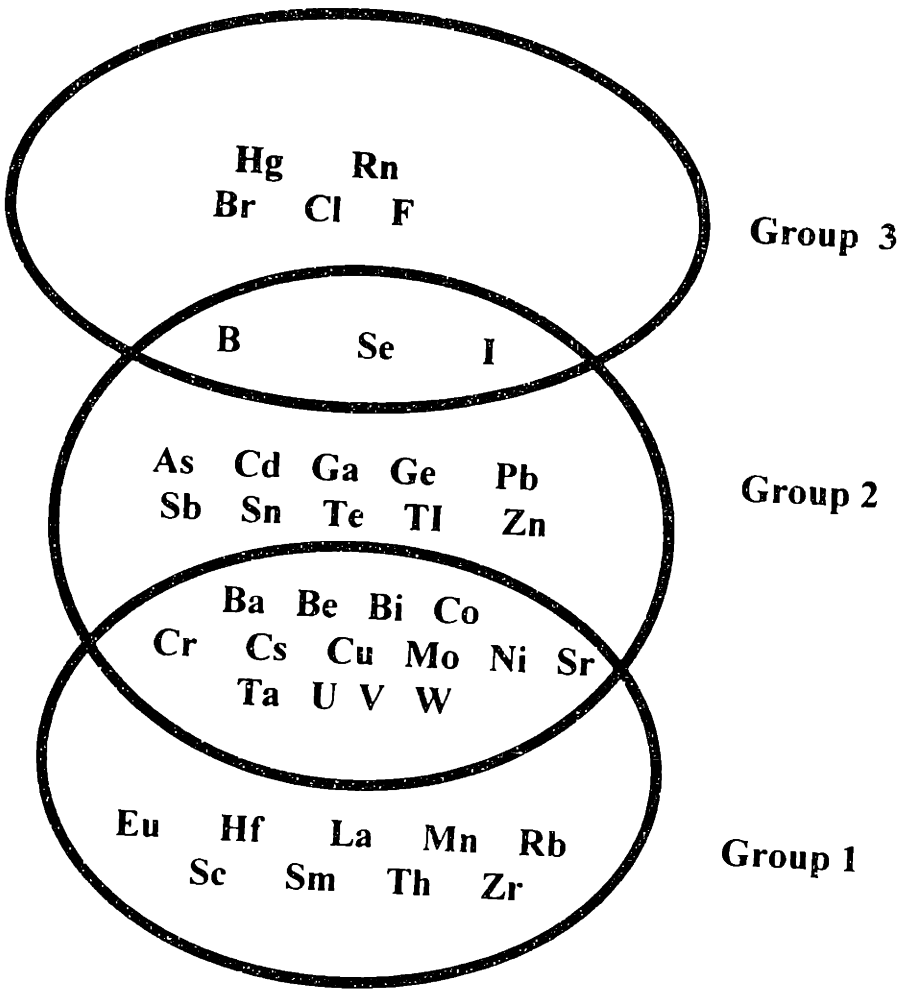

Figure 1-2. Classification of trace elements by their behavior during combustion and gasification

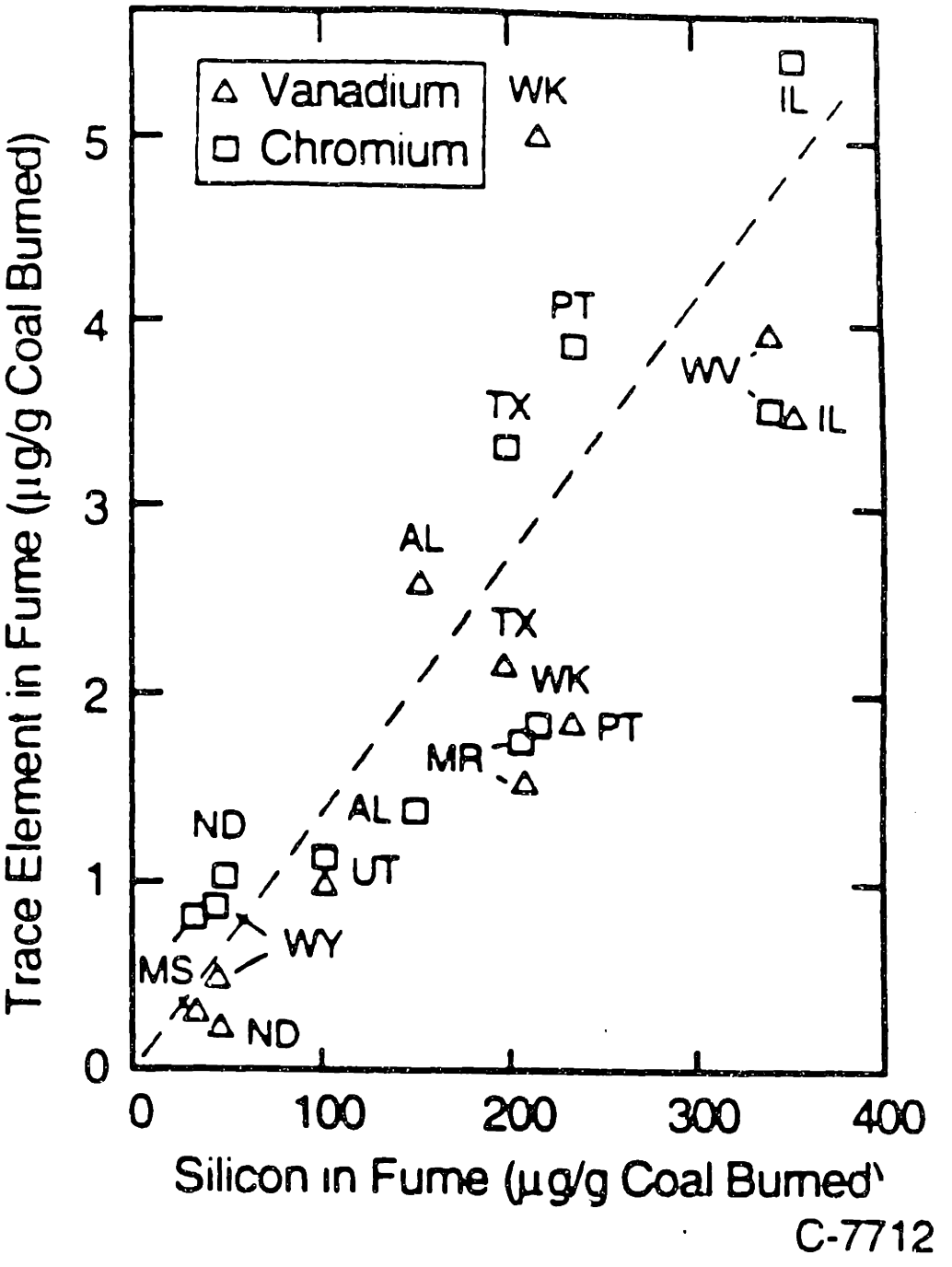

Figure 1-3 Chromium and vanadium vaporization results (from Quann et al. 1990)

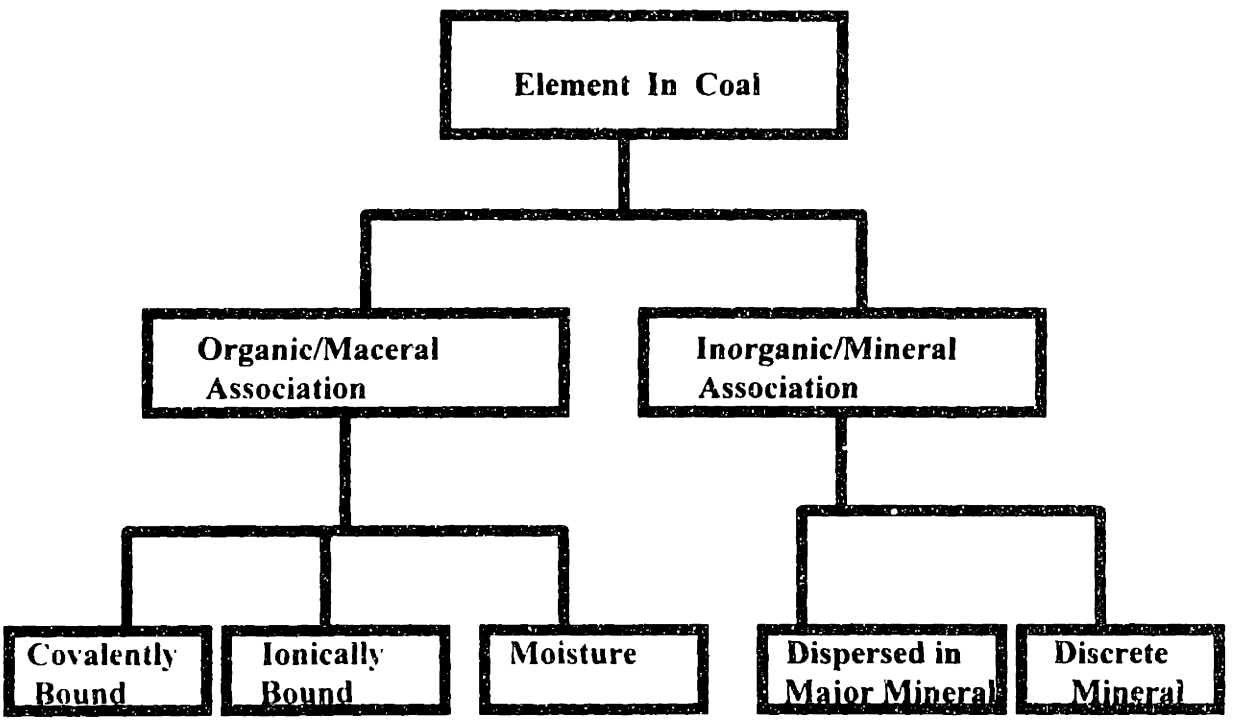

Covalently Bound: Involves direct covalent-M-C-or similar bond
E.g. Se-Thiophene, Ni-porphyrins
Ionically Bound: Involves an ionic bond with polar organic group
E.g.-CH COO-M+;t-NH+Br-
Moisture Species: Soluble anionic or cationic species in maceral pores
E.g. Chloride anions, Na+
Dispersed Mineral: Substitution of minor element for major element
E.g. As for S in Pyrite; Rb for K in illite
Discrete Mineral: Element is essential to mineral's existence
E.g. Clausthalite, PbSe; sphalerite, ZnS

Figure 1-4 A Classification scheme for elemental modes of occurrence

Chapter 2 Experimental Apparatus and Procedures

Most of the experimental apparatus used in this thesis has been used for many years. Previous graduate students have described them in detail. However, for completeness, a description of the equipment used in this study is also given here, in addition to descriptions of the coal characterization work at the University of Kentucky and the US geological survey (USGS). Much of the present thesis was part of a project on trace element transformation during coal combustion, sponsored by DOE, including the characterization studies at Kentucky and USGS which is a integral part of the research.

2.1. Separation Apparatus

In the preparation of the test samples, the coal was first put into seven standard (ASTM) sieves and vibrated for 45 minutes. Since the fine particles adhere to the large particles, a small vacuum was applied through the bottom of the sieves to separate and remove the fine particles. The homogeneity of the coal size fractions was examined using a microscope. It was found that the coals were separated into well-defined size ranges.

The next step was to obtain density-segregated coals using the size segregated samples. An air separator, a small fluidized bed (Figure 2-1), was used to separate the coals into different densities following the procedure developed by Hurt(1995). Each time, samples of coal up to a height of 27 cm in the separator were utilized. Compressed Ar or He gas was used as a working fluid. First, a high gas rate was used to fluidize the coal particles well, then the flow rates were decreased gradually to the point at which the particles were at the incipient fluidization velocity. The conditions of incipient fluidization were maintained for about 5 minutes, and then the gas flow was stopped. A small vacuum pump was used to extract the stratified coal. The coal in the top 9 cm was selected as the low density fraction, and the coal in the bottom 9 cm as the high density fraction.

2.2 Pyrolysis Experiments

The system used in the devolatilization experiments is shown in Figure 2-2 (Nenniger, 1986). This reactor configuration was chosen to achieve particle heatup rates and residence time similar to those in an industrial coal-fired furnace. The amount of sample required for analyses of the three aerosol components was also a consideration. In addition, the flow pattern within the reactor is rather simple.

Details of the system are given in the following sections. However, to provide perspective, a brief summary of the experimental procedure is presented here. Prepared coal is weighed, evacuated and flushed with argon before it is loaded into a fluidized feeder. The fluidized feeder sends a dilute stream of coal through a hypodermic tube and into the furnace. Preheated argon gas flows through a honeycomb flow straightener and entrains the cold particle jet. The particle heating rates are on the order of 10^4 - 10^5 K/sec for the entire range of temperatures studied. The product stream is collected in a water-cooled collection probe. Rapid quench for the pyrolysis products is provided by radial injection of argon at the top of the probe. Additional argon is injected radically along the length of the probe through sintered stainless steel tubing to eliminate deposits on the walls. The solid products (i.e., char and aerosol) are removed from the product stream in the collection/separation apparatus. Fully assembled, the apparatus stands approximately nine feet high. Much of the height is needed to allow for insertion of the collection probe and installation of the aerosol separation equipment.

2.2.1 Pyrolysis furnace

The furnace is an Astro Industries Model 1000-3560 PP furnace. A diagram of the furnace is shown in figure 2-3. There are two major sections: a preheat zone and a reaction zone. Both sections are heated electrically by a graphite element which surrounds the preheat tube and the inner muffle tube (reaction zone). All internal parts, with the exception of the feeder probe

and the electrical connectors to the heating element, are graphite. The electrical connectors are copper. The feeder probe is constructed with stainless steel. The insulation is graphite felt; it is held in place by an outer muffle tube. The rest of the internal parts are machined from porous graphite.

The preheat zone consists of an outer tube (preheat tube) with six radiation baffles and two honeycomb flow straighteners. The radiation disks are held in place by short sections of tubing which fit snugly inside the outer tubing. There is a sleeve which runs through the center of the radiation disks and rests on top of the honeycomb flow straighteners. This sleeve does not contact the water-cooled feeder probe along its length. The only point of contact between the feeder probe and furnace internals is a ¼ inch rim at the lower edge of the bottom honeycomb flow straightener. The bulk of the furnace gas (main gas) enters a preheat section above the honeycomb flow straighteners. The OD of the injection tubing to the preheat zone is small to help prevent arcing between the heating element and the entrance tubing. The preheat zone parts are supported by the muffle tube of the reaction zone.

The reaction zone is surrounded by an inner muffle tube. The reaction zone length and diameter are six inches and two inches respectively. There are seven optical access ports located in the reaction zone. Three window pairs permit line of sight viewing through the reaction zone; they are aligned vertically. The seventh port is located ninety degrees from the center window pair; it provides optical access to the exterior of the outer muffle tube. Five of the ports are fitted with quartz windows. Two of the ports on one side are sealed with insulation to reduce heat losses. The interior furnace wall temperature is measured through the window of the paired ports with an optical pyrometer (model No. 95, Pyrometer Instrument Company).

Two large, flat, water-cooled stainless flanges seal off the top and bottom of the furnace shell. The lower shell flange supports insulation and the outer muffle tube. Attached to each shell flange is a smaller aluminum flange - the upper and lower tubing flanges. The upper tubing flange is used to center the preheat tube. The lower tubing flange supports the inner muffle tube

and the preheat parts. Attached to the upper tubing flange is the feeder probe. Attached to the lower tubing flange is the sidearm flange; it is a stainless steel flange, with cooling provided to the tubular section. A gas access port is bored through the lower face of the sidearm flange. This port is used to bleed off gas when the ball value is closed, such as when the furnace is being outgassed. And finally, attached to the sidearm flange is a ball valve. The collection probe is inserted through this ball valve.

The resistance between the furnace shell and the heating element is monitored constantly while the furnace is being assembled to ensure that none of the internal parts of the furnace shell contact the heating element. Special precautions are taken to ensure that the particles travel along the centerline. Once assembled, the furnace is leveled. The lower tubing flange, the sidearm flange and the ball valve are then centered with respect to the upper tubing flange and the feeder probe flange using a plumb line. After exposure to the atmosphere, the furnace must be outgassed at high temperature (2500 K) to remove oxygen adsorbed to the high surface area of the graphite insulation and porous graphite parts. Otherwise , it is impossible to make accurate measurements of CO and CO_2 gas concentrations. Normally , when not in use , the furnace is maintained under 10 psi of argon. Frequent checks are made for leaks; tests are conducted at 15 psi pressure and 30 inches H_g vacuum.

2.2.2 Fluidized feeder

The coal feed rate can have an enormous effect on aerosol particle size. Therefore , it is essential to have a feeder which can feed small quantities of coal steadily and reproducibly. The feeder is shown in Figure 2-4; basically ,it consists of a sample cell, a syringe pump , a vibrator and a length of hypodermic tubing. Coal is entrained by gas (carrier gas) flowing through the sample cell. The entrained coal exits through the hypodermic tubing and is carried into the furnace. The level of coal is maintained at a constant position relative to the hypodermic tubing by the syringe pump. Low levels of vibration are provided by the vibrator (an engraver) to keep the coal surface level. (Higher levels result in erratic feeding.)

The syringe pump is a Sage Instruments Model 314A syringe pump; 22 pumping speeds are possible. Coal feedrates are shown in Figure 2-5 as a function of syringe pump setting. Most experiments were carried out at the high number 6 setting. The coal feedrate at this setting is approximately 2.6 g/hr.

The feeder sample tube is made from glass tubing (6 mm O.D., 4 mm I.D.). One end of the tubing is bent at 90 degree angle and sealed ≈ ½ inch from the bend. The length of the sample tube is 5-6 inches; it holds approximately one gram of coal. The sample tube is installed in a holder which is glued to the syringe pump driver. The holder is made from a section of 3/8 inch thin wall stainless tubing. Sections of the tubing (270 degrees of the radius) are removed to allow one to observe the coal level in the sample tube. As the sample tube is installed in the holder, it is also threaded through a ring attached to the vibrator. A ¼ inch Cajon T fitting is attached to the top of the sample cell. The sample cell fits into one of the T runs. A GC septum (Supelco 11 mm Tight-set) is installed in the other T run. A ¼ inch line is attached to the T branch; this line supplies vacuum and argon carrier gas to the sample cell.

Before the syringe pump is turned on, the coal sample is evacuated and flushed with argon. (Care must be taken to avoid drawing coal into the vacuum system. Otherwise, errors in the coal mass fed to the furnace will result.) The hypodermic tubing is then inserted through the septum, and adjusted such that the tip is near the coal surface. Next, the hypodermic tubing is fixed in a stationary position by a screw clamp. The clamp fastens onto a rod (1/4 inch Odx1 inch length) which is soldered onto the tubing. The hypodermic tubing is stainless steel, 18 gauge tubing; its total length is approximately 50 inches. The end of the tubing which is inserted through the septum is ground to a high angle to facilitate insertion.

2.2.3 Feeder probe

The designs for the feeder probe are of two basic types: concentric annulus and

segmented annulus. The concentric annulus probe consists of three concentric tubes. Water flows down to the probe tip through one annuli and back through the other. The intermediate tube acts as a baffle, forcing all of the water to pass through the tip region. In the segmented annulus design, there is only one annulus. The intermediate tube is replaced by a series of tubes, evenly-spaced in the annulus. See Figure 2-6. Water flows to the probe tip through these tubes and returns through the spaces between the tubes, or vice versa. For a given application, a choice can be made between the two designs by calculating the hydraulic diameter available for each design. Feeder probes from both designs were constructed for this study. As predicted from calculations, the water flowrate for probes with a segmented annulus is 30 percent higher than for probes with a concentric annulus.

The feeder probe design is shown in Figure 2-6. The outer tube is thick wall 3/8 inch tubing with a spun tip. There are three segment tubes; these are extra thin wall 12-1/2 gauge tubing. The ends of the segment tubes at the probe tip are ground at an angle and oriented so that cooling water flow is toward the probe exterior. The center tube is thin wall 1/8 inch tubing. The center tube is welded to the spun tip of the outer tube. A sleeve (1/2 inch O.D. x 3/4 inch length) is welded 12-3/8 inches from the probe tip. This sleeve butts against a recess in the ½ inch fitting of the feeder probe flange ; it allows one to position the probe exactly in the furnace without shutting the furnace down, such as when the hypodermic tubing has to be replaced. The hypodermic tubing from the feeder is inserted into the tip of the feeder probe. A plug in the tip of the feeder probe ensures that the hypodermic is precisely centered. The hypodermic tubing is ground flat and flush with the probe tip. A short rod (1/4 inch O.D.x1 inch length) is soldered to the hypodermic tubing at the top of the probe. This rod is joined to the center tubing with a ¼ x 1/8. Inch reducing union.

2.2.4 Collection probe

The pyrolysis products, both gaseous and solid, are collected in a water-cooled collection probe. A simplified schematic of the probe is shown in Figure 2-7. The probe OD is 1-3/8 inches;

the ID is ½ inch; the length is 37 inches. Like the feeder probe, water travels to the probe tip through a segmented annulus. Rapid quench for the products is provided by argon injected radially through sintered stainless tubing (5/8 inch OD, ½ inch ID) at the top one inch section of the probe. The sintered tubing lines the entire length of the probe. Additional argon gas is injected at a slower rate along the remaining length of the sintered tubing to eliminate deposits on the walls. The high quench rate region is separated from the rest of the probe length by an o-ring which lodges between the sintered tubing and the inside probe wall. The sintered tubing is made from five micron spheres.

Due the high temperature of this study, a special cap for the probe was required. The cap design, along with dimensions, is shown in Figure 2-8. With this design, maximum cooling to the probe cap is provided by the quench gas before it exits through the sintered tubing. While the cap is rather difficult to install, it does prevent the cap melting down at higher temperatures. When collecting samples at temperatures higher than 1800K, it is important to polish the probe sides and cap to a bright, shiny luster, in order to keep radiation heating to a minimum.

2.2.5 Collection equipment

One or more of the following three devices - absolute filter, cascade impactor, and electrostatic precipitator - were used to collect and or characterize the combustion aerosol as it exited the collection probe. Figure 2-9 shows the different collection systems. The three systems will be discussed below.

A. Absolute filter

The simplest aerosol collection system shown in figure 2-9 is an absolute filter which was designed to separate all particulate matter from the gas stream. The teflon/polyethylene filter was chosen for this experiment, because it is the most durable and is truly an absolute filter.

B. Cascade impactor

A cascade impactor was used to obtain ash particle size distribution. The cascade impactor was also used to remove the residual, supermicron ash and to capture the remaining submicron ash for submicron ash study (see Figure 2-10).

As shown in Figure 2-10, a cascade impactor consists of a series of stages, each composed of an orifice, or a set of orifices, through which the aerosol flows and a collection surface normal to the flow immediately after the orifices upon which the aerosol impinges. Those particles with too much inertia cannot follow the gas streamline, and hence impact on the collection surface and are separated from the gas stream. The process is repeated with several consecutive stages, with each subsequent stage removing smaller particles.

The cascade impactor used was a Mark II Model 20-800 non-viable ambient particle sizing sampler manufactured by Andersen 2000 Inc. The manufacture's collection efficiency curves for each of the eight impactor stages and the preseparator are shown in Figure 2-11 for a gas flow rate of 30 l/min. Using the preweighed aluminum foil substrates which were covered with a silicone spray grease (to prevent particle bounce and re-entrainment) and dried at 110^0C, fly ash particle size distributions were determined from the combustion of a variety of coals in the laminar, entrained-flow reactor under a range of operating condition.

The purpose of the cascade impactor in this study was (1) to collect and size classify fly ash particles, and (2) to remove the residual, supermicron ash in order to isolate the submicron ash for subsequent collection and characterization. The impactor collection efficiency curves in Figure 2-11 were used to optimize the impactor configuration to remove particles greater than 1 micron. This was accomplished by operating the impactor with the preseparator and only the first stages. The cumulative penetration curve for this configuration is given in Figure 2-12 for different furnace operating conditions. These penetration curves are based upon aerodynamic diameter which is the diameter of a sphere with a specific gravity of one with the same Stokes

number as the particle. The Stokes number is proportional to density x (diameter)^2; therefore, a sphere of specific gravity 3 will have an aerodynamic diameter $1/\sqrt{3} = 1/1.73$ times its actual diameter. The cutoff for the two operating conditions was 1 and 1.2 microns, aerodynamic diameter. One should note that the penetration curves in Figure 2-11 defines of what is collected as submicron ash. In this work, the cut off for diameter of submicron particle is 1.1 microns.

2.3 Oxidation Furnace(Kang, et al., 1992)

Most of the oxidation furnace system design is the same as that in the pyrolysis furnace system. Thus a brief description is given here.

As shown in Figure 2-13 , the laminar, entrained-flow reactor was a vertically oriented, externally heated aluminum tube containing gas in downward flow. The high temperature was provided by an Astro Model 1000A-3500 graphite element furnace. The heated section was 430 mm long. The first 170 mm served as a preheat section upstream of the particle injection. The last 50 mm of the preheat section (i.e., between 120 and 170 mm) was filled with an aluminum honeycomb to act as a flow straightener in order to ensure laminar flow. Six thousand std ml/min of main gas entered through this preheat section.

The water-cooled injection probe passed through the center of the preheat section and was flush with the bottom of the honeycomb. Particles were injected concurrently into the center of the preheat main gas flow with approximately 80 std ml/min of entrainment N_2 at room temperature. The heated reaction zone following the particle injection location was 50 mm in diameter and 260 mm in length.

After injection, the particles were entrained in the main gas and passed through the heated reaction zone. The reaction zone was designed to operate between 373K and 1750 K. The maximum residence times at these temperatures, assuming fully developed laminar velocity profiles (particles were injected on the reactor centerline where the gas velocity was twice the

mean velocity) with 6 slpm of main gas, were 0.77 and 0.44s, respectively.

After passing through the reaction zone the entire gas stream was extracted through the water-cooled collection probe. The reactor was designed so that the collection probe could be inserted to any position within the heated reaction zone, thus allowing for control of the residence time. In order to rapidly quench the reaction products, 10 to 20 slpm of room temperature N_2 were added to the 6 slpm of main gas within the first 20 mm of the collection probe. This was accomplished by constructing the inner wall of the collection probe from porous sintered stainless steel through which N_2 was transpired. The amount of quench gas added was varied depending on the outlet temperature desired. In order to prevent deposition on the inside walls of the collection probe after the quench section, an additional 4 slpm was radically transpired through the remaining 690 mm of the sintered stainless tube. This brought the total volumetric flow of gas exiting the collection probe to between 20 and 30 slpm. The exit gas and particles were then pulled through an aerosol collection/classification device and vacuum pump which is the subject of Subsection 2.2.5.

The entrainment system restricted the operating conditions. Dry size-classified particle samples between 40 and 150μ (typical size cuts: 63 to 75 μm, 90 to 105 μm) were fed successfully. However , moisture and fines caused agglomeration. Agglomeration and oversize particles caused plugging in the hypodermic tubing. Feedrates of 0.002 to 0.02 g/min were easily achieved with char samples. Feedrates greater than 0.2 g/min often plugged the hypodermic tubing. Thus, most experiments were run with feed rates of 0.01 to 0.02 g/min.

The centerline gas temperature was measured as a function of axial furnace location under normal operating conditions using a 1.6 mm (1/16 in.) O.D. molybdenum sheathed tungsten-rhenium thermocouple. Considerable error due to heat conduction along the thermocouple was introduced when steep gradients in temperature where measured. In order to bracket the uncertainty, the temperature measurements were made with thermocouple inserted through both the injection and collection probes. The temperature profiles are shown in Figure 2-14 with the

uncertainty represented by the shaded areas. Note that both the furnace setting and the position of the collection probe impact the temperature profile.

The I.D. of the collection probe was one-half of an inch; consequently the entrance to the probe from the reaction zone was an abrupt contraction and any large particles further than one-quarter of an inch from the reactor centerline could have been inertially separated and would have remained in the furnace. Care was taken to routinely align the injection probe so as to place the particles near the reactor centerline.

Previous researchers tested the collection efficiency under normal operating conditions and reported that when the injection probe was aligned correctly , over 90 % of most elemental species fed to the furnace were recovered.

2.4 TGA (Du, 1990)

A schematic of the thermogavimetric analyzer (TGA) system is shown in Figure 2-15. The micro-balance, mounted inside a Pyrex glass housing, is an electro-mechanical transducer that measures the force applied onto the balance beam by the current a motor coil needs to counterbalance the applied torque. The ultimate sensitivity of the balance is about 0.1 μ g. The quartz furnace tube is 1 inch diameter with a 1 ½ section of heavy wall 26 mm quartz tubing attached to one end. This end was precision ground and polished to the correct outside diameter to provide a tight connection to the Cajun o-ring fitting. A thermocouple of type K is mounted through the bottom of the furnace tube, which provides the input signal for the temperature controller. The sample pan is suspended by a hang-down wire of 0.1 mm nichrome. Gases from a gas flow system, either inert or reactant, enter the TGA with a constant flow rate of 200 cc/min through the inlet port mounted just above the furnace tube, and exit at the bottom of the furnace tube. The pressure in the TGA is kept about 12 cm water above atmospheric pressure during operation, monitored with a water manometer that has a safety release at 42 cm water.

The furnace tube is heated with a standard resistance furnace. The temperature is controlled with a Micricon 823 process controller, which is able to maintain a steady state temperature within 1 K of the set point.

The weight versus time data were recorded on a Bascom-Turner model 410 digital recorder and data storage system, which has a maximum data acquisition rate of 100 milliseconds per datum point. The derivative of the TGA data (weight vs. Time) was calculated using software available in the Bascom-Turner operating program.

2.5 Additional Characterization Method

The work reported here on trace elements formed part of a large project to develop a comprehensive model for trace elements emissions from coal-fired power plants. The coals studied in this thesis were analyzed in parallel by other researchers. The results of these collaborative investigations will be used to interpret the results of this work. Several specialized analytical methods were used on coal and ash samples as described below.

2.5.1 Computer Controlled Scanning Electron Microscopy (CCSEM) (Senior, et al. 1997)

Computer controlled scanning electron microscopy has been used for about 17 years for the determination of the discrete mineral matter in coals. The original concept (Lee et al. , 1980; Huggins and Huffman, 1983) has not changed significantly over the years. The basis for coal minerals analysis by CCSEM is the statistical determination of the types and relative quantities of different minerals in a random, representative coal sample. The coal sample is pulverized and divided according to ASME procedures to generate a sufficient quantity (5 to 10 g) of a finely ground (<100mesh) representative sample of the coal, from which a 1-inch diameter by 2-inch long pellet can be pressed. The pellet was prepared by mixing the fine coal with a small amount of epoxy that was allowed to set in a cylindrical die under pressure. The resulting cylinder of coal was sectioned, ground, and polished to provide a flat surface with a minimum of relief that was

suitable for examination in the SEM.

The sectioned pellet was placed in the SEM after the polished surface had been given a thin carbon coating in an evaporator. The SEM operating voltage was set to 25 keV and the section was examined in the back-scattered electron (BSE) mode. In this mode, any physical differences in relief of the mineral particle vis-à-vis the epoxy/maceral matrix were minimized and the mineral particles were distinguished from the matrix almost entirely by their brightness in the BSE image. The brightness of a mineral in the BSE image was a function of its chemical composition: the higher the average atomic number (Z) of the mineral, the brighter it will appear in the BSE image. A threshold level in the BSE brightness was defined so that all of the minerals were brighter than this level, whereas the maceral/epoxy matrix falls below the level. This level was used by the computer to discriminate between mineral and maceral and to define the edges of mineral particles in the carbon-rich matrix. Hence it is simple to determine the physical extent of mineral grains in the cross-section of the coal. The area of cross-section of each parameters, such as the perimeter, minimum and maximum diameters, aspect ratio, etc., were also determined at the same time. The computer then located the electron beam at the center of the particle and an energy dispersive X-ray (EDX) spectrum was recorded from the particle for four seconds. The computer recorded the intensity of the 14 most common inorganic elements(Na, Mg, Al, Si, P, S, Cl, K, Ca, Ti, Fe, Cu, Zn, Ba). The relative intensities of the X-rays for these elements are used to identify the mineral that give rise to the grain in the cross-section. A quantitative analysis was not done; the rationale being that nearly all common minerals in coal can be readily identified from their uncorrected EDX spectra. Once the computer located a mineral particle, determined its size parameters, and recorded the EDX spectrum, it would look for a new mineral particle and the size and chemistry determinations were repeated. The beam-control software in the CCSEM included routines that minimize the possibility of multiple counting of particles.

2.5.2 Mossbauer Spectroscopy

Iron-57 Mossbauer spectroscopy provides complementary information to both CCSEM

and XAFS spectroscopy in two important areas: (i) it provides detailed information regarding the iron minerals in coal and iron phases in ash, and (ii) it gives an indication of the degree of oxidation of pyrite, the major coal mineral most sensitive to oxidation, and hence, of the overall coal as a whole.

Analysis of Mossbauer spectra is based on using a least-square fitting procedure built around a lorentian peak shape. Mossbauer absorption features are fit as single peaks, two-line quadrupole doubles, or six-line magnetic hyperfine sextets. The parameters derived from the isomer shift (I.S.) and is reported in mm/s relative to metallic iron, the separation of the quadrupole components, which is known as the quadrupole splitting (Q.S.) and is also reported in mm/s, and the separation of peaks 1 and 6 in a magnetic sextet, which is known as the magnetic hyperfine splitting (H_0) and is reported in kGauss. These three parameters derived in the computer fitting are usually sufficient to identify and determine the iron-bearing mineral species present in virtually all coal samples.

2.5.3 XAFS Spectroscopy

XAFS spectroscopy is basically a measurement of the variation (or fine structure) of the X-ray absorption coefficient with energy associated with one of the characteristic absorption edges of the absorbing element. The XAFS spectrum is normally divided into two distinct regions for analysis: the X-ray absorption near-edge structure (XANES) region and the extended X-ray absorption fine structure (EXAFS) region. These regions incorporate the fine structure in the vicinity of the edge itself and further away from the edge, respectively. To generate an XAFS spectrum, the absorption by the sample is measured as a function of the monochromator angle or, equivalently, the energy of the incident X-ray beam. After a complicated mathematical processing, a radial structure function that describes the position and coordination number of atomic shells for the atom or ion can be obtained. These techniques and procedures are well described in a textbook by Koningsberger and Prins (1988).

In analyzing the coal samples used in this thesis, the XAFS spectroscopy was performed at the National Synchrotron Light Source (NSLS) at Brookhaven National Laboratory and the Stanford Synchrotron Radiation Laboratory under the direction of Profs. Huffman and Huggins of the University of Kentucky.

REFERENCES

Du, Z., Kinetic modeling of carbon oxidation, MIT ScD thesis, 1990

Hurt, R., Davis, K., Yang, N., and Hardesty, D., The origin and properties of unburned carbon from pulverized coal combustion, Report to EPRI, EPRI TR-105743, Project 8005, 1995

Kang, S. G., Sarofim, A. F., Graham, K. A. and Beer, J. M., in Transformation of inorganic coal constituents in combustion system (Ed. Helble, J.J.) , Final report to DOE (contract No. DE-AC22-86PC90751), 1992

Koningsberger, D. C., and Prins, R., X-ray Absorption Principles, Applications, Techniques of EXAFS, SEXAFS, and XANES, John Wiley & Sons, 1988

Nenniger, R. D., Aerosol produced from coal pyrolysis, MIT ScD thesis, 1986

Senior, C. L., Bool, L.E., Morency, J., Huggins, F., Huffman, G. P., Shah, N., Wendt, J. O. L., Shadman, F., Peterson, T., Seames, W., Wu, B., Sarofim, A. F., Olmez, I., Zeng, T., Crowley, Kolker, A., Palmer, C. A., Finkelman, R., Helble, J. J., Wornat, M. J., Toxic Substances from Coal Combustion - A Comprehensive Assessment, Final Report to DOE (contract No. DE-AC22-95PC95101), 1997

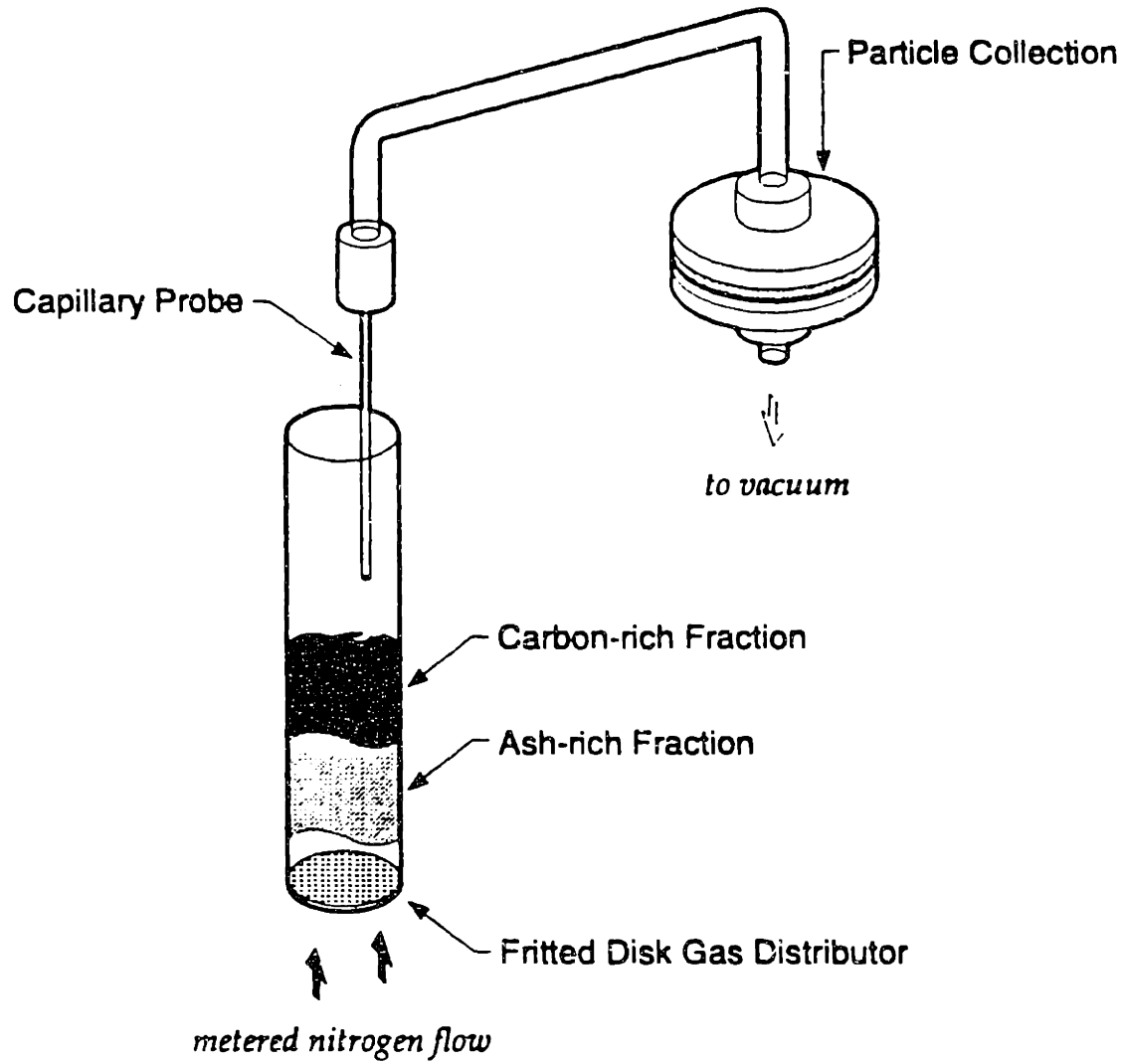

Figure 2-1 Coal separator

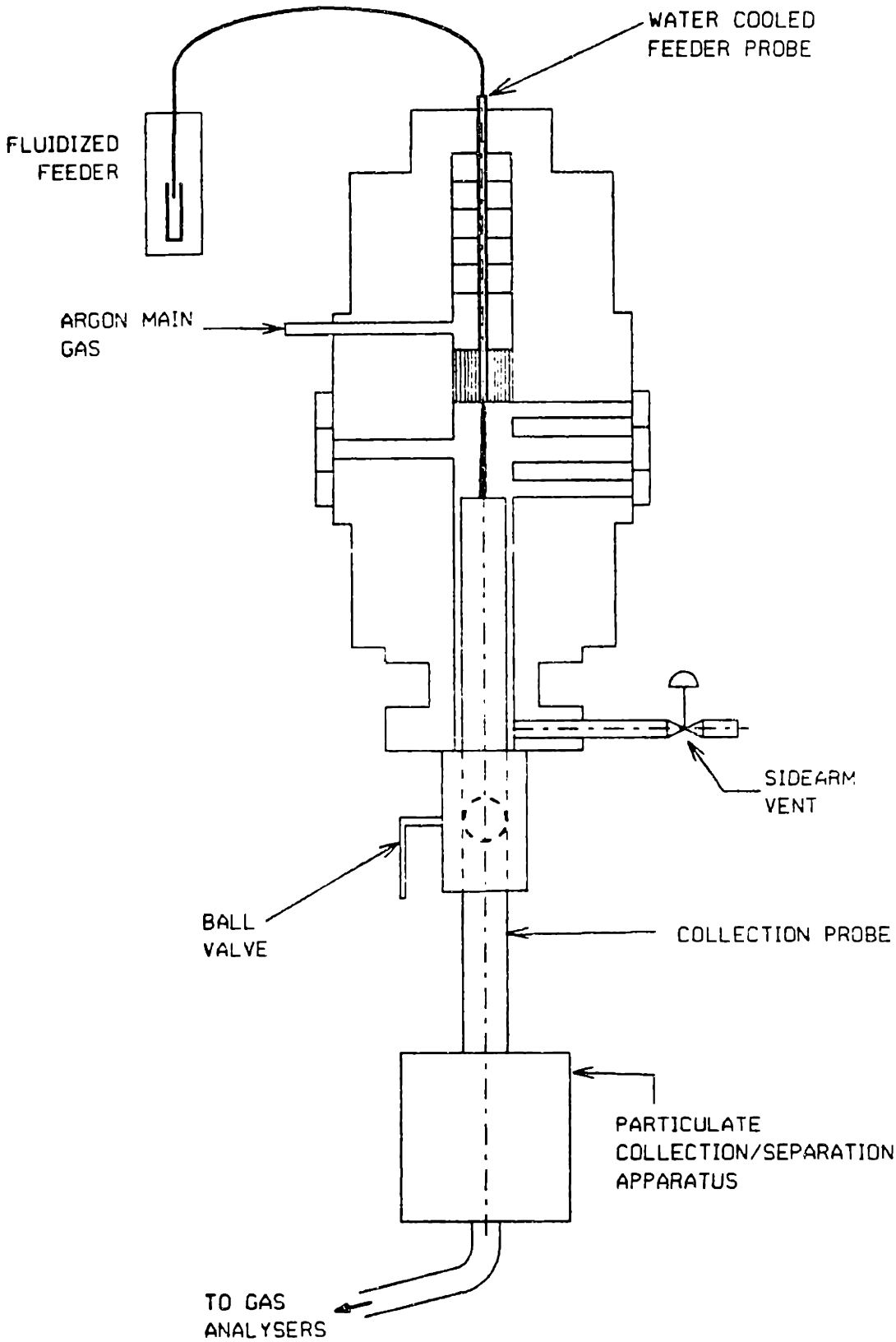

Figure 2-2 Pyrolysis furnace set-up

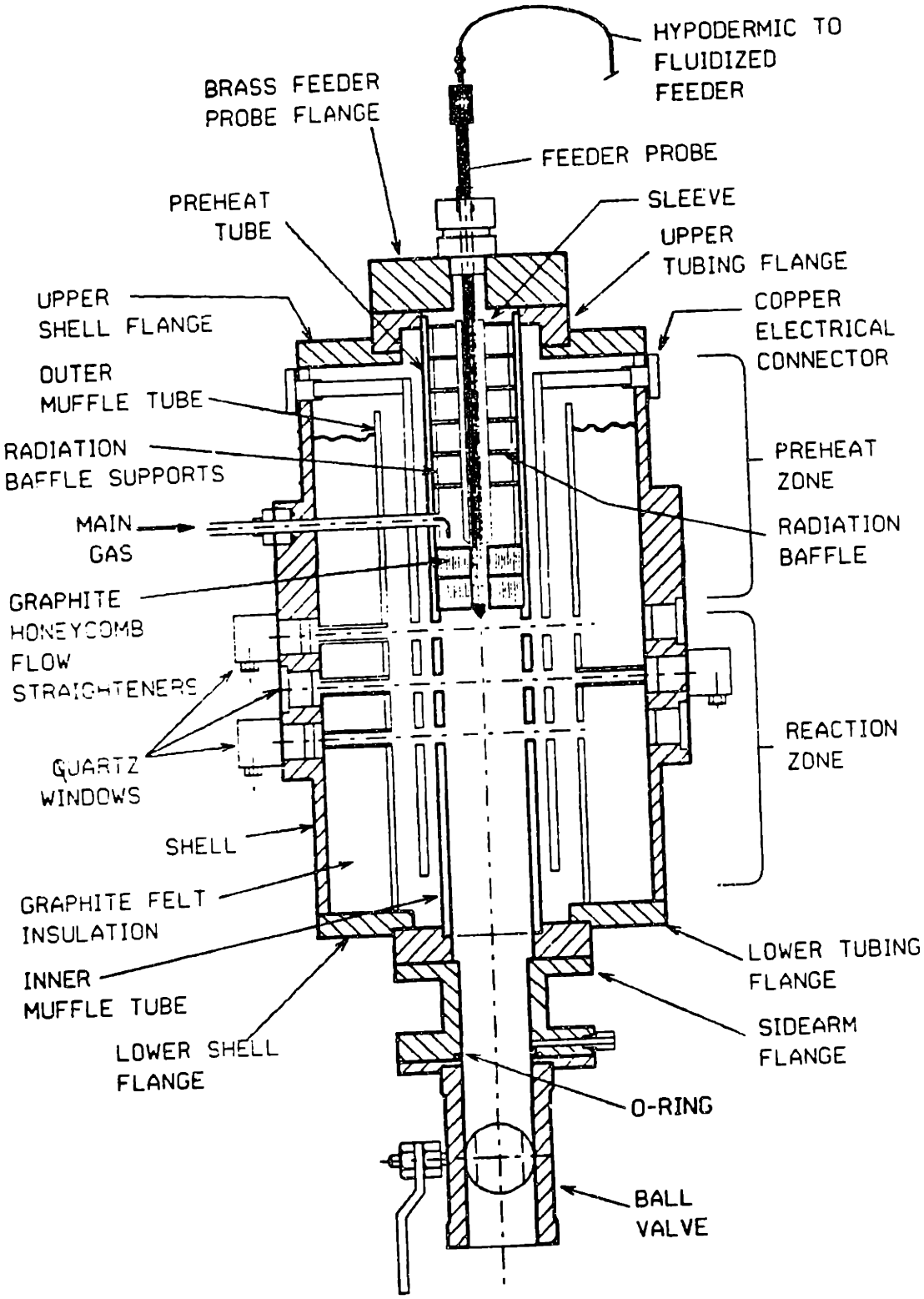

Figure 2-3 Pyrolysis furnace

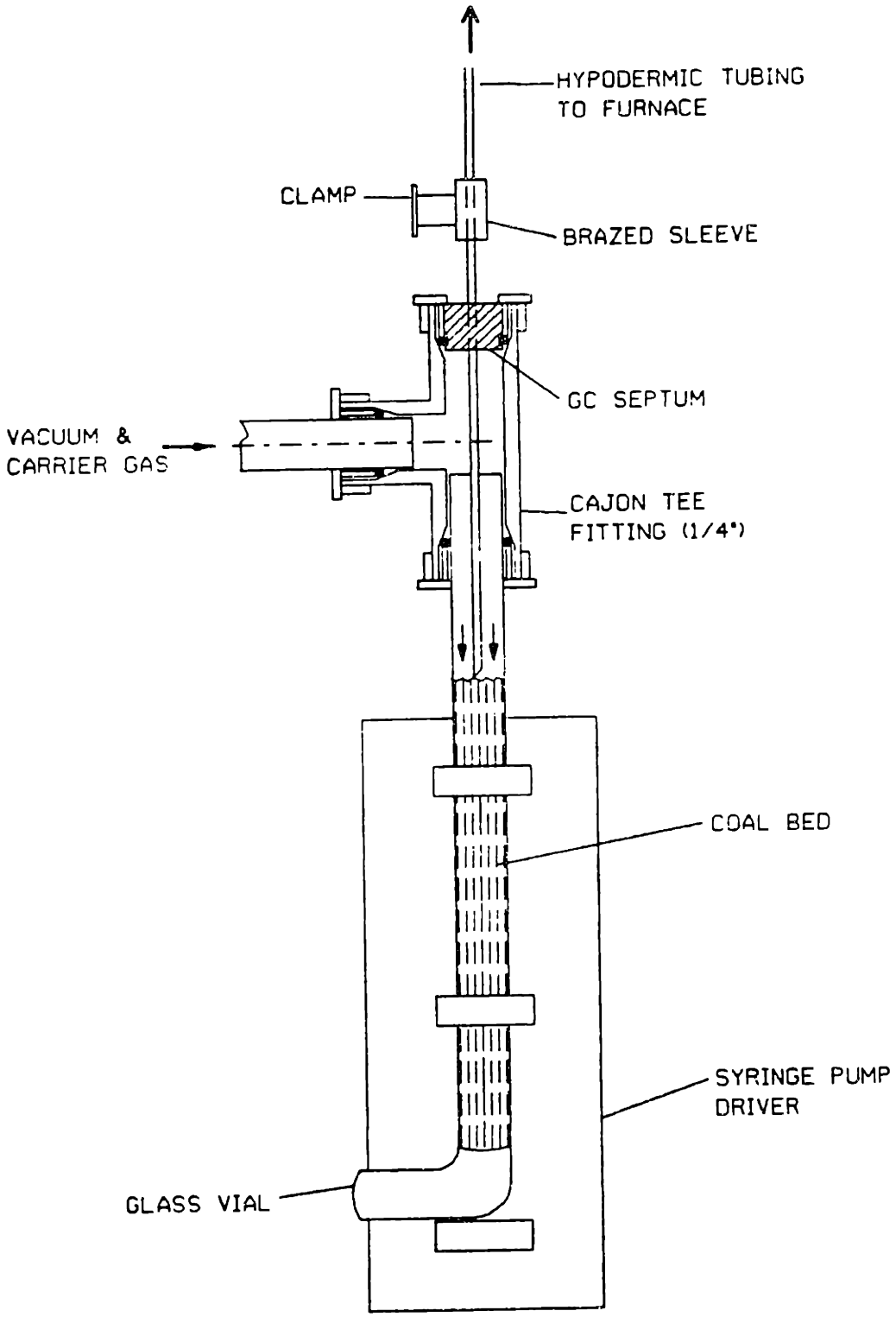

Figure 2-4 Fluidized coal feeder

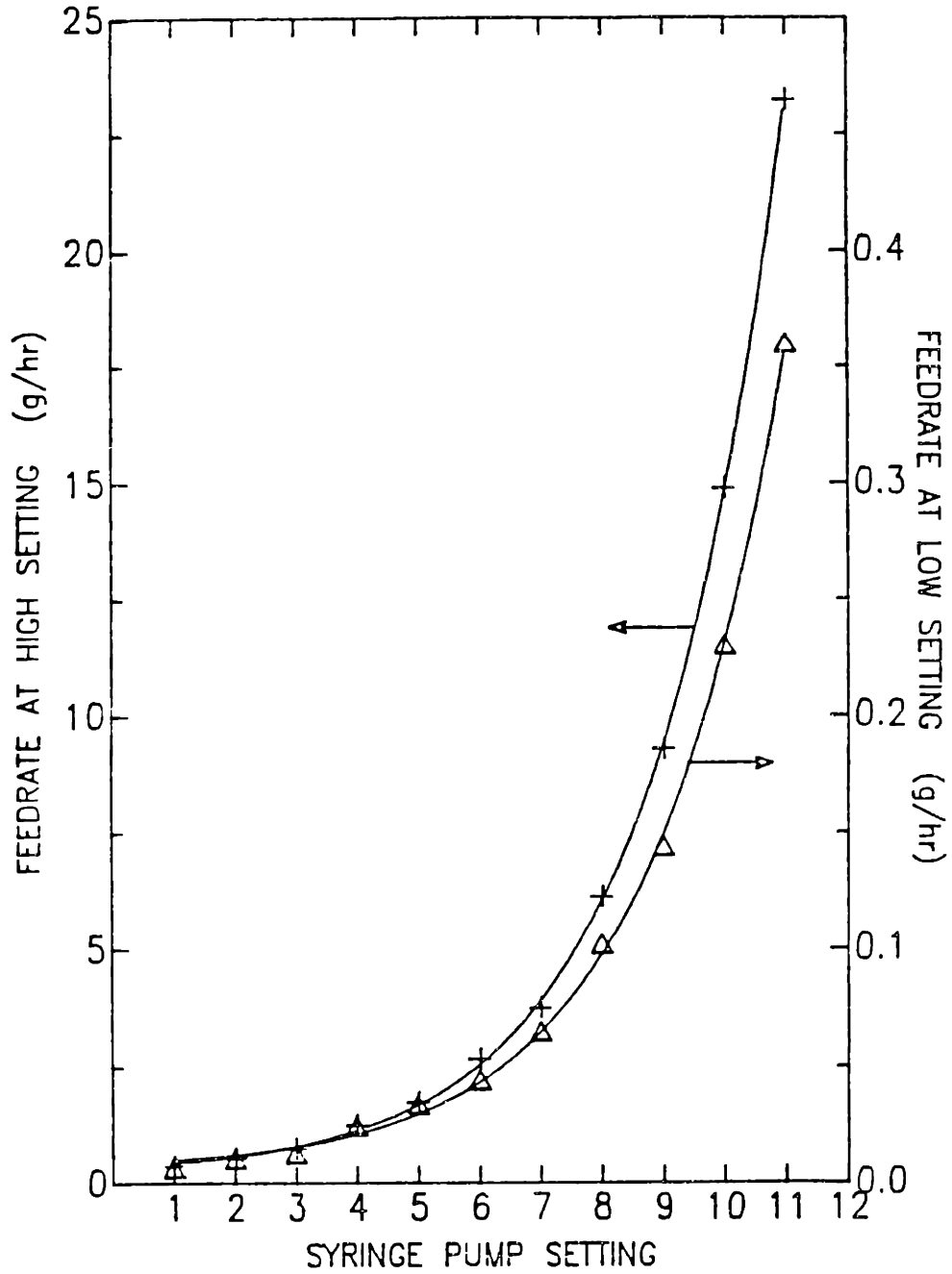

Figure 2-5 Coal feedrates as a function of syringe pump setting

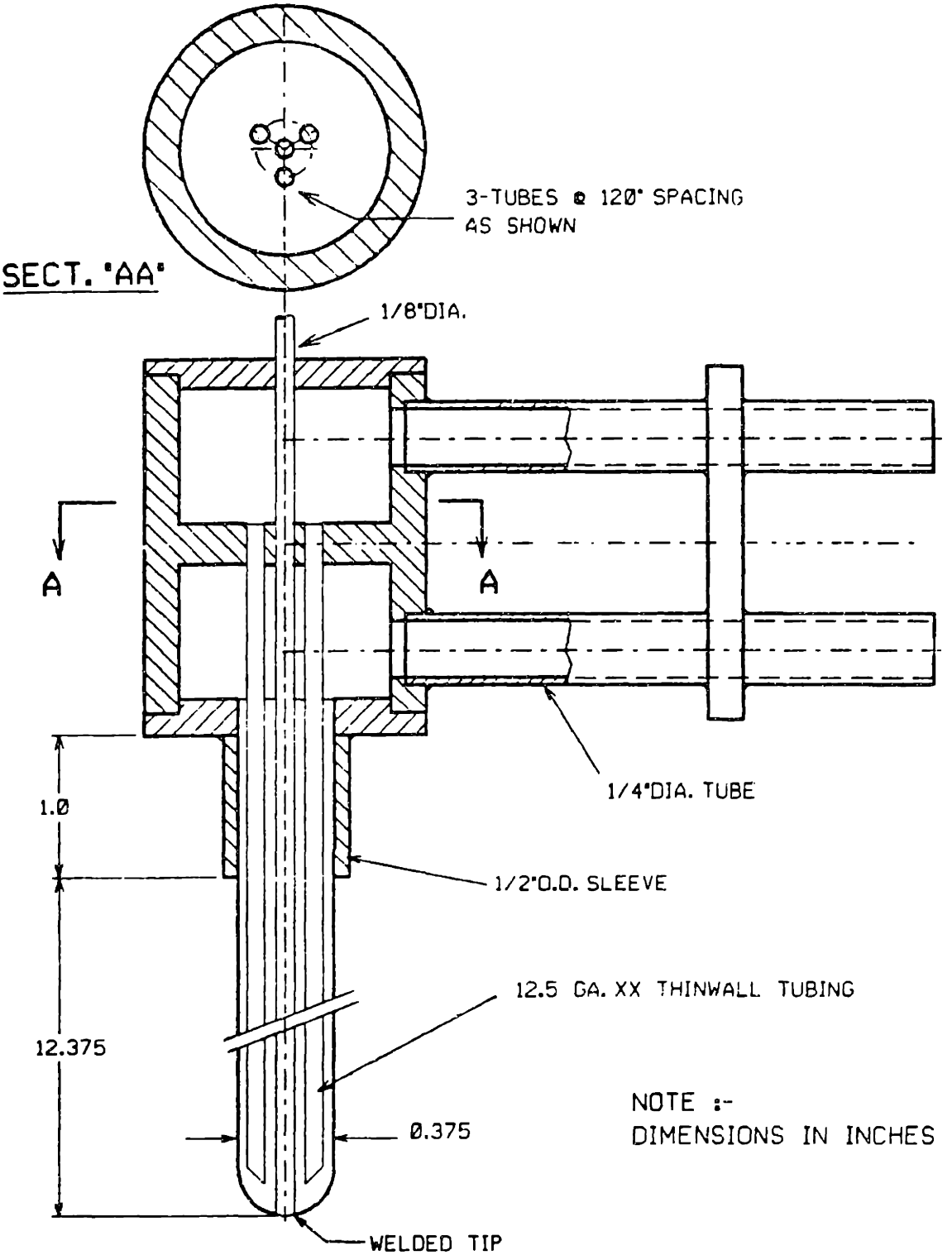

Figure 2-6 Feeder probe design

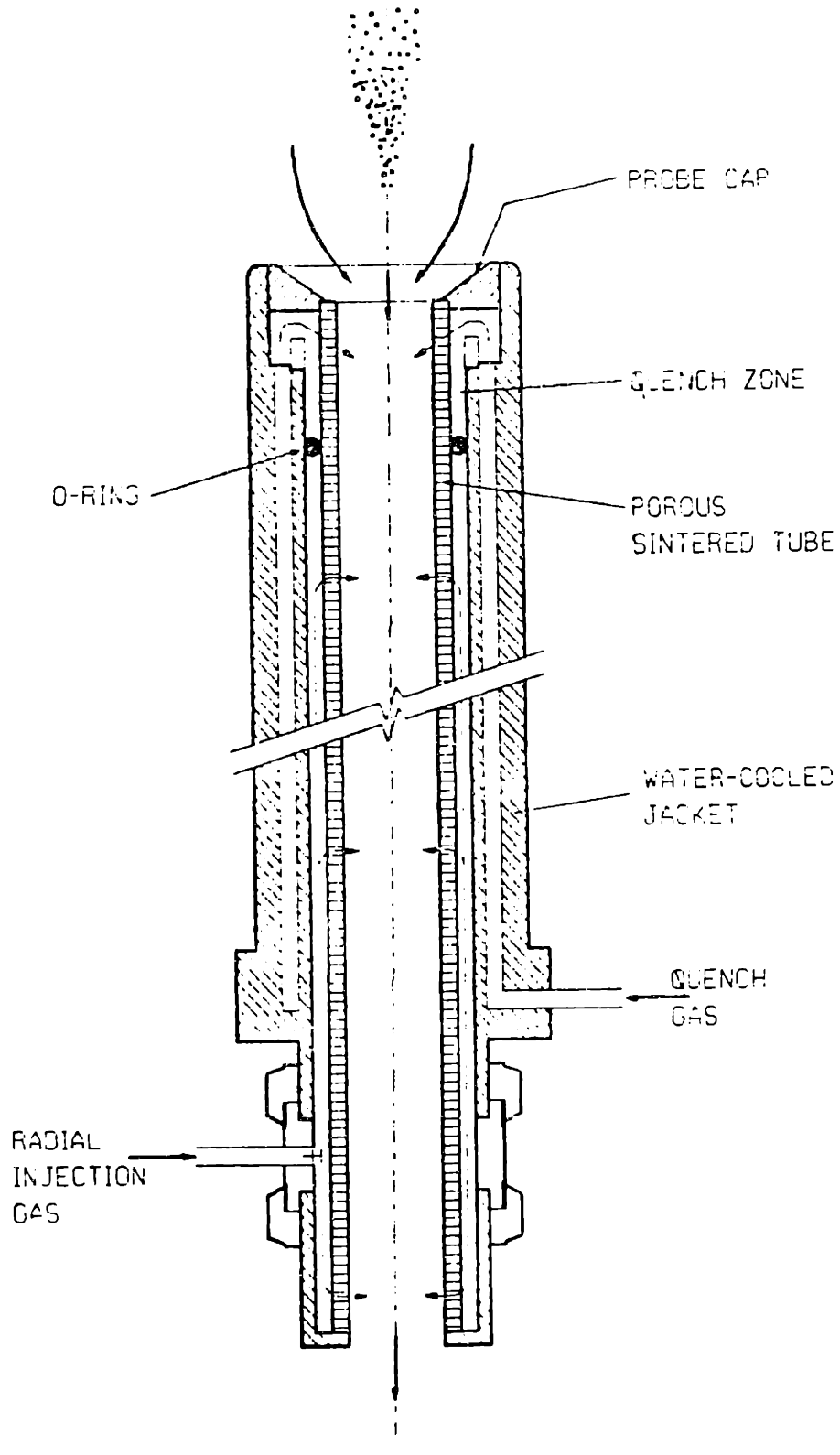

Figure 2-7 Water-cooled collection probe

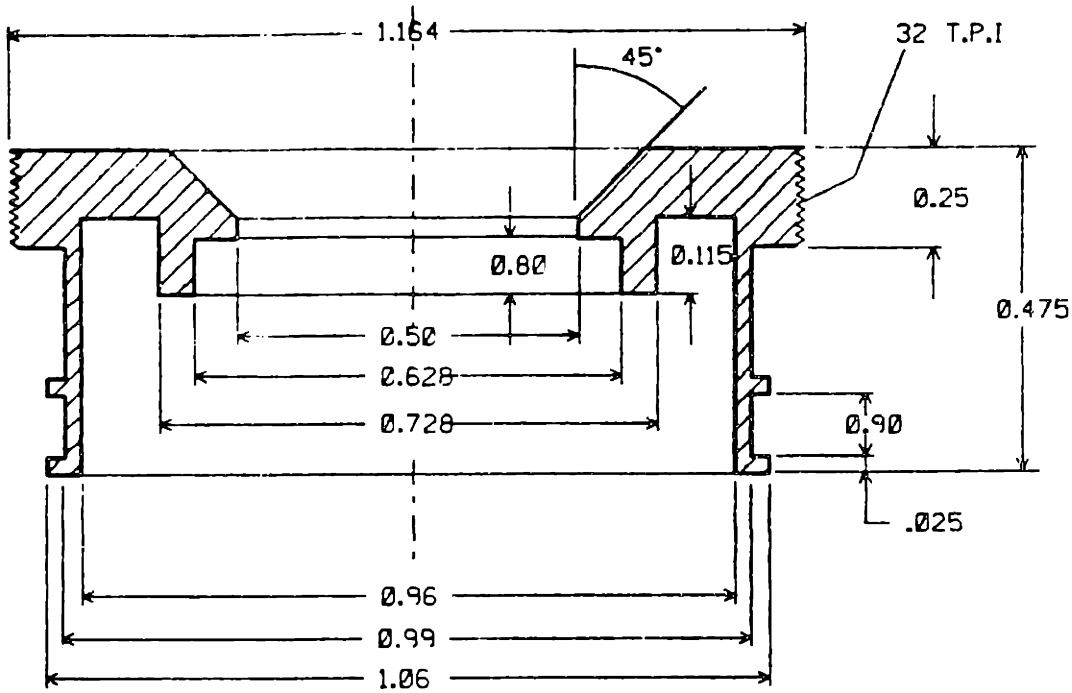

CAP DETAIL

NOTE:
MATL.- BRASS
DIMENSIONS IN INCHES

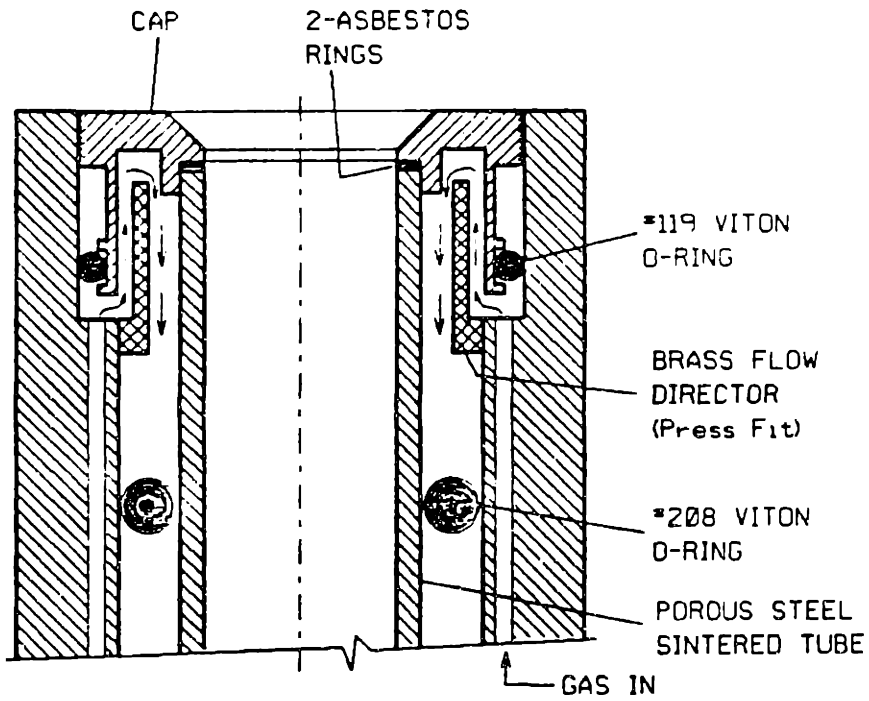

Figure 2-8 Collection probe cap design and assembly

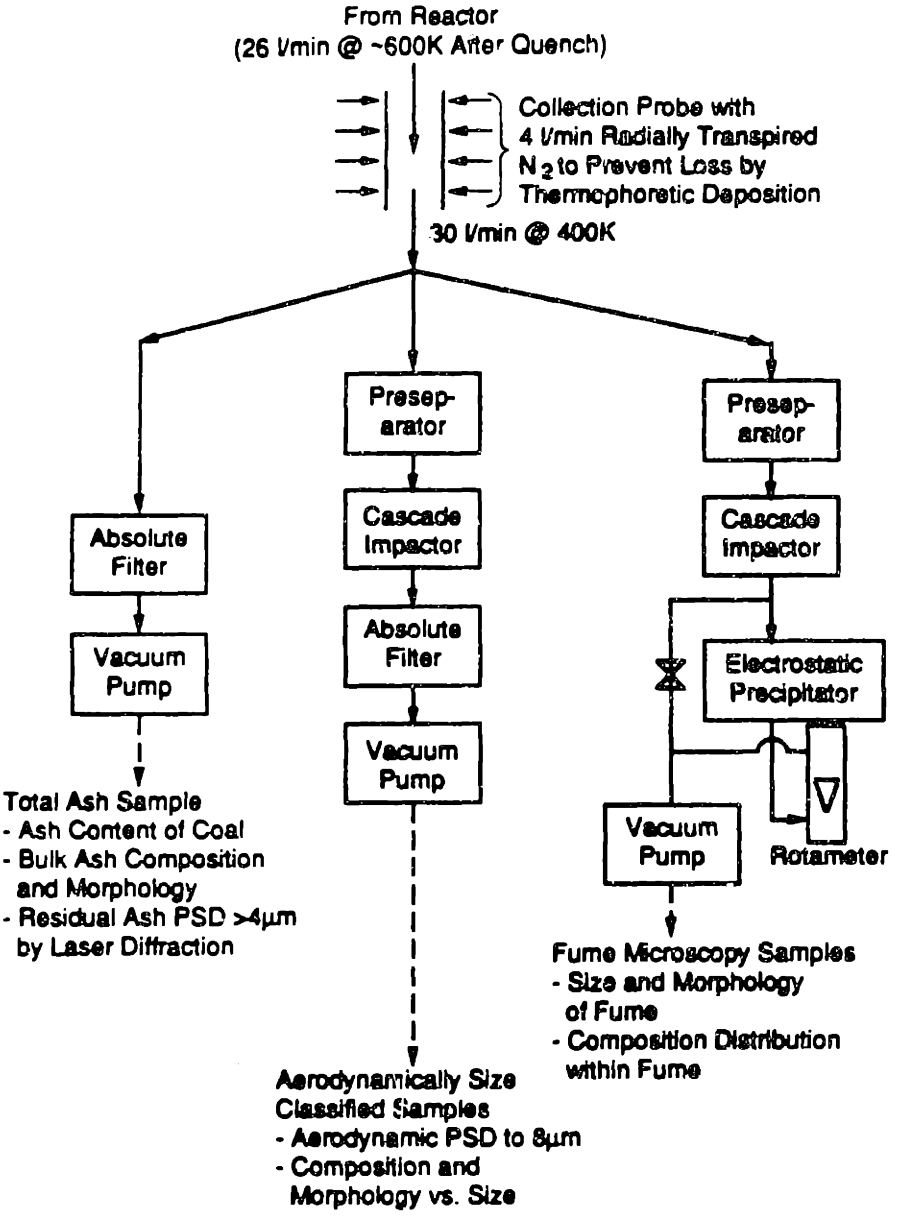

Figure 2-9 Aerosol collection system

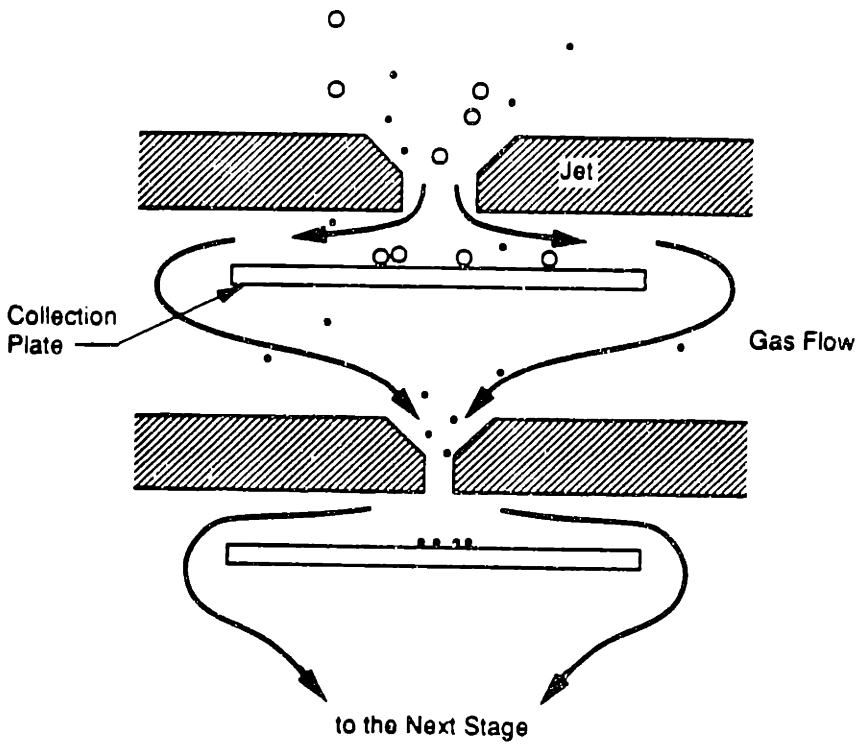

FIgure 2-10 Cascade impactor

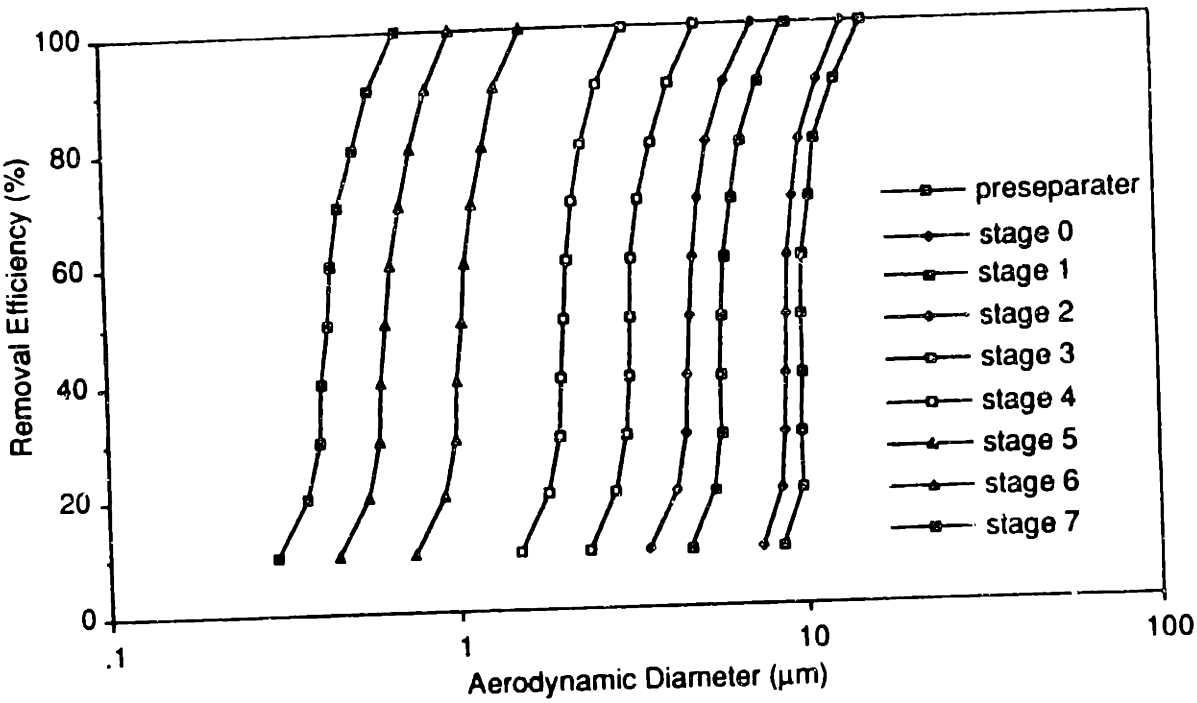

Figure 5-11 Remove efficiency versus particle size for each stage of the cascade impactor

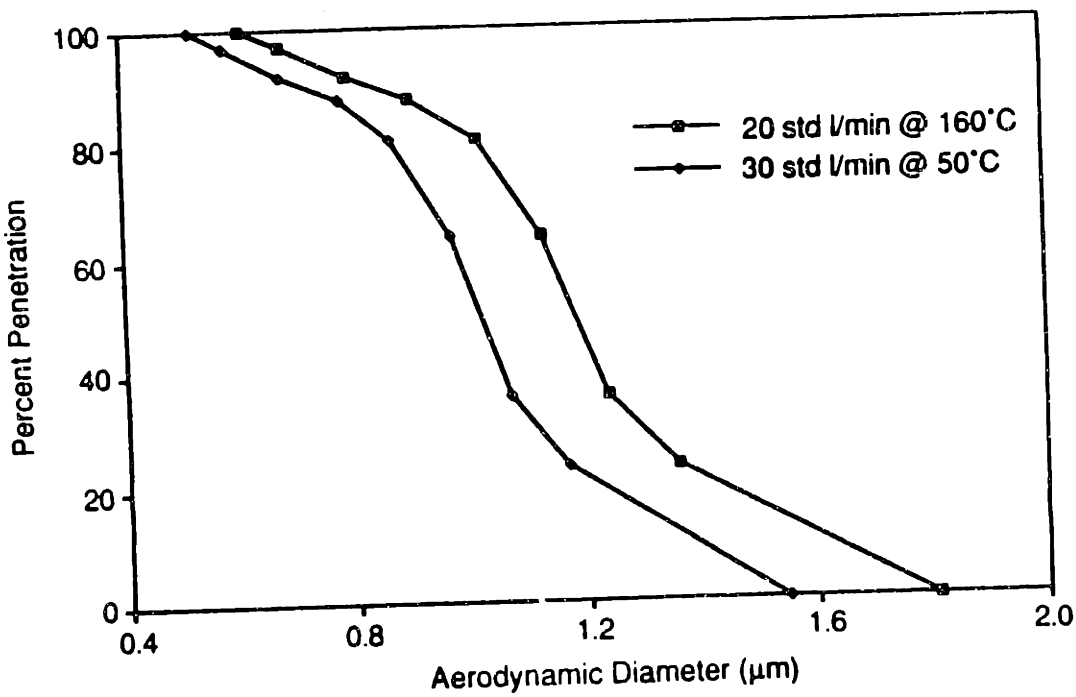

Figure 2-12 Cumulative penetration curve for first six impactor stages

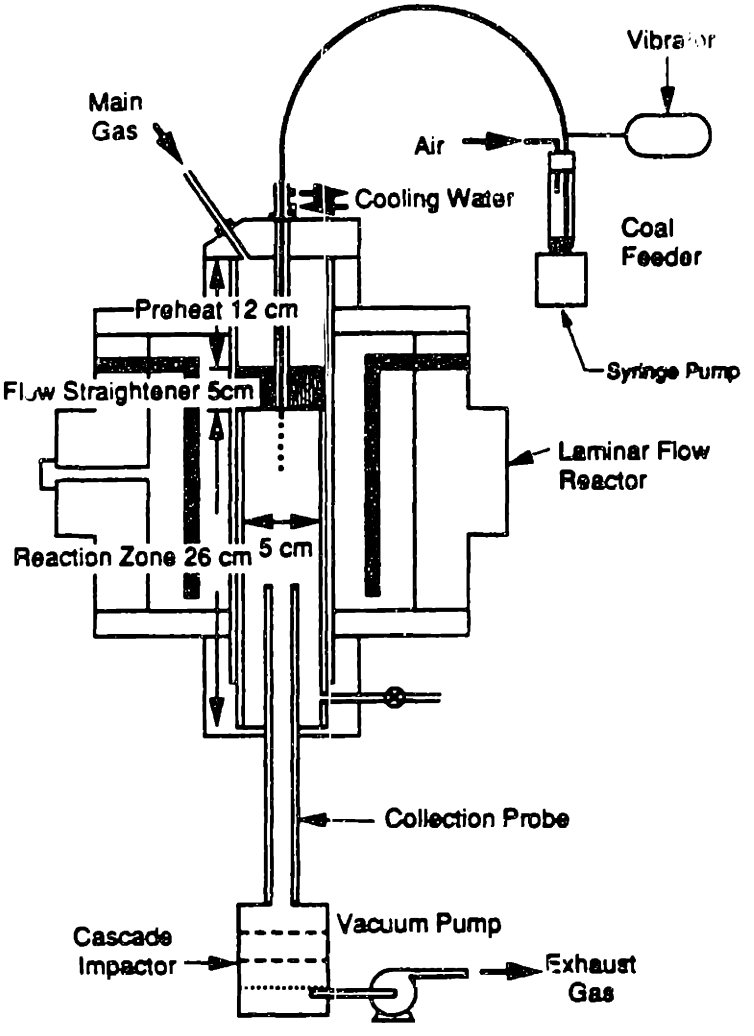

Figure 2-13 MIT laminar entrained flow reactor

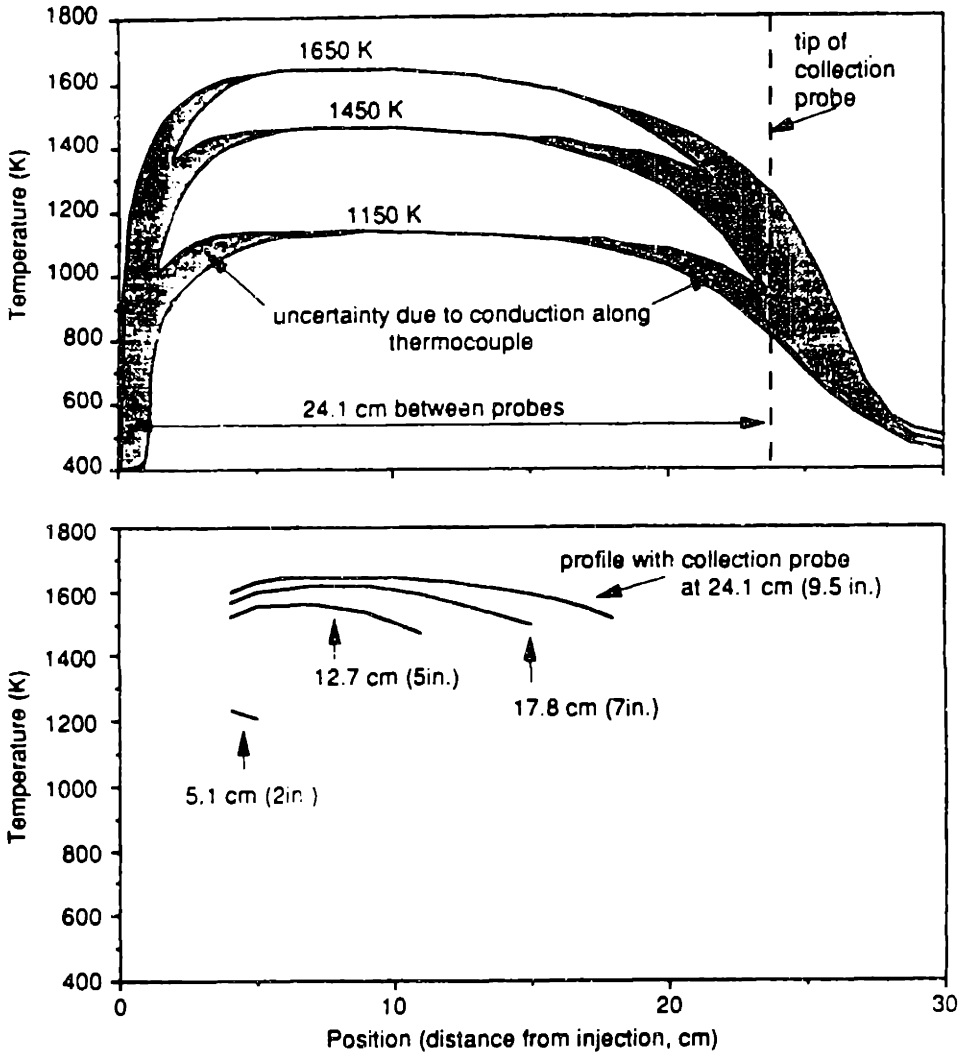

Figure 2-14 Temperature profiles in the MIT laminar flow reactor

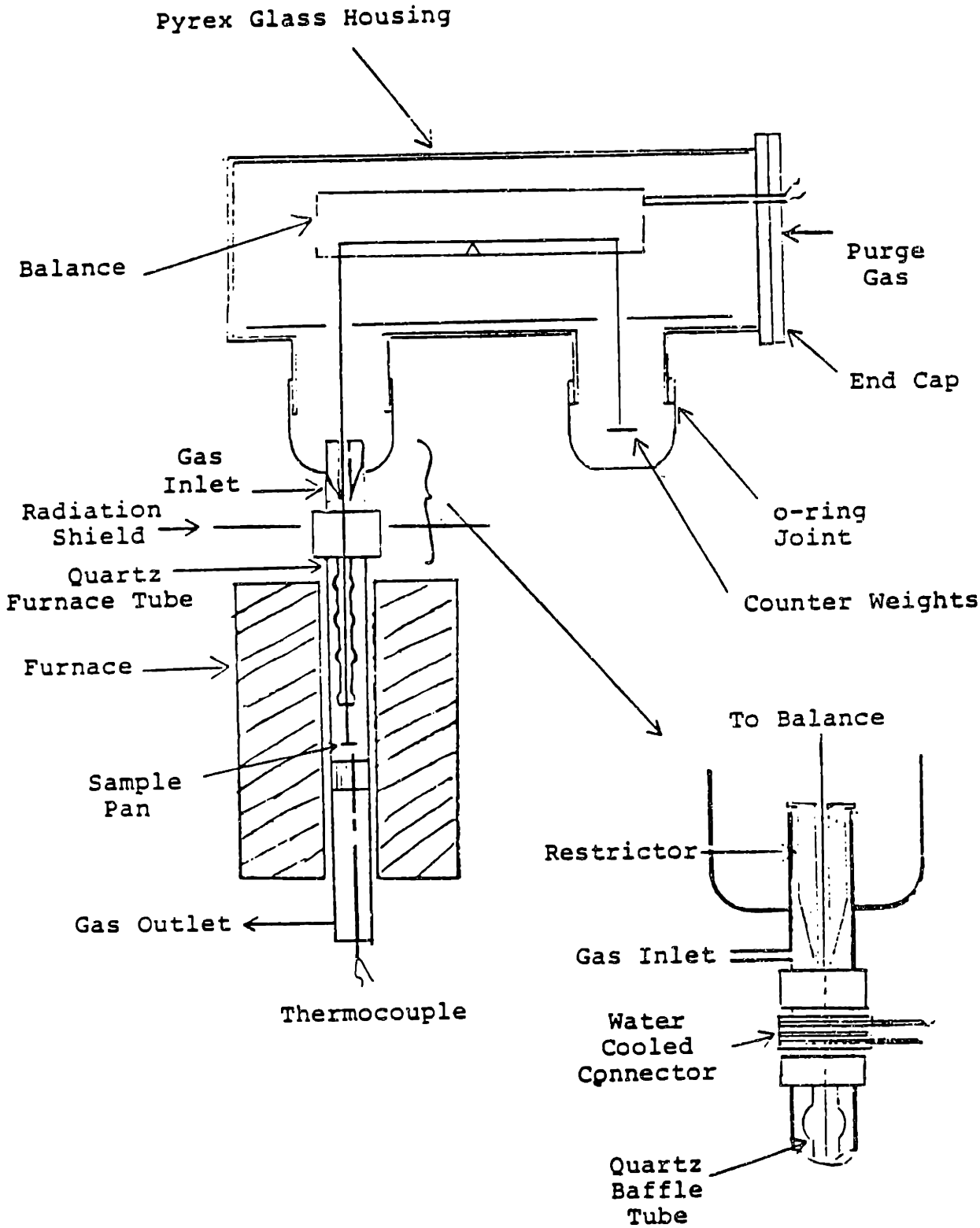

Figure 2-15 A schematic of the thermogravimetric analyzer (TGA)

Chapter 3 Coal and Mineral Characterization

One cannot underscore the importance of coal and mineral properties in every aspects of coal combustion. In this research project, the properties of coal and mineral were characterized extensively at MIT, the University of Kentucky and the USGS, and those results will be used in the study of transformation of iron and trace elements.

3. 1 Properties of parent coal

Table 3.1 Ultimate and proximate analysis of coal (as received)

	Pittsburgh	Pittsburgh beneficiated	Illinois No.6	Elkhorn/hazard	Wyodak
Proximate(wt %)					
fixed carbon	61.99	56.42	53.16	56.46	43.14
volatile matter	30.22	36.37	33.27	33.80	36.44
moisture	1.44	2.00	3.31	2.33	13.06
ash	7.01	5.21	10.26	7.41	7.36
Ultimate (wt %)					
Carbon	76.62	78.83	67.7	74.87	53.20
Hydrogen	4.80	5.39	4.73	4.59	4.59
Nitrogen	1.48	1.37	1.18	1.43	0.83
Oxygen	6.91	8.98	9.20	7.01	20.74
Sulfur	1.64	1.71	3.60	0.82	0.22
Chlorine	0.098	NA	0.034	0.17	NA
Moisture	1.44	2.00	3.31	2.33	13.06
Ash	7.01	5.21	10.26	7.41	7.36
Ash composition (wt %)					
SiO_2	42.92	49.2	44.38	55.83	53.20
Al_2O_3	22.87	24.80	17.35	34.27	18.04
Fe_2O_3	19.18	19.0	19.80	5.18	5.81
TiO_2	1.71	1.1	0.91	1.71	1.80
CaO	1.84	2.4	4.00	1.84	24.35
MgO	0.60	1.2	0.85	0.60	2.61
Na_2O	0.32	0.6	0.63	0.32	0.90
K_2O	1.53	1.2	1.80	1.53	0.70
SO_3	1.45	2.4	4.62	1.45	12.93
P_2O_5	0.23	0.5	0.12	0.23	1.10

Note that the beneficiated Pittsburgh coal was used only in the study of iron transformation. The other four coals were used in the study of trace element transformation, as well as mineral

transformation including iron. In the following sections, the coals generally refers to the four coals used for trace element transformation, but the Pittsburgh beneficiated coal would be specified.

3.2 Separation of coal

The four selected coals were segregated into 3-density layers using the small fluidized-bed separator. The portions with high density and low density were used in this study. The ash contents for the total 16 classified coals were analyzed using the ASTM standard. The results are presented in Table 3.2.

Table 3.2 Ash content of classified coals

	KYH4563	KYL4563	KYH90106	KYL90106	PTH4563	PTL4563	PTH90106	PTL90106
Ash (%)	7.2	6.5	10.3	5.5	7.1	5.9	10.5	5.6

	ILH4563	ILL4563	ILH90106	ILL90106	WYH4563	WYL4563	WYH90106	WYL90106
Ash(%)	9.3	7.4	11.0	6.4	5.8	5.6	7.1	6.6

In the table, KY represents the Elkhorn/Hazard coal, PT is Pittsburgh coal, IL means Illinois coal, WY is Wyodak coal. "H" represents the portion from the high density layer, "L" represents the portion from the low density layer, 4563 means that the coal size is between 45 and 63 μm, and 90106 means that the coal size is between 90 and 106 μm.From the table, it can be seen that except for the Wyodak coal, ash content for the coal with sizes between 90 and 106 microns in the high density fraction are about twice those in the low density fraction; the difference in ash content for the different density fractions are not as large for coals with sizes between 45 and 63 microns. For the Wyodak coal, the differences in ash contents between the different density fractions are very small.

3.3 Properties of Minerals in Parent Coals - CCSEM Results

The CCSEM results for the well-specified coals are presented in Appendix A. Some results from CCSEM are depicted in Figures 3-1 and 3-2. Figure 3-1 shows that most minerals have sizes smaller than 20 microns. In section 3.2., it was shown that ash is

concentrated in the large dense coal particles, which is consistent with CCSEM observations. Figure 3-2 shows that for Pittsburgh coal, the effect of density segregation on the elemental distribution is mainly due to the concentration of pyrites in the dense and large particle fractions. This can be used to explain why Wyodak coal can not be separated into distinguishable density cuts, because it contains negligible amount of pyrites.

3.4 Neutron Activation Analyses (NAA) of the program coals

The trace elements for the size segregated and density segregated coals were analyzed using the Neutron Activation Analysis (NAA) at the MIT nuclear reactor laboratory. The results for the four program coals are tabulated in Tables 3-3 - 3-6, and are also depicted in Figures 3-3 to 3-8. In those figures the ratios of concentrations are presented for several elements in each coal. A ratio greater than one indicates that the element is enriched in one fraction.

As shown in Figure 3-3, arsenic, zinc, mercury, and selenium are concentrated in the high density fraction (45 to 63 microns size cut) of the Pittsburgh and Elkhorn/Hazard coals. For the Illinois No. 6 coal, only zinc was enriched in the high density fraction. For Wyodak coal, all the elements are uniformly distributed. Arsenic and mercury were also enriched in the high density fraction for the 90 to 106 microns size range of the Pittsburgh and Elkhorn/Hazard coals. Fe, a major constituent of the mineral matter, was also found to be enriched in the high density fraction in those samples (Figure 3-4).

Figure 3-5 illustrates the partitioning of the various elements between two size cuts. As shown in this figure, zinc was enriched in the smaller size fraction for all coals. Arsenic, iron, mercury, sodium, cobalt, chromium, and selenium are uniformly distributed between these two size cuts.

Figures 3-6 and 3-7 show the effect of size on the trace elements concentration in a given density split. Zinc, arsenic, and selenium are enriched in the smaller sizes (low density fraction) in the Pittsburgh coal, while only zinc is enriched in this size range for

the Elkhorn/Hazard coal. Generally, the elements are uniformly distributed between the two size cuts for the low density cuts. For the high density cut, most of the elements were found to be enriched in the large size ranges. The only exceptions are zinc, arsenic, and mercury in the Pittsburgh coal and zinc in the Elkhorn/Hazard coal. For Wyodak coal, most elements are uniformly distributed; only Zn, Hg, As and Se are enriched in the smaller sizes for the high density cut and Zn and Hg for the low density cut.

Figure 3-8 shows the distributions of Fe and Na as a function of size in Illinois and Elkhorn/Hazard coals. It is found that, Fe and Na are enriched in the smaller coal particles (smaller than 45 μm), and depleted in bigger coal particles (bigger than 106 μm). However, the differences for the coal particles with size between 45 and 106 μm are not very large.

3.5 Occurrences of Iron and Trace Elements in Coal

As discussed above, extensive coal characterization was carried out in parallel to this project(Senior, et al., 1997), and the results presented below are based upon the work at the University of Kentucky and the US Geological Survey(USGS). Since those data are indispensable to the study of transformation of iron and trace element, they are presented here.

3.5.1. Elements forms of occurrence by selective leaching

The sequential selective leaching procedure used in this study is similar to that described by Palmer et al. (1993) and Finkelman et al. (1990). In this procedure, duplicate 5 g samples were sequentially leached in 50 ml polypropylene tubes using 35 ml each of 1 N ammonium acetate, 3 N hydrochloric acid, concentrated hydrofluoric acid (HF; 48%), and 2 N (1:7) nitric acid. Each tube was shaken for 18 hours on a Burrel wrist action shaker. Because of the formation of gas during some of the leaching procedures, it was necessary to enclose each tube in double polyethylene bags, each closed with plastic coated wire straps. The bags allow gas to escape, but prevent the release of liquid. Approximately 0.5 g of residual solid was removed from each tube for instrumental neutron activation analysis (NAA). The solutions were saved for inductively coupled argon plasma atomic emission spectroscopy (ICP-AES) analysis and

inductively coupled argon plasma mass spectroscopy (ICP-MS) analysis.

Arsenic

Pittsburgh and Illinois No. 6 coals: The bulk of the arsenic in the Pittsburgh and Illinois No. 6 coals is in pyrite, as indicated by high percentages of arsenic leached by HNO_3 (Figure 3-9a). The high total percentage of arsenic leached in the Pittsburgh and Illinois coals suggests little or no organic association. Minor amounts of arsenic (10 - 20%) were leached by HCl, which may indicate an association with mono-sulfides such as sphalerite or galena. Percentages for the mode of occurrence diagram (Figure 3-10a) were derived directly from the leaching percentages.

Elkhorn/Hazard Coal: The Elkhorn/Hazard coal may have several modes of occurrence for arsenic. 30% of arsenic in the Elkhorn/Hazard coal was leached by HCl and 25% of arsenic was leached by HNO_3. A minor amount of arsenic was leached by HF (5%). Leaching of arsenic by HCl may indicate the presence of arsenates that were formed by the oxidation of pyrite. It is also possible that HCl-soluble arsenic-bearing sulfides (such as spahlerite or galena).

Because only 60% of the total arsenic in the Elkhorn/Hazard coal was leached, an organic association for arsenic or the presence of organically encapsulated (shielded) arsenic-bearing pyrite might be suggested. However, petrographic and SEM analysis of solid residue from the nitric acid leach have identified the presence of both shielded and unshielded pyrite grains in the solid residues. To estimate the total amount of arsenic present in pyrite, the amount of nitric acid leached arsenic (25%) was adjusted by adding the amount of unleached arsenic (40%), to give the total arsenic in pyrite (60%, Figure 3-10a).

Similar to the Elkhorn/Hazard coal, the Wyodak coal has more than one mode of occurrence for arsenic. 35% of arsenic in the Wyodak coal was leached by HCl; 15% of arsenic was leached by HF. Leaching by HCl may indicate an association with iron oxide; leaching by HF probably indicates an association with clays (possible illite). 50% of the total arsenic was not leached in the Wyodak coal, which may be associated with organics.

Iron

In the Pittsburgh and Illinois coals, the leaching behavior of iron is similar to that of arsenic. Iron was leached primarily by HNO_3 (85-90%). In the Elkhorn/Hazard coal, only 75% of the total iron was leached, and only a small portion of iron (15%) was leached by HNO_3. Base upon the observations of unleached pyrite grains in the nitric acid solid residue, it was estimated that the sum of leachable iron in pyrite and unleached iron iron (25%) was approximately equivalent to the total amount of iron in pyrite (40%) (Fig. 3-10b). The assumption that the Elkhorn/Hazard coal contains little or no organically-bound iron is inherent in this estimate. The ratio of leachable iron in pyrite to total iron in pyrite (15/40) is approximately 38%.

In the Wyodak coal, 65% of the iron was leached by HCl and 25% by HF. In contrast to arsenic, nearly all of the iron was leached (90%). It is therefore inferred that the iron is primarily associated with iron oxides or carbonates (as indicated by leaching with HCl) and clays (as indicated by leaching with HF).

Selenium

In the Pittsburgh coal, selenium was leached to a large degree by nitric acid (90%), suggesting an association with pyrite (Fig. 3-9c). An association of selenium with pyrite is also evident in the Elkhorn/Hazard coal, where selenium was leached primarily by nitric acid (50%). In the Ekhorn/Hazard coal and Illinois coals, an association with the organics was expected, because the total amount of selenium leached is fairly low (45% and 60% respectively). In the Pittsburgh and Elkhorn/Hazard coals, selenium was leached to some degree (5% and 15% respectively) by HCl. The HCl soluble selenium may be in accessory mono-sulfides such as aphalerite (ZnS) and galena (PbS).

In the Wyodak coal, selenium was leached primarily by ammonium acetate (20%). Only 30% of the total selenium was leached, suggesting an association with organics.

3.5.2 Elements forms of occurrence by XAFS

Arsenic

The results by XAFS spectroscopy and the leaching method are presented in table 3-7.

Table 3-7 Arsenic forms in coals

	XAFS Spectroscopy		Leaching method		
	As in pyrite	AsO_4^{3-}	As (HNO_3+residue)	As(HF)	As(HCl+Amm.)
Elkhorn/Hazard	61	39	65	5	30
Illinois	86	14	80		20
Pittsburgh	88	12	90		10
Wyodak	50(carboxyl)	50	50 (residue)	15	35

It is believed that, an arsenate (AsO_4^{3-}) form, was most likely formed from the arsenical pyrite upon exposure to air. In other word, the arsenic in the form of AsO_4^{3-} is actually embedded in pyrite (pyrrhotite). From the table above, it can be seen that, the results by the two methods are quite consistent. In summary, arsenic is present in the coals as follows:

Elkhorn/Hazard: 100% associated with Fe-S

Pittsburgh: 100% associated with Fe-S

Illinois: 100% associated with Fe-S

Wyodak: 50% associated with Fe-S; 50% As^{3+}(as carboxyl)

Chromium

Chromium in the four coals is estimated to occur as follows:

Elkhorn/Hazard: 70% to 85% amorphous CrCOOH, 10% to 20% Cr^{3+}/illite and Fe spinel

Pittsburgh: 50%-70% amorphous CrCOOH, 30%-50% Cr^{3+}/illite

Illinois: 80%-90% amorphous CrOOH, 10-20% Cr^{3+}/illite

Wyodak: > 80% carboxyl-bound Cr^{3+}

The major results on the occurrences of forms of elements in coal can be summarized as: (1) nearly all As is associated with pyrites except for Wyodak coal which has very low arsenic content (about 2ppm) and very low content of pyrites; (2) selenium is mainly associated with pyrites; (3) chromium is probably presented in -COOCr; (4) zinc is mostly in the form of ZnS in Illinois coal, while Zn may be associated with other minerals in other coals, (5) iron is mostly presented in pyrite, except for Elkhorn/Hazard coal which has a significant part of jarosite.

Table 3-3 Concentrations of elements in Elkhorn/Hazard coal

	High 45<d<63	Medium 45<d<63	Low 45<d<63	High 90<d<106	Medium 90<d<106	Low 90<d<106
Na	283±20	235±16	245±16	300±20	220±15	203±13
Sc	3.9±.1	3.4±.2	3.6±.2	4.0±.3	3.8±.2	3.4±.2
Cr	17±1	14±1	15±1	13±1	14±1	12±1
Fe	4125±175	1428±75	1433±80	4055±210	1190±70	1073±70
Co	6.9±.4	5.7±.4	6.4±.4	6.5±.4	6.3±.4	5.7±.3
Zn	35±5	34±6	33±5	21±3	17±3	16±3
As	5.6±.6	1.8±.2	1.9±.2	2.6±.8	2.2±.3	1.4±.2
Se	3.3±.9	2.6±.8	3±.8	2.8±.7	3.8±.8	2.5±.7
Br	28±8	26±7	28±7	125±35	144±40	135±40
Rb	3.7±1.2	1.4±.6	2.9±1.2	2.5±1.5	2.7±1.4	2.6±1.6
Mo	4.2±1.0	3.4±.9	3.6±.9	2.8±.7	2.6±.7	2.3±.6
Cd	.17±0.12	.18±.11	.11±.07	.20±.19	.26±.2	.31±.12
Sb	1.1±.1	.89±.07	.97±.1	.85±.06	.86±.07	.79±.06
Cs	.23±.1	.22±.09	.30±.1	.25±.11	.34±.1	.29±.1
Ba	110±17	83±13	67±13	70±15	73±14	65±15
La	14±1	12±1	12±1	14±1	13±1	11±1
Ce	25±1	22±1	21±1	27±1	25±1	21±1
Sm	2.5±.2	2.2±.2	2.3±.2	2.6±.2	2.4±.2	2.1±.2
Eu	.37±.07	.41±.08	.34±.07	.57±.09	.45±.07	.37±.07
Yb	1.5±.0	1.3±.2	1.3±.2	1.5±.3	1.4±.2	1.2±.2
Lu	.23±.06	.22±.06	.23±.06	.24±.05	.23±.05	.21±.05
Hf	1.2±.1	.73±.06	.75±.12	1.3±.1	.86±.08	.82±.07
Au*	.88±.24	.73±.17	.71±.22	.58±.28	1.0±.3	.95±.29
Hg	.13±.03	.11±.02	.095±.03	.077±.023	.042±.021	.049±.021
Th	4.2±.2	3.6±.2	3.9±.2	4.4±.3	4.0±.2	3.6±.2

* bbm

Table 3-4 Concentrations of elements in Illinois coal

	COAL1		COAL13		COAL2	
Element	ILH90106 heavy(bottom)	+/-	ILM90106 medium(middle)	+/-	ILL90106 light(top)	+/-
ppm						
Na	310	20	310	20	290	20
Sc	2.1	0.1	2.1	0.1	1.9	0.1
Cr	14	1	16	1	13	1
Fe	23000	1000	7500	300	6700	300
Co	3.7	0.2	2.7	0.2	2.7	0.2
Zn	130	20	13	3	7.7	1.9
As	4.1	0.4	1.3	0.1	1.2	0.1
Se	1.7	0.4	1.3	0.4	1.1	0.3
Br	3.5	0.9	3.8	1	3.8	1
Rb	11	2	10	2	8.5	1.6
Mo	5.4	1.2	5	1.1	4.7	1
Cd	0.17	0.14	0.049	0	0.11	0
Sb	0.45	0.04	0.41	0.03	0.35	0.03
Cs	0.64	0.11	0.75	0.13	0.76	0.12
Ba	26	10	44	11	30	9
La	3.7	0.2	3.5	0.2	3.2	0.2
Ce	7.6	0.4	7.5	0.4	6.4	0.3
Sm	0.79	0.07	0.78	0.07	0.69	0.06
Eu	0.23	0.05	0.19	0.04	0.17	0.05
Yb	0.48	0.08	0.48	0.08	0.42	0.07
Lu	0.072	0.016	0.11	0.02	0.079	0.017
Au*	0.29	0	0.28	0.6	0.1	0.06
Hg	0.18	0.01	0.048	0.012	0.068	0.01
Th	1.4	0.1	1.6	0.1	1.4	0.1
U	1.5	0.1	1.8	0.1	1.7	0.1

* ng/g

	COAL9		COAL7		COAL11	
Element	ILH4563 heavy(bottom)	+/-	ILM4563 medium(middle)	+/-	ILL4563 light(top)	+/-
ppm						
Na	290	19	320	20	320	20
Sc	1.9	0.1	2.1	0.1	2	0.1
Cr	13	1	14	1	15	1
Fe	14000	1000	11000	1000	10000	1000
Co	2.9	0.2	2.8	0.2	2.6	0.2
Zn	71	10	67	9	27	4
As	2.5	0.2	1.9	0.2	1.8	0.2
Se	1.2	0.4	1.8	0.6	1.7	0.5
Br	3	0.8	3.8	1	3.6	1
Rb	8.4	1.7	7.7	1.5	10	2
Mo	3.9	0.9	4.3	0.9	3.7	0.8
Cd	0.29	0.16	0.098	0.075	0.066	0
Sb	0.35	0.03	0.36	0.03	0.35	0.03
Cs	0.85	0.14	0.87	0.14	0.68	0.12
Ba	23	9	29	9	43	9
La	3.2	0.2	3.4	0.2	3.3	0.2
Ce	6.4	0.3	7.3	0.4	6.9	0.4
Sm	0.69	0.06	0.74	0.06	0.74	0.06
Eu	0.19	0.04	0.23	0.05	0.21	0.04
Yb	0.42	0.07	0.46	0.08	0.46	0.08
Lu	0.078	0.017	0.085	0.019	0.089	0.019
Au*	0.55	0.21	0.42	0.15	0.9	0.37
Hg	0.085	0.012	0.073	0.018	0.065	0.016
Th	1.3	0.1	1.5	0.1	1.5	0.1
U	0.094	0.03	1.9	0.1	1.4	0.1

* ng/g

Table 3-5 Concentrations of elements in Pittsburgh coal

	COAL10		COAL5		COAL6	
Element	PittH90106 heavy(bottom)	+/-	PittM90106 medium(middle)	+/-	PittL90106 light(top)	+/-
ppm						
Na	540	30	480	30	490	30
Sc	1.8	1.1	1.7	0.1	1.6	0.1
Cr	9.4	0.4	7.8	0.3	8.4	0.4
Fe	30000	1000	4400	200	3900	200
Co	3.8	0.2	1.9	0.1	2.2	0.2
Zn	6.3	2.1	8.7	2.5	5.6	2.9
As	16	2	1.8	0.2	1.5	0.2
Se	2.1	0.6	0.96	0.56	1.1	0.6
Br	15	4	18	5	18	5
Rb	6	1.7	5.3	1.3	3.5	1.3
Mo	1.3	0.3	0.91	0.22	0.71	0.17
Cd	0.031	0	0.057	0.035	0.055	0.033
Sb	0.47	0.04	0.21	0.02	0.2	0.02
Cs	0.65	0.15	0.42	0.1	0.38	0.09
Ba	76	14	90	12	83	12
La	5.2	0.3	4.5	0.3	4.5	0.3
Ce	9.9	0.5	8.2	0.4	7.8	0.4
Sm	0.86	0.07	0.71	0.06	0.71	0.06
Eu	0.23	0.05	0.14	0.04	0.12	0.04
Yb	0.47	0.08	0.4	0.07	0.34	0.06
Lu	0.067	0.015	0.055	0.012	0.054	0.012
Au*	0.23	0.19	0.17	0.07	0.13	0.09
Hg	0.28	0.02	0.061	0.019	0.045	0.013
Th	1.3	0.1	1.2	0.1	1.1	0.1
U	0.18	0.02	0.31	0.02	0.3	0.02

	COAL8		COAL4		COAL3	
Element	PittH4563 heavy(bottom)	+/-	PittM4563 medium(middle)	+/-	PittL4563 light(top 4563)	+/-
ppm						
Na	380	20	450	30	460	30
Sc	1.4	0.1	1.7	0.1	1.7	0.1
Cr	6.6	0.3	8.3	0.3	8.5	0.4
Fe	14000	1000	7200	300	6900	300
Co	2.3	0.2	2.5	0.1	3	0.2
Zn	14	3	6.7	1.1	9.3	1.9
As	6.1	0.6	3.3	0.4	3	0.3
Se	0.87	0.33	0.41	0.12	0.45	0.16
Br	13	3	17	5	17	5
Rb	3.8	1.3	4.6	0.8	4.8	1.3
Mo	0.63	0.15	1	0.2	0.85	0.21
Cd	0.45	0.21	0.19	0	0.19	0
Sb	0.31	0.02	0.25	0.02	0.28	0.02
Cs	0.43	0.1	0.35	0.06	0.45	0.09
Ba	98	11	92	10	84	12
La	3.7	0.2	4.4	0.3	4.3	0.3
Ce	6.6	0.3	7.4	0.4	7.5	0.37
Sm	0.62	0.05	0.72	0.06	0.72	0.06
Eu	0.17	0.03	0.24	0.04	0.15	0.05
Yb	0.28	0.05	0.34	0.06	0.36	0.06
Lu	0.047	0.01	0.06	0.013	0.053	0.012
Au*	0.36	0.14	0.33	0	0.2	0.09
Hg	0.13	0.01	0.09	0.02	0.071	0.019
Th	0.99	0.06	1.1	0.1	1.2	0.1
U	0.15	0.01	0.25	0.02	0.23	0.02

Table 3-6 Concentrations of elements in Wyodak coal

	A	B	C	D	E
1		WYH9010	WYL9010	WYH4563	WYL4563
2	Na	800	760	830	870
3	K	300	780	150	100
4	Sc	16	16	18	18
5	Cr	8	7	10	8
6	Fe	2800	2300	3000	2700
7	Co	2.6	3.3	3	3.3
8	Zn	30	40	87	130
9	As	0.8	1	1.4	1.1
10	Se	4	6	6	5
11	Mo	1.3	1	1	1.5
12	Cd	0.3	0.6	0.3	0.2
13	Sb	0.4	0.25	0.2	0.2
14	Ce	0.8	0.005	0.4	0.7
15	La	3.8	0.7	4	4
16	Sm	0.8	0.7	0.009	0.9
17	Au	6	0.9	2	6
18	W	0.25	0.5	0.3	0.3
19	Ta	0.7	0.1	0.5	0.6
20	U	0.8	0.8	1	1
21	Hg	0.12	0.08	0.37	0.18

Figure 3-1 Mineral distributions as a function of mineral size (CCSEM results)

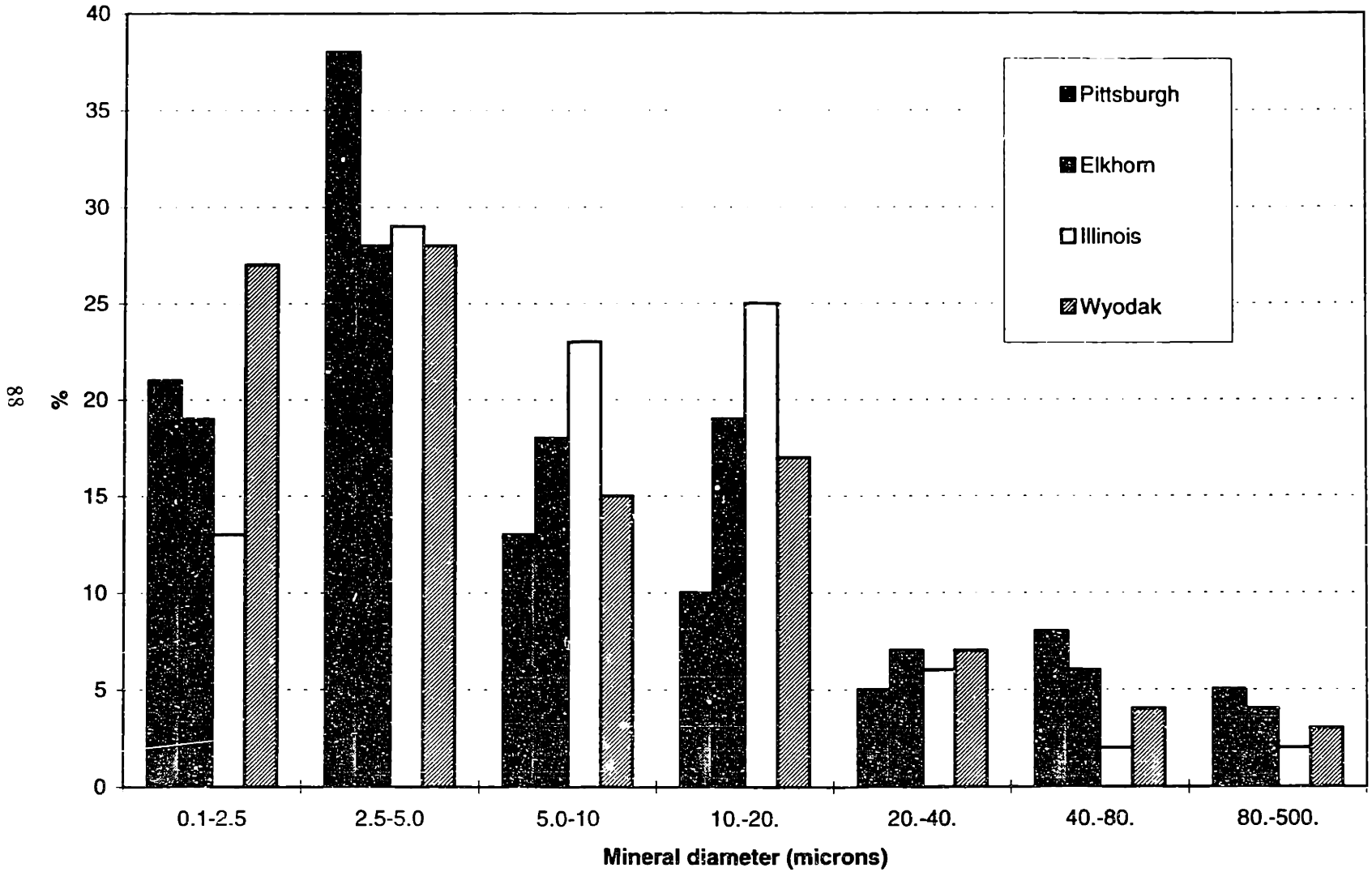

Figure 3-2 Mineral and pyrite distribution for PTH90106 coal

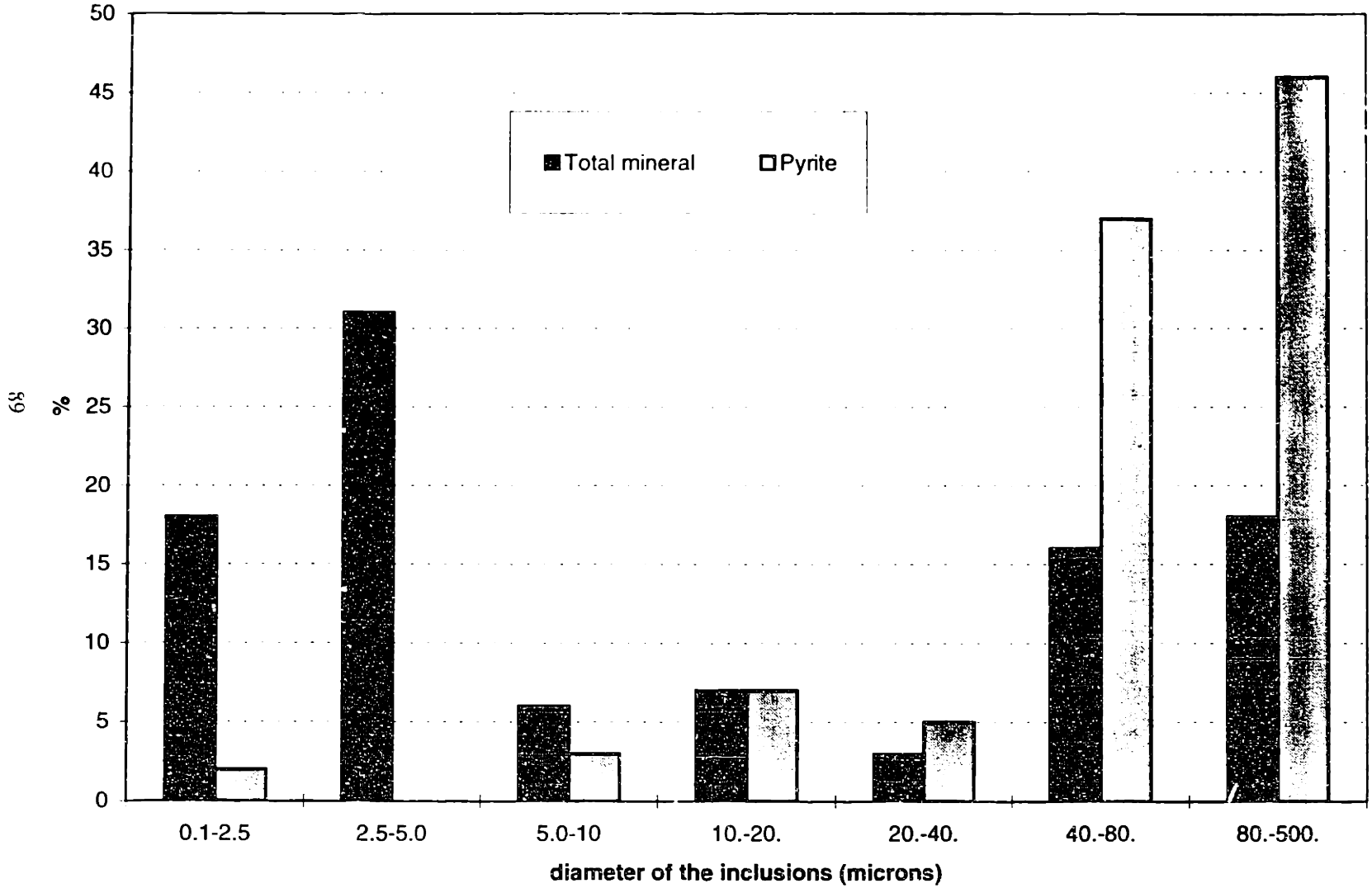

Figure 3-3 Relative element concentrations in two density fractions of the 45 to 63 microns cut of the four program coals

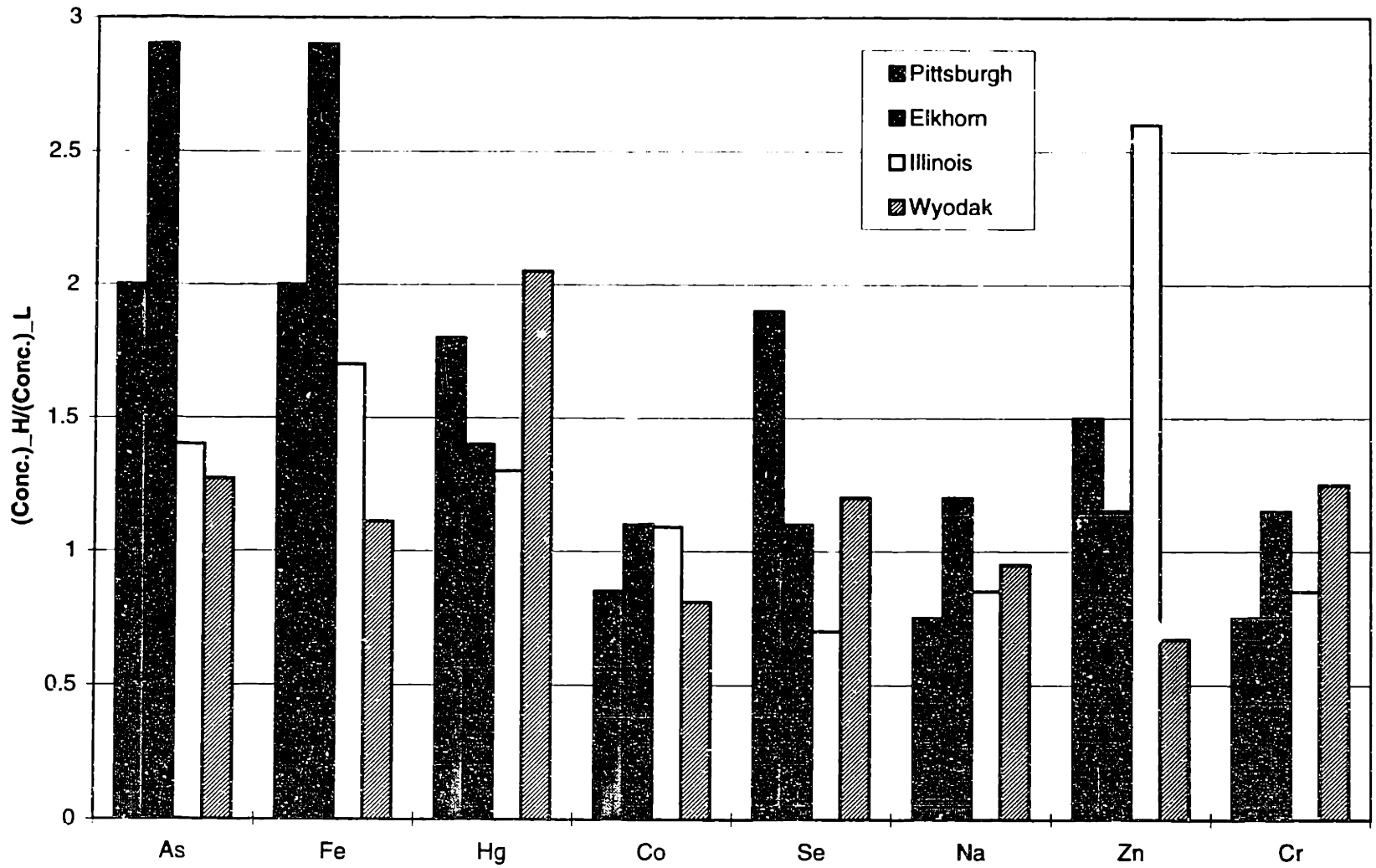

Figure 3-4 Relative element concentrations in two density fractions of the 90 and 106 microns cut of the four program coals

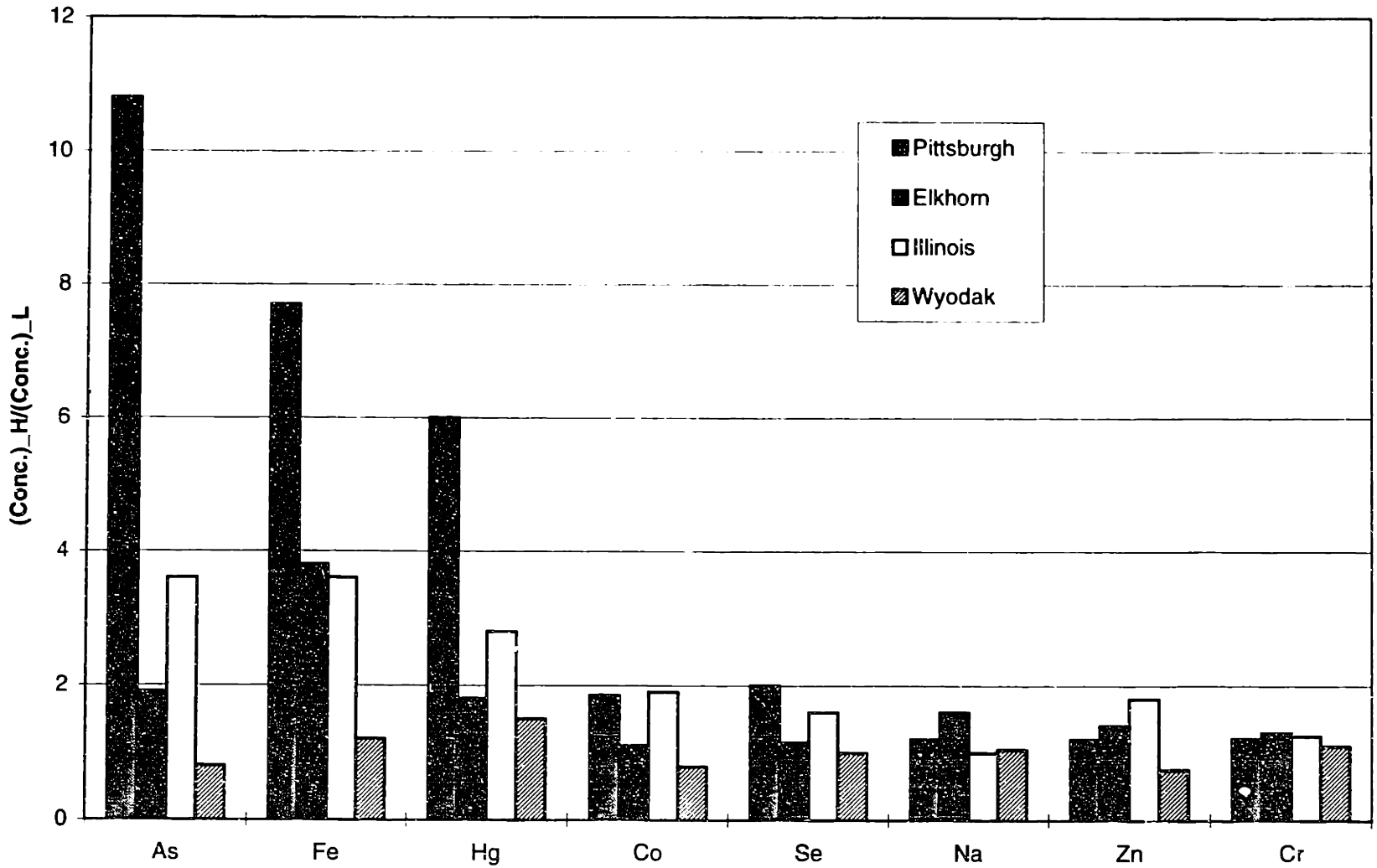

Figure 3-5 Relative element concentrations in two size fractions of the four program coals

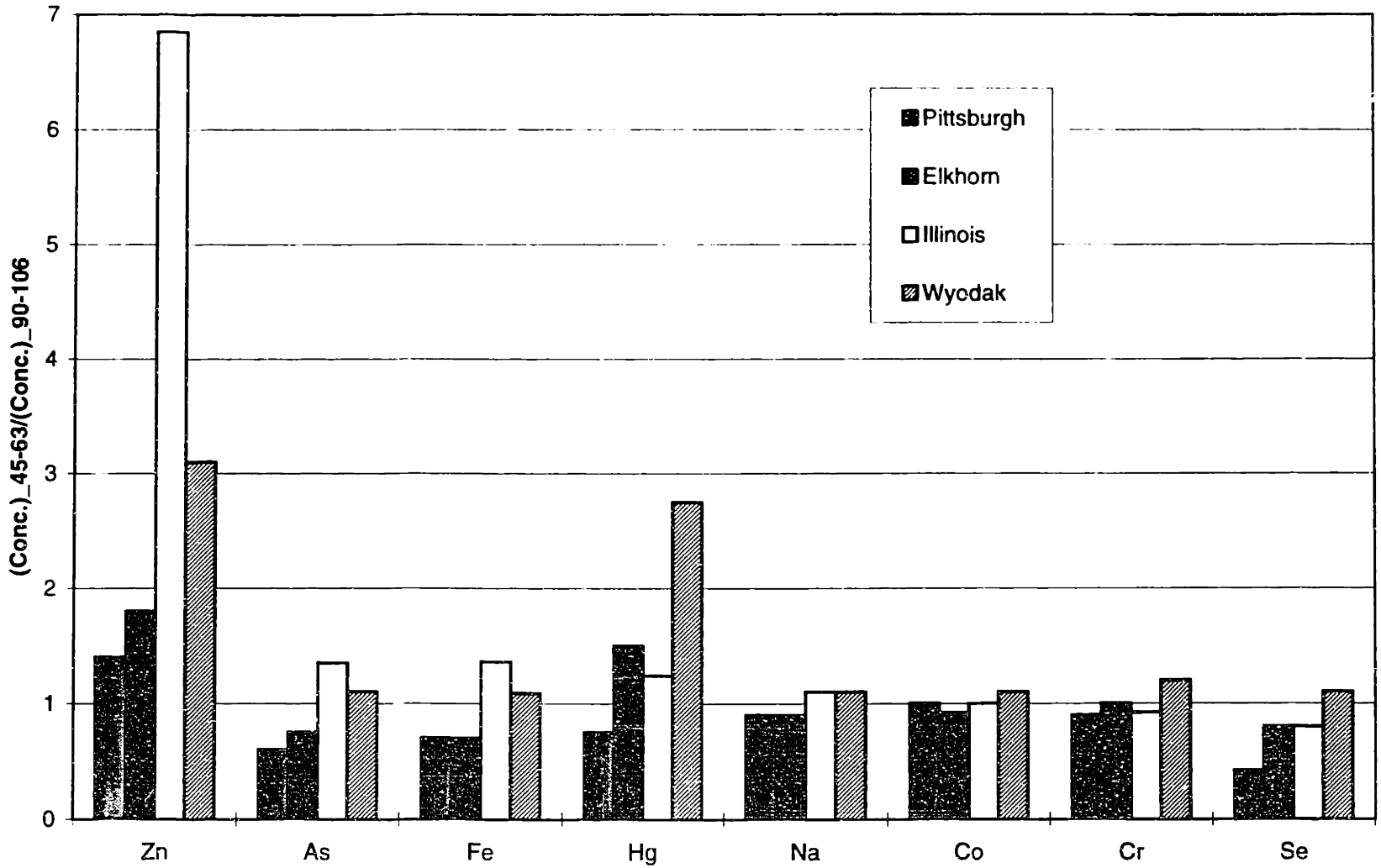

Figure 3-6 Relative element concentrations in the low density fraction of two size cuts of the four program coals

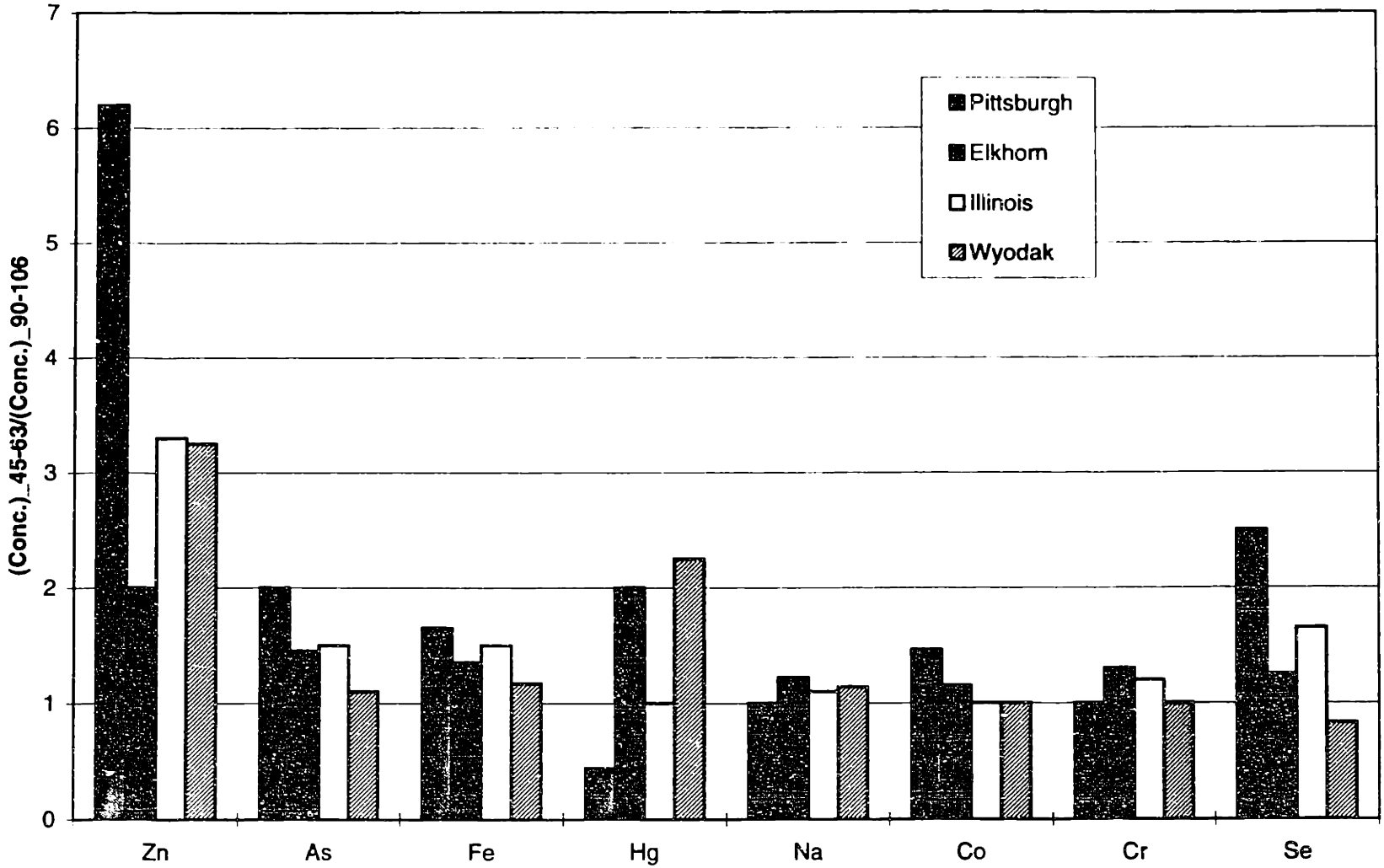

Figure 3-7 Relative element concentrations in the high density fraction of the two size cuts of the four program coals

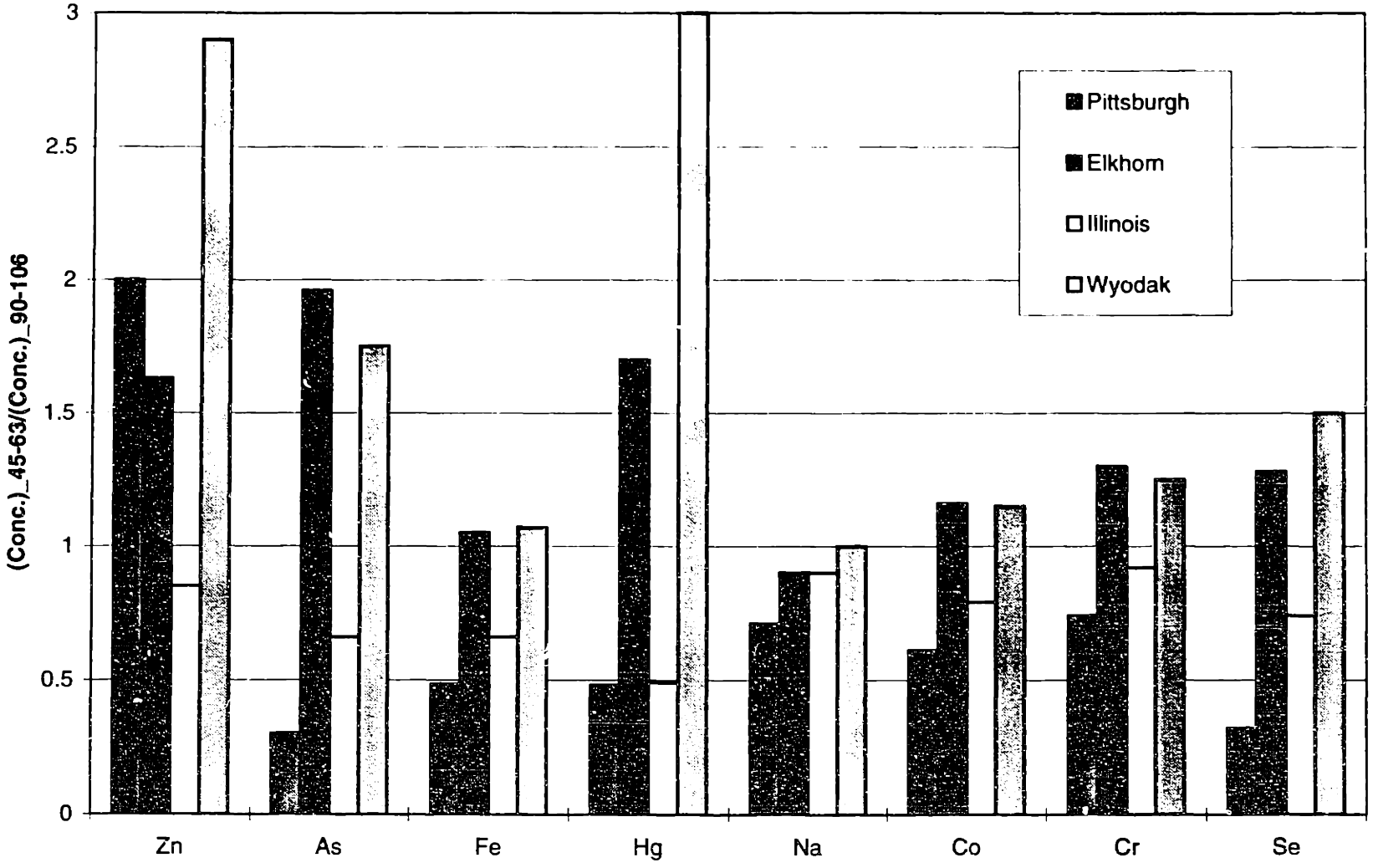

Figure 3-8 (a) Concentrations of Fe and Na in size cuts for Illinois coal

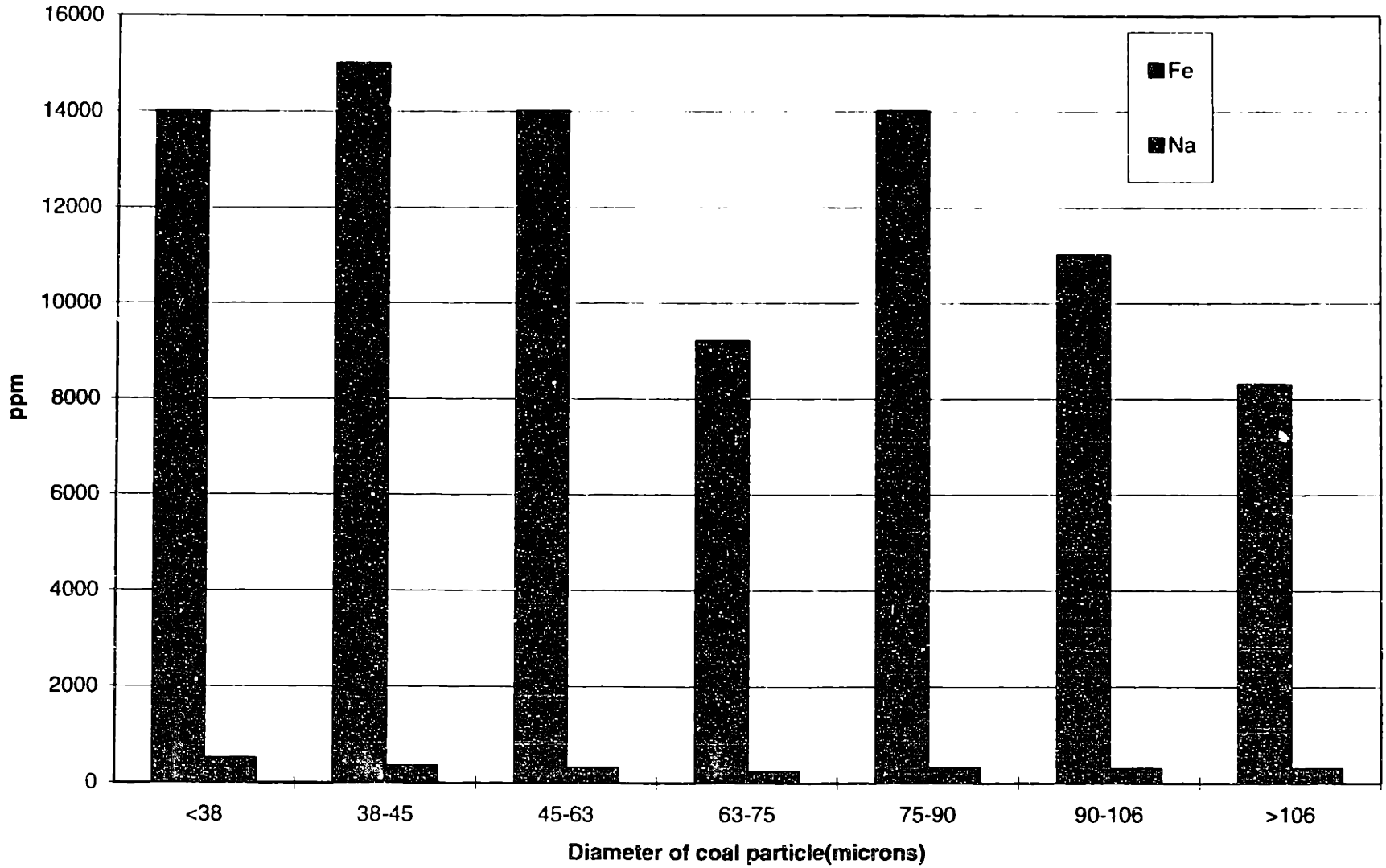

Figure 3-8 (b) Concentrations of Fe and Na in size cuts for Elkhorn/Hazard coal

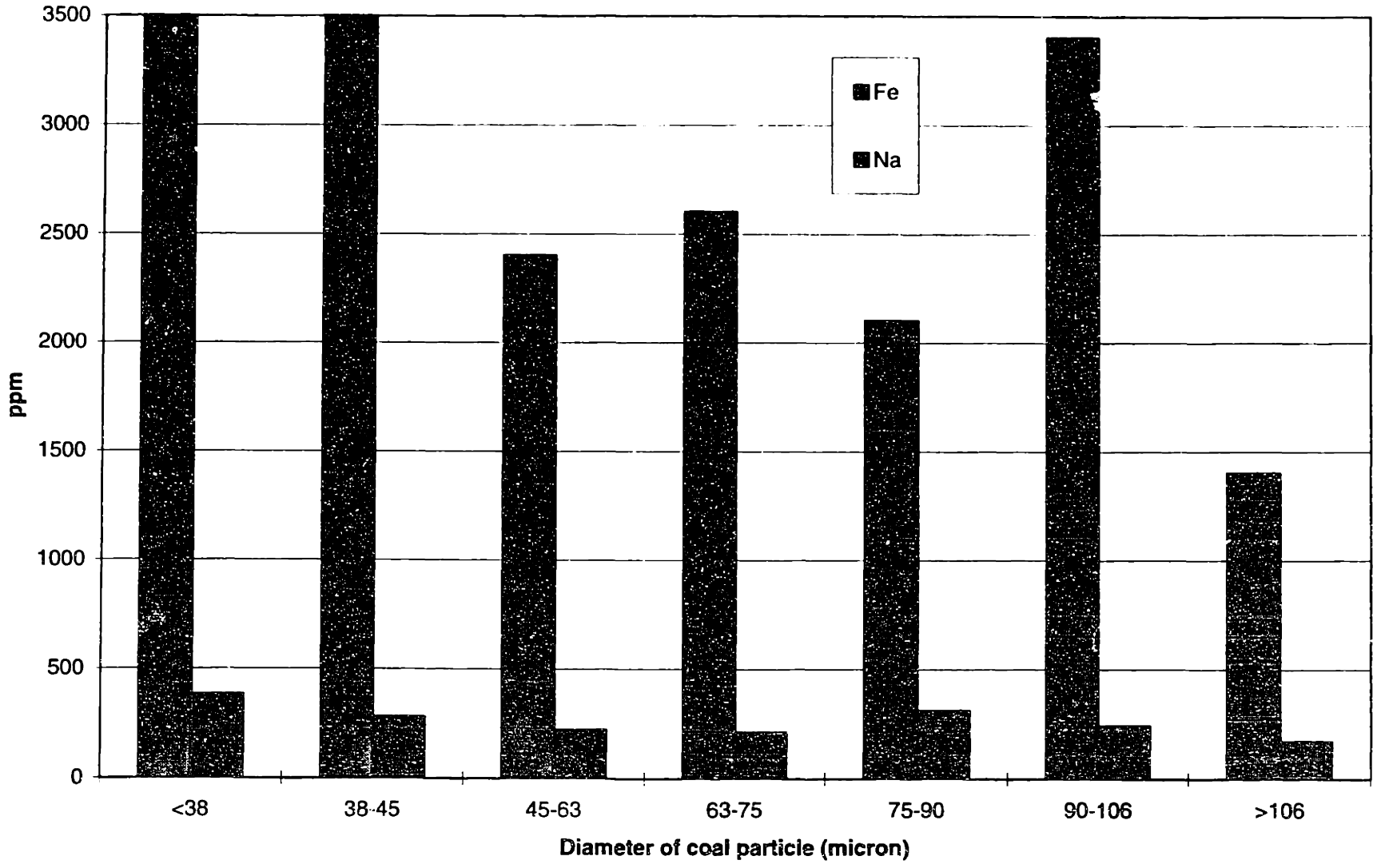

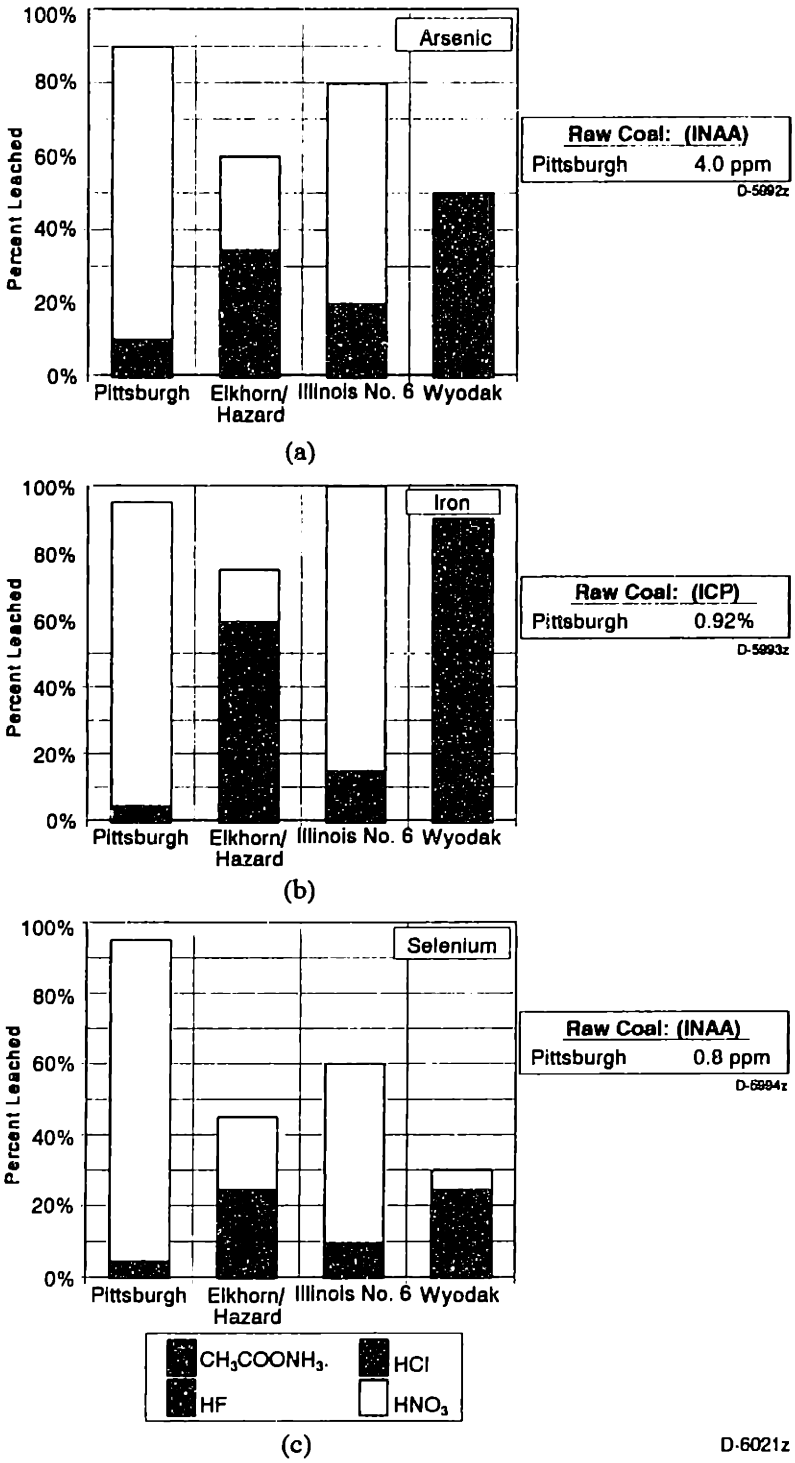

Figure 3-9 Bar charts showing the percentage of each trace element leached arsenic (a), iron (b), selenium (c), chromium (d), nickel (e), and mercury (f) by each leaching agent (ammonium acetate, hydrochloric acid, hydrofluoric acid, and nitric acid) compared to the concentration of the element in the raw coal (senior, et al., 1997)

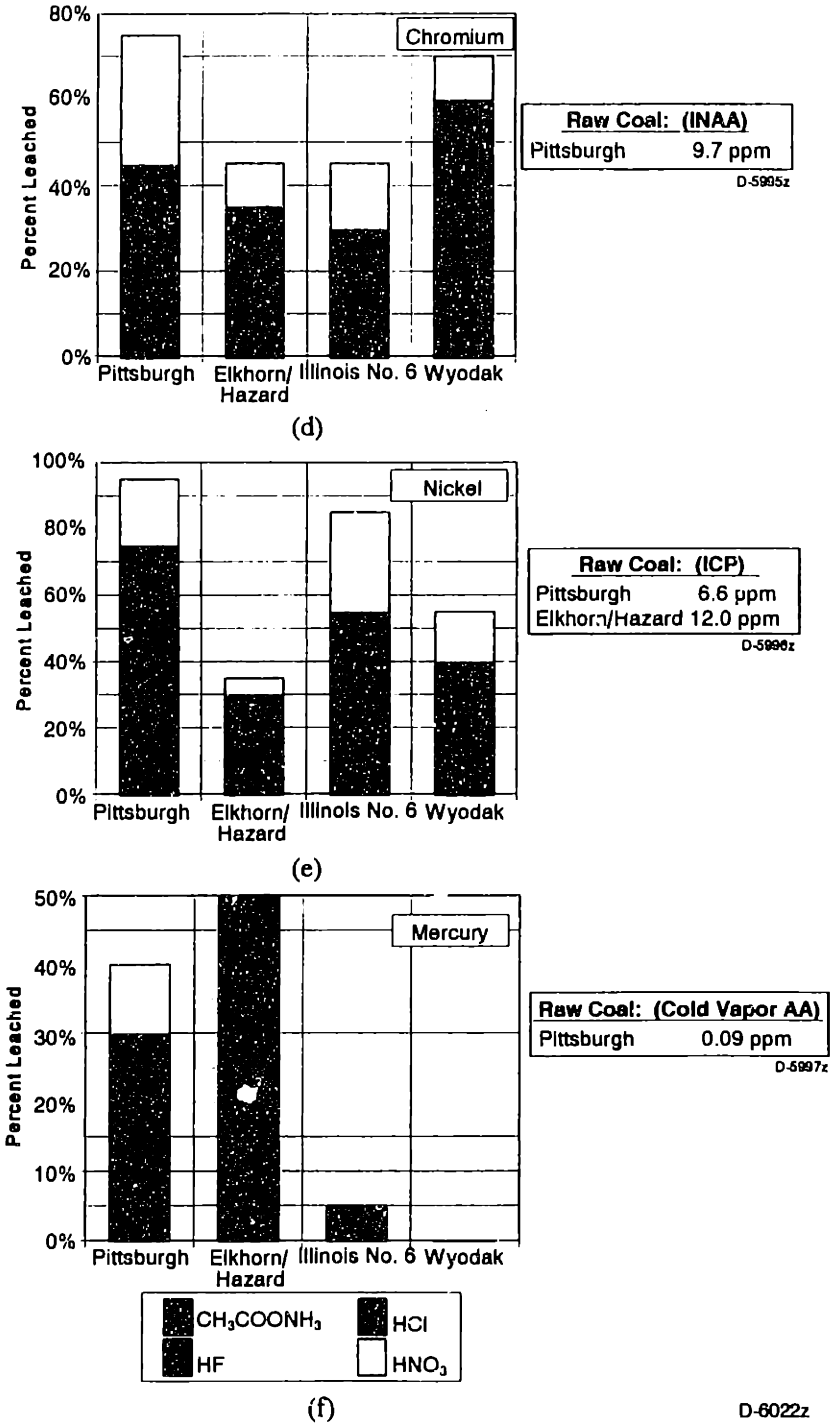

Figure 3-9 (continued) Bar charts showing the percentage of each trace element leached arsenic (a), iron (b), selenium (c), chromium (d), nickel (e), and mercury (f) by each leaching agent (ammonium acetate, hydrochloric acid, hydrofluoric acid, and nitric acid) compared to the concentration of the element in the raw coal

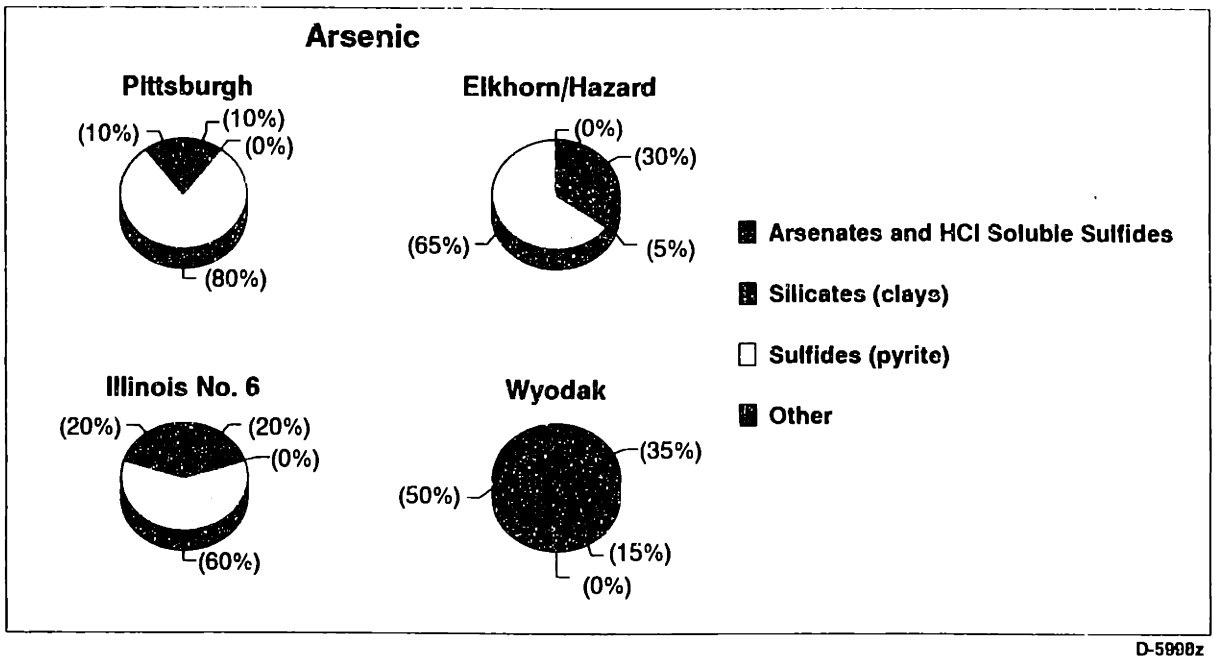

(a)

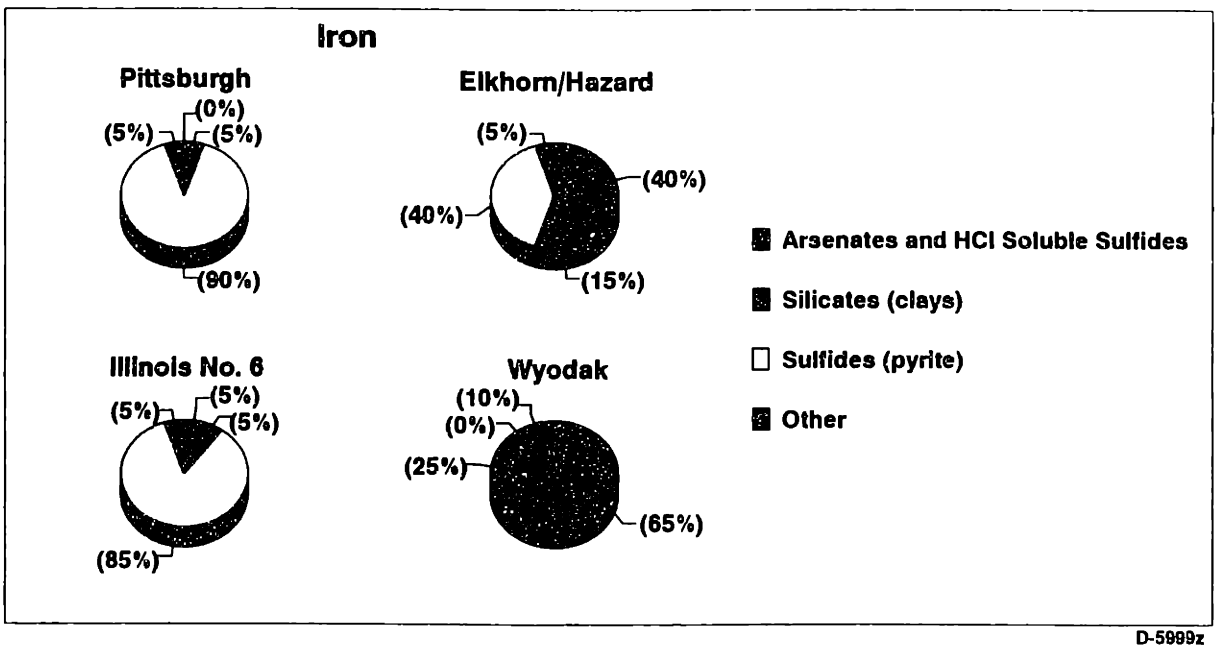

(b)

Figure 3-10 Mode of occurrence diagrams for arsenic (a), iron (b), selenium (c), and nickel (d) in the Pittsburgh, Elkhorn/Hazard, Illinois No. 6, and Wyodak coals (senior, et al., 1997)

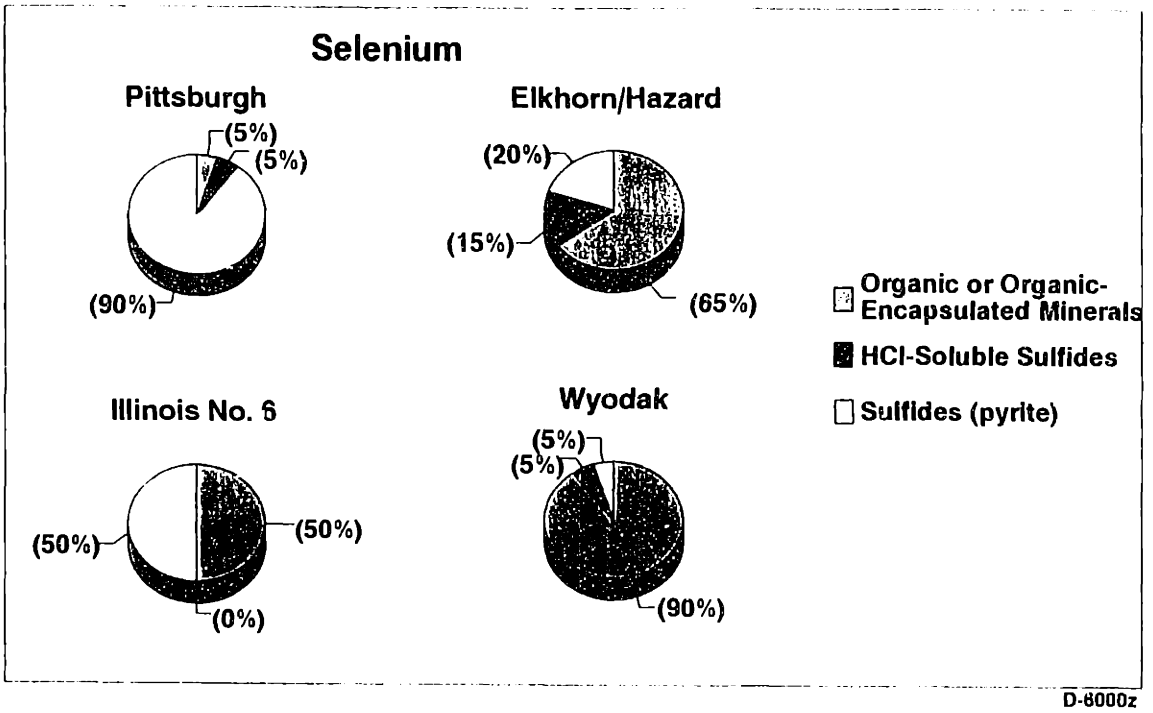

(c)

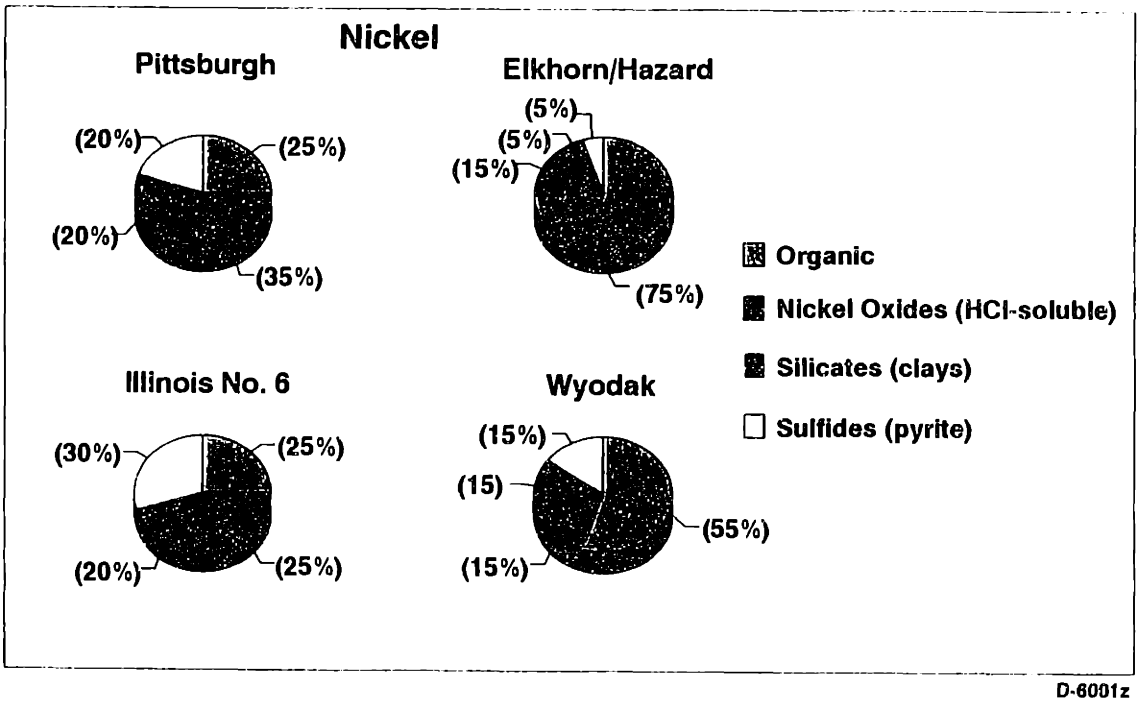

(d)

Figure 3-10 . (continued) Mode of occurrence diagrams for arsenic (a), iron (b), selenium (c), and nickel (d) in the Pittsburgh, Elkhorn/Hazard, Illinois No. 6, and Wyodak coals

Chapter 4 TRANSFORMATION OF IRON DURING COMBUSTION

4.1 Introduction

Although coal combustion technology has developed rapidly, there continues to be major uncertainty on how to cope with fouling and slagging associated with the inorganic constituents or ash in coal, resulting from changes in design, operation, and , most importantly, fuel composition. Many of these changes, such as the introduction of Low-NO_x burners and the use of fuel blending to reduce the emission of the oxides of sulfur, are driven by considerations of environmental quality.

Inorganic elements may be present in micron or larger sized mineral inclusions, or in extraneous mineral particles. Inorganic elements may also be intimately dispersed within the organic matrix of the coal. This latter inorganic component is generally referred to as "atomically dispersed" or "organically bound". During combustion, the majority of the inorganic species remain within the char, coalesce to form a variable number of ash particles. The extraneous minerals - those liberated from the coal during grinding - will also undergo physical and chemical transformations as they pass through the hot zones in the boiler. A small portion of the inorganic constituents contained within coal are released during devolatilization (Baxter et al. 1993) and others vaporized during char burnout (Quann and Sarofim, 1982). The vaporized constituents can homogeneously nucleate to form a submicron aerosol or condense on or react with the surfaces provided by boiler heat transfer tubes and the fly ash. The particles, vapor, and aerosol will be carried to the boiler walls by a series of mechanisms, predictions of which require knowledge of complex, flow and temperature fields, changing with time because of ash deposition. Some appreciation of the complexity of the processes governing fouling and slagging can be gained from the schematic diagram shown in

Figure 1-1, focusing mainly on the transformation of the minerals in coal during combustion.

Therefore coal mineral transformation during combustion is a complicated physicochemical process which needs to studied under well-defined conditions. For example, combustion temperature is dependent upon the coal/char physical properties, the environment under which the coal/char particle burns, and the ratio of CO/CO_2 (Zeng and Fu, 1995). Unfortunately, one parameter is difficult to change while keeping other parameters constant. Therefore the objective of this research is to distinguish the effects of oxygen concentration and other variables on the mineral transformation and how they affect the process.

Of the elements of interest, iron is the main concern of this study, because the state of the iron is directly related with the tendency of ash deposition. Previous research shows that when iron is agglomerated with aluminosilicate melts, the melting point and the viscosity of the ash particles is dramatically changed. Bool and Helble (1995) and Senior and Srinivasachar(1995) showed that any increase in particle viscosity due to oxidation of Fe(II) to Fe(III) in glassy particles will cause a decrease in particle stickiness at a given temperature. It is the ratio of Fe^{2+}(glass)/Fe^{3+}(glass) which plays an important role in determining the propensity of ash slagging and fouling.

Since the main form of iron in many bituminous coals is pyrite or pyrite-like, it is indispensable to know the transformation of pure pyrite when oxidation. It was found that(Jorgensen, 1981; Asaki, et al.,1985; Huffman, et al.,1989; Srinivasachar and Boni, 1989): at about 970 K, pyrite decomposes to pyrrhotite rapidly, and then forms Fe-S-O melt with rapid escalation of particle temperature. The molten sulphide-oxide mixture was subsequently oxidized to magnetite, which is the dominant oxide, and finally haematite. The oxidation rates are governed predominantly by the resistance to oxygen diffusion through the particle boundary layer and the within the melt.

The fate of pyrite in coal combustion, however, is much more complicated. As one of many minerals in coal, pyrite or pyrite-like iron has a fate that is governed by its own properties, the combustion conditions of the coal particles and its interaction with other minerals especially the silicates. Baxter (1990) found that during coal heatup and the early stage of combustion, each pyrite grain decomposes to two to three fragments. Quann and Sarofim(1986) observed that during coal combustion, the organically bound metals form submicron grains of ash on the char surface after slight char burnout, and finally form smaller particles with diameter of 1 to 8 microns by shedding of ash particles. Meanwhile the char particles themselves will also be fragmented (Baxter, 1992; Helble and Sarofim, 1989). And the char fragmentation is dependent upon the coal type and especially the macroporosity of the char. Simultaneously, mineral grains in the fused state in the coal particle can also coalesce with each other to form bigger mineral (ash) particle or grain(Sarofim et al., 1977). So big ash particles are formed by disintegration of char structure, shedding of coalescence minerals and decomposition of mineral grains, which determines the fate of iron presented in big ash particles. It is also well known that under reducing conditions, minerals are vaporized during coal combustion, and submicron ash particles are formed by homogeneous nucleation in gases or heterogeneous condensation on the preexisting fine particles in the boundary layer surrounding the char particle (Flagan, 1978; McNallan, et al., 1981; Quann and Sarofim, 1982; Neville and Sarofim, 1982; Quann, et a., 1982; Helble, et al., 1986; Gallagher, 1990). A significant amount of iron is vaporized, and is found preferentially enriched in the inner core of the submicron ash particles while sulfur is found preferentially on the particle surface.

Baxter and Mitchell(1992) studied iron transformation under a combustion condition similar to the those encountered in practical boilers. During the combustion of Illinois No. 6 coal, they found that 40% - 70% of the iron in the coal is released within a 25 ms period following coal devolatilization. The mechanism for the rapid loss of iron is attributed to the formation of iron fume by chemical reaction of pyrrhotite grains with oxygen. Bool et al.(1995) investigated comprehensively the transformation of iron state during coal

combustion. It was postulated that the extraneous ash does not interact appreciably with the inherent ash or with itself. The extraneous pyrite reacts with oxygen only to form magnetite/hematite. By contrast, the inherent pyrite can agglomerate and sinter with silicate to form iron glass on the coal surface. And the fraction of magnetite and iron-glass can be explained and predicted using this model.

However, the mechanism for the formation of iron on submicron particles is still unclear. There are three postulated mechanisms for formation: 1. Expulsion of organometallic iron with the volatiles, 2. Fragmentation of pyrite particles, and 3. Vaporization in the locally reducing zone in the char. The purpose of this study is to experimentally determine the composition and state of iron submicron ash particles, thus a direct evidence on iron vaporization is provide in this way study. To achieve this goal, the effects of oxygen concentrations on the distributions of iron states during the combustion of beneficiated Pittsburgh #8 coal was investigated. It was found that the iron state was different for the coarse ash particles and submicron ash particles. For the submicron ash particles, most iron is in the glassy state, while some iron is pyrrhotite, magnetite and haematite. The iron silicate is presumably formed from the condensation aerosols produced from the vaporized iron and silicon monoxide in the boundary layer of the particles. This shows that most iron on submicron ash particles comes from iron vaporization, while some iron is from direct formation of iron fume.

To quantitatively determine how much is from the formation of fume and how much is from vaporization, another experiment was performed, in which the combustion temperature was the same as the temperature during devolatilization for the coal particle. The experiment showed that at the same temperature, more iron was collected on the submicron ash particles for the combustion condition. This again shows that most of the iron in submicron ash particles is from vaporization, and the vaporization is controlled by the reduction reaction in the char.

The amount of iron in the submicron aerosol by vaporization during combustion was obtained by subtracting the part of devolatilization from the total iron on submicron ash particles.

The vaporization rate was approximated by using a revised version of Quann and Sarofim's equilibrium model(1982).

4.2 Experiment Study for the Beneficiated Pittsburgh Coal

The experiments were carried out on a drop tube furnace described in chapter 2. However close attention was paid to the reliability of the experiment, so the experimental system was calibrated carefully.

4.2.1 Furnace testing

The furnace was rebuilt for the present experiments and the collection probe was replaced by a new design. The furnace was exhaustively tested for leaks, and the new flow meters were calibrated. When the flow rate was low (less than 5ml/min), a bulb method was applied. When the flow rate was high (greater than 6 ml/min), a wet standard test meter was used. Calibration curves were thus obtained.

The recovery efficiency of particles from the furnace was carefully calibrated prior to a combustion experiment. Coals with sizes between 106 and 126 microns was fed into the furnace at ambient temperatures. The probe, preseparator and cascade impactor described above were used to collect the coals. Several operations were performed. Representative results as follow:

Coal fed in: 1.34977g
Coal collected: 1.19185g
Recovery rate = 1.19185/1.34977 = 88.3%

As mention by Graham(1991), a good recovery for this system is around 85%.

The collection efficiency was also measured at combustion conditions. First we used Al_2O_3 power. The results were as follows:

Operational condition: T=1650K, total flow rate=30l/min

Test sample: Al_2O_3 power with diameter ≤ 200 μm

Sample fed = 2.554g

Sample captured = 2.1522g

Recovery rate = 2.1522/2.554 = 84.6%

In addition to using Al_2O_3 power as a test sample, the ash in the coal was also used to test the mass balance. By using the ASTM procedure, the ash content for the beneficiated Pittsburgh #8 coal was found to be 4.61%(It is recognized that the amount of ash produced under combustion conditions is different from that under ASTM conditions, but this difference is neglected here). Then this coal was tested for mass balance under combustion condition:

Operational condition: T = 1650 K, 100% O_2 (30 l/min)

Sample: 0.063 mm ≤ d_p ≤ 0.075 mm

Coal fed = 0.6888g

Ash captured = 0.02799g

Collection efficiency = 0.02799/(0.6888*4.61%) = 88.1%

This recovery rate was repeatable.

4.2.2 ICPES

ICPES(Inductively Coupled Plasma Emission Spectroscopy) can measure elements with concentrations at the ppm level. The elements to be analyzed by ICPES were K, Na, Ca, Mg, Fe, Al, Ti, and Si. The operating conditions and wavelength of ICPES analysis are listed in Table 4-1.

Table 4-1 ICPES Operating Conditions and Wavelength

Argon flow rate (l/min) : 2.4 -3.5							
Wavelength (nm)							
Al	Fe	Ca	Mg	K	Na	Ti	Si
396.125	238.204	393.366	279.533	766.49	589.592	334.941	251.611

First, we calibrated the ICP with multi-element standard solutions which were prepared by using the standard atomic emission reference solutions. The calibrated results are summarized in Table 4-2. Calibration repeat showed less than 0.1% deviation. To use ICPES, the samples to be analyzed should be dissolved by using HF solution and added water to generate a solution with concentration measurable by the ICP.

Table 4-2 Calibration of ICP

Fe	AV	599.5	SD	4.9	CV	0.8
Si	AV	3179.0	SD	202.2	CV	6.4
Mg	AV	1313.0	SD	4.2	CV	0.3
Ti	AV	1207.5	SD	10.6	CV	0.9
Ca	AV	3341.0	SD	17.0	CV	0.5
Al	AV	872.0	SD	2.8	CV	0.3
Na	AV	7199.5	SD	87.0	CV	1.2
K	AV	2170.0	SD	11.3	CV	0.5

Fe	CC	1.0000	SLOPE	1988.8077	INT	675.5377
Si	CC	0.9997	SLOPE	681.7288	INT	3464.5195
Mg	CC	1.0000	SLOPE	96250.265	INT	1257.4453
Ti	CC	1.0000	SLOPE	8605.7695	INT	1160.1920
Ca	CC	1.0000	SLOPE	81573.132	INT	2889.4453
Al	CC	1.0000	SLOPE	373.3192	INT	864.8459
Na	CC	0.9978	SLOPE	83576.789	INT	8469.6416
K	CC	0.9993	SLOPE	80.1154	INT	2167.4038

Where AV = average intensity of signals SD = standard deviation
CV = coefficient of variation CC = correlation coefficient
SLOPE = slope of the correlation line INT = intercept of the correlation line

4.2.3 Mossbauer Spectroscopy

In addition to analyzing some iron-bearing minerals at the University of Kentucky, analyses were carried out by using Mossbauer Spectroscopy in the National Magnet Laboratory at MIT because of the proximity of the facility. The use of the MIT facility to analyze the iron-bearing coal particle or ash particle was facilitated by using the samples which were analyzed by the University of Kentucky for comparison. Figures 4-1 and 4-2 are the calibration results, which are in good agreement with the results by the University of Kentucky.

4.2.4 Experimental Results and Discussion

The experimental results can be classified into three classes: the photomicrographs of the samples obtained in the furnace; the distributions of mineral elements by ICP; the distributions of different iron states by Mossbauer spectroscopy. The experiments performed in this study were carefully designed to reveal the transformation of minerals

especially the iron. The following table provides the size classification for the cascade impactor used:

Table 4-3 Size Classification - MIT Cascade Impactor

Stage	preseparat-or	1	2	3	4	5	6	7	final	filter
Particle (μm)	>10	9.0-10	5.8-9.0	4.7-5.8	3.3-4.7	2.1-3.3	1.1-2.1	0.65-1.1	0.43-0.65	<0.43

4.2.4.1 Pictures for the Ash

- SEM picture for ash

Figure 4-3 is a picture of the ash obtained using the SEM (Scanning Electron Microscopy) from previous researchers (Quann and Sarofim, 1986). The white spheres are ash particles, while those with irregular shape and darker color are char. It clearly shows that during coal combustion ash comes to the surface of the char particle and forms a separate particle at the char surface instead of forming a shell around the char particle at least for the coals studied in this project. The ash particles stick to the surface during char combustion. As we know, there are two limiting models for describing coal combustion. Those include: the shrinking char particle oxidation model with a constant density (representative of a lignite char), and the model for combustion at constant diameter and decreasing density. Correspondingly, for the first model, ash will come to the char surface and form a separate particle as char burning; for the latter model mineral inclusions will remain at the original positions and form a shell around the char particle. Those two models determine the char combustion rate and the transformation of minerals. When calculations are made to predict the combustion rates and mineral transformation, identifying the combustion mode is the first step.

- Microscopy picture for ash particles

Figure 4-4 are the color pictures for ash particles with different size. The pictures were obtained using an optical microscope at different magnitude. The microscope is a WILD M8 Stereomicsoscope with WILD MPS 55/51 photoautomat. The microscope can display a stereo-picture of the sample. The ash particles in Figure 4-4 were obtained under: 100 O_2, $T_{furnace}$ = 1650K, reaction time ≈ 0.2 seconds (calculated and shown later). The colors of the particles change from black of the biggest particles (> 10 μm) to red of the smallest particle (<0.43 μm). The red color is indicative of ferric iron. The black color shows that the particles have some unburnt char. The systematic changes of the colors are visible evidence that the fate of iron and other minerals with different sizes are determined by differences in oxidation states.

4.2.4.2 Distributions of Mineral Elements with ICP

The following results are for the washed #8 Pittsburgh coal. The operating conditions were as follows:

Coal: washed Pittsburgh #8
Residence time: 0.2 s
Coal feeding rate: 0.08 g/min
O_2 concentration in the main gas: 0 to 100%
Particle size: 63-75 μm
Furnace wall temperature: 1650 K
Main gas: 6 l/min

The samples should be dissolved in HF solution in order to be analyzed by the ICP. Since HF solution can only dissolve inorganic materials, carbon must be removed from the char/ash samples collected by the cascade impactor. Here carbon was removed by the standard ASTM procedure: ASTM standard number D3174 [1984].

- Ash distribution with 100% O_2 and 0% O_2

As shown in Figure 4-5, about one-third of the ash collected is found on stage 10 (filter holder) for 100% O_2, while only a negligible amount of ash was found on stage 10 for 0% O_2. According to Wibberly and Wall (1986) and Wall (1992), particles with size between 0.02 μm and 0.2 μm are formed by heterogeneous / homogeneous nucleation and subsequent coalescence of vaporized inorganic species. The samples on stage 10 should therefore be oxidized ash only. The differences of combustion condition between 100% O_2 and 0% O_2 are both in the combustion temperature and in the reaction atmosphere. At 100% O_2 , the combustion temperature is much higher than 1650K. Note that at 100% O_2, the primary gas at the char surface is CO, the particle is actually under reducing condition during combustion; and after char combustic is complete, the ash particles formed will be further oxidized in oxygen. The formation of submicron ash particle is determined by combustion temperature and the reducing condition at the char surface during char combustion. At 0% O_2, ash formation of submicron particles is under inert conditions, and the fraction of ash on submicron particles is basically determined by the devolatilization temperature. Prior work has shown that the refractory inorganic oxides which account for most of the ash mass do not begin to vaporize appreciably until the temperature exceeds 1650 K (Quann and Sarofim, 1982), which was the case in this study. 29% of the mass of the coal feed is recovered on stage 1. This char contains 70% of the total ash. In other words, the larger char particles contain a higher content of mineral inclusion, while the smaller particles contain smaller amounts of mineral matter.

- Ash distribution with 60% O_2, 30% O_2

The ash distribution generated under combustion conditions of 1650 K, 60 % and 30% O_2 in Figure 4-6 shows some similarities with distribution generated in 100% O_2 from stages 5 to 9: with significant amounts found on stages 5 and 6. However, the distribution from stages 1 to 4 is quite different for the combustion in different oxygen atmospheres. The shift of ash particle size toward smaller size shows that, more ash particles per coal particle are generated

at higher combustion temperatures presumably due to increased fragmentationof minerals and char at higher temperature.

- Elemental size distributions

Figures 4-7a to g show the distributions of the major elements as concentration versus impactor stage for different conditions. The amount of Na is too low to be detected by the ICP. The vaporization order is K > Fe > Si > Mg > Ti > Ca > Al for this coal. At 30% O_2, except for stage 10, the fraction of each element decreases as particle size decreases. At 60% O_2, the fractions of elements decrease from stage 1 to stage 4; the concentrations on stage 5 or 6 are, however, much higher than those on stage 4. Concentrations (% of each element per stage) decrease from stage 5 to 9. It can be seen that, except for the fraction forming submicron particles, all elements have very similar distribution for the coarse ash particles. This means that the minerals in parent coal coalescence and sinter each other during coal combustion to form coarse ash particles before char fragmentation. So a coarse ash particle will have similar composition. Furthermore elemental composition on different coarse ash particles with different size will show similar distribution. This is proved by Figure 4-8. In Figure 4-8, the elemental composition on coarse ash particle is very similar for the combustion conditions at 30% O_2 and 60% O_2. However, except for aluminum, the fraction of element in submicron ash particle increases with oxygen concentration(combustion temperature), which shows two possible consequences: (1) in spite of coalescence between minerals, vaporization always occurs prior to coalescence; (2) even in aluminosilicates, elements (Fe, Ca, Ti, K) can still be vaporized. Since the chemical activation coefficient of an element in aluminosilicate is generally very low, the first reason is preferred and adopted in this thesis. This argument will be used in modeling.

4.2.4.3 Distribution of Iron State with Mossbauer Spectroscopy

Transformation of iron is the main concern of this study. The iron distribution

between different particle size was obtained using ICP. In this section, results are presented to show chemical transformation of iron under different combustion conditions by using Mossbauer spectroscopy.

● Effects of oxygen concentration on iron state

Table 4-4 shows the iron state of ash or char samples generated at different oxygen concentrations. It can be seen that the main iron state in the parent coal is pyrite. Not surprising, in the ASTM ash, nearly all the iron is in the form of hematite, because at temperature less than 1600 K, hematite is thermodynamically favored. It is interesting to note that at 0% oxygen, or devolatilization at 1650 K, while 60% jarosite is retained, 40% jarosite and all pyrite are converted into iron metal, pyrrhotite, and iron carbide. In other words, at high temperature, a lot of iron in coal is changed into volatile state (metal Fe). Therefore unlike other refractory elements which can be reduced only under reducing conditions, iron can be changed into metal state under the inert atmosphere. Note that nearly all metal iron and iron carbide exist in coarse char particles, because the melting point of metal iron is 1808K, and its boiling temperature is 3023K. The iron metal was still in a solid state for the pyrolysis condition in this study.

The table also shows that as oxygen concentrations increase from 10% to 100%, the percentage of iron in the glassy glass will increase from 47% to 83%. Iron glass is formed by the coalescence between iron or iron compounds and silicate, while magnetite and hematite are formed by the crystallization during cooling down of melt of iron oxides. As oxygen concentrations increase, combustion temperature will also be increased. Therefore silicate and iron compound will be fused more quickly, and they come together faster. So more iron glass will be produced. On the other hand, when the combustion temperatures increase, more char will be broken up. Helble and Sarofim(1989) found that the observable fragmentation of char takes place at the late stage of char combustion. This result show that the glassification of iron is always faster than the disintegration of

the char particles. This implication is also supported by the nearly uniform elemental distribution in Fig. 4-8. It can be inferred that for a given combustion condition, if the residence time is longer, more iron glass will be produced provided that iron and silicate are in melt state.

It is interesting to note that, at 10% O_2 and 30% O_2, no haematite was produced, whereas at 60% O_2 and 100% O_2, some haematite was produced. As already stated, only below 1597 K for 5% O_2, 1662 K for 21% O_2, and 1738K for 100% O_2 (Srinivasachar and Boni, 1989), haematite can be formed. If magnetite are attached to the char, since the char combustion temperature is above 2000 K for 60% O_2, there will be no formation of haematite. Then haematite can only be produced in the fragments or in the residual ash.

● Distribution of iron state with different ash size

Ash samples generated at 40% O_2 and 100% O_2 and with furnace temperature of 1650 K, and size classified ashes with the cascade impactor, were analyzed using Mossbauer spectroscopy. The results are presented in Tables 4-5 and 4-6. For 40% O_2, for ash particles with sizes greater than 10 microns, about 50% of the Fe is in glassy state, and 22% is haematite. The iron state with ash particles with size between 1.1 and 9.0 microns (on stage 2 to stage 7), are nearly the same: the glassy state takes up about 70%, of which about 75% is Fe^{+++}(glass).The iron state in the submicron ash particles is quite different to that of other ash particles. Although about 70% Fe is in glassy state, nearly all of it is in the Fe^{+++}(glass). The other difference is that Fe-metal and $Fe_{1-x}S$ together take up about 10 % of Fe, while they account for only about 6% of the coarse ash particles.

The iron states in the ash produced at 100% O_2 show a very similar trend as at 40% O_2. About 50% Fe is in glassy state, 28% is haematite, and 6% is Fe-metal and $Fe_{1-x}S$. This composition is nearly the same as the ash with particle size greater than 10 micron produced at 40% O_2 ! The iron state with the ash particle size between 2.1 and 9

microns, is almost identical: about 85% Fe is in glassy state, of which about 90% is Fe^{+++}(glass). The iron state with the ash particles with size between 1.1 and 2.2 microns also has about 80% Fe^{+++}(glass), which is similar to the bigger ash particles. But it has only 2.5% Fe^{++} (glass), which is similar to the submicron ash particles. The iron state of the submicron ash particles are again quite different from the coarse ash particles: about 65% is in glassy state, nearly all of which is Fe^{+++} (glass). About 10% is Fe-metal and $Fe_{1-x}S$. Note that this fraction is the same as the submicron ash produced under 40% O_2.

4.2.5 Discussion

From Figure 4-9, it can be seen that as oxygen concentration or combustion temperature increases, more iron will be transformed into the glassy state, of which more Fe^{+++}(glass) will be produced. As has been stated that the fate of iron is determined by a number of simultaneously competing processes.

- Formation of Coarse Ash Particles by Coalescence and Fragmentation

The shift of the average diameter of the coarse ash particles as shown in Figure 4-6 shows that fragmentation of char particles occurs during combustion. Such kinds of fragmentation can only happen when the porosity of the char reaches a critical value (Kang, et al., 1988). In other words, only when a significant amount of char has been burnt out, will the residue of the minerals be separated from the the mother char. This allows the iron and the silicates appearing on the char surface to have enough time to agglomerate and sinter. So the distributions of the iron states of the ash particles with size range of 2 and 9 microns are the same. The agglomeration and sintering rate is proportional to the contacting probability of interacting species, and it can be expressed as a formula similar to the Arrhenius law(Bool, et al.,1995; Nowok, 1990; Jung and Schobert, 1991). As stated by the expression, as temperature increases or oxygen

concentration increases, the sintering rate is increased significantly. This again explains why more iron glass is produced at 100% O_2 than at 40% O_2 for the ash particles with the same size range.

At 30% O_2, no haematite is produced, whereas at 40% O_2, haematite is produced. As haematite can only be formed below a given temperature for a given O_2, the haematite was probably produced from residual ash. It can be inferred that the observed trends in size distribution reflect increased fragmentation with increasing temperature. More haematite was seen with the coarse particles with size bigger than 9 microns for both 40% and 100% O_2. Note that 42% pyrite within the coal is with the particle size bigger than 20 microns. When the pyrite is fragmented, it is divided into 2-3 smaller particles(Baxter, 1990).Therefore most haematite is with the coarse ash particles.

Ash particles greater than 10 microns in size consist of extraneous minerals, and residual ash formed by the agglomeration of mineral inclusions in coal. Although the combustion temperature is uniform within the char particle and is nearly a constant during the combustion(Zeng and Fu, 1996; Timothy et al., 1982), the fraction of the iron melt and silicate in contact is much less than that on the char surface because of the lack of contact. Therefore the probability of contact between the necessary species is small excepting at high burn out, and less glassy iron can be produced. Also because the coarse ash particles are the residues of the char cores, the oxygen diffused to the core is much smaller, so less fraction of Fe^{+++}(glass) is produced. The similarity among the mineral compositions of the ash particles on different impactor stages shows a statistical average of many coal particles.

- Submicron Ash Particles Produced via Disintegration and Vaporization

Table 4-4 shows that a lot of iron is transformed into iron-metal and pyrrhotite at 0% O_2 i.e. devolatilization condition. About 9% iron in the submicron ash particles is in

the state of iron-metal and pyrrhotite as shown in Tables 4-5 and 4-6 for combustion at 40% and 100% O_2. This part of the iron is from the direct disintegration of pyrrhotite and iron-metal which is produced in the early stage after the coal particles are injected into the furnace. This is consistent with the studies by Baxter and Mitchell(1992), and Wall(1992), in which an iron fume was believed to be produced in the early stage of coal combustion. The tiny disintegrated iron fragments remain in the un-oxidized state because it is very difficult to be ignited due to its very small particle size.

However, most iron in submicron ash particles is in the glassy state. Since silicon in submicron particles can only be produced under reducing condition, iron glass should be produced by coagulation of silicon and iron vaporized simultaneously. As suggested by Helble et al. (1986), the coagulation between two types of elements occurs in the boundary layer surrounding the char particles.

- Conversion of Fe^{++}(glass) to Fe^{+++}(glass)

Once Fe^{++}(glass) is formed, it can be changed into Fe^{+++} (glass), provided that the particle temperature is under 1652K at 20 % O_2 (Srinivasachar and Boni, 1989; Cooper, et al., 1996). In other words, Fe^{+++}(glass) cannot be produced on the char surface during the present oxidation experiments since the surface temperature were significantly above 2000K. Conventionally, the reaction between melt Fe^{++}(glass) and oxygen was described by oxygen diffusivity through the melt(Kingery, 1963; Hauffe, 1965). Recently, it was found that the reaction is actually driven by the cation diffusivity (Cooper, et al., 1996). Fe^{++} cation diffuses to react with oxygen to form magnetite, transformation of magnetite to haematite occurs at another front. However no mathematical model is available to calculate the reaction rates.

4.2.6 Summary

The fate of iron during coal combustion is determined by a couple of simultaneously competitive processes, in which different iron compounds are produced. For the submicron ash particles, about 10% iron is formed by fragmentation. And most of iron is in the state of Fe^{+++}(glass), which is from vaporization and recondensation of coagulated iron and silicates. For the ash particles with size between 1 and 9 microns, most of the ash is from shedding of coalesced minerals, and the rest is from fragmentation of char. The fraction of glassy iron is high because of the high contact probability between iron melt and silicates. For the coarse ash particles with size greater than 9 microns, extraneous pyrite is changed into haematite, iron in the core of the char is changed into glassy state. Since the contact probability between iron and silicates is low except at high burnout, the fraction of iron in the glassy state is also low.

4.3 Experimental Study for Pittsburgh Coal and Wyodak Coal

In last section, by directly analyzing size segregated ash particles, it was found that iron in submicron ash particles exists main in the form of iron glass, which comes from iron vaporization; while some of iron exist in the form of pyrrhotite, haematite, which comes from iron fume produced by fragmentation during heat up. The objective of this study is to experimentally determine the relative importance of these two sources, to find out the reaction governing vaporization, and based upon those experiment observations to set up a semi-empirical model to explain and predict the formation rate of iron in submicron particles.

The oxidation furnace and the pyrolysis furnace were used to burn and devolatilize the coal respectively. The two furnace systems were described in Chapter 2. All the coal/char and ash samples were analyzed using the Neutron Activation Analysis (NAA). The experimental results are presented as follows.

Table 4-7 shows a result used to compare the effects of combustion with pyrolysis. The

fraction of iron in submicron particles at combustion is higher than that at pyrolysis conditions for the same reaction temperature. The difference between those two experiments is their chemical atmosphere: in pyrolysis experiment, the gases are neutral(Argon); while in combustion experiment, the dominant gases on the char surface is reducing (CO). This shows that: (1)iron can be devolatilized at high temperature; (2) the formation of iron on submicron particles is enhanced by the presence of CO or the vaporization is controlled by the presence of CO.

Table 4-7 Fraction of iron in submicron ash or char particles

Coal type	conditions	coal particle temperature (K)	fraction in submicron particles
PTH90106	combustion at 10% O_2 and 1700K	1950(calculated)	5.1%
	pyrolysis	2040(measured)	4.1%
WYL90106	combustion at 5% O_2 and 1700K	1995(calculated)	19.8%
	pyrolysis	2040(measured)	13.2%

However, it can not be concluded that the difference of the fraction is due to the reducing reaction by CO. Figure 4-10a shows the fractions of iron in submicron char at different pyrolysis temperature for the PTH90106 coal, 4-10b shows the fractions of iron in submicron char at different oxygen concentration at a furnace temperature of 1700K. A well-prepared study by Srinivasachar and Boni(1989) shows that, pyrite will decompose to porous pyrrhotite at a temperature between 800-900 K, then the pyrrhotite fragments into much smaller pyrrhotite, until the pyrrhotite particle melts at a temperature of 1356 K. And the fraction is dependent upon the heating rate. It was discovered that an iron fume is produced because of the fragmentation before combustion or at the beginning of combustion (Baxter and Mitchell, 1992). Therefore, the iron fume is generated when and only when the pyrrhotite temperature is above 800K and below 1356K. There is no quantitative relation available to describe the fraction. Nevertheless, it can be inferred that if the heating rate is the same, the fraction should be the same. For this study, it is estimated that the amount of iron fume for the case of 10%, 20%, and 30% at 1700K is the same

as for devolatilization at about 1700K, or 3.5% of the total parent iron. For the case of 100% O_2, coal ignition is very fast, the heating up rate is faster than other cases. Therefore, more iron fume is generated. This speculation is consistent with the results in Tables 4-5 and 4-6: more pyrrhotite and magnetite/haematite is formed for 100% O_2 than for 40% O_2.

4.4 Modeling

The differences in pyrite transformation during oxidation between pure pyrite and pyrite in coal particles are the combustion temperature and the environment. However the combustion temperature and the environment for the particle are generally not easy to measure. In this section, some basic calculations were performed to obtain these basic parameters for further development of models.

4.4.1. Estimation of Combustion Kinetics for Coal

4.4.1.1. Transport properties of reacting gas

It is well known that the combustion of the char particle can be classified into three regions: region I -- kinetically controlled combustion, in this region char reacts with oxygen in the whole particle, region II -- kinetically and diffusively controlled combustion, in this region oxygen penetrates into the particle to some depth, and region III -- diffusively controlled combustion, in this region reactions occur only on the particle surface. Under general combustion condition, the char combustion is in region III. So the transport properties are essential to this study.

- The diffusion coefficient for O_2 - N_2

The main compositions of the reacting gases surrounding the particle are CO, CO_2, O_2 and N_2. The dominant gases in this system are O_2 and N_2. So the diffusion between

the gases can be taken as O_2 - N_2. We can calculate the diffusive coefficient according to Lienhard(1987):

$$D_{o_2\text{-}N_2} = \frac{(1.83583\times10^{-7})T^{3/2}}{p\sigma_{AB}^{2}\Omega_D}\sqrt{\frac{1}{M_A}+\frac{1}{M_B}} \tag{1}$$

where p = 1 atm, σ_{AB} = 3.5785, Ω_D = 0.6558, M_A = 32, M_B = 28

At T = 2000 K, $D_{O2\text{-}N2}$ = 5.024 x 10^{-4} m/s

At other temperatures:

$$\frac{D(T)}{D(2000)} = \left(\frac{T}{2000}\right)^{\frac{3}{2}} \tag{2}$$

● Density of reacting gas

We take the gas as ideal gas, so

$$P = \rho R T$$

or

$$\rho = \frac{P}{RT} \tag{3}$$

4.4.1.2. Estimation for Reaction Time

The momentum equation for char particle in gas

$$m\frac{dV}{dt} = mg - 3\pi\mu d(V - V_g) - \frac{m}{\rho}\rho_a g \tag{4}$$

$$\frac{dV}{dt} = g - \frac{3\pi\mu d(V - V_g)}{m} - \frac{\rho_a}{\rho} g \qquad (5)$$

The pathway of the particle is composed by two sections: the first one is the vertical path from the coal feeder to the reaction zone, and the second one is in the reaction zone. For the first section, the vertical length is 0.57m, the section-area of the feed pipe is

$$S = \frac{\pi}{4} D^2 = \frac{\pi}{4}(0.3175\times10^{-2})^2 = 7.9168\times10^{-6} m^2$$

and the feed flow rate is

$$Q = 150 \text{ ml/min}$$
$$= 2.5\text{x}10^{-6} \text{ m}^3 / \text{s}$$

So the velocity of gas is

$$V_g = Q/S = 0.31578 \text{ m/s}$$

The initial condition for particle is

$$V (t = 0) = V_g$$

By using MAPLE, a symblic calculation software, we can easily calculate

$$V (z = 0.57 \text{ m}) = 0.5224 \text{ m/s} \text{ for } d_p = 75 \mu\text{m}$$

For the second section in reaction zone, the flow rate of the main gas is

$$Q = 6 \text{ l} / \text{min} = 0.1\text{x}10^{-3} \text{ m}^3 / \text{s}$$

The section - area of the furnace is

$$S = \frac{\pi}{4}(2\times2.54\times10^{-2})^2 = 2.0268\times10^{-3} m^2$$

The furnace temperature is 1650 K, so

$$V_g = \overline{V}_{gas} = \frac{(0.1\times10^{-3})\times\frac{1650}{300}}{2.0268} = 0.271 m/s$$

The length with T_{wall} = 1650 K is 3.5 inches or 0.0889 m.

- When the particle is very small, it will follow the main gases in the furnace, then the reacting time for the particle is $\frac{L}{\overline{V}_{gas}} = 0.33$ s

- When the mass of the particle does not change or decreases slightly (corresponding to low carbon conversion), we can simply integrate equation (5) to obtain V (t). Then we can calculate $\overline{V}_p = 0.518$, so the reaction time for the particle is $\frac{L}{\overline{V}_p} = 0.17$ s.

4.4.1.3. Estimation of Chemical Kinetics for Char Combustion

The calculation of the reaction rates of char oxidation is always the core of coal combustion research. There are numerous articles and methods on this topic. However, acknowledging that the char combustion is essentially carbon reaction, we can greatly simplify the combustion analysis. The reactions for carbon oxidation are as follows:

$$C + O_2 \rightarrow CO_2 \quad (a)$$

$$C + \tfrac{1}{2} O_2 \rightarrow CO \quad (b)$$

$$C + CO_2 \rightarrow 2\,CO \quad (c)$$

The reaction rates for these reactions can be written as:

$$\frac{dm(a)}{dt} = K_{oa}(\rho_s Y_{o,s})^{n_a} \exp(-\frac{E_a}{RT_p})\frac{M_{co_2}}{M_{o_2}} \quad (6)$$

$$\frac{dm(b)}{dt} = K_{ob}(\rho_s Y_{o,s})^{n_b} \exp(-\frac{E_b}{RT_p}) \frac{M_{co}}{\frac{1}{2}M_{o_2}} \tag{7}$$

$$\frac{dm(c)}{dt} = K_{oc}(\rho_s Y_{co_2,s}) \exp(-\frac{E_c}{RT_p}) \tag{8}$$

In a previous study, the kinetic parameters have been determined for solid pure carbon particle [Zeng and Fu, 1996]:

$K_{oa} = 3500,\ n_a = 0.88,\ E_a = 113000$

$K_{0b} = 1.05 \times 10^6,\ n_b = 0.64,\ E_b = 180000$

$K_{0c} = 10^8,\ E_c = 270000$

The difference between the solid pure carbon particle and the coal particle is that the coal particle has porosity within the particle. As mentioned in section 4.4.1.1, when the coal combustion is region I and II, the porosity may increase the reaction area, while in region III, the porosity may not have effects on reaction area or decrease the reaction area. For example, Hecker et al. [1992] found that the intrinsic rates of char partially burned out at high temperatures decrease with burnout level. For simplification we take the kinetic parameters as constants. This can be achieved by multiplying a constant K to the expressions for reaction rates of solid pure carbon particle. So

$$\frac{dm_{char}}{dt} = K[K_{oa}(\rho_s Y_{o,s})^{n_a} \exp(-\frac{E_a}{RT_p}) + K_{ob}(\rho_s Y_{o,s})^{n_b} \exp(-\frac{E_b}{RT_p}) + K_{oc}(\rho_s Y_{co_2,s}) \exp(-\frac{E_c}{RT_p})] \tag{9}$$

Measurements on solid pure carbon particle [Zeng, 1996] and pulverized coal particle [Timothy, 1982] showed that the combustion temperature of particles kept constant during combustion. So we can take the combustion processes to be quasi-steady. Then we

can write the energy equation for the particle as follows:

$$Q_a K\frac{dm_a}{dt} + Q_b K\frac{dm_b}{dt} - Q_c K\frac{dm_c}{dt} = -\lambda_a\frac{dT}{dr} + \epsilon\sigma(T^4{}_p - T^4{}_g) \tag{10}$$

The particle diameter can be computed from:

$$\frac{d(\rho\frac{4}{3}\pi r^3)}{dt} = -\frac{dm}{dt} \tag{11}$$

By solving the mass conservation equations and the energy conservation equations governing the species and temperature distributions surrounding the particle, we can obtain the oxygen concentration on the particle surface in terms of the combustion temperature [Zeng, 1996][Makino, 1986]. Thus we can predict mass loss of the particle. Take the following experimental results into consideration:

Furnace temperature (T_g) = 1650 K	Bulk oxygen concentration ($Y_{0\infty}$) = 10 %
Particle diameter (d_p) =63- 75 μm	Reaction time = 0.2 s (from section 4.4.1.2)
Carbon conversion = 41 %	Coal type = Pittsburgh #8 (beneficiated)

By adjusting K, we can make the prediction consistent with the experimental results. Therefore we obtain

$$K = 0.2$$

Note that the pre-frequency K is less than 1.It is worthwhile to point out that, the carbon used in Zeng and Fu's study was a solid carbon particle (no pores). In recent days, it is believed that, the char can be carbonized during combustion - the structure of char becomes more like solid carbon . However, this study shows that, the overall kinetics of char is less than solid carbon at high temperature. One explanation is that the kinetic parameters depend upon the combustion

temperature, for example the activation energy may increase with increasing temperature.

4.4.2. Prediction of Combustion Processes

In the same method in section 4.4.1 and with K = 0.2, we can predict the combustion processes under other combustion conditions (the combustion is still in region III). A typical result is shown in Figures 4-11 to 4-14. They show that the combustion is near region III, since the surface oxygen concentration is of the order of 1 % . While there is some CO_2 at the char surface, the dominant gas is CO.

The background of this basic research is on low NOx coal combustion, under which the stoichiometry (oxygen / fuel) is below 1 for the early stage of coal combustion in the boiler. The calculations show that under general combustion conditions in the drop-tube furnace the char particle is in fact in reducing condition.

4.4.3. Vaporization of Iron

As part of the broader modeling effort, the vaporization rates of iron during the coal combustion were calculated based upon the calculations in sections 4.4.1. and 4.4.2.

4.4.3.1 Reducing Mechanism

It is generally believed that refractory oxides such as SiO_2, CaO, et al. are much more difficult to be vaporized than the corresponding volatile suboxide or metal. As shown in the previous section, CO dominates for the environment on the particle surface: the concentration of CO is more than 50 times than that of O_2 . Therefore the reaction of the refractory oxides can only be a reducing reaction if any reaction with gases for the oxides exist. There are two possible reactions for iron vaporization. One is that

$$FeS \rightarrow Fe + \tfrac{1}{2} S_2$$

While this reaction is possible, the formation rate is obviously determined by decomposition of

FeS. This rate is independent of the gas atmosphere. Thus, the vaporized iron for combustion and pyrolysis under the condition of same particle temperature should be the same, which is not consistent with the experimental observation. In contrary, the experiments show that iron vaporization is enhanced by the presence of CO. So the governing reaction is

$$FeS + CO \rightarrow COS + Fe(l) \quad \text{And} \quad Fe(l) \leftrightarrow Fe(g) \tag{12a}$$

This reaction is further assumed to be at equilibrium at the surface of each inclusion within the char particle (Quann,1982):

$$FeS + CO \leftrightarrow COS + Fe(g) \tag{12b}$$

And the partial pressure of Fe at the inclusion surface is determined from the equilibrium constant Ke and the local gas compositions:

$$Ke = \frac{P^e Pcos}{aPco} \tag{13}$$

where a is the activity of FeS, which is assumed to be 1. Since there is no other source of COS, the concentration of COS is taken to be of the same concentration as Fe. Therefore the concentration of Fe can be calculated by the following equation:

$$P^e = Pcos = (Ke\ Pco)^{1/2} \tag{14}$$

4.4.3.2. Calculation Strategy

The methods to calculate the vaporization rates of Fe is based upon the work by Quann [1982] and is described briefly here. If ρ_l is the number density of inclusions in a single coal particle, then the vapor mole fraction profile x_m with respect to the coal particle's internal radial coordinate is :

$$cD_e \nabla^2 x_m + \rho_I V_I^i(r) = 0 \tag{15}$$

where V^i_I is the vaporization rate for a single inclusion and is approximately given by

$$V^i_I = 4\pi r_i c D_e (x^e_m - x_m) \tag{16}$$

where x^e_m is the equilibrium mole fraction of the vapor at the inclusion surface, D_e is the effective diffusivity for Knudsen diffusivity in the char pore, and r_r is the radius of inclusions. Equation (16) is valid under the conditions that the inclusions are embedded in an isotropic porous medium with pore size much less than the inclusion size.

During combustion, inclusions initially embedded in the coal matrix will continuously come to the char surface. The contribution of these surface inclusions to the total vaporization from the char is neglected. As discussed in 5.3.4.2, the surface inclusions will coalescence with silicate to form Fe/ glass or to be oxidized instead of being reduced. The number of inclusions, N_I, within the char is given by

$$N_I = \theta\left(\frac{r_p}{r_i}\right)^3 \tag{17}$$

where θ is the inclusion volume fraction in the char, r_p is the char radius. During combustion, N_I decreases and θ and ρ_I keep constant. Here the model of constant char density is used. r_p can be calculated with the method in 5.4.2. The boundary conditions are:

$$r = 0: \frac{dx_m}{dr} = 0$$

$$r = r_p: -4\pi r_p^2 c D_e \frac{dx_m}{dr}\Big|_{r=r_p} = 4\pi r_p D_o \alpha x^s_m$$

The factor α, a correction for Stefan flow, is

$$\alpha = [1 - \exp(-\frac{D_o}{D_m}\ln(1 + x^{b}_{o}))]^{-1} \ln(1 + x^{b}_{o})$$

where, D_m , D_o , and x_o^b are gas diffusivity of the inorganic vapor , diffusivity of oxygen , and the mole fraction of O_2 .

Equation (15) is analogous to the problem of diffusion and reaction in a porous catalyst pellet, with the Thiele module :

$$\phi = (3\theta)^{1/2} r_p/r_i \tag{18}$$

The total instantaneous rate of vaporization V_c (moles/sec) from a single char particle is determined from

$$V_c = 4\pi r^2_p c D_e \frac{dx}{dr}|_{r=r_p} = 4\pi r_p c D_{O_2} \alpha x^{s}_{m} \tag{19}$$

with the vapor mole fraction at the char surface

$$x^{s}_{m} = \frac{\frac{D_e}{\alpha D_o}(\frac{\phi}{\tanh\phi} - 1)}{1 + \frac{D_e}{\alpha D_o}(\frac{\phi}{\tanh\phi} - 1)} x^{e}_{m} \tag{20}$$

The effectiveness factor is

$$\eta = \frac{3}{\phi}\left[\frac{1}{\tanh\phi} - \frac{1}{\phi}\right]\left[1 + \frac{D_e}{\alpha D_o}\left(\frac{\phi}{\tanh\phi} - 1\right)\right]^{-1} \tag{21}$$

η is the ratio of the total vaporization rate of Fe with particles interacting and with external diffusion control over that of the rate of N_I isolated ash droplets in the char. The instantaneous rate can be re-expressed as

$$V_c = \eta\, N_I\, V^{ni}_I \tag{22}$$

where V^{ni}_I is the vaporization rate for a single noninteracting inclusion:

$$V^{ni}_I = 4\,\pi\, r_i\, c\, D_e\, x^e_m \tag{23}$$

At a given combustion condition, the combustion temperature and the gas constituents can be calculated. Then the equilibrium constant, Ke, can be calculated using thermodynamic values from the JANAF's table. And the concentration of Fe vapor can be computed. The instantaneous vaporization rate can be obtained. By integrating the instantaneous rate, the total Fe vaporized can be obtained.

4.4.3.3 Calculation Results

Figures 4-15 and 4-16 show typical calculation results. As shown in the figures, we have estimated that the partial pressure of Fe on the particle surfaces and the vaporization rates change with time (particle size). Obviously the Fe vapor will react with O_2 and Si vapor in the boundary layer near the char particle to form Fe/glass or Fe oxides. In order to estimate the composition of the Fe/glass and iron oxide in the submicron particles there is a need for reaction kinetic parameters for the relevant

reactions.

As to the iron distribution in the coarse particles with size $\geq 1\mu m$, iron containing compounds will coalesce with silicate to form Fe/ glass (Bool, 1995) or react with O_2 to form Fe oxides. However since these oxidation reactions cannot occur at the char surface, a comprehensive model accounting for the coalescence between iron and silicates and the fragmentation of char should be included.

4.5 Conclusions

An iron fume can be produced at high temperature devolatilization due to fragmentation of pyrrhotite into fine particles. Most of the iron in the submicron fume produced during coal combustion is from vaporization controlled by reduction with CO. The vaporization rate can be estimated using the equilibrium - transport model by Quann and Sarofim(1982).

References

Asaki, Z., Mosi, S., Ikeda, M. and Kondo, Y., Oxidation of pyrrhotite particles falling through a vertical tube, Metallurgical Transactions (B) 16B, pp.627-638, 1985

Barta, L.E., Horvath,F., Beer, J.M., and Sarofim, A.F.,Variation of mineral matter distribution in individual pulverized coal particles: application of the 'URN' model, Twenty-third Symposium (International) on Combustion, The Combustion Institute, pp.1289-1296, 1990

Baxter, L.L., Char fragmentation and fly ash formation during pulverized-coal combustion, Combust. Flame 90, pp.174-184, 1992

Baxter, L.L. and Mitchell, R.E., The release of iron during the combustion of Illinois No.6 coal, Combust. Flame 88, pp.1-14, 1992

Baxter, L.L., The evolution of mineral particles size distributions during early stages of coal combustion, Frog. Energy Combust. Sci. 16: 261-266, 1990

Bool, L.E. and Helble, J.J. , Iron oxidation state and its effects on ash particle stickness, presented on the Engr. Found. Conf. on Application of Advanced Tech.

to Ash-related Problems in boiler, July, 1995

Bool, L.E., Peterson, T.W. and Wendt, J.O.L., The partitioning of iron during the combustion of pulverized coal, Combust. Flame 100, pp.262-270, 1995

Cooper, R.F., Fanselow, J.B., Weber, J.K.R., Merkley D. R. and Poker, D.B., Dynamics of oxidation of a Fe2+-bearing aluminosilicate (baseltic) melt, Science 274: 1173-1176, 1996

Flagan, R.C., Submicron particles from coal combustion, Seventeenth Symposium (International) on Combustion/ The Combustion Institute, 1978, pp.97-104

Gallagher, N.B., Bool, L.E., Wendt, J.O.L. and Peterson, T.W., Alkali metal partitioning in ash from pulverized coal combustion, Combust. Sci. and Tech. 74, pp.211-221, 1990

Graham, K.A., Submicron ash formation and interaction with sulfur oxides during pulverized coal combustion, PhD thesis, MIT, 1991

Hauffe, K. Oxidation of metals, Plenum Press, N.Y., 1965, pp.91-92

Hecker, W.C., McDonald, K. M., Reade, W., Swensen, M. R. and Cope, R. F.,Effects of Burnout on Char Oxidation Kinetics, Twenty-Fourth Symposium (International) on Combustion / The Combustion Institute, 1992, pp. 1225-1231

Helble, J.J., Peterson, T.W., Gallien, D., Sarofim, A.F., and Zeng, T., Fundamental study of ash formation and deposition, Quarterly Report to DoE, PSI-1178, February 1995

Helble, J.J. and Bool, L.E., Fundamental study of ash formation and deposition, Quarterly Report to DoE, PSI-1178, 1995

Helble, J.J. and Sarofim, A.F. , Influence of char fragmentation on ash particle distribution, Combust. Flame 76, pp.183-196, 1989

Helble, J.J., Neville, M. and Sarofim, A.F., Aggregate formation from vaporized ash during pulverized coal combustion, Twenty-first Symposium (International) on Combustion, The Combustion Institute, pp.411-417, 1986

Huffman, G.P., Huggins, F.E., Levasseur, A.A., Chow, O., Srinivasachar, S. and Mehta, A.K., Investigation of the transformations of pyrite in a drop tube furnace, Fuel 68, pp.485-490, 1989

Huffman, G.P., Huggins, F.E. and Dunmyre, G. R., Investigation of the high-temperature behavior of coal ash in reducing and oxidizing atmospheres, Fuel 60, pp.585-597, 1981

Huffman, G.P. and Huggins, F.E., Mossbauer studies of coal and coke: quantitative phase

identification and direct determination of pyritic and iron sulphide sulphur content, Fuel 57, pp. 592-604, 1978

Jorgensen, F.R.A., COmbustion of pyrite concentrate under simulated flash-smelting conditions, Trans. Inst. Min. Metal 90: C10-16 (1981)

Jung, B. and Schobert, H.H., Viscous sintering of coal ashes. 1. relationships of sinter point and sinter strength to particle size and composition, Energy and Fuel 5:555-561, 1991

Kang, S.G., Helble, J.J., Sarofim, A.F. and Beer, J.M., Time-resolved evolution of fly ash during pulverized coal combustion, Twenty-second Symposium (International) on Combustion, The Combustion Institute, pp.231-238, 1988

Kaufherr, N., Shenasa, M. and Lichtman, D., X-ray photoelectron spectroscopy studies of coal fly ashes with emphasis on depth profiling of submicron meter particle size fractions, Environ. Sci. Technol. 19, pp.609-614, 1985

Kauppinen, E.I. and Pakkanen, B.F., Coal combustion aerosol: A field study, Environ. Sci. Technol. 24, pp.1811-1818, 1990

Kerstein, A.R. and Edward, B.F., Percolation model for simulation of char oxidation and fragmentation time histories, Chem. Eng. Sci. 42, pp.. 1629-1634, 1987

Kingery, W.D., Introduction to Ceramics, John Wiley & Sons, Inc., N.Y., 1963, pp.225-229

Lienhard, J. H., A Heat Transfer Textbook, 2nd edition, Prentice Hall, Englewaood Cliffs, 1987, p. 531

Makino, A. and Law, C. K., Quasi-Steady and Transient Combustion of a Carbon Particle: Theory and Experimental Comparisons, Twenty - First Symposium (International) on Combustion, The Combustion Institute, 1986, pp. 183-191

Markowski, G.R. and Filby, R., Trace element concentration as a function of particle size in fly ash from a pulverized coal utility boiler, Environ. Sci. Technol.. 19, pp.796-804, 1985

McNallan, M.J., Yurek, G.J. and Elliott, J.F., The formation of inorganic particulates by homogeneous nucleation in gases produced by the combustion of coal, Combust. Flame 42: 45-60(1981)

Neville, M. and Sarofim, A.F., The stratified composition of inorganic submicron particles produced during coal combustion, Nineteeth Symposium (International) on Combustion, The Combustion Institute, pp.1441-1449, 1982

Neville, M., Quann, R.J., Haynes, B.S. and Sarofim, A.F. , Vaporization and condensation of mineral matter during pulverized coal combustion, Eighteenth Symposium (International) on Combustion, The Combustion Institute, pp. 1267-1274, 1980

Nowok, J.W., Benson, S.A., Jones, M.L. and Kalmanovitch, D.P., Sintering behaviour and strength development in various coal ashed, Fuel 1020-1028, 1990

Quann, R.J. and Sarofim, A.F., A scanning electron microscopy study of the transformations of organically bound metals during lignite combustion, Fuel 65, pp.40-46, 1986

Quann, R. J. and Sarofim, A.F., Vaporization of Refractory Oxides During Pulverized Coal Combustion, Nineteenth Symposium (international) on Combustion / The Combustion Institute, 1982 , pp. 1429-1440

Quann, R.J., Neville, M., Janghorbani, M., Mims, C.A. and Sarofim, A.F., Mineral matter and trace-element vaporization in a laboratory-pulvarized coal combustion system, Environ. Sci. Technol. 16: 776-781, 1982

Rassk, E. , Mineral impurities in coal combustion, Washington, Hemisphere Publisher Comp., 1985

Sarofim, A.F. and Helble, J.J., Mechanisms of ash formation and deposit, Quarterly report to DoE, PSI-1178SR-703, 1993

Sarofim, A.F., Howard, J.B. and Padia, A.S., The physical transformation of the mineral in pulverized coal under simulated combustion conditions, Combust. Sci. Technol. 16, pp.187-204, 1977

Senior, C. L. and Srinivasachar, S., Viscosity of ash particles in combustion systems for prediction of particle sticking, Energy and Fuel, 1995

Senior, C.L. and Flagan, R.C., Synthetic chars for the study of ash vaporization, Twentieth Symposium (International) on Combustion, The Combustion Institute, pp. 921-929, 1984

Srinivasachar, S., Helble, J.J. and Boni, A.A., Mineral behavior during coal combustion 1. pyrite transformations, Prog. in Energy Combust. Sci. 16, 281-292, 1990

Srinivasachar, S. and Boni, A.A., A kinetic model for pyrite transformations in a combustion environment, Fuel 68, pp.829-836, 1989

Timothy, L. D., Sarofim, A. F. and Beer, J. M. , Characteristics of single particle coal combustion, Nineteenth Symposium (International) on Combustion / The Combustion Institute, 1982, pp. 1123-1130

Wall, T.F., Mineral matter transformations and deposition in pulverized coal combustion, Twenty-fourth Symposium (International) on Combustion, The Combustion Institute, pp.1119-26, 1992

Wibberly, L.J. and Wall, T.F., An investigation of factors affecting the physical characteristics of fly ash formed in a laboratory scale combustor, Combust. Sci. Technol. 48, pp.177-190, 1986

Zeng Taofang and Fu Weibiao , The ratio CO/CO2 of carbon oxidation on a burning carbon surface, Combust. Flame 107:197-210, 1996

Table 4-4 Iron distribution under different combustion conditions

% O2	Phase Present	I.S.	Q.S.	HO	%Fe
parent coal	pyrite	0.33	0.56		41
	jarosite	0.38	1.06		59
0	Fe^{+++} / jarosite	0.37	0.97		25
	γ Fe Metal	-0.08			6
	Fe Metal	-0.01	0	327	17
	$Fe_{1-x}S$	0.74	-0.09	305	24
	Fe Carbide	0.14	0	197	29
10	Fe^{++} / glass	0.96	1.89		19
	Fe^{+++} / glass	0.32	0.99		29
	γ Fe Metal	-0.06			2
	Fe Metal	-0.02	0	328	8
	Magnetite	0.31	0	486	17
	Magnetite	0.63	0	448	15
	$Fe_{1-x}S$	0.75	0	299	11
30	Fe^{++} / glass	0.86	2.33		22
	Fe^{+++} / glass	0.39	0.95		51
	Magnetite	0.35	0	494	12
	Magnetite	0.65	0	443	8
	$Fe_{1-x}S$	0.67	0	302	8
60	Fe^{++}/ glass	0.77	2.56		11
	Fe^{+++}/ glass	0.36	1.08		66
	α-Fe_2O_3	0.36	-0.08	496	9
	Magn.+ Fe_2O_3	0.40	-0.08	427	4
100	Fe^{++}/ glass	0.73	2.74		8
	Fe^{+++} /glass	0.35	1.17		75
	α-Fe_2O_3	0.37	-0.07	498	4
	Magn.+Fe_2O_3	0.39	-0.05	429	14
ASTM Ash	Fe^{+++}/ glass	0.34	0.90		7
	α-Fe_2O_3	0.39	-0.08	514	55
	α-Fe_2O_3	0.37	-0.1	494	39

Table 4-5 Iron distribution with 40% O2

Stage	Size range	Compositions	Percentage
1	>10	Fe^{++}(glass)	16
		Fe^{+++}(glass)	33
		Fe_3O_4 + -Fe_2O_3	23
		- Fe_2O_3	22
		Fe-metal	4
		$Fe_{1-x}S$	2
2	9.0-10.0	Fe^{++}(glass)	16
		Fe^{+++}(glass)	52
		Fe_3O_4 + -Fe_2O_3	8
		- Fe_2O_3	21
		$Fe_{1-x}S$	3
3	5.8-9.0	Fe^{++}(glass)	19
		Fe^{+++}(glass)	54
		Fe_3O_4 + -Fe_2O_3	12
		-Fe_2O_3	8
		Fe-metal	3
		$Fe_{1-x}S$	4
4	4.7-5.8	Fe^{++}(glass)	16
		Fe^{+++}(glass)	57
		Fe_3O_4 + -Fe_2O_3	14
		-Fe_2O_3	7
		Fe-metal	4
		$Fe_{1-x}S$	2
5	3.3-4.7	Fe++(glass)	13
		Fe+++(glass)	62
		Fe_3O_4 + -Fe_2O_3	15
		-Fe_2O_3	5
		Fe-metal	3
		Fe1-xS	2
6	2.1-3.3	Fe^{++}(glass)	12
		Fe^{+++}(glass)	56
		Fe_3O_4 + -Fe_2O_3	17
		-Fe_2O_3	7
		Fe-metal	3
		$Fe_{1-x}S$	5

7	1.1-2.1	Fe^{++}(glass)	10
		Fe^{+++}(glass)	48
		Fe_3O_4 + -Fe_2O_3	17
		-Fe_2O_3	7
		Fe-metal	3
		$Fe_{1-x}S$	8
8	0.65-1.1	Fe^{++}(glass)	0
		Fe^{+++}(glass)	73
		Fe_3O_4+ -Fe_2O_3	19
		Fe-metal	2
		$Fe_{1-x}S$	6
9	0.43-0.65	Fe^{++}(glass)	0
		Fe^{+++}(glass)	67
		Fe_3O_4 + -Fe_2O_3	22
		Fe-metal	0
		$Fe_{1-x}S$	11
10	<0.43	Fe^{++}(glass)	2
		Fe^{+++}(glass)	73
		Fe_3O_4 + -Fe_2O_3	14
		Fe-metal	2
		$Fe_{1=-x}S$	9

Table 4-6 Iron distribution at 100% O2

Stage	Size range	Compositions	Percentage
1	>10	Fe^{++}(glass)	18
		Fe^{+++}(glass)	34
		Fe_3O_4 + -Fe_2O_3	14
		- Fe_2O_3	28
		Fe-metal	2
		$Fe_{1-x}S$	4
2	9.0-10.0	Fe^{++}(glass)	15
		Fe^{+++}(glass)	62
		Fe_3O_4 + -Fe_2O_3	8
		- Fe_2O_3	15

3	5.8-9.0	Fe^{++}(glass)	13
		Fe^{+++}(glass)	80
		Fe_3O_4 + -Fe_2O_3	3
		-Fe_2O_3	4
4	4.7-5.8	Fe^{++}(glass)	13
		Fe^{+++}(glass)	78
		Fe_3O_4 + -Fe_2O_3	6
		-Fe_2O_3	3
5	3.3-4.7	Fe^{++}(glass)	8
		Fe^{+++}(glass)	78
		Fe_3O_4 + -Fe_2O_3	8
		-Fe_2O_3	6
6	2.1-3.3	Fe^{++}(glass)	11
		Fe^{+++}(glass)	71
		Fe_3O_4 + -Fe_2O_3	13
		-Fe_2O_3	5
7	1.1-2.1	Fe^{++}(glass)	2.5
		Fe^{+++}(glass)	79
		Fe_3O_4 + -Fe_2O_3	14.5
		-Fe_2O_3	4
8	0.65-1.1	Fe^{++}(glass)	2
		Fe^{+++}(glass)	58
		Fe_3O_4 + -Fe_2O_3	31
		Fe-metal	5
		$Fe_{1-x}S$	4
9	0.43-0.65	Fe^{++}(glass)	3
		Fe^{+++}(glass)	60
		Fe_3O_4 + -Fe_2O_3	28
		Fe-metal	5
		$Fe_{1-x}S$	4
10	<0.43	Fe^{++}(glass)	2
		Fe^{+++}(glass)	66
		Fe_3O_4 + -Fe_2O_3	20
		Fe-metal	5
		$Fe_{1-x}S$	7

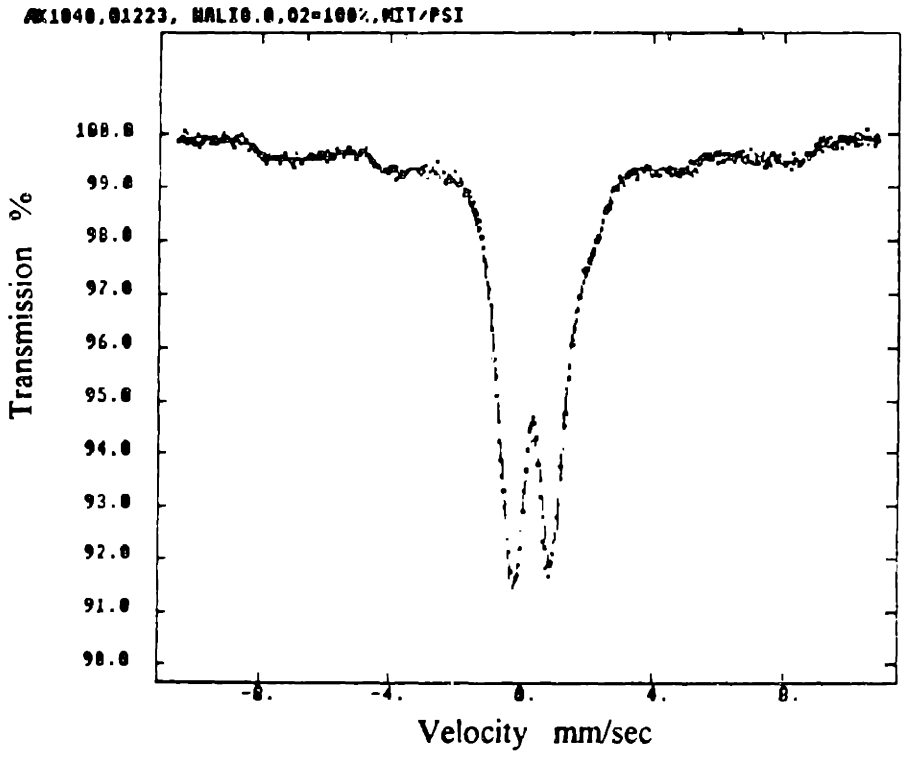

U. of K. results (%)

Fe++/glass	8
Fe+++/glass	75
α-Fe_2O_3	4
Fe_3O_4+Fe_2O_3	13

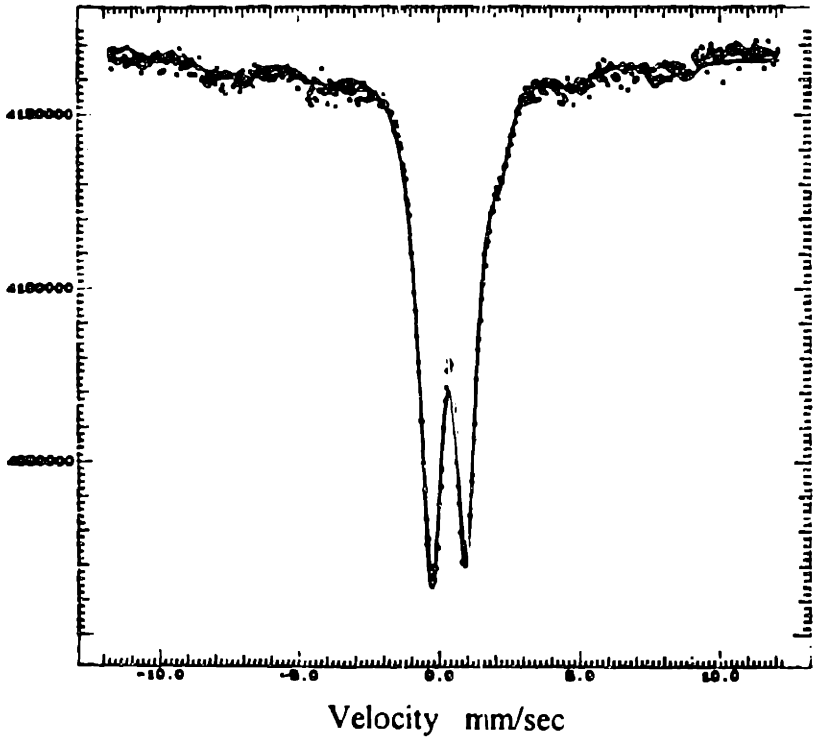

MIT results (%)

Fe++/glass	9.9
Fe+++/glass	79.1
α-Fe_2O_3	3.8
Fe_3O_4+γ-Fe_2O_3	7.2

Figure 4-1 Calibration of Mossbauer at MIT

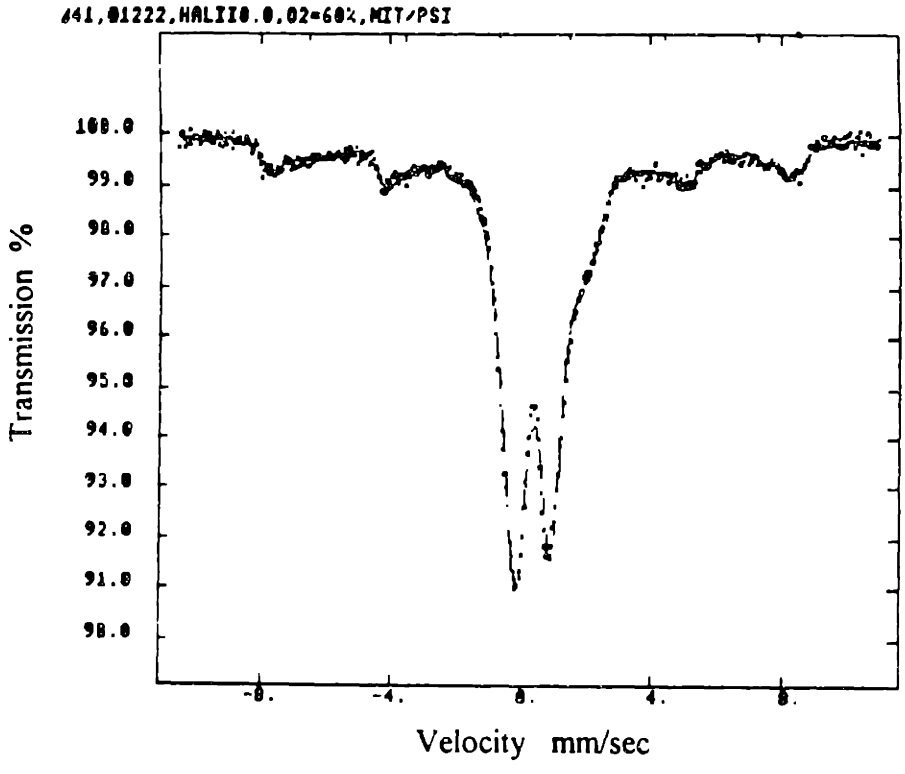

U. of K. results (%)

Fe++/glass	11
Fe+++/glass	66
α-Fe_2O_3	9
Fe_3O_4+Fe_2O_3	14

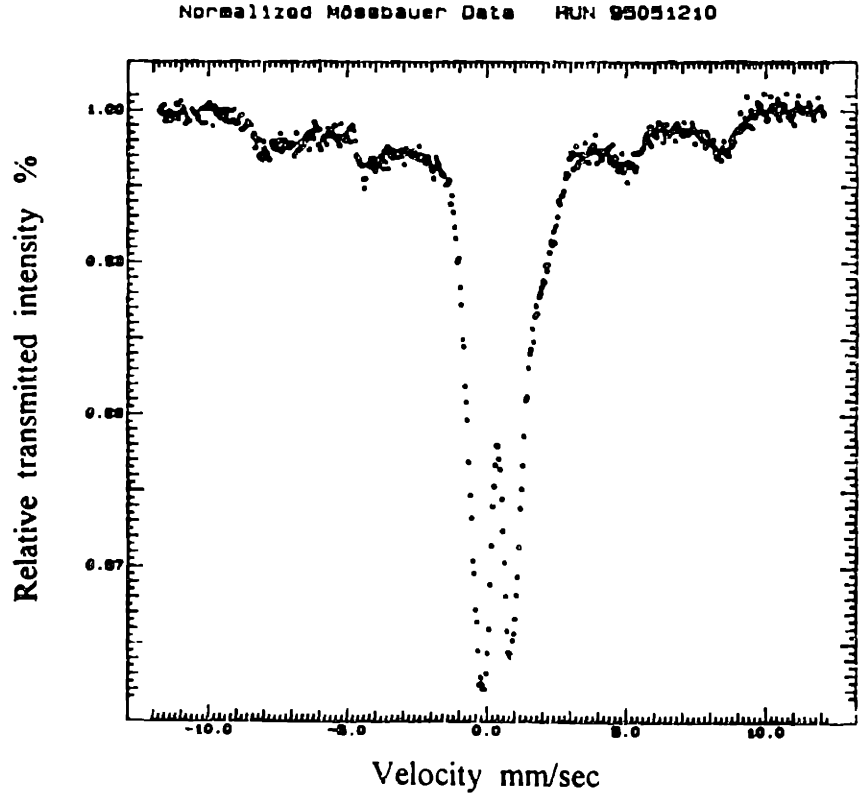

MIT results (%)

Fe++/glass	10.4
Fe+++/glass	67.7
α-Fe_2O_3	9.8
Fe_3O_4+Fe_2O_3	12.1

Figure 4-2 Calibration of Mossbauer at MIT with sample #1222

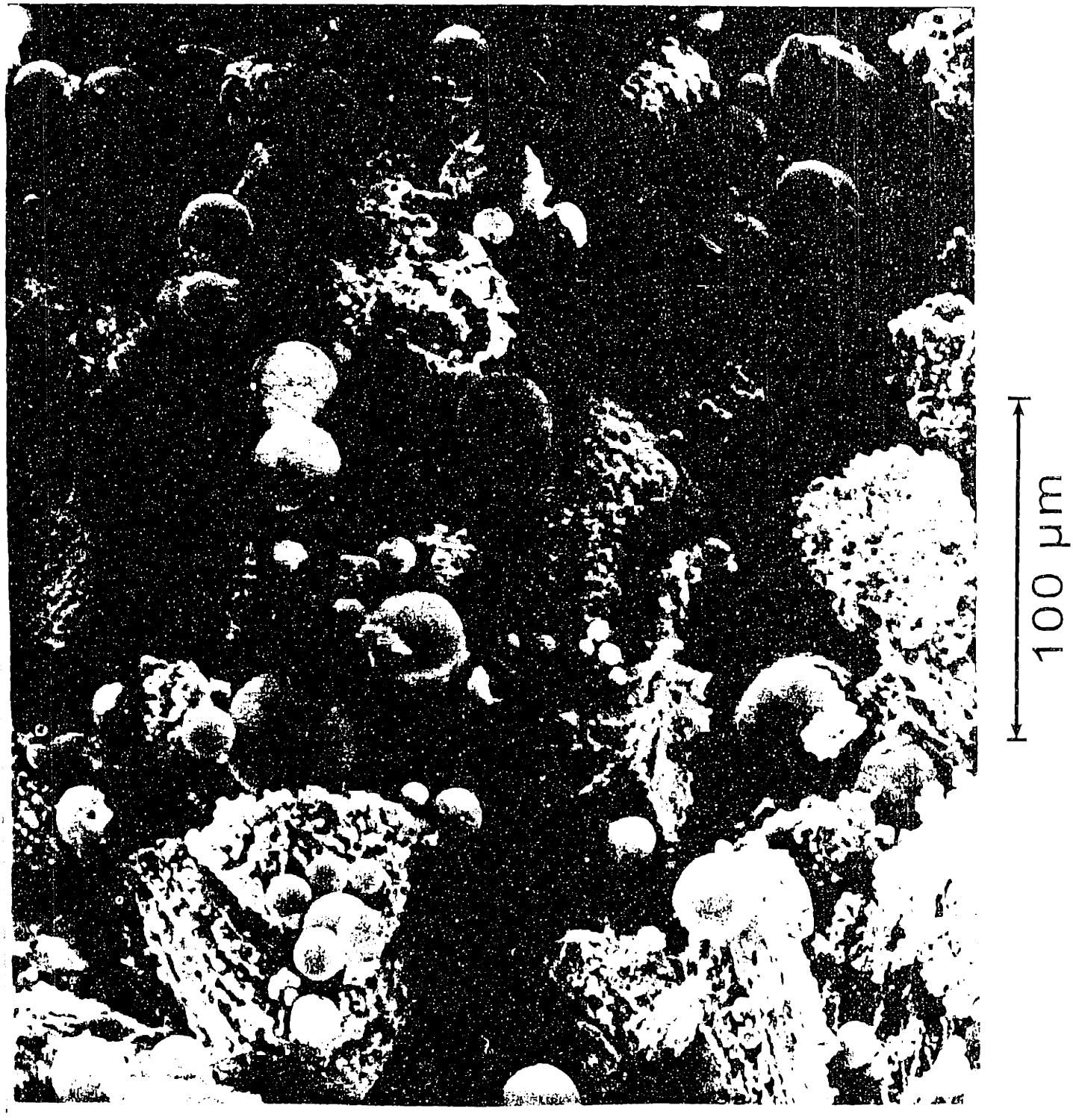

Figure 4-3 SEM picture for partially burnt char

Ash at 100% O_2 T_g=1650K

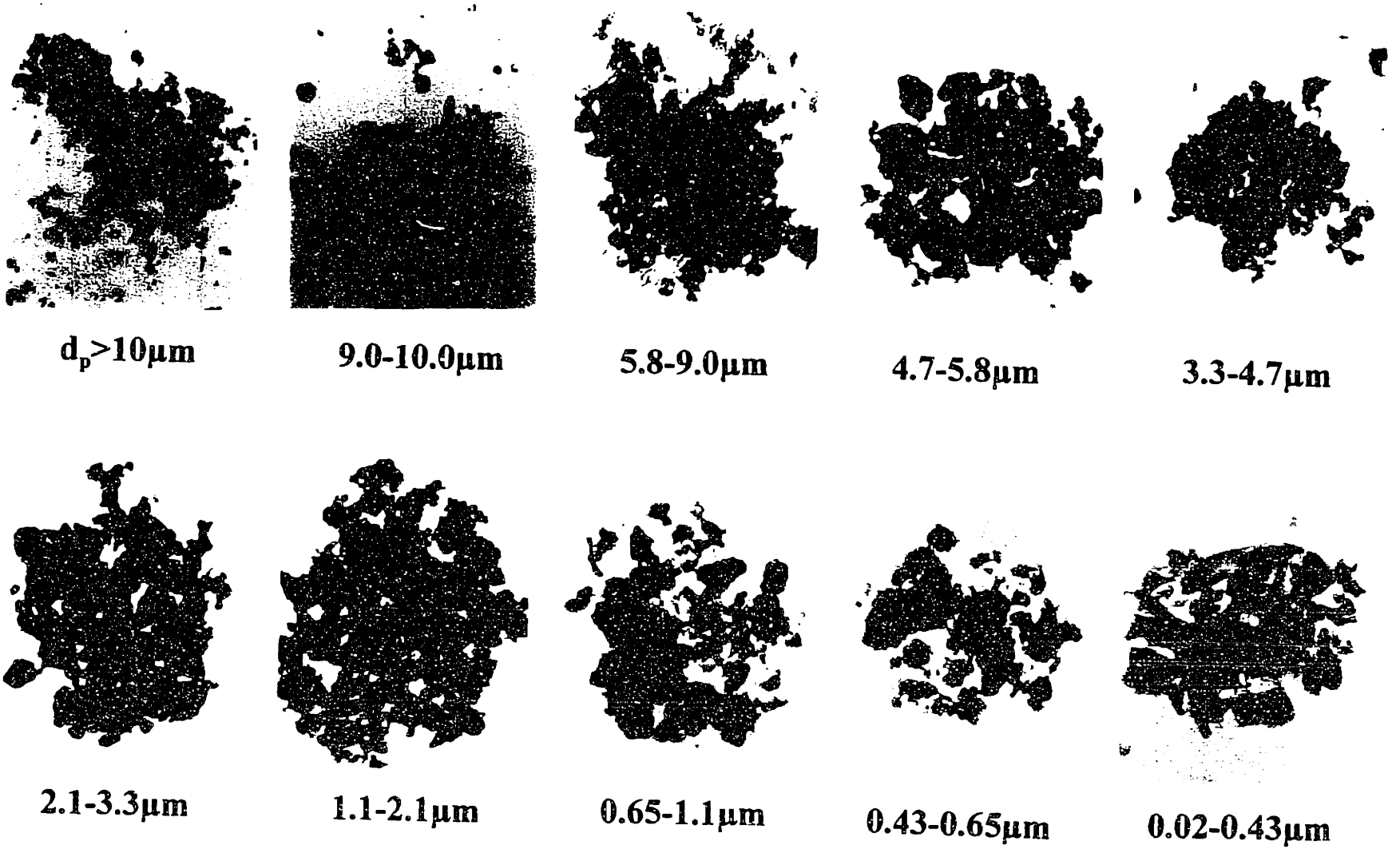

Figure 4-4 Microscopy picture for ash particles with different size (magnitude is different)

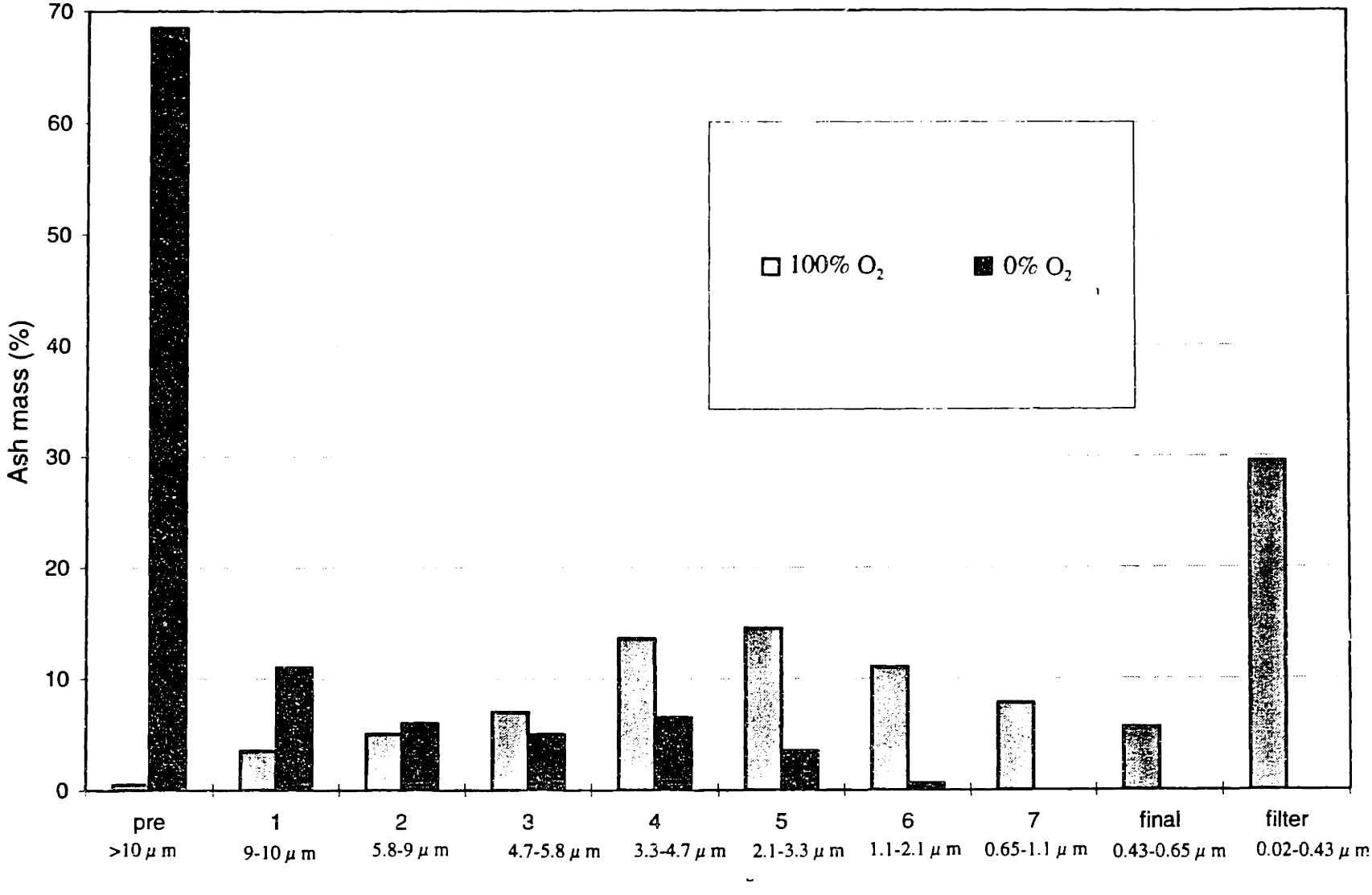

Figure 4-5 Ash distribution with 100% O2 and 0% O2

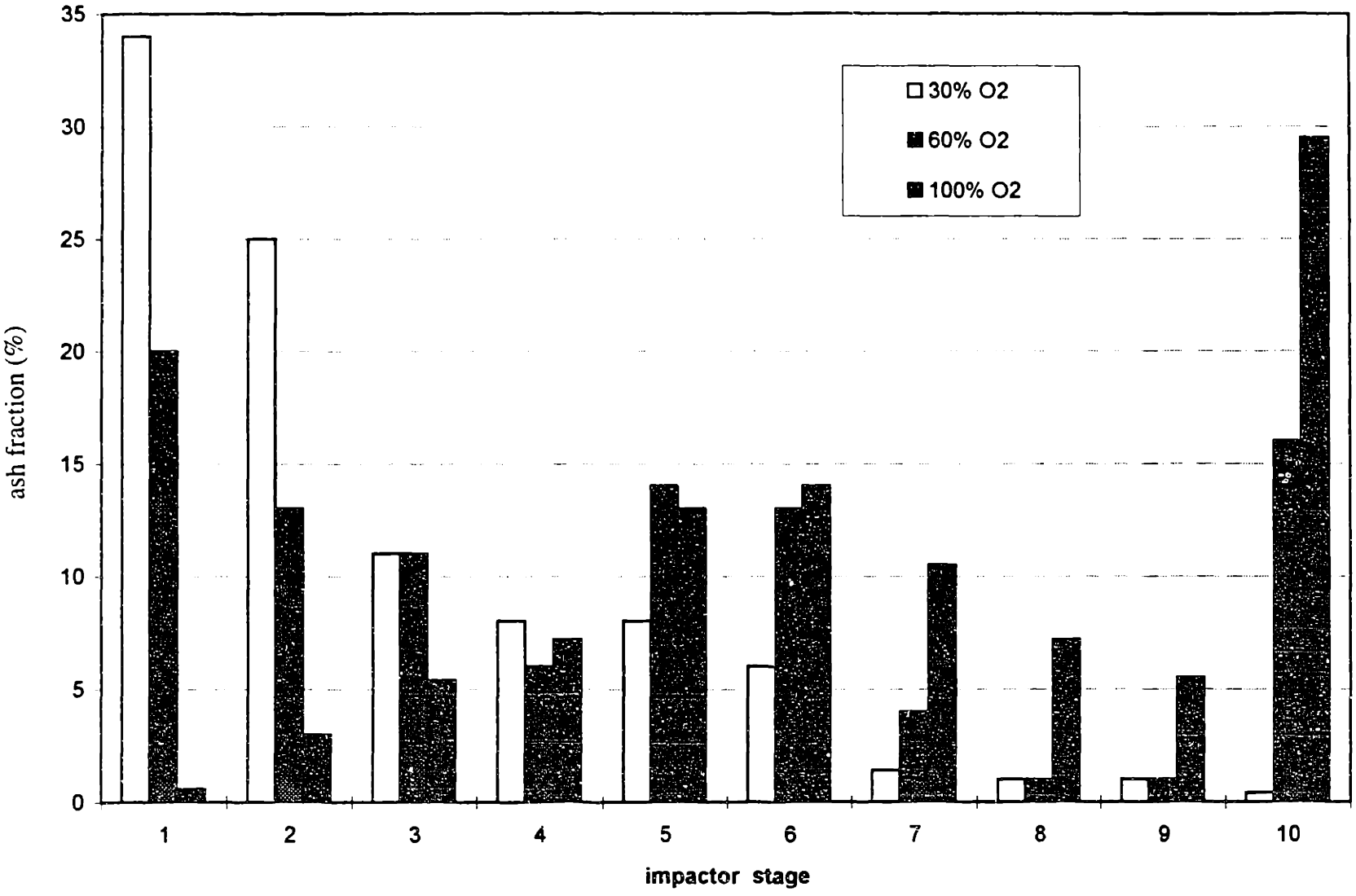

Figure 4-6 Ash distributions as a function of O_2 concentrations

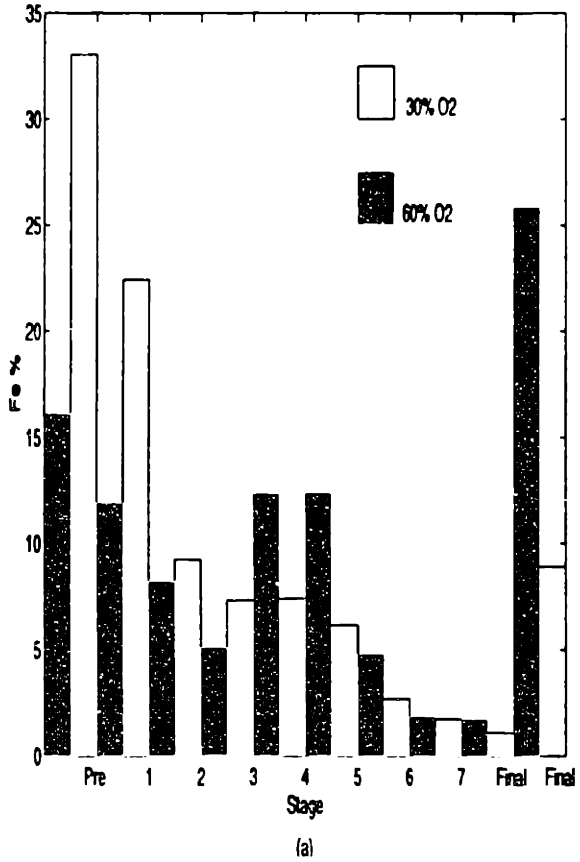

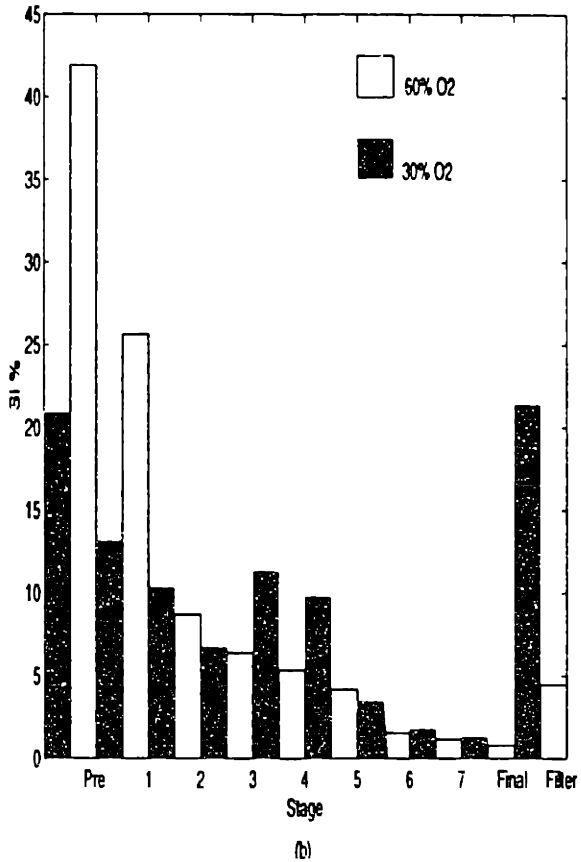

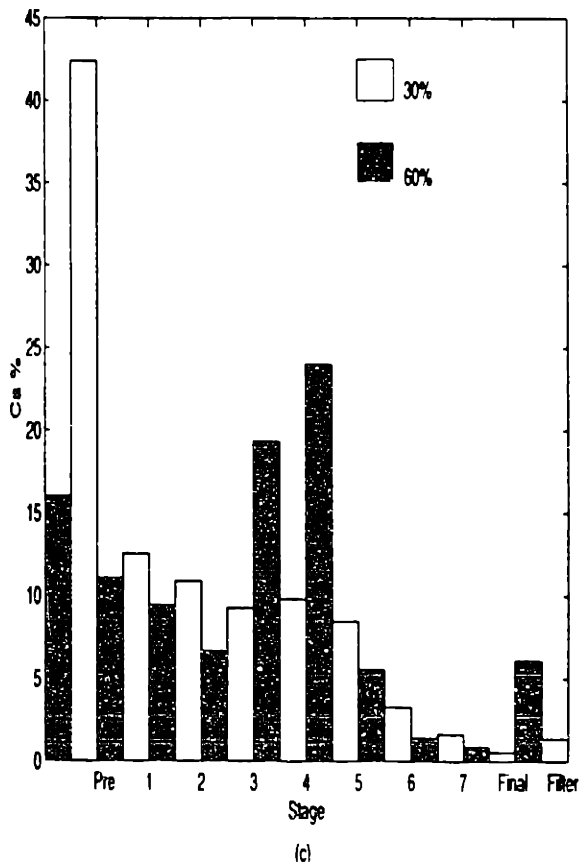

Figure 4-7 a) Fe distribution; b) Si distribution; c) Ca distribution

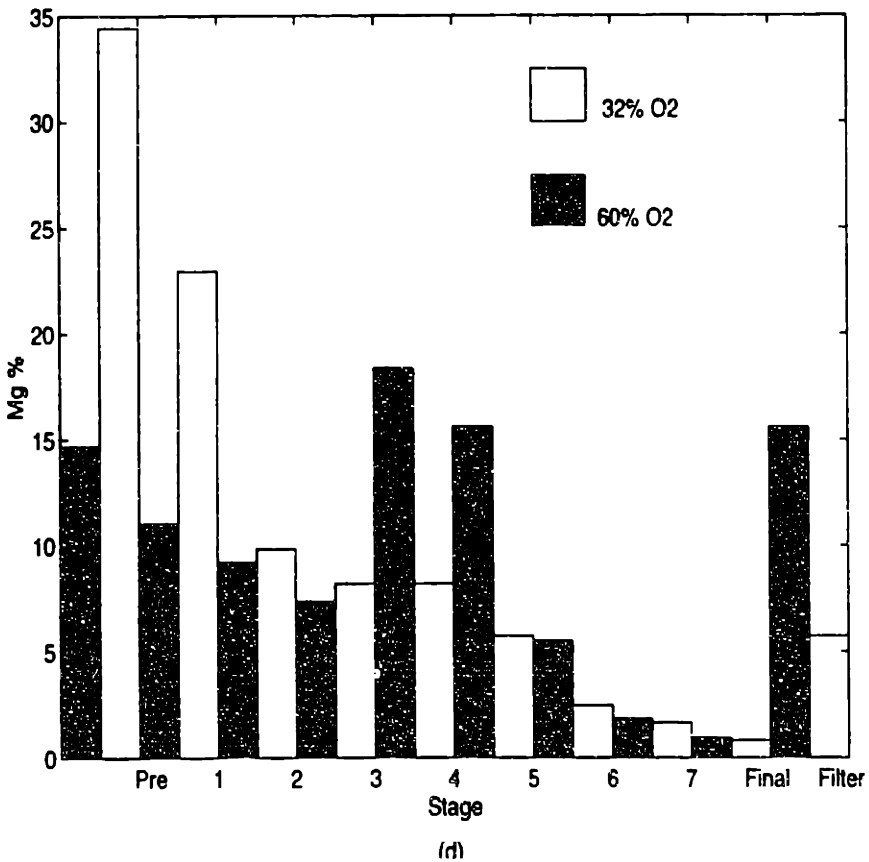

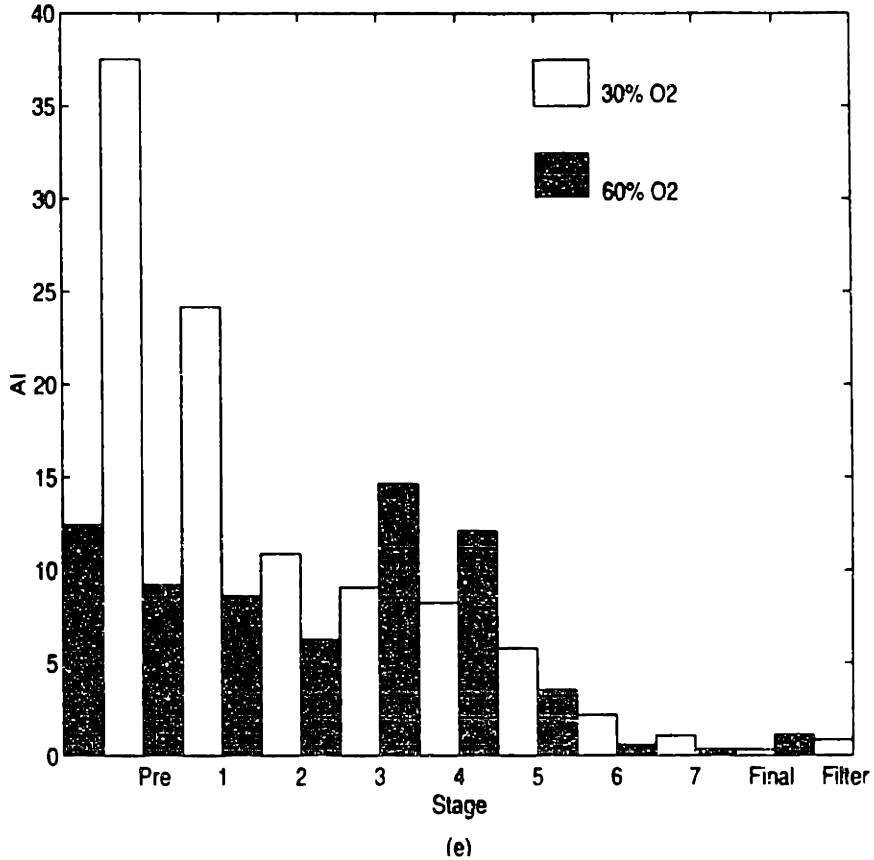

Figure 4-7 d) Mg distribution; e) Al distribution

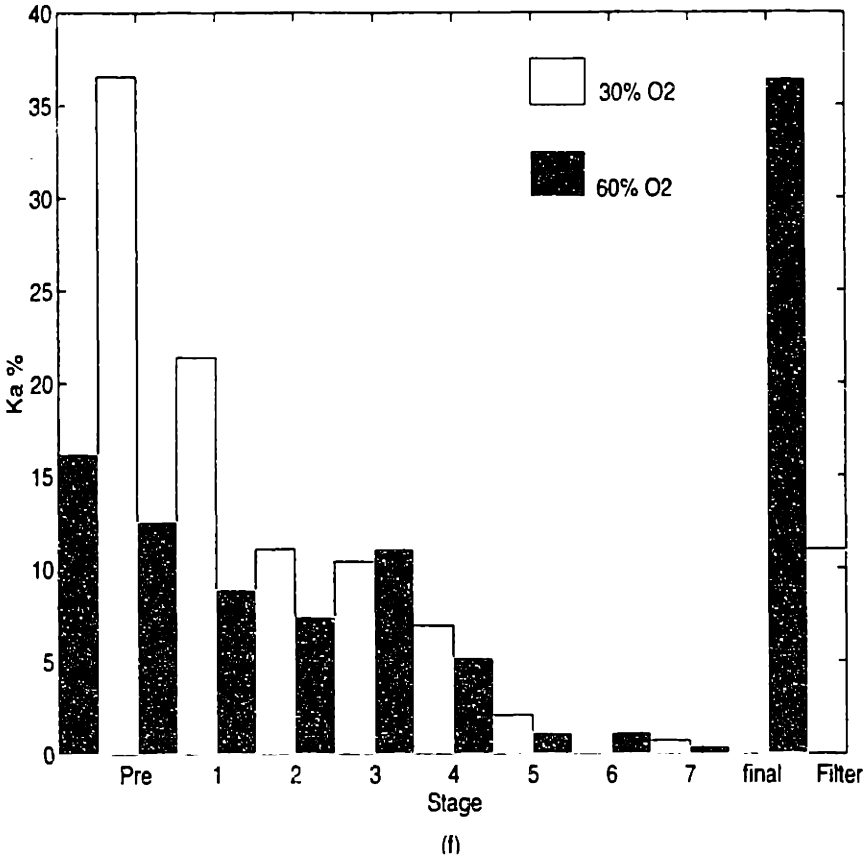

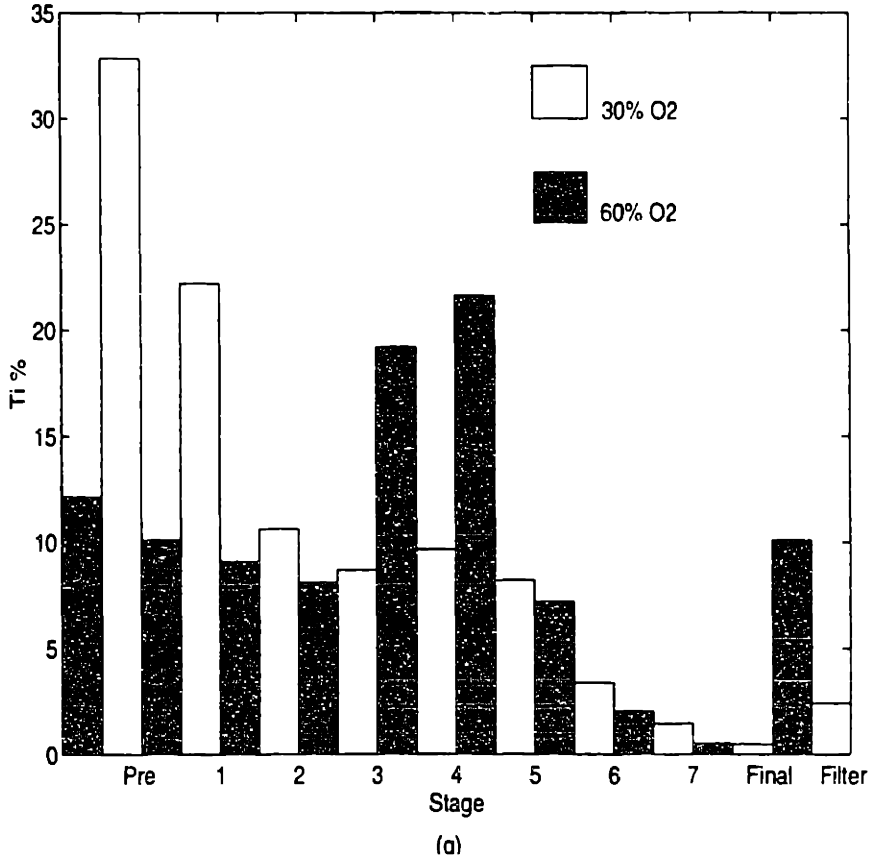

Figure 4-7 f) K distribution; g) Ti distribution

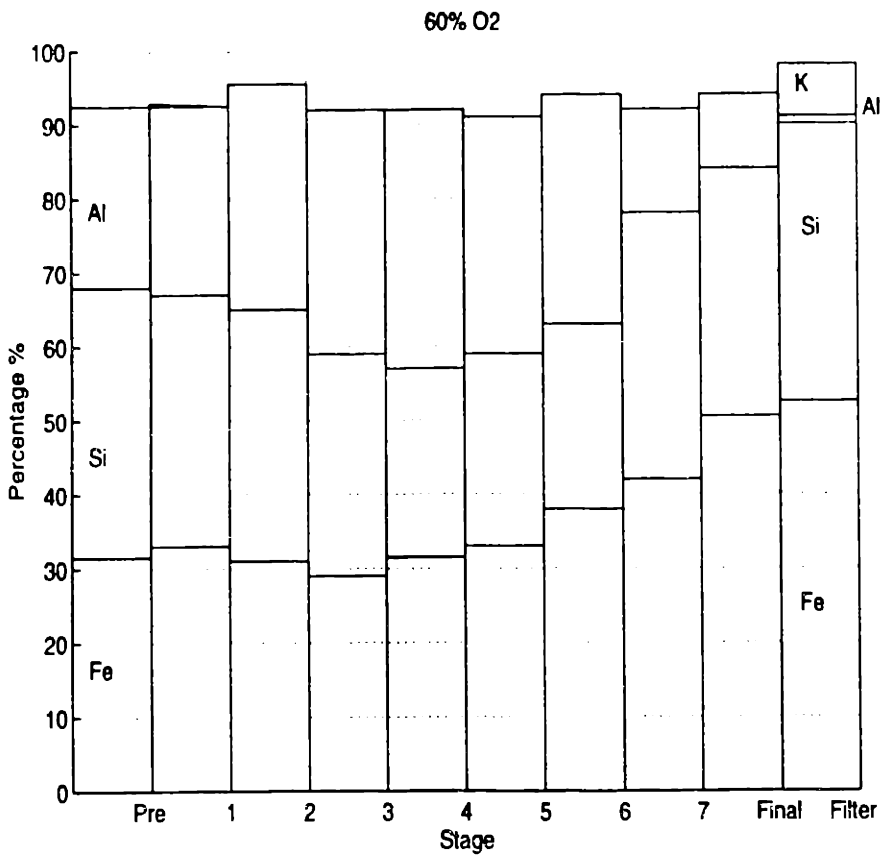

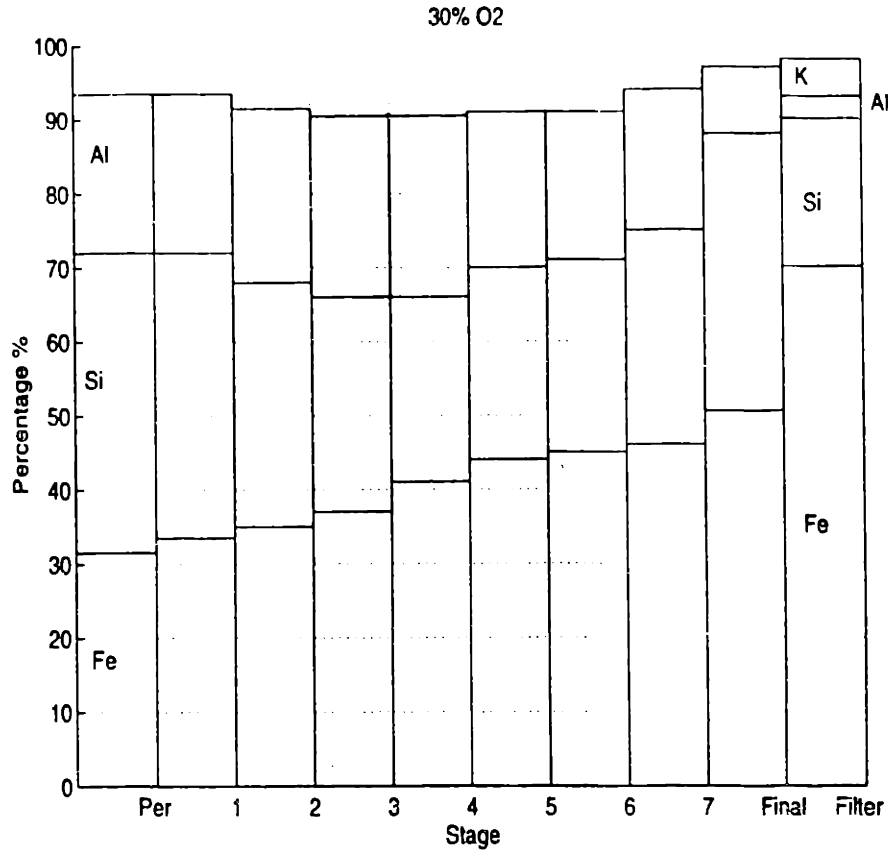

Figure 4-8 Composition of mineral

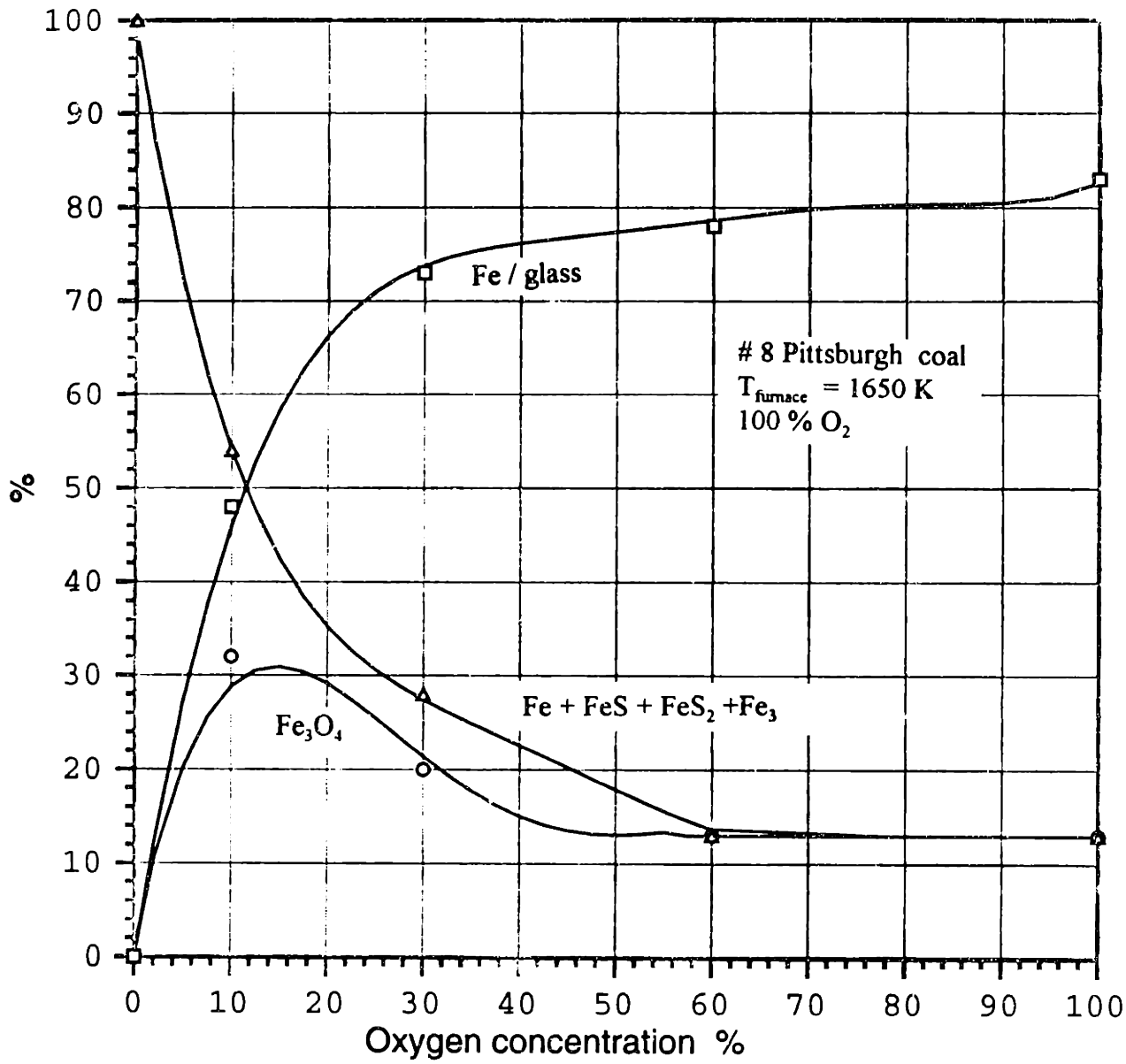

Figure 4-9 a Conversion of Fe as a function of oxygen concentration

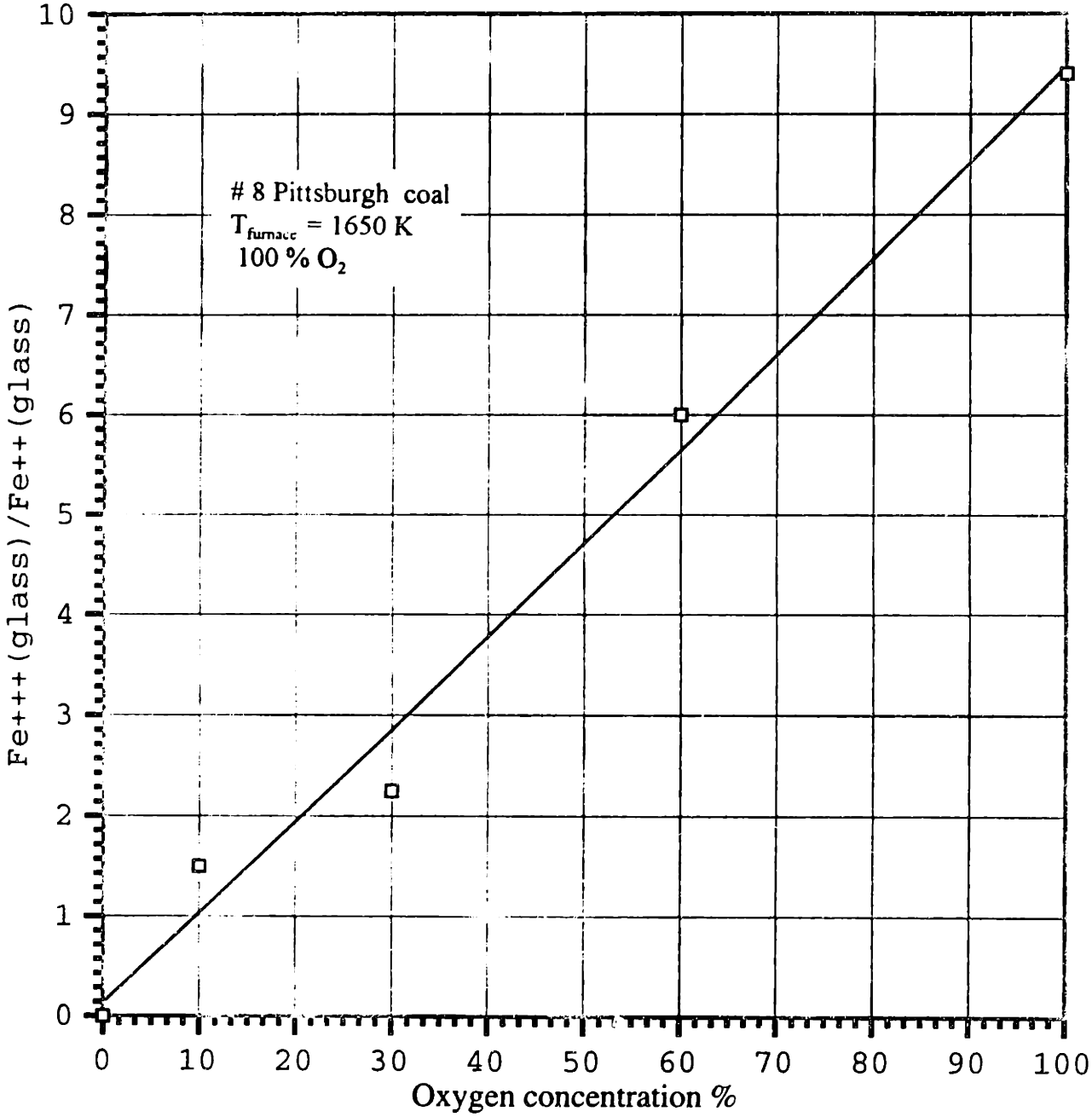

Figure 4-9b Fe+++(glass)/Fe++(glass) as a function of oxygen concentration

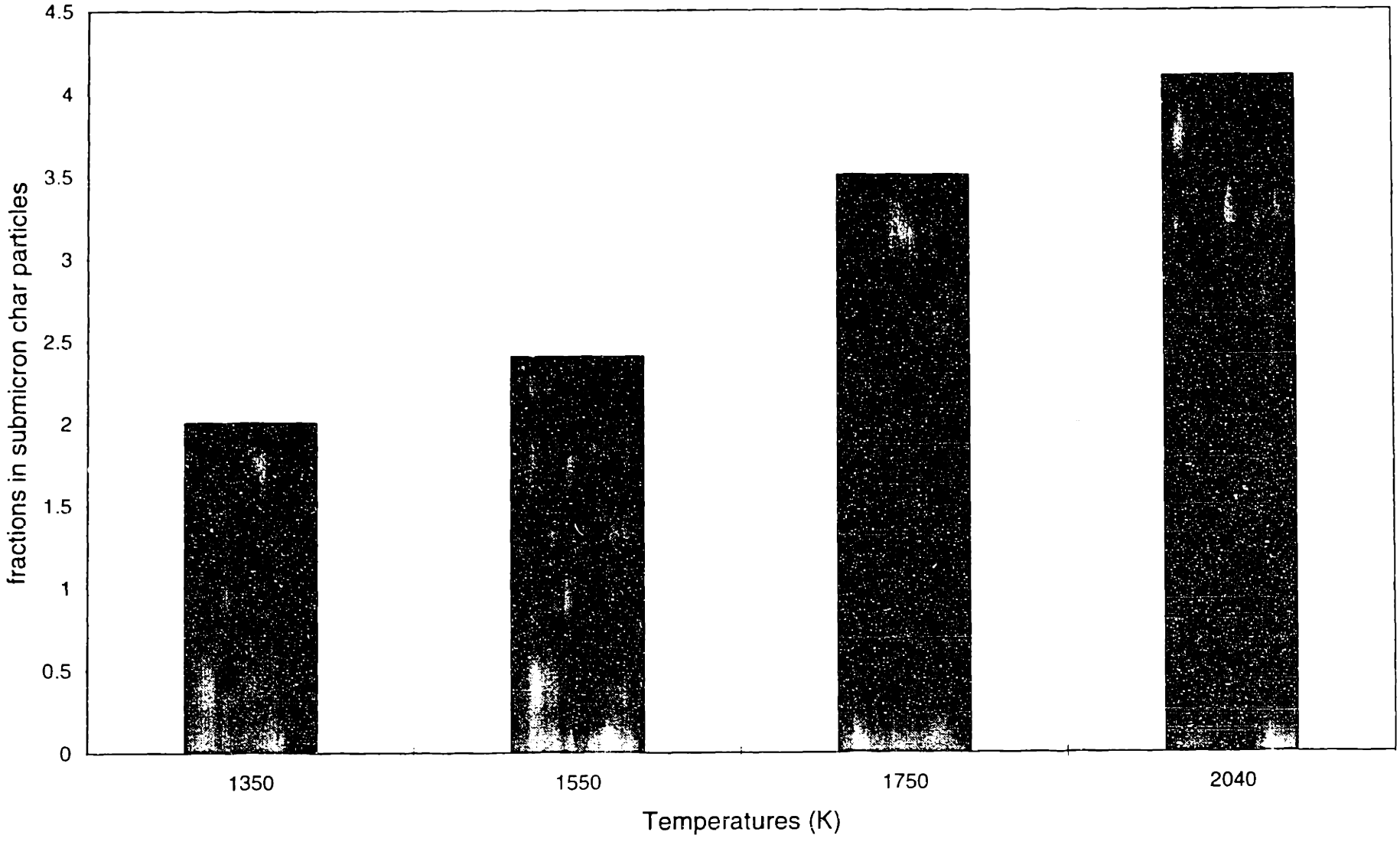

Figure 4-10a Fractions of iron in submicron char particles at different pyrolysis temperatures

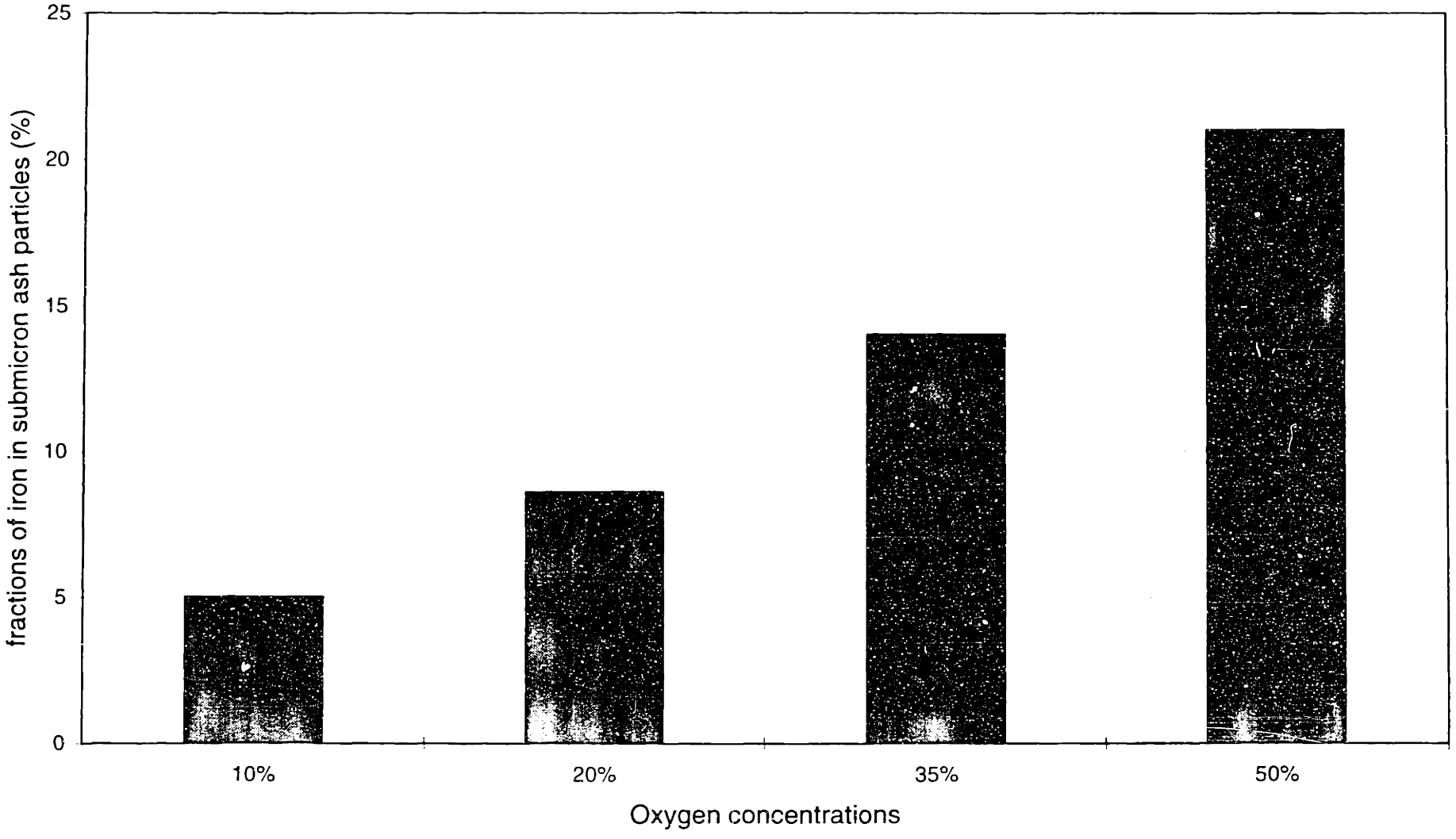

Figure 4-10b Fractions of iron in submicron ash particles with different O2 concentrations at Tg=1700 K

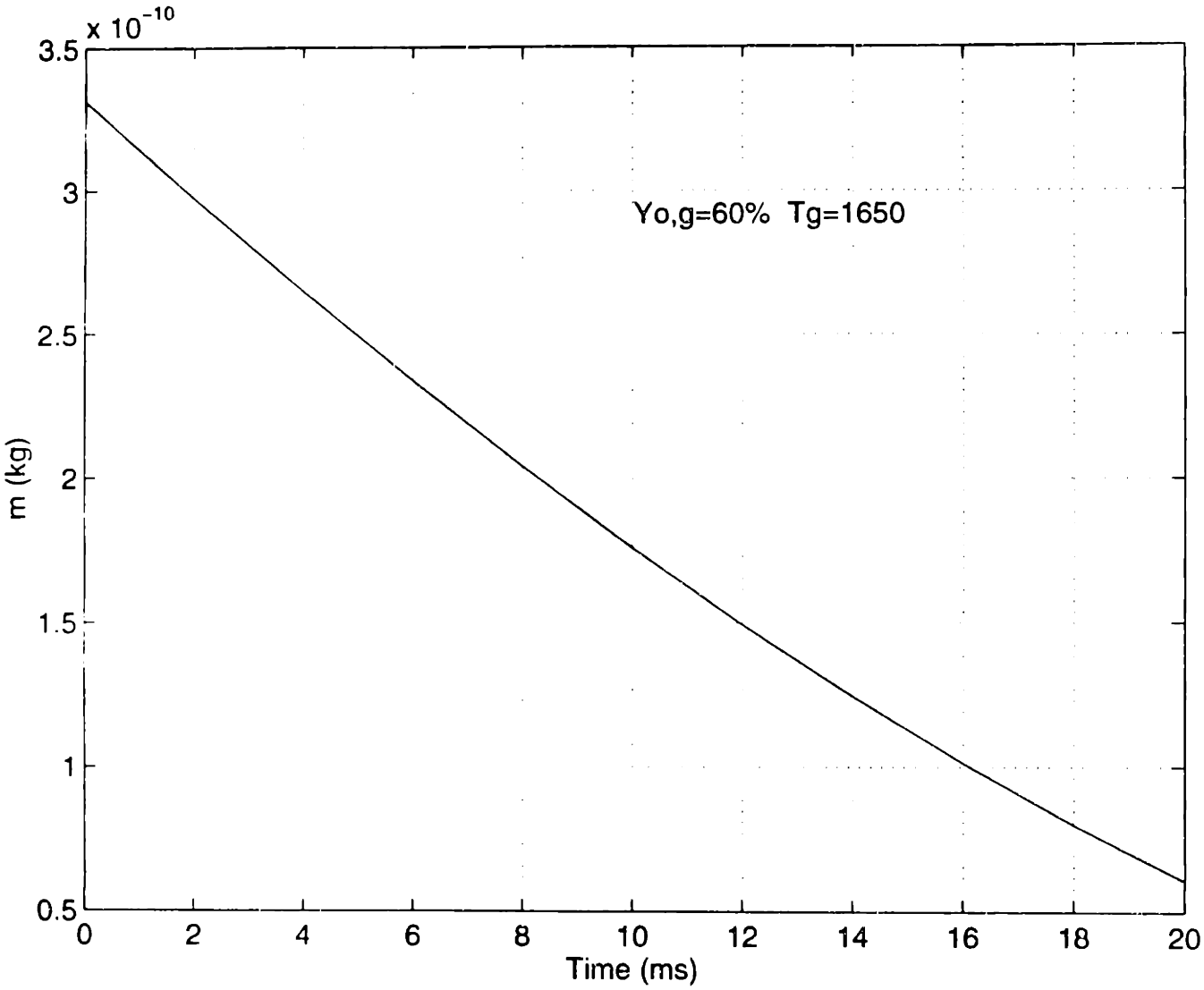

Figure 4-11 Char mass as a function of time

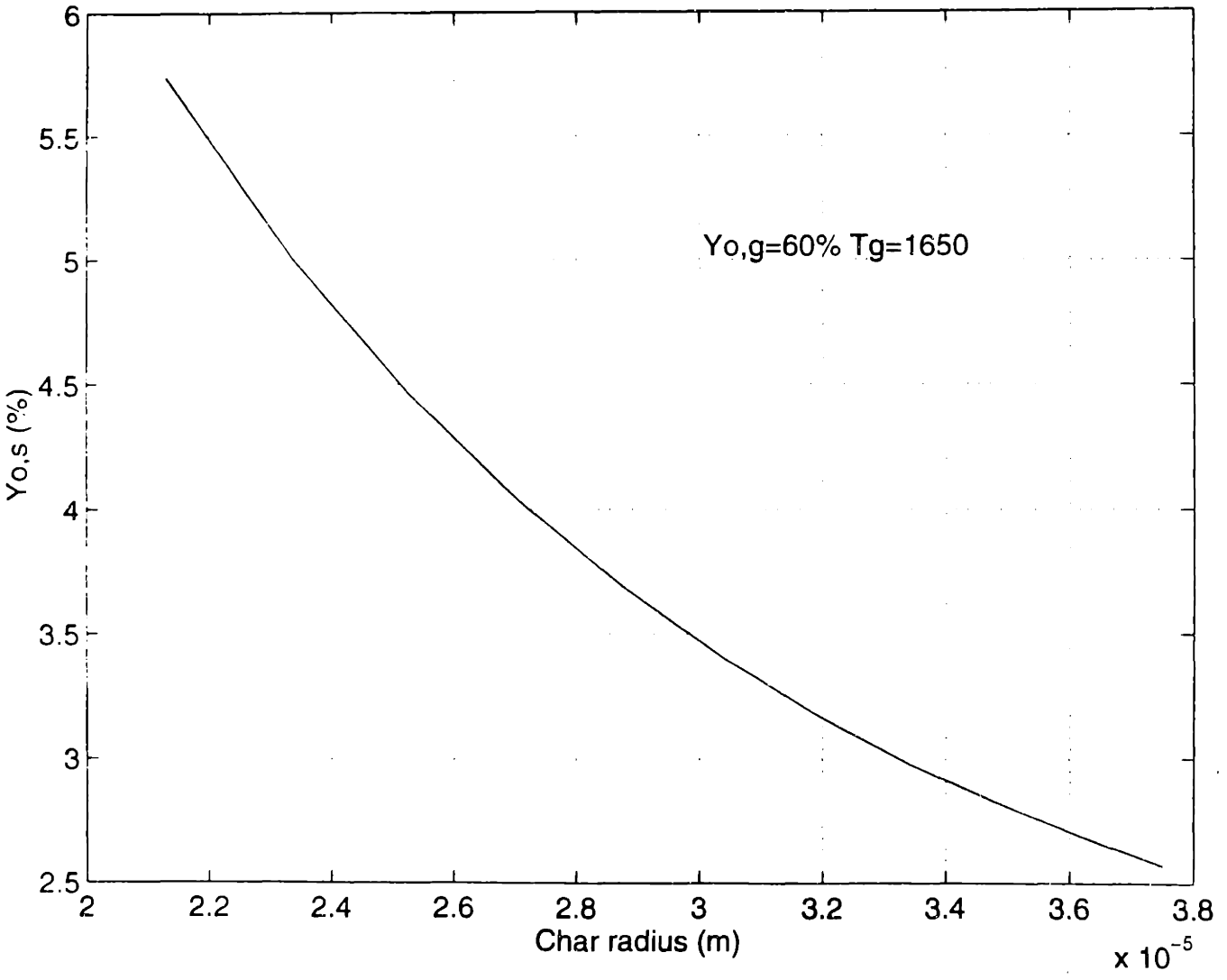

Figure 4-12 O_2 concentrations on char surface as a function of particle size

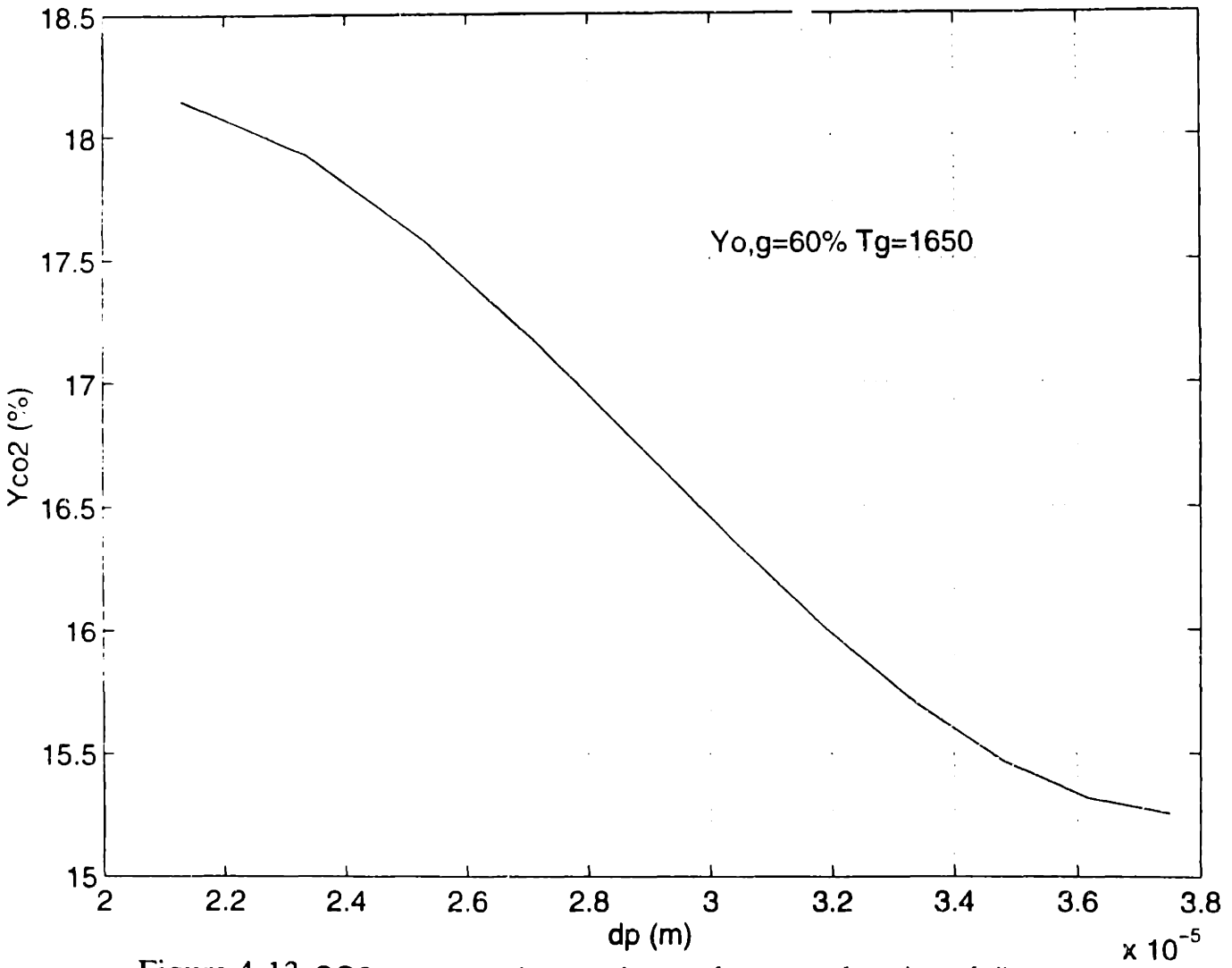

Figure 4-13 CO2 concentration on char surface as a function of diameter

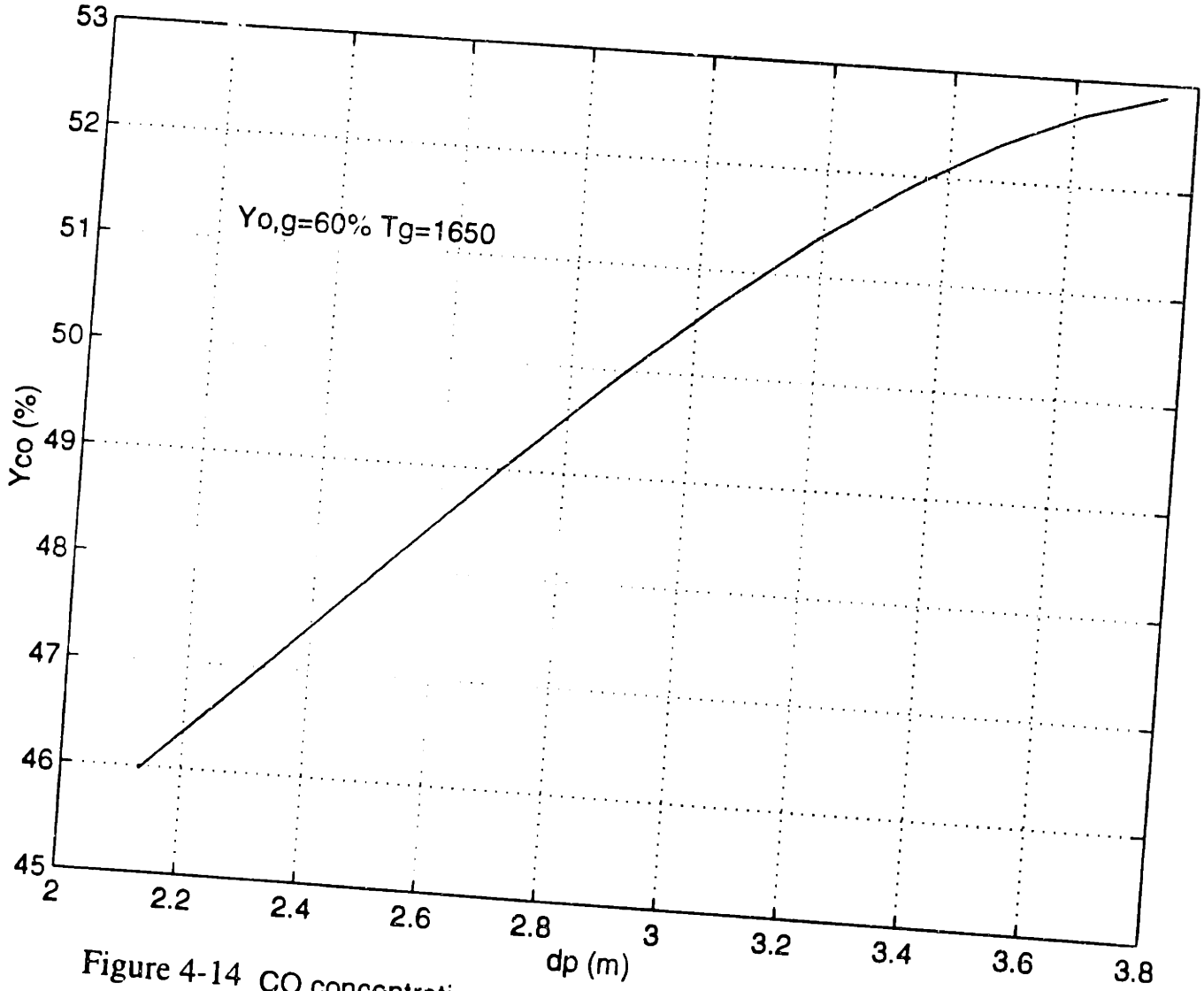

Figure 4-14 CO concentration on char surface as a function of diameter

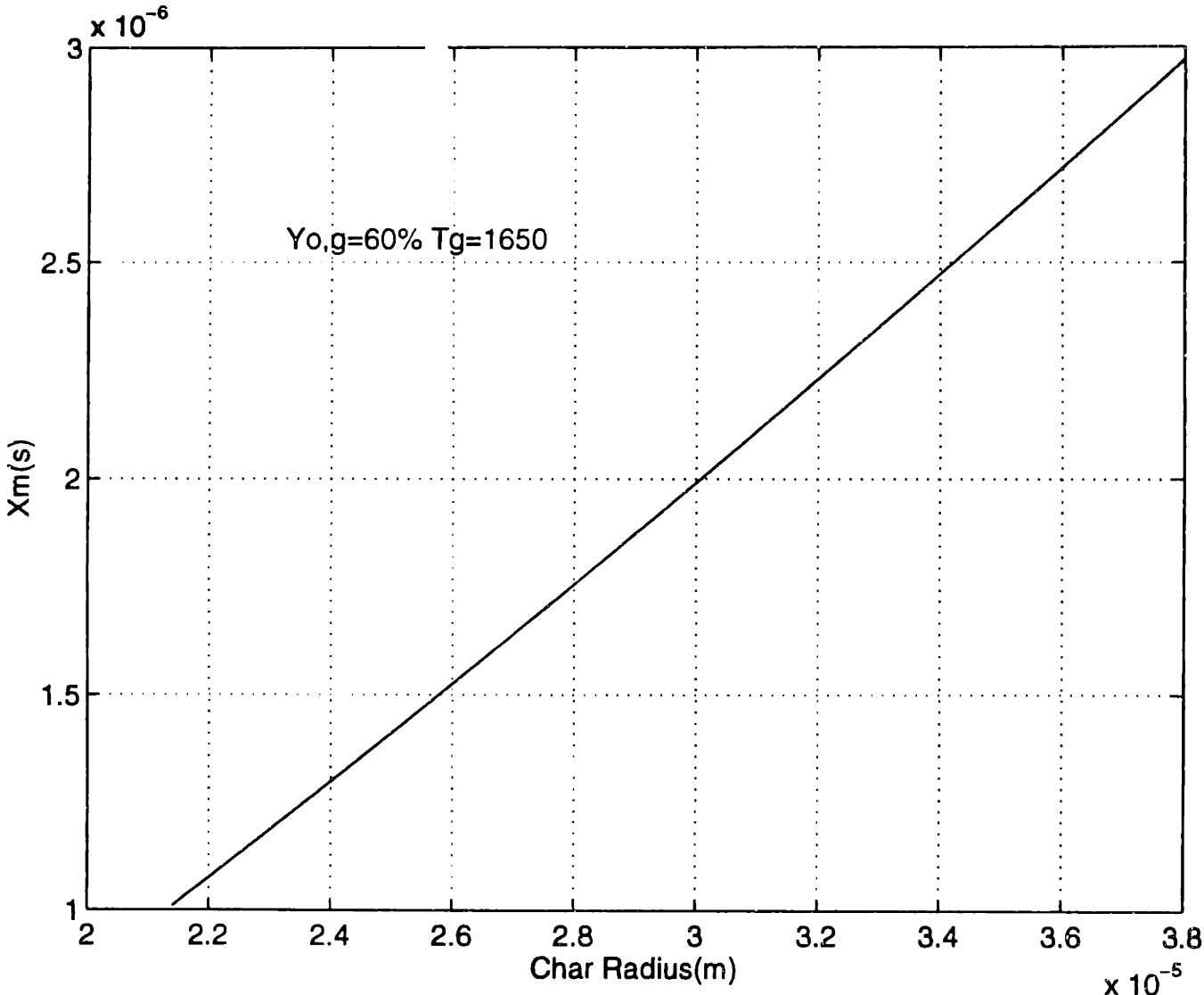

Figure 4-15 Fe vapor mole fraction at char surface as a function of particle size

Chapter 5 TRANSFORMATION OF TRACE ELEMENTS DURING COMBUSTION

5. 1 Introduction

Toxic trace elements are now attracting attention because of the association of increased human morbidity and mortality with aerosols. Toxic trace elements emitted by power stations are a potential source of toxic elements in the atmosphere. By using advanced instrumentation such as SEM-EDX and XAFS, the occurrences of trace elements can be determined(Finkelman, 1995; Huggins, et al., 1993; Swaine, 1990). Interestingly, many toxic trace elements are associated with iron as sulphides. The chalcophilic trace elements associated with iron include As, Cd, Co, Cu, Cr, Mn, Hg, Mo, Pb, Ni, and Se(Palmer and Filby, 1984; Raask, 1985). Th, Hf, Ta, and Ti are associated with the accessory minerals, rutile which is iron containing TiO_2. However, their behavior is quite different during combustion. Kauppinen and Pakkanen (1990) found that, for a boiler firing pulverized bituminous coal, 22% of Cu, 34% of Cd and 9% of Pb were in the submicron fine-mode ash particles, whereas only about 5% of Na, Fe, Mn and Zn were found in the fine-mode ash particles. Also in a pulverized coal utility boiler (Markowski, 1985), it was found that the submicron fume is enriched in volatile elements such as As, Sb, Se and Ga while the submicron fume is depleted in refractory elements such as Al, Sc, Th, La. Analysis(Mamane, et al., 1986) of individual fly ash particles revealed that Zn, As and Pb are uniformly distributed in fine ash particles from a power plant. It is also found that the amount of trace elements is also dependent on the density of the ash (Fuiichi, et al. 1987). The discrepancies between different results result partly from the different sampling methods and the operational conditions of different power stations.

In order to understand the mechanisms of vaporization and condensation of minerals constituents, well-controlled condition are desired. Quann et al. (1990, 1982a) studied

transformation of trace elements using a well-controlled drop-tube furnace. The main conclusions were: the volatile trace species are enriched in submicron ash particles; significant differences in both the amount and composition of submicron particles were found between coals, particularly between coals of different ranks; the detailed characterization of the occurrence and distribution of elements in coals is necessary for the understanding of their fate in combustion. By using thermochemical equilibrium modeling, it was found that, arsenic vapors reacts to form calcium arsenate during combustion of a high-calcium subbituminous coal, but condensed as arsenic oxide during combustion of a low-calcium bituminous coal(Bool and Helble, 1995).

However, iron, mainly in the form pyrite, is not vaporized as much as As, Sb, which are usually associated with pyrite. It is unknown whether the so-called volatile elements are released during pyrolysis or whether they are released during oxidation. On the other hand, elements such as Zn, Cr, which are considered to be incorporated in with silicates, vaporize at a rate which parallels silicon vaporization

Detailed examination for the fly ash particles from coal-fired power station shows that the so-called volatile trace elements are not only concentrated in the smaller ash particles, but also concentrated on the surface of residual ash particles(Stinespring and Stewart, 1981).

The mechanisms used to explain the phenomena of surface enrichment and enrichment in the fume are generally the condensation or surface reaction of vaporized elements on the pre-existing particles and the vaporization mechanism is due to the volatilization of trace elements during combustion. In addition, there is evidence that Ti exits as sub-submicron grains(Allen and VanderSander, 1984) in coal. Those fine grains may be emitted into submicron ash particles if they are not coalescenced with other minerals during combustion. However, only part of the Ti ends up in the submicron ash particles.

There are several postulates for the presence in the submicron particles of major elements. (1) Baxter(1992) postulates that much of inorganics are ejected with pyrolysis products during devolatilization; (2) Quann et al. (1982b) believe that, the refractory oxides are reduced to more volatile matters such as SiO, Mg by the char combustion product CO. The vaporization is controlled by the vapor pressure of the reduced species and their rate of diffusion within the char pores; (3) Neville(1982), Wendt(1996) and Lindner(1988) show that the net rate of vaporization is controlled in part by the capture of volatile species by reaction either as they diffuse out of a char particle or after they are released.

The extent to which the above postulates are applicable for the trace elements is being critically evaluated in this study. In other words, the objective of this research is to find the mechanism governing the vaporization of trace elements. To achieve this goal, four types of coal were segregated into two narrow size cuts with high density and low density. All those 16 coals were burned at the same conditions (20% O2 and 1700K). One type of coal was burned at four oxygen concentrations(10%,20%, 35% and 50% O_2). And all the coals were also devolatilized at about 2040K. By using the same coal with different density (accordingly different concentrations of trace elements), the relationship between the concentration and vaporization rate can be obtained. By burning the same coal at different oxygen concentrations, one can know the relation between the combustion temperature and the vaporization rate. By pyrolysis of the coal, the effect of devolatilization on the fate of trace elements can be evaluated. Furthermore, by comparing the results from combustion and pyrolysis experiments, one can know the effect of diffusion through the char pores and the effect of mineral coalescence on the char surface.

5.2 Behavior of Inorganic Matter During ASTM Devolatilization and Materials Balance

It is well known that volatile matter in coal is released during pyrolysis. Nothing is known about the fate of inorganic matter during pyrolysis, however. An ASTM standard pyrolysis procedure was performed to obtain the devolatilized char. Table 5-1 present the

inorganic material left in the char residue.

Table 5-1 Materials retained by char(wt %)

	Na	K	Ca	Sc	Cr	Fe	Co	Zn	As	Se
KYH90106 char	80.5	53.3	33.5	71.1	99.2	98.6	63.3	57.9	44.8	12.8
PTH90106 char	85.2	63.0	142	88.8	28.2	100.4	74.3	105	73.7	63.9

	Mo	Cd	Sb	Cs	La	Ce
KYH90106 char	40	22.4	64	64	71	93.7
PTH90106 char	256	2	81.9	76.7	93.2	135

Note: the volatile content for KYH90106 is 36.0 wt%, for PTH90106 is 36.1 wt%, which are comparable to the values determined by other persons'.

Some values are greater than 100, which are obviously due to the errors of the measurement. So those elements, Ca, Mo, and Ce will not be considered. It is to be expected that the recovery rate for Fe is almost 100%. Since the melting point of Fe is 1808K, much higher than the pyrolysis temperature(1163K), all Fe should be retained by the char. However, even though the pyrolysis temperature is higher than the boiling temperatures of K(1033), As(876), Se(958), Cd(1040),Cs(944), those elements were not vaporized completely. On the other hand, even though the melting points of Sc(1814), Cr(2130), Co(1768), La(1191), are higher than the pyrolysis temperature, significant fractions were devolatilized. As shown in Chapter 3, Cr (and probably also Sc, Co, and La) is organically bound to the coal matrix, K is associated with minerals such as illite, and As, Se, (probably Cd, Cs also) are combined with pyrite. The results of fraction of elements devolatilized clearly shows that the behavior of an element during pyrolysis(combustion) is also dependent upon its occurrence in the coal.

One test of the validity of the results was provided by a material balance on the ash constituents fed into the furnace and collected with the fly ash. As an example, Table 5-2 shows the material balance for some elements in Elkhorn/Hazard coal burned under the condition of a furnace temperature of 1700 K with 20% O_2.

Table 5-2 Material balance for Elkhorn/Hazard (KYH90106) coal

element	% recovered in submicron particles	% recovered in coarse particles	% recovered with all particles
Fe	6	81	87
As	58	25	83
Na	32	51	83
Cr	13	68	81
Co	36	24	60
Sb	39	24	63

Recall that recovery rate for Al_2O_3 powder is 85% as measured in Chapter 4. So the recovery rates for Fe, As, Na, and Cr are consistent with the ash recovery rate. And the recovery rate for Co and Sb are above 71%. Regarding to the uncertainty of the NAA method itself (the measurement error can be as high as $\pm$ 20%), the recovery rates for the elements are adequate.

Detailed calculations of elements balance are provided as Appendix B. While the elemental recovery rates under pyrolysis conditions are close to 100%, the recovery rates under combustion conditions are not. It can be seen that the recovery rates for Fe, Na, Sc, La, Sm are generally above 80%, but the recovery rates for Zn, Cr, Co, As, Se, Sb, the more volatile elements, are always small. Possible explanations for the low recovery rates include: (1) those volatile elements, once vaporized, do not re-condense on the pre-existing submicron particles due to the extremely dilute ash concentration in the gas stream; (2) some vaporized elements, for example As, can be easily reacted with other materials for example the aluminum wall of the furnace; (3) Measurements for Se, Co may not accurate because of their very long half life-times. Therefore, the uncollected fractions of the elements are believed to be in vapor phase or in very fine particle with size less than 0.04 microns which passed through the Teflon filter. Thus subtraction from the fraction presented in coarse ash particles gives total vaporized fraction of Cr, Co, As, Sb, Se. For the elements of Fe, Na, La, Sm, Sc , the fraction of an element presented in submicron char particles is the vaporization fraction.

5.3 Pyrolysis Study

There are three possible mechanisms by which trace elements leave a coal particle when heated at high temperature without oxygen: devolatilization, fragmentation and vaporization. Devolatilization denotes the formation of gaseous product directly from the coal structure; fragmentation includes breakup of char into several individual pieces, shedding of surface particles during combustion, and physical fracturing of individual inorganic mineral grains; and vaporization refers to the formation of a near-equilibrium gas partial pressure of a species over its condensed phase. Volatile, such as CO, CH_4 are released by devolatilization; while inorganic materials such as pyrite, rutile are transformed by fragmentation and vaporization, which includes ejection with pyrolysis products of fine-grained materials(Miller and Schobert, 1993). However, little is known about the volatilization of the volatile inorganic elements such as selenium (Se) and arsenic(As). The purpose of this study is to find the mechanism by which different elements are released during devolatilization, especially how different associations of elements determines the fate of devolatilization.

5.3.1 Experiment

Coal particles were fed into the pyrolysis furnace at the top using argon as a carrier gas. The temperature of the furnace was kept at about 2040 K. The residence time of the particles was about 0.225 seconds (Nenniger, 1986).The product char/soot samples were collected using a cascade impactor. The samples obtained were analyzed using Neutron Activation Analysis (NAA).

5.3.2 Results

It has been realized that the fractions collected in submicron char particles for As, Sb, Cr, Co, Se are not the total vaporized fraction. However for comparison, the values of fraction collected in submicron char particles are depicted and discussed as following.

From figure 5-1, it can be seen that, while the data is scattered, each type of coal has a approximately consistent vaporization fraction of iron. The Wyodak coal has the highest, while the Pittsburgh coal has the lowest. The submicron iron fume is believed to be formed by the fragmentation of pyrite(Raask, 1984; Miller and Schobert, 1993) and vaporization. The mechanism can be explained in terms of table 5-3, which shows that, the lower the pyrite content, the more the submicron iron fume. Other forms of iron include iron clay and jarosite. This shows that, iron clay and jarosite are easier to be fragmented. It can be seen that even though the pyrite particle size is quite different for the Pittsburgh coal and the Illinois coal, the amount of the submicron iron fume is almost the same. It was believed that bigger pyrite is easier to be fragmented. However, if the pyrite particle is bigger, then the total number of pyrite will be less. Those two factors cancel each other, thus the total amount of pyrite fragmented is not significantly affected by their sizes. It should be noted that the content of aluminum and silicon have negligible effect on the production of iron fume. This implies that during devolatilization, minerals are not coalesced significantly.

Table 5-3 Effect of Fe compositions on Fe devolatilization

	Wyodak	Elkhorn	Illinois	Pittsburgh
Fe in submicron fume(%)	14	9.2	5	4.1
pyrite in parent mineral(%)	0.9	6	29.8	18
Iron in pyrite (%)	38	58	97	97
in clay and jarosite/FeO_2H	62	42	3	3
pyrite with d > 20 μ (%)	not detected	14	20	73

Al in parent mineral (%)	23	27	11	19
Si in parent mineral (%)	63	51	42	44

* high density coal, with size between 90 to 106 microns

Figure 5-2 shows the effect of coal type on the production of Na fume. The average fraction of Na in submicron particles is 27%. Sodium is generally believed to be associated with other minerals, for example jarosite. How sodium is released at high temperature is unknown, however. One possible mechanism may be due to the breakup of bonds of Na with carboxylic acid groups for the ion exchange. And since the vapor pressure of Na is high , the vaporization rate should be high. Figure 5-2 shows that the Illinois coal has the highest fraction of Na in submicron particles, the Pittsburgh coal is second, while the Wyodak coal and the Elkhorn/Hazard coal have the lowest fraction in submicron particles. According to table 5-3, it can be seen that the more the (Al+Si), the less the amount of the Na in submicron particles. Therefore Na may be captured by aluminum silicates. This observation is consistent with the results by Gallagher et al. (1990).

Figure 5-3 shows the behavior of Cr during coal devolatilization. The average fraction of Cr collected in submicron char (soot) particles is about 25%. The occurrence of chromium is CrOOH associated with organics or in clays(illite) according to Chapter 3. If all Cr is in CrOOH, then all Cr will be vaporized. By contrast, if all Cr is in clays, then little Cr will be vaporized. The fraction of Cr in submicron particles probably reflects the fraction of Cr in the state of CrOOH.

Figure 5-4 shows the results for cobalt devolatilization. The average fraction of Co collected in submicron particles is 20% under this experimental condition. The occurrence of Co in coal is not specified. However, it is uniformly distributed within a given type of coal. Furthermore, the Pittsburgh coal, Illinois coal and the Wyodak coal all have the same content of Co (3 ppm), while the Elkhorn/Hazard coal has a higher

content of 6 ppm of Co. Since the boiling point of cobalt is 2900°C (Greenwood and Earnshaw, 1984), and the working temperature of the pyrolysis furnace is 2050K (1780C), the possible explanation for relatively high Co vaporization is that: Co is organically bound to other elements. When the coal is heated, cobalt is released like other volatiles.

Figure 5-5 shows the results for arsenic devolatilization. The average fraction of arsenic collected in submicron particles is 36%. Nearly all As is associated with pyrite in the form of As_2S_3-FeS_2 as determined in chapter 3. Under heating As_2S_3 decomposes as follows,

$$2\ As_2S_3 \text{ ------> } 3\ S_2 + 4\ As$$

At 2040K, the equilibrium vapor pressure is 4725 atm. If As_2S_3 is not associated with other refractory materials, all the As will be vaporized under this experimental condition. Since As_2S_3 is associated with pyrite, and under high temperature, pyrite is in liquid state, As_2S_3 is trapped in the melt of pyrite. Therefore the vaporization processes consists of a series of processes: the diffusion of As_2S_3 through the melt, vaporization of As_2S_3 on the melt surface and the diffusion of gaseous As through the char pores. A detailed model will be presented in section 5.4. It will be shown that the vaporization of As is basically controlled by the diffusion process within the melt.

Figure 5-6 shows the Se concentration in the coal on the total Se collected in submicron particles. The average fraction of Se in submicron particles for the Elkhorn/Hazard coal, Illinois coal and Pittsburgh coal is 20%, while the fraction is about 50% for the Wyodak coal. The most common compound for selenium is Se-S. It has been determined that most Se is associated with pyrite except for the Wyodak coal which has 100% organically bound Se. Selenium is basically as volatile as arsenic, however the fraction found in the submicron char particle is less than for arsenic. This again shows that the vaporization is controlled by the diffusion through the pyrite melt. In addition, the much lower vaporization rate of Wyodak coal may be due to different association of Se with other minerals and possible reaction with the alkali metals

5.3.3 Calculated results

The possible mechanisms for the formation of elements on submicron particles in inert gas at high temperature include: fragmentation such as pyrite, vaporization such as As and Se from pyrite melt, devolatilization or breakup of chemical bonds such as Cr, Co and Na. Equilibrium vapor pressures for pure substances are calculated for purposes of comparison. From the JANAF Thermochemical Tables(1985), at T=2040 K, for Fe, log K_f = -3.1875; for Cr, log K_f = -2.712; for Co, log K_f = -3.495, then the vapor pressure can be calculated using these equilibrium constants.. For Na, at T = 1100K, log K_f = -0.278, so P = $10^{-0.278}$ = 0.5272 atm. By looking at the enthalpy, H (T=2050K) - H(T=1100K) = 19.75 KJ/mol, then the vapor pressure at T = 2040K can be calculated from the Clausius-Clapeyron equation (Eq. (1)). For arsenic, from Greenwood and Earnshaw(1984), at T=1089K, p = 38.6 atm; from Hultgen et al.(1973)'s, at T = 1473 K, p = 500 atm. $\Delta H / R$ can be calculated using the Clausius-Clapeyron equation. Then the vapor pressure at T = 2050 K can be estimated. The total vapor pressure for Se at T = 1000K is 1.7 atm (Hultgen, et al. 1973), and the vapor pressure at T = 2040 K is estimated to be 771 atm at 2040 K. The equilibrium vapor pressures for pure substance and the fraction of elements produced in submicron char(soot) particles for PTH90106 coal are presented in Table 5-4.

$$\frac{\ln P_1 - \ln P_2}{\left(\frac{1}{T}\right)_1 - \left(\frac{1}{T}\right)_2} = -\frac{\Delta H}{R} \qquad (1)$$

where, the subscripts denote any two different states 1 and 2, P is the vapor pressure.

From this table, it can be easily seen that, while the equilibrium vapor pressures for pure substances differ by several orders of magnitude, the fractions of the elements found in the submicron particles are of the same order of magnitude. This shows that it is not only the vapor pressures of elements that controls vaporization during pyrolysis. A comprehensive model was developed to explain and predict the vaporization process for

As in the next section, while for the refractory trace metals Cr and Co, a devolatilization model like the pyrolysis model for volatile gases was developed to explain and predict the dissociation of (weak) chemical bonds between the metal and the organic matrix. Once the metals dissociate from their original composition, they are expelled with the volatile matter(Gat, et al., 1984).

Table 5-4 Equilibrium vapor pressures for pure substances

	Fe	Na	Cr	Co	As	Se
melting point(K)	1808	371	1173	1765	1089	490
boiling point(K)	3023	1154	2963	3373	888	958
Vapor pressure at 1473 K (atm)	8.3e-8	1.038	3.31e-7	3e-8	500	68
Vapor pressure at 2040K(atm)	6.5e-4	1.435	1.94e-3	3.2e-4	4725	771
Total Fractions of elements vaporized*	4.1 %	32 %	35%	26%	36%	>90%

* Note: from subtraction of coarse char particles for the elements of Cr, Co, As, Se

5.3.4 Conclusions

One can draw the following conclusions from the preceding sections: (1) Under the same pyrolysis conditions, the fraction in submicron particles are the same for the same coal. There is little dependence upon the particle sizes or the ash content; (2) The greatest

factor determining ash vaporization is the temperature of the particle during pyrolysis; (3) when arsenic and selenium are associated with pyrite in the parent coal, their release during pyrolysis is composed of a series of processes; (4) The release of weakly bonded elements, such as Na, Cr, Co, is due to the break-up of the chemical bonds, which is similar to the release of volatile matter during pyrolysis.

5.4 Combustion Study

It is already known that the fate of trace element is determined by its association with minerals. For example, if the trace element is atomically dispersed in the organic matrix and does not interact with minerals, then all the trace element should be carried away as the carbon burns out. No research so far shows such experimental observations. Thus there should be associations or interactions between trace elements and minerals during coal combustion. If the combustion temperature of the coal particle is the same as that in the pyrolysis experiment, then the difference between combustion and pyrolysis is that the carbon is burnt out during combustion, while the carbon remains during pyrolysis. Thus there will be more vapor diffusion resistance in the pyrolysis experiment as well as a different gaseous environment. By normalizing the combustion conditions for temperature and time, the importance of these parameters can be determined.

5.4.1 Experimental procedures

The experiments were carried out in a laminar flow furnace as described in Chapter 2. The well characterized coal was fed into the furnace using argon as carrier gas. The temperature of the furnace was kept at 1700K. The oxygen concentration in the bulk gas in the furnace was 20%. For the coal of PTH90106, oxygen concentrations of 10%, 35% and 50% were also used. While the residence time in this oxidation furnace is about 0.33 seconds(Sarofim and Zeng, 1995), the particles flow along the center line and are not completely burnt out if the oxygen is depleted locally. However, the actual reaction time is calculated to be much less than 0.3 s under

the combustion condition in this study. The ash samples were analyzed using the Neutron Activation Analyzer (NAA) at MIT and XAFS by the University of Kentucky.

5.4.2 Results

A similar study was performed by Quann et al. (1990), which provides interesting trends on the extent of the vaporization and condensation of different elements. But the detailed mineral characterization was not available in that study. In this study, the data (fractions of elements presented in submicron ash particles) are compared with those results of Quann et al.(1990). As pointed out in Section 5.2, the fraction of As, Cr, Co, Sb, Se, Zn collected in submicron ash is not the total fraction vaporized. Nevertheless the comparison can provide us the confidence to the experiment and useful information for obtaining mechanisms.

5.4.2.1 Results for the all four selected coals under the same combustion condition

The results for selected elements are presented below. For each element, the data on the amount of the element collected in the submicron aerosol is plotted on the ordinate, and the amount of the element in the coals plotted on the abscissa. A least mean square line fitted through the data gives an average measure of the fraction of the element in the coal that is vaporized and recondensed.

Arsenic:

The results are all fitted by the same line with modest scatter (Figure 5-7). The fraction is 40%. The points that depart significantly from the correlation are the low rank coals (MS, MR, WY). In Quann et al.'s paper, it was postulated that in these coals there is opportunity for the vaporized arsenic to react with calcium oxide in the residual fly ash, thus reducing the amount that condenses in the submicron aerosol. However, in present study the low rank coal - Wyodak coal shows the highest fraction in the submicron

particles. The calculation in the following section shows that the combustion temperature for the Illinois coal, Pittsburgh coal and the Elkhorn/Hazard coal are almost the same, while the combustion temperature for the Wyodak coal in this study is higher than those for the other 3 coals. From this figure, it can be inferred that, the vaporization rate is proportional to the As concentration, because while the concentration of As in samples tested are different, the fractions in the submicron ash particles are the same. The particle size has a small effect on vaporization. The effect of coal type can be attributed to their different combustion temperature under the same conditions and probably the association with coal. Because while the equilibrium vapor pressure of arsenic is very high under the current combustion condition, a significant amount of arsenic exists in coarse particles.

Zinc:

The data in Quann et al.'s paper(1990) (Figure 5-8) were correlated with two lines (fractional vaporization of 6% and 26%), one for the low rank and the other for the high rank coals. The data in the present study show the interesting anomaly that the result for the Elkhorn / Hazard coal (namely, KY) are more consistent with the low rank coals in Quann et al.'s study(1990) than the bituminous coal. There is also an interesting size dependence of the vaporization of the zinc in the density fraction of the Illinois coal. This difference may be due to the different occurrences of Zn in different coals. In some coal, Zn is mainly in ZnS, while for other coals, Zn is mainly organically associated.

Iron:

The data for iron (Figure 5-9) show a smaller vaporization than arsenic and zinc, with a fractional vaporization of between 2% and 20% for different coals. The points lying above the line are the low rank coals from Quann et al.(1990) and the Wyodak coal and the Elkhorn / Hazard (KY) coal from the present study. Again, the Elkhorn / Hazard coal shows a resemblance to low rank coals instead to the high rank coal. The iron fraction in

submicron ash particles for the Wyodak coal and Elkhorn/Hazard coal is higher than that for the Illinois coal and the Pittsburgh coal. This again is the same tendency as for the pyrolysis experiments.

Chromium:

The data show considerable scatter (Figure 5-10). Recall that, the data for the pyrolysis experiment also show scatter. Insights on the cause for this scatter may be obtained from the differences seen with changing density for the 45/63 micron fractions for the Illinois No.6 (IL), Pittsburgh (PT), and Elkhorn / Hazard (KY) coals. Since the boiling point of metallic Cr is 2963K, and the particle temperature in this study is generally lower than 2900K, the fraction of Cr in submicron ash particles is not from the vaporization of metallic Cr. As shown in Chapter 3, much of Cr is bound in the form of COOCr. Thus when the coal is heated, the weakly bounded Cr can be volatilized.

Sodium:

For the present coals, the Pittsburgh coal shows a lower vaporization than the Elkhorn / Hazard (KY), Illinois No.6, and Wyodak coals (Figure 5- 11). There is also considerable scatter in the results of Quann et al., which may be caused by the same inter-coal differences. One possible explanation for these differences may be difference in the extent of reaction between sodium and silica in the different coals(Kang et al., 1990). If this were the case, then the vaporization of the sodium for the low rank coals should be higher than those for the higher rank coals. This seems to be the case, as observable amount of sodium is associated with silica mineral inclusions only in Pittsburgh coal by CCSEM results.

Vanadium:

In Figure 5-12, the vanadium concentration in the coals are compared to the amount appearing in the submicron ash particles. A good correlation of this type exists for bituminous coals, with an average fraction of 13% appearing in the submicron fraction. The values for the low rank coal are scattered. It is generally believed that the part of vanadium is associated with aluminum-silicates, while the rest may be organically bound in the coal matrix. Therefore the fraction appearing in the fume reflects the vaporization extent by the organically bound vanadium.

5.4.2.2 Results for the PTH90106 coal with different O_2 concentrations

From the above results for combustion, one can see that: (1) the effects of coal size is minor, if not negligible, while the vaporization rate is proportional to the concentration of the elements or the coal density; (2) the effects of coal type and the association of elements with other minerals are important. The effect of coal type is mainly due to their different combustion temperatures under the same combustion condition. In order to investigate the effect of combustion temperature, the PTH90106 coal, namely, the Pittsburgh coal in the high density cut, with size between 90 and 106 microns, was burned at the same furnace temperature of 1700K and with different bulk oxygen concentrations of 10%, 20%, 35% and 50%. The results are presented in Figure 5-13. Note that, the residence time for the pyrolysis furnace is longer than that in the oxidation furnace.

Figure 5-13 illustrates the fractions of the selected elements that are found as submicron particles(Fe, Zn, Na) and the fractions retained in coarse particles(As, Se, Cr, Co) at different pyrolysis temperatures and oxygen concentrations. It can be seen that the fractions in submicron particles(coarse particles) increase(decrease) with oxygen content or combustion temperature exponentially. The experimental data for 50% O_2 are close to that of Quann et al. (1982a). Except for that a very small amount of carbon converted into soot, all the carbon should be burnt out for 35% and 50% O_2. If any mineral or element exists in the coal

only in the organically- bound form, then it will vaporize with a high efficiency if no interaction occurs with the residual ash. The experimental data show that with the exception of Zn at 35% and 50% O_2, only portions of the elements , As, Na, Fe, Cr, Co, Se, are found in the submicron fume. In Chapter 3, it has been shown that elements do exist in the coal independently, some elements in minerals, as Fe, As, Se in pyrite; some elements in matrix or organic state, as Cr, Co, Ti, some in compounds as Na. Experimental data strongly show that interactions between minerals take place during coal combustion.

Elements with high boiling temperatures, also interact with other minerals, mainly aluminum silicates, and show low extents of vaporization. Therefore there are competitive processes for element vaporization and diffusion out of the char and capture by major minerals. The experimental data show that as combustion temperature increases, vaporization takes precedence over the coalescence process.

For the elements with high vapor pressure, such as Na, As and Se, the higher combustion temperatures facilitate the vaporization in two ways: the diffusivity within the melt is enhanced; and the vapor pressure increases.

In summary, (1) the occurrences of elements determine their fates during coal combustion; (2) at a fixed temperature the vaporization rate of an element is proportional to its concentration; (3) the vaporization rate is a function of combustion temperature.

5.4.3 Char combustion calculation

Based upon above experiments, two types of models were set up for trace elements: one for the elements such as Na, As and Se which are included in low concentrations in an inorganic matrix such as pyrites or silicates, the other for elements such as Cr, Co, which are assumed to be organically bound to the char. The first step in a model is to calculate the coal particle temperature. The calculation in this section is basically from

Larry Bool's thesis (1993), with some modification.

The fate of elements during coal combustion is basically determined by the rate of char oxidation which determines char combustion temperature. The char reaction rate used here, Equation (2), was taken from Bool's thesis. According to this equation, the global char combustion rate is a function of char external surface area (SA_{char}), oxygen partial pressure (P_{O2s}), and the char particle temperature (T_p):

$$\frac{d(CHAR)}{dt} = -A_0 \exp(\frac{-E}{RT_p}) SA_{char} (P_{O2s})^{1/2} \quad \text{[kg/s]} \tag{2}$$

Where, the pre-frequency constant A_0 and the activation energy E are global constant and were fitted empirically. They are a function of the coal carbon content. Here the activation energy E was modified as that in Equation (3):

$$E = -0.02487 + 1.486 * 10^{-3} \text{ (wt \%C \_ash and moisture free)} \quad \text{kJ/kmol} \tag{3}$$

the pre-frequency A_0 is determined from Equation (4):

$$A_0 = \frac{1}{\sqrt{98100}} \exp(28 - 0.758(wt\%C) + \frac{E}{R \bullet 1750}) \qquad \text{kg/(m}^2\text{.s.Pa}^{0.5}\text{)} \tag{4}$$

It should be noted that in Bool's thesis, it was found that lower rank coals burned in the diffusion controlled regime. And this effect had already been taken into account during the derivation of the parameters in above equations. Therefore, the global rate equation (2) allows the lower rank coal to burn faster than the bituminous coals. It was also assumed that the coals do not swell or shrink appreciably as the char in burned away (constant density), and that the combustion product is CO. Four limiting treatments of the CO are: (1) no oxidation (frozen flame); (2) infinitely thin flame so that no oxygen penetrates to the char surface; (3) the CO oxidation is at the char particle, thus all the heat release by CO oxidation is imparted to the char particle, equivalent to having an oxidation product of CO_2;(4) an finite oxidation rate of CO, with part of the heat released by CO imparted to the char particle(Makino and Law, 1986; Zeng and Fu, 1996). In Bool's study, the oxygen concentration is calculated using approach 3, but the heat release is assumed to be from $C+1/2O_2 \rightarrow CO$. Obviously, the fourth approach is the most appropriate. However, it is very complicated. Therefore, the first approach is used here. The

convection heat transfer coefficient and mass transfer coefficient between the coal particle and the surrounding gases can be calculated from:

$$Nu = \frac{hd_p}{K} = 2 + 0.43\,\mathrm{Re}^{0.8}\,\mathrm{Pr}^{0.4} = 2 \tag{5}$$

for the limiting case of negligible slit between particle and gas. Where h is the convection heat transfer coefficient (w/m^2sK), d_p is the particle size, K is the thermal conductivity of the gases surrounding the particle. And the mass transfer coefficient can be calculated from:

$$Sh = \frac{h_m d_p}{\rho D} = 2 + 0.43\,\mathrm{Re}^{0.8}\,Sc^{0.4} = 2 \tag{6}$$

where h_m is the mass transfer coefficient (kg/m^2s), ρ is the density of the gases surrounding the particle(kg/m^3), D is the diffusive coefficient of the oxygen(m^2/s). With the assumption of frozen flame, the oxygen which penetrates to the particle is consumed by the char oxidation:

$$C + \frac{1}{2}O_2 \rightarrow CO$$

Therefore,

$$h_m(x_{o2,\infty} - x_{02,s}) = \frac{16}{12}\frac{d(CHAR)}{dt} \tag{7}$$

where, $x_{o2,\infty}$ is the mass fraction of oxygen in bulk gases, $x_{o2,s}$ is the mass fraction of oxygen at char surface. By substituting the expression for $\frac{d(CHAR)}{dt}$ into the above equation, one can obtain:

$$\frac{D}{r_c}\frac{P_{o2,\infty} - P_{o2,s}}{RT_m} = \frac{A_0}{24}\exp(\frac{-E}{RT_p})\,P_{o2,s}^{1/2} \tag{8}$$

where, T_m is the average temperature of particle T_p and gas temperature T_g. From this equation, one can solve for the oxygen partial pressure,

$$P_{o2,s} = \left(\frac{1}{2A}\left(-B + \sqrt{B^2 - 4AC}\right)\right)^2 [Pa] \tag{9}$$

where,

$$A = \frac{24D}{r_c R T_m} \quad [\text{kg/(m}^2\text{sPa)}]$$

$$B = A_0 \exp\left(\frac{-E}{RT_p}\right) \quad [\text{kg/(m}^2\text{sPa}^{1/2}\text{)}]$$

$$C = -A\ P_{o2,\infty} \qquad [\text{kg/(m}^2\text{s)}] \tag{10}$$

The diffusion coefficient D is calculated from Jorgensen's paper (1981) with a reference temperature of T_{ref} = 1800 K:

$$D = 4.26\left(\frac{T_p + T_g}{2T_{ref}}\right)^{1.75} \quad [\text{cm}^2/\text{s}] \tag{11}$$

Taking into account conduction, radiation and reaction terms for the char burnout, the energy balance for the particle is:

$$\frac{dT_p}{dt} = \frac{SA_{char}(h(T_g - T_p) + \varepsilon\sigma(T_w^4 - T_p^4)) + \Delta H_c \frac{d(CHAR)}{dt}}{C_p m_{char}} \tag{12}$$

where T_w is the wall temperature of the furnace. Correlation for the heat of the reaction heat ΔH_c, the specific heat capacity C_p and the particle emissivity ε were given from Gallagher's thesis(1992). σ is the Stefan-Boltzmann constant. Other parameters in the equation are given as:

$$\Delta H_c = \frac{1}{12}\left(106462 + 3.4332T_p + 0.00126T_p^2 + \frac{891788}{T_p}\right) \quad [\text{kJ/kg}] \tag{13}$$

$$C_p = \frac{1}{12}\left(16.873 + 0.004773T_p - \frac{854107.2}{T_p^2}\right) \qquad [\text{kJ/kg K}] \tag{14}$$

$$T_w = T_g + 50[K]; \varepsilon = 0.8; \sigma = 5.67 \times 10^{-8}[\frac{w}{m^2 K^4}]$$

From, Equation (5), and combined with the conductivity of the air with a reference temperature of T_{ref}, the heat transfer coefficient h can be calculated from:

$$h = \frac{0.0242[\frac{W}{mK}]}{r_p[m]}\left(\frac{T_g + T_p}{2T_{ref}}\right)^{0.75} \tag{15}$$

The gas temperature is assumed to increase linearly from 700K to 1700 K in 0.08 seconds (Kang, 1991), i.e.,

$$T_g = 700 + \frac{1700 - 700}{0.08} t \quad [K] \qquad \text{when } t \le 0.08 \text{ second}$$

$$T_g = 1700 \ [K] \qquad \text{when } t \ge 0.08 \text{ second} \tag{16}$$

Figure 5-14 shows the calculated temperature history for the ILL4563 coal at a furnace temperature of 1100K with a 20% bulk oxygen concentration together with the experimental measurement. The calculated curve with A_0 calculated from equation(4) shows a lower temperature than the experiment. However, if the pre-frequency factor is adjusted to $A'_0=1.15\ A_0$, the prediction agrees well with the experiment. The reason for this may be due to the limitation of the fitting for the kinetic parameters in Hurt and Mitchell's paper(1994). In their paper the bulk gas temperature was about 1750K. The calculated temperature history for the PTH90106 coal at a furnace temperature of 1500K with a bulk oxygen concentration of 20% together with the experimental measurement data are shown in Figure 5-15. It can be seen that the calculation agrees fairly with the experiment, though the prediction is a little bit low than the experiment. Since the furnace temperature of this study is 1700K (within the Hurt's scope), the confidence for particle temperature prediction is thus set up.

Calculated temperature histories for the PTH90106 coal at a furnace temperature of 1700K with different bulk oxygen concentrations are presented in Figure 5-16. Also presented is the temperature history for the pyrolysis at a temperature of 2040K. The calculated peak temperatures for other coals are presented in Table 5-5. Note that since we assume that there is no slip between particles and their surrounding gas, the smaller particles have higher rate of convection heat transfer, and the coal particles with smaller sizes burn at lower temperatures than the larger particles.

Table 5-5 Calculated combustion temperatures and time for the four program coals

Coal type	Illinois		Pittsburgh		Elkhorn		Wyodak		PTH90106	
radius (μm)	27	49	27	49	27	49	27	49	35%	50%O_2
peak temperature(K)	2230	2230	2150	2190	2170	2200	2310	2330	2660	2960
average temperature(K)	2200	2200	2110	2180	2140	2190	2280	2300	2610	2880
time (ms)	50	180	70	190	65	185	40	160	80	60

Note:Combustion conditions are with 20% O_2,1700K; for PTH90106 coal with 35% and 50% O_2

5.4.4 Modeling the vaporization of arsenic in Pittsburgh, Illinois, and Elkhorn/Hazard coals

From above discussions and results, it is already known that arsenic is associated or embedded with pyrite; at particle combustion temperatures, the pyrite(FeS_2) becomes pyrrhotite (FeS), which is in liquid state or is a melt. Thus it is assumed that all the arsenic is atomically dispersed or dissolved in the liquid pyrrhotite(melt). It is known that when the char is burnt out, a part of the melt carried to the char surface will coalescence with aluminum silicates to form iron glass. In this case, the trace element will diffuse into the glass, which further dilutes the concentration of the element. Vaporization of trace elements from glass is not well characterized, however. For simplicity, the effect by the coalescence and sintering of iron with aluminum silicates is neglected. A comprehensive model is developed in this section based upon Ohno's work(1991).

5.4.4.1 Theory

A. Thermodynamics considerations

To have an understanding of the kinetics of vaporization of trace elements from a liquid melt, one needs to have information on the vapor pressures of constituent gas species above the

melt. However, little if no data are available on vapor pressures of elements above their dilute solutions in liquid pyrrhotite or iron glass. Nevertheless, vapor pressure of pure elements are more or less known, and a comparison of their values at temperatures of interest can be used as a rough guide in determining those elements which should exhibit preferential vaporization. As a first approximation, dissolved elements with higher vapor pressure can be expected to vaporize preferentially.

Once the vapor pressure of the pure elements, P_i^0, is known, then the equilibrium partial pressure of the element in the melt can be calculated, provided its activity coefficient is known:

$$P_i^e = P_i^0 \gamma_i Y_i \quad \text{[Pa]} \tag{17}$$

where, P_i^e is the equilibrium vapor pressure of solute i ; γ_i is Raoultian activity coefficient of solute i in an infinitely dilute solution; Y_i is the mole fraction of solute i in melt.

However, since solute vapor pressure for one element or component, may be dependent on the presence and amounts of other dissolved elements, vapor pressure based upon binary solution data does not precisely represent the case for a component's separation from a multi-component solution.

A parameter, relative volatility, α, is used to compare the vapor pressure of one pure substance with another. For solute vaporization from metal baths, the coefficient has been defined(Olette, 1961). In this study, the melt is FeS, so α is defined as:

$$\alpha = \frac{\gamma_i}{\gamma_{FeS}} \left(\frac{P_i^0}{P_{FeS}^0} \right) \tag{18}$$

In a dilute solution. the solvent (FeS) follows Raoult's law and hence, γ_{FeS} is unity. Also, the solute i at sufficiently low concentrations will follow Henry's law. Neglecting solute-solute interactions, the activity coefficient, γ_i, can be taken equal to γ_i^0. Then α becomes:

$$\alpha = \gamma_i^0 \frac{P_i^0}{P_{FeS}^0} \tag{19}$$

Values of α can be calculated for elements at different temperatures using the thermodynamic data and are reported in Table 5-6. In the calculation, γ_i^0 in the FeS melt was estimated indirectly. The activity of As in liquid Cu is 0.006 (Lynch, 1980). Lau et al. (1983) found that

$$\gamma^0(\text{As in melt of Fe - S - Cu}) = 4.1\ \gamma^0(\text{As in Cu})$$

Thus in this study, the activity of As in melt of Fe-S is taken to be that in melt of Fe-S-Cu ($\gamma^0 = 0.0246$) . If α is unity or near unity, no preferential separation is possible, as the concentration of the two components in the vapor will tend to be the same as in the condensed phase. Substances that can be readily separated have large or small values of α .

Table 5-6 Calculated relative volatility

T (K)	1470	2040	2250	2500	2750
P_{As}^0 (atm)	500	4725	7865	13262	20335
P_{FeS}^0 (atm)	1.06×10^{-6}	1.15×10^{-3}	4.3×10^{-3}	0.016	0.046
α	1.16×10^{7}	1.01×10^{5}	4.5×10^{4}	2.04×10^{4}	1.09×10^{4}

B. Overall rate

It has already been shown that the vaporization rate of an element is proportional to its concentration in the coal and in pyrite. Therefore, the overall mass transport rate can be described as:

$$J_i = K\frac{S}{V}C_i^b \quad [\text{mole/m}^3\text{s}] \tag{20}$$

where, K, [m/s], is the overall rate constant; S, [m^2], is the total surface area of the melt; V, [m^3], is the total volume of the melt; C_i^b, [mole/m^3], is the bulk concentration of solute i in melt. At low molar concentrations,

$$-\frac{dX_i}{dt} = K\frac{A}{V}X_i \tag{21}$$

where, X_i is the weight percent of solute i. Integrating above equation, one can obtain:

$$\ln\left(\frac{X_i}{X_{i,0}}\right) = -K\frac{S}{V}(t - t_0) \tag{22}$$

The overall rate constant, K, can be calculated from the slope of the curve resulting from a plot of $\ln\left(\frac{X_i}{X_{i,0}}\right)$ versus time.

One can compute K from three limiting steps for the transfer of atoms of trace elements from the bulk liquid melt to a condenser surface (Figure 5-17). These are:

(i) transport of molecules or atoms through the bulk liquid to the melt/gas interface,

(ii) vaporization,

(iii) transport of molecules/atoms through the pores of the char to the atmosphere,

(iv) transport through the boundary layer surrounding the char particle.

The overall mass transfer coefficient, K, will be a function of the liquid phase mass transport, K_L, the vaporization rate, K_E, the gas phase mass transfer coefficient, K_G. The mass transfer through the external boundary layer is neglected when the internal resistance is controlling in this study. Liquid phase mass transport can be estimated with reasonable accuracy from the diffusion. Mass transport through the char pores can be estimated from Quann and Sarofim (1982).

B.1. Transport from interface to gas at melt surface for one inclusion or melt particle

For mineral inclusions which are of the same order magnitude or smaller than the mean free path of the molecules, a resistance by vaporization must be considered. Using the kinetic theory of gases, Langmuir derived an expression for the maximum vaporization rate of a solute from a fluid surface subjected to a high vacuum:

$$J_{i,vap} = \frac{\alpha^{\cdot} P_i^e}{\sqrt{2\pi RTM_i}} \quad [\text{mole}/(\text{m}^2\,\text{s})] \tag{23}$$

where, $\alpha^{\cdot}$ -recondensation coefficient can generally be taken as unity for liquids. For the case of dilute solutes, the equilibrium partial pressure above the melt surface, P_i^e, is related to the equilibrium vapor pressure for pure liquid, i, at the same temperature by:

$$P_i^e = P_i^0 \gamma_i Y_i^{\bullet} \tag{24}$$

where,

$$Y_i^{\bullet} = \frac{M_{FeS}}{\rho_{FeS}} C_i^{\bullet} \tag{25}$$

$Y_i^{\bullet}$ is the mole fraction of solute i at interface; $C_i^{\bullet}$, [mole/m^3], is the surface mole concentration of solute i. The maximum molar flux of i can be obtained by substituting Eqs. (25) and (24) into Eq. (23):

$$J_{i,vap} = \frac{P_i^0 \gamma_i M_{FeS}}{\rho_{FeS}\sqrt{2\pi RTM_i}} C_i^{\bullet} \tag{26}$$

or

$$J_{i,vap} = K_E C_i^{\bullet} \tag{27}$$

where

$$K_E = \frac{P_i^0 \gamma_i M_{FeS}}{\rho_{FeS}\sqrt{2\pi RTM_i}} \quad [\text{m/s}] \tag{28}$$

Eqs. (23) to (28) are valid only for the case of high vacuum. When a high vacuum above the melt is not applied, the partial vapor pressure of the element just above the melt will not equal to zero, and the solute's rate of vaporization from the melt surface will be less than its maximum limiting value. Under this circumstance, the vaporization rate is given by the Langmuir-Knudsen equation(Richards, 1974):

$$J_{i,vap} = \frac{(P_i^e - P_i^*)}{\sqrt{2\pi RTM_i}} \tag{29}$$

where P_i^* is the partial pressure of solute i on the interface.

B.2. Transport of vapor from melt surfaces to bulk atmosphere for a whole char particle

The transport of vapor from melt surface to bulk atmosphere has been solved by Quann and Sarofim (1982). The result is:

$$V_c = \eta N_I 4\pi r_i D_i C Y_i^* \qquad \text{[mole/s]} \tag{30}$$

where, $\eta = \frac{3}{\phi}\left(\frac{1}{\tanh\phi} - \frac{1}{\phi}\right) \bullet \left[1 + \frac{D_i}{\beta D_{oxy}}\left(\frac{\phi}{\tanh\phi} - 1\right)\right]^{-1}$, $\qquad \phi = (3\theta)^{1/2}\frac{r_p}{r_i}$

$$\beta = \left[1 - \exp\left(-\frac{D_{oxy}}{D_m}\ln(1 + x_{oxy}^b)\right)\right]^{-1} \ln(1 + x_{oxy}^b)$$

D_i, effective Knudsen diffusivity;

D_{oxy}, oxygen diffusivity in bulk gas; D_m , diffusivity of element i in bulk gas

x_{oxy}^b , mole fraction of O_2 in bulk gas

$N_I = \theta\left(\frac{r_p}{r_i}\right)^3$, number of inclusion(melt) of FeS (or FeS_2) in one char particle

θ , volume fraction of inclusion(melt)

r_p , [m], char particle radius, calculated from section 5.3.3; r_i , [m], inclusion(melt) radius

Y_i^* , mole fraction of vapor i at inclusion (melt) surface

C, [mole/m^3], concentration of gases

Since, $CY_i^* = \frac{P_i^*}{RT}$, one can obtain:

$$V_c = \eta N_l 4\pi r_i D_i \frac{P_i^*}{RT} \tag{31}$$

B.3. Transport from liquid to interface within a melt particle

The molar flux of element i during transfer of the solute atoms through the metal to the metal-gas interface is expressed as:

$$J_{i,vap} = K_L (C_i^b - C_i^*) \tag{32}$$

where, K_L, [m/s], is the mass transfer coefficient within the melt. It is generally obtained by the Machlin model (Machlin, 1960). The Machlin model assumes that the melt adjacent to the gas-melt interface moves as a "rigid body", and hence vaporization of solute atoms are transferred only by diffusion from the melt at the interface. Thus, in this study, the conception of diffusion is adopted. Instead of using the Machlin expression, a first order approximation as derived in Lynch's paper (1980) is used here:

$$J_{i,vap} = \frac{1}{r_i} D_{l,i} (C_i^b - C_i^*) \tag{33}$$

Therefore,

$$K_L = \frac{1}{r_i} D_{l,i} \quad [m/s] \tag{34}$$

where, it is known that the melt diffusion coefficient can be expressed as(Harris, 1984):

$$D_{l,i} = D_0 \exp(-\frac{E_D}{RT}) \tag{35}$$

where, D_0 [m^2/s], and E_D [J/mole.K], are constants to be determined. Note that, $J_{i,vap}$ can be converted to total vaporization rate by multiplying $4\pi r_i^2 N_l$. By combination of Eqs.(29) and (31), one can obtain:

$$P_i^* = J_i (\sqrt{2\pi RTM_i} + \frac{r_i RT}{\eta D_i}) \tag{36}$$

For dilute solutions, the equilibrium pressure for solute element i is given by:

$$P_i^s = P_i^0 \gamma_i \frac{M_{FeS}}{\rho_{FeS}} C_i^* \tag{37}$$

Substituting Eq.(37) into Eq.(36), one obtains:

$$C_i^* = J_i \left(\frac{\rho_{FeS} \sqrt{2\pi RT \overline{M_i}}}{P_i^0 \gamma_i M_{FeS}} + \frac{\rho_{FeS} r_i RT}{P_i^0 \gamma_i M_{FeS} \eta D_i} \right) \tag{38}$$

Combining Eqs.(38) and (33) to eliminate C_i^* yields:

$$J_i = \frac{C_i^0}{\left(\frac{1}{K_L} + \frac{1}{K_E} + \frac{\rho_{FeS} r_i RT}{P_i^0 \gamma_i M_{FeS} \eta D_i} \right)} \tag{39}$$

Defining K_U as:

$$K_U = \frac{P_i^0 \gamma_i M_{FeS} \eta D_i}{\rho_{FeS} r_i RT} \quad \text{[m/s]} \tag{40}$$

Recalling that:

$$K_L = \frac{1}{r_i} D_0 \exp\left(\frac{-E_D}{RT} \right)$$

$$K_E = \frac{P_i^0 \gamma_i M_{FeS}}{\rho_{FeS} \sqrt{2\pi RTM_i}}$$

Then the overall mass transfer coefficient is:

$$\frac{1}{K} = \frac{1}{K_L} + \frac{1}{K_E} + \frac{1}{K_U} \tag{41}$$

5.4.4.2 Results

In the calculation for the PTH90106 coal, the following parameters are used:

$r_p = 49\,\mu m$, $r_i = 4\ \mu m$, $\theta = 3.7\%$ (pyrite fraction in coal), $\rho_{FeS} = 5000$ kg/m^3

$D_i = 5 \times 10^{-7}$ m^2/s

Results for the transport coefficients for the PTH90106 coal are presented in table 5-7. K_L is calculated from K, K_E and K_U. Form the table, it is clearly that, $K_E >> K_U >> K_L$ in the

considered temperature range. In other words, the vaporization process is controlled by the diffusion within the melt. And since :

$$K_L = \frac{1}{r_i} D_0 \exp\left(\frac{-E_D}{RT}\right)$$

Table 5-7 Calculated results for the transport coefficients of As in pyrite

	Pyrolysis	20%O_2	35%O_2	50%O_2
Temperature(K)	2040	2180	2610	2880
K (m/s)	$.035 \times 10^{-4}$	$.17 \times 10^{-4}$	$.64 \times 10^{-4}$	1.103×10^{-4}
K_E (m/s)	2.29	3.13	1.91	4.66
K_U (m/s)	8.25×10^{-4}	9.85×10^{-4}	2.26×10^{-3}	2.61×10^{-3}
K_L (ms/)	$.0351 \times 10^{-4}$	$.173 \times 10^{-4}$	$.66 \times 10^{-4}$	1.15×10^{-4}

Data in Table 5-7 combined with Fig. 5-18 can be used to derive the following values for the constants D_0 and E_D:

$E_D/R = 13600K$, $D_0/r_i = 0.0105$ m/s

Eq.(22) can be used to predict the vaporization rate of arsenic for other types of coal. The predicted results and the experimental data are compared in Figure 5-19. They agree with each other. In the same way, the fate of other elements associated with pyrite, for example selenium, nickel, copper, antimony can be explained and predicted.

5.4.5 Modeling for vaporization of antimony (Sb)

The vaporization of antimony can be calculated with the same approach in Section 5.4.4, Again the activity of Sb in pyrrhotite melt is not available. However, the activity of Sb in liquid can be found from Sigworth and Elliott's paper (1974): $\gamma^0 = 0.014$. Using the same argument of Lau et al. (1983): γ^0(As in melt of Fe-S-Cu)=4.1 γ^0 (As in Cu), we have γ^0(Sb in Fe-S) = $4.1 \times 0.014 = 0.057$. Results for the transport coefficients for the PTH90106 coal are presented in Table 5-8. From this table, it can be seen that, at low temperature(1550K), the diffusivity through the pore is comparable to the diffusivity through the melt, and phase change also play a role in determining the vaporization rate. At high temperatures, the vaporization rate of Sb is controlled by transport in the melt.

Table 5-8 Calculated results for the transport coefficients (Sb)

	pyrolysis	20% O_2	35%O_2	50%O_2
particle temp.(K)	1553	2180	2610	2880
time (s)	0.29(Nenniger)	0.19 (Calcu.)	0.08(Calcu.)	0.06(calcu.)
fraction retained	0.91	0.16	0.09	0.04
P_{sb}^0 (Harris,1984),Pa	221.27	40928	33962	928491
K (m/s)	$0.466x10^{-6}$	$12.861x10^{-6}$	$40.134x10^{-6}$	$71.532x10^{-6}$
K_E(m/s)	$70.61x10^{-6}$	0.011	0.084	0.2174
K_U(m/s)	$6.488x10^{-6}$	$207.9x10^{-6}$	$1441x10^{-6}$	$3570x10^{-6}$
K_L(m/s)	$0.502x10^{-6}$	$13.708x10^{-6}$	$40.283x10^{-6}$	$72.99x10^{-6}$

$P_{sb}^0 = -12160/T + 10.19$ (Harris, 1984)

By using those data, the constants D_0 and E_0 can be calculated :

$E_D/R = 16700$ K $\qquad D_0/r_i = 0.0254$ m/s

5.4.6 Modeling for vaporization of Cobalt (Co)

From section 3.5.1., it is known that, cobalt and chromium is weakly bonded in coal. This is the reason why Co and Cr can be vaporized during coal combustion even though they have very high boiling temperatures. Accordingly, the data can be fitted with a simple first order model like the volatile devolatilization(Solomon and Colket, 1978):

$$\frac{dC}{dt} = -CA_i \exp\left(\frac{-E}{RT_p}\right) \tag{42}$$

The constants in above equation can be calculated using the data in Figure 5-13:

$E_{Co}/R = 12500$, $A_{co} = 1356$ /s

Again, the fate of Co for other types of coals is calculated using the constants. And the predictions agrees well with the experimental ones(Figure 5-20). The same approach can be used for chromium and for As in Wyodak coal.

5.4.7 Conclusions

The fate of trace elements is largely determined by their occurrences in coal and by the combustion temperatures. For those elements associated with pyrites, such as As, Se, Ni, Cu, the

release is determined by the atomic diffusion through the melt of pyrrhotite. For the elements, which are weakly bonded in the coal, they are released like volatile matter.

REFERENCES

Allen, R. M. and VanderSander J. B., Analysis of submicron mineral matter in coal via scanning transmission electron microscopy, Fuel 63:24-29, 1984

Baxter, L.L. and Mitchell, R.E., The release of iron during the combustion of Illinois No. 6 coal, Combust. Flame 88:1-14, 1992

Bool, L.E., III, and Helble, J.J., A laboratory study of the partitioning of the trace elements during pulverized coal combustion, Energy and Fuels 9: 880-997, 1995

Bool, L.E., III, The partitioning of iron during the combustion of pulverized coal, The University of Arizona, PhD thesis, 1993

Du, Z., Kinetic modeling of carbon oxidation, MIT ScD thesis, 1990

Finkelman, R.B., Modes of occurrence of environmentally sensitive trace elements in coal, in Environmental Aspects of Trace Elements in Coal (Eds. Swaine, D.J. and Goodarzi, F.), Kluwer Academic Publishers, 1995, pp.24-50

Fuiichi, K., Miyajima, Y., Chiba, T. and Kikuchi, T., Elemental Characterization of particle size-density separated coal fly ash by spectrophotometry, inductively coupled plasma emission spectrometry, and scanning microscopy-energy disperse X-ray analysis, Environ. Sci. Technol. 21:898-903, 1987

Gallagher, N.B., Bool, L.E., Wendt, J.O.L. and Peterson, T.W., Alkali metal partitioning in ash from pulverized coal combustion, Combust. Sci. Tech. 74: 211-221, 1990

Gallagher, N.B., Peterson, T.W., and Wendt, J.O.L., Twenty-sixth Symposium (International) on Combustion, The combustion Institute, Pittsburgh, 1996, pp. 3197-3204

Gallagher, N.B., Alkali metal partitioning in ash from pulverized coal combustion, The university of Arizona PhD thesis, 1992

Gat, N., Cohen, L. M., Witte, A. B., and Denison, R. M., Ash loss and the "seed-tracer" technique for the determination of mass balance in rapid heating coal pyrolysis experiments, Combust. Flame 57: 255-263, 1984

Greenwood, N. N. and Earnshaw, A. , Chemistry of the Elements, Pergamon Press,1984

Harris, R., Vacuum refining copper melts to remove bismuth, arsenic, and antimony, Metall. Trans. 15B:251-257, 1984

Huggins, F.E, Shah, N., Zhao, J., Lu, F. and Huffman, G.P., Nondestructive determination of trace elements speciation in coal and coal ash by XAFS spectroscopy, Energy Fuels 7: 482-489, 1993

Hultgen, R., Desai, P.D., Hawkins, D.T., Gleiser,M. and Kelly, K.K., Selected values of the Thermodynamic Properties of the Elements, American Society for Metals, 1973

Hurt, R., Davis, K., Yang, N., and Hardesty, D., The origin and properties of unburned carbon from pulverized coal combustion, Report to EPRI, EPRI TR-105743, Project 8005, 1995

JANAF Thermochemical Tables, J. Phys. Chem. Ref. Data, Vol. 14, Suppl.1., 1985

Jorgensen, F.R.A., Combustion of pyrite concentrate under simulated flash smelting conditions,

Trans. Inst. Min. Metall. 90: C10-16, 1981

Kang, S. G., Sarofim, A. F., Graham, K. A. and Beer, J. M., in Transformation of inorganic coal constituents in combustion system (Ed. Helble, J.J.) , Final report to DOE (contract No. DE-AC22-86PC90751), 1992

Kang, S.G., MIT PhD thesis, 1991

Kauppinen, E.I. and Pakkanen, T. A., Coal combustion aerosols: a field study, Environ. Sci. Technol. 24:1811-1818, 1990

Lau, K.H., Lamoreaux, R.H. and Hildenbrand, D.L., Vapor pressure determination of arsenic activity in molten Cu-Fe-S matte, Metall. Trans. 14B:253-258, 1983

Lindner, E. R., University of Newcastle (Australia) PhD thesis, 1988

Lynch, D. C., Activity of arsenic in copper, Metall. Trans. 11B: 623-629, 1980

Machlin, E.S., Trans. TMS-AIME, 218:314-326, 1960

Makino, A. and Law, C.K., Twenty-first Symposium (International) on Combustion, The Combustion Institute, Pittsburgh, 1986, pp. 183-191

Mamane, Y. , Miller, J.L. and Dzubay, T.G., Characterization of individual fly ash particles emitted from coal and oil fired power plants, Atmospheric Environment 20: 2125-2135, 1986

Markowski, G.R., Trace elements concentration as a function of particle size in fly ash from a pulverized coal utility boiler, Environ Sci. Technol. 9:796-804, 1985

Miller, S. F. and Schobert, H. H., Effect of the occurrence and composition of iron composition on ash formation, composition, and size in pilot-scale combustion of pulverized coal and coal-water slurry fuels, Energy Fuels 7: 1030-38, 1993

Nenniger, R. D., Aerosol produced from coal pyrolysis, MIT ScD thesis, 1986

Neville, M. and Sarofim, A. F. , The stratified composition of inorganic submicron particles produced during coal combustion, Nineteenth Symposium (International) on Combustion/The combustion Institute, 1982, pp. 1441-1440

Ohno, R., Kinetics of removal of bismuth and lead from molten copper alloys in vacuum induction melting, Metallurgical Transactions 22B: 447-465, 1991

Olette, M. , Physical chemistry of process metallurgy, 1961, vol. 8, no. 2

Palmer, C.A. and Filby, R.H., Distribution of trace elements in coal from the Powhatan No. 6 mine, Ohio, Fuel 63: 318-328, 1984

Quann, R.J., Neville, M. and Sarofim, A.F., A laboratory study of the effect of coal selection on the amount and composition of combustion generated submicron particles, Combust. Sci. Tech. 74:245-263, 1990

Quann, R.J., Neville, M., Janghorbani, M., Mims, C.A. and Sarofim, A.F., Mineral matter and trace-element vaporization in a laboratory-pulverized coal combustion system, Environ. Sci. Technol. 16: 776-781, 1982a

Quann, R.J. and Sarofim, A.F., Vaporization of refractory oxides during pulverized coal combustion, Nineteenth Symposium (International) on Combustion/The Combustion Institute,

pp.1429-1440 , 1982b

Raask, E., The mode of occurrence and concentration of trace elements in coal, Prog. Energy Combust. Sci. 11: 97-118, 1985

Raask, E. J. Inst. Energy 57, 231, 1984

Richardson, F. D., Physical Chemistry of Melts in Metallurgy, 1 st ed., Academic Press Inc., London,

Sarofim. A.F . and Zeng, T., in Fundamental study of ash formation and deposition (Ed. Helble, J. J.), Final report to DOE (contract No. DE-AC22-93PC92190), 1995

Sigworth, G. K. and Elliot, J. F., The thermodynamics of dilute liquid copper alloys, Canadian Metallurgical Quarterly 13: 455-461, 1974

Solomon, P. R. and Colket, M. B., Coal devolatilization, Seventeenth Symposium (International) on Combustion, The Combustion Institute, 1978, pp.131-140

Stinespring, C.D. and Stewart, G.W., Surface enrichment of aluminosilicate minerals and coal combustion ash particles, Atmospheric Environment 15: 307-313, 1981

Swaine, D.J., Trace Elements in Coal, Butterworth & Co. (Publishers) Ltd, 1990

Zeng, T. and Fu, W.B., The ratio CO/CO_2 of oxidation on a burning carbon surface, Combust. Flame 107:197-210, 1996

Figure 5-1 Effects of Fe concentration in the coal on the total Fe collected on submicron char particles

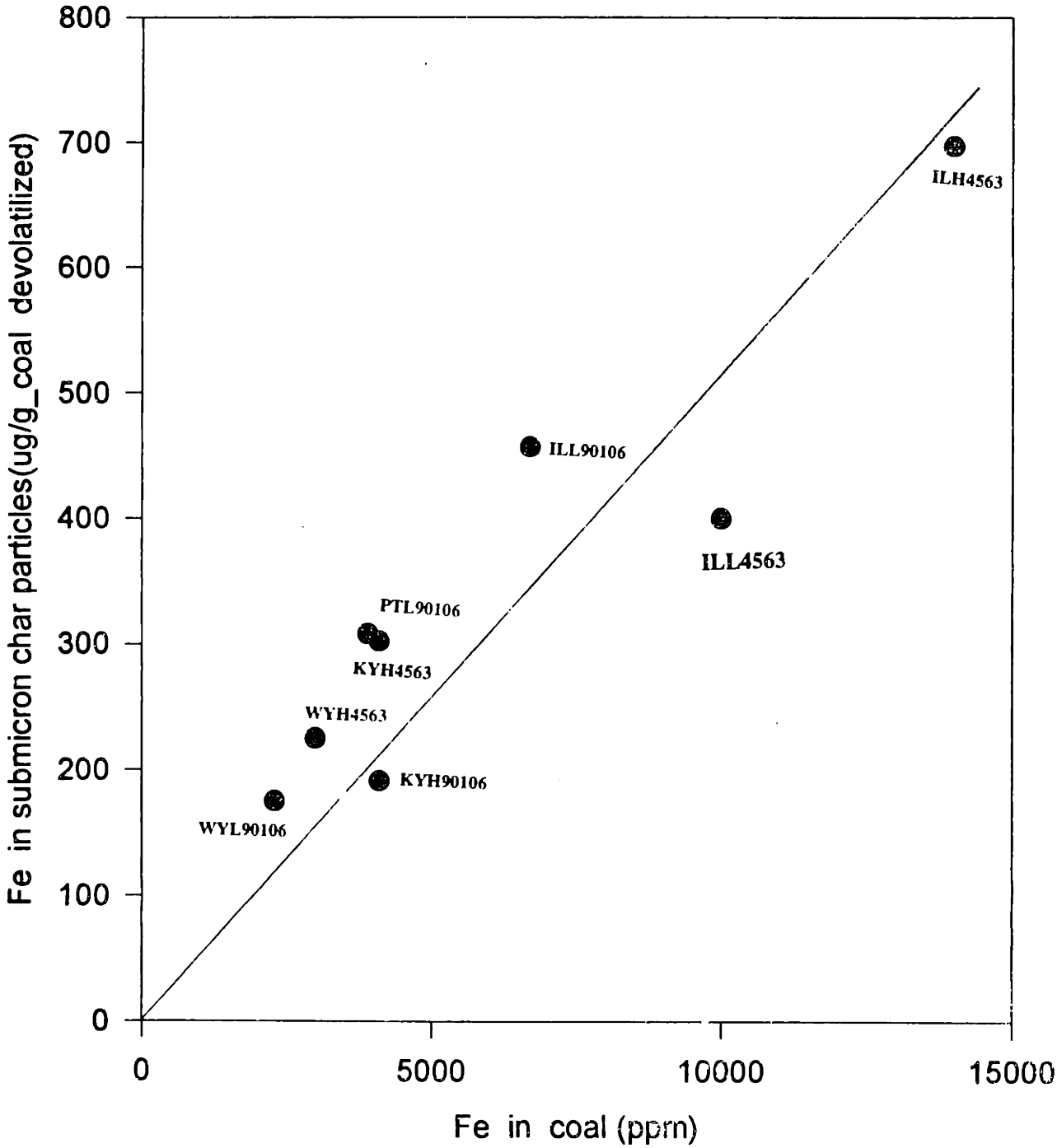

Figure 5-2 Effects of Na concentration in the coal on the total Na collected on submicron char particles

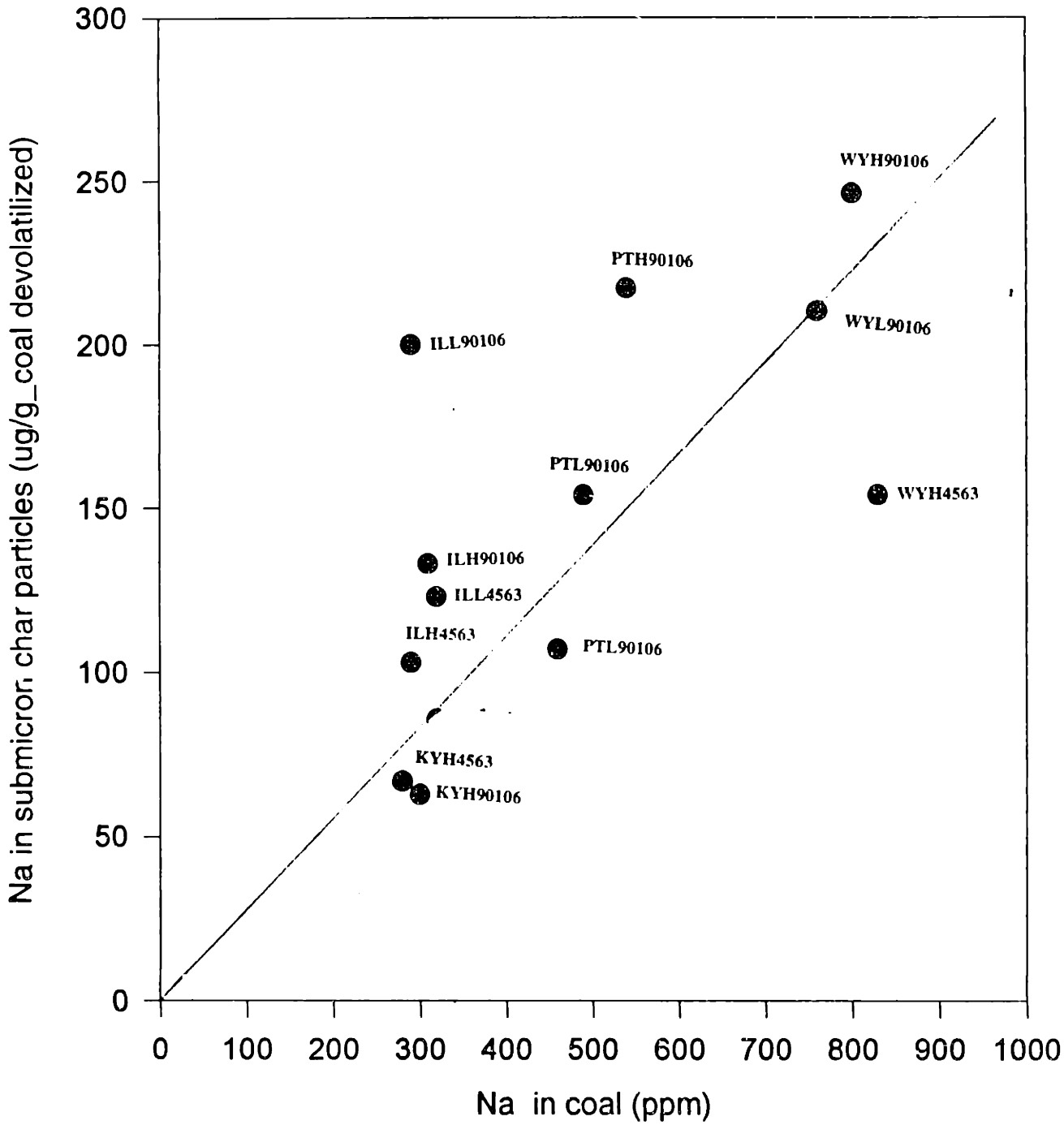

Figure 5-3 Effects of Cr concentration in the coal on the total Cr collected on submicron char particles

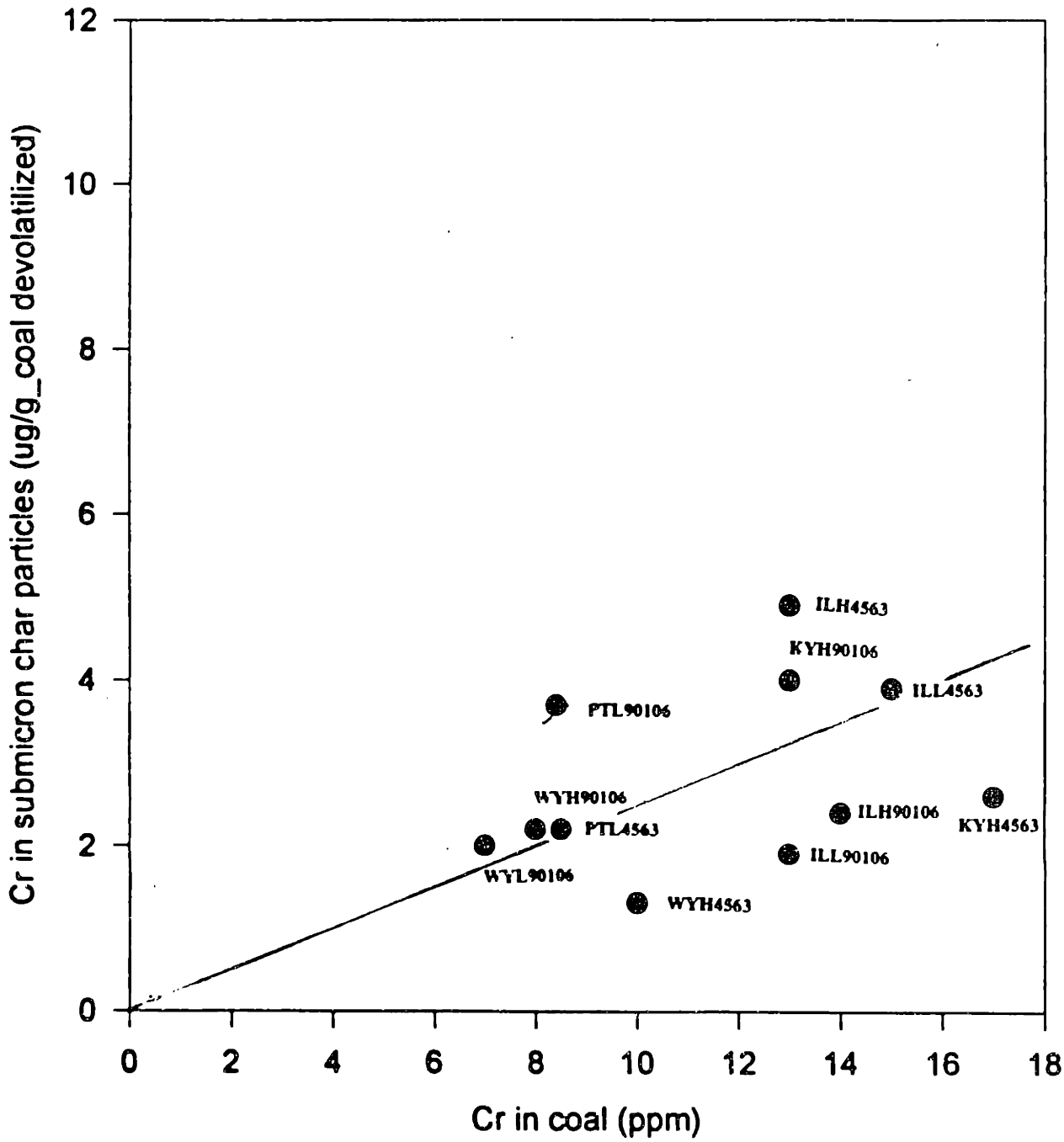

Figure 5-4 Effects of Co concentration in the coal on the total Co collected on submicron char particles

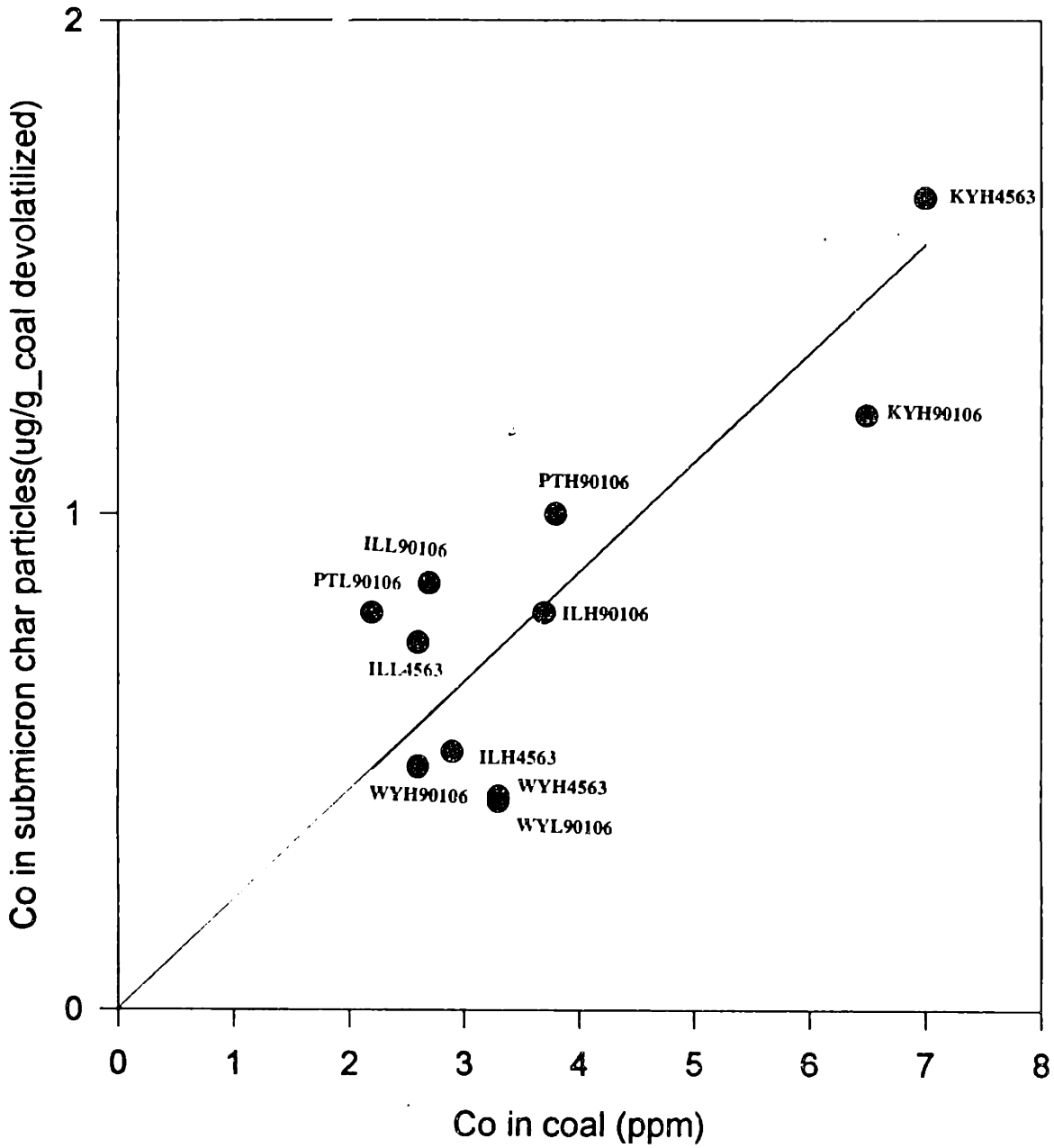

Figure 5-5 Effects of As concentration in the coal on the total As collected on submicron char particles

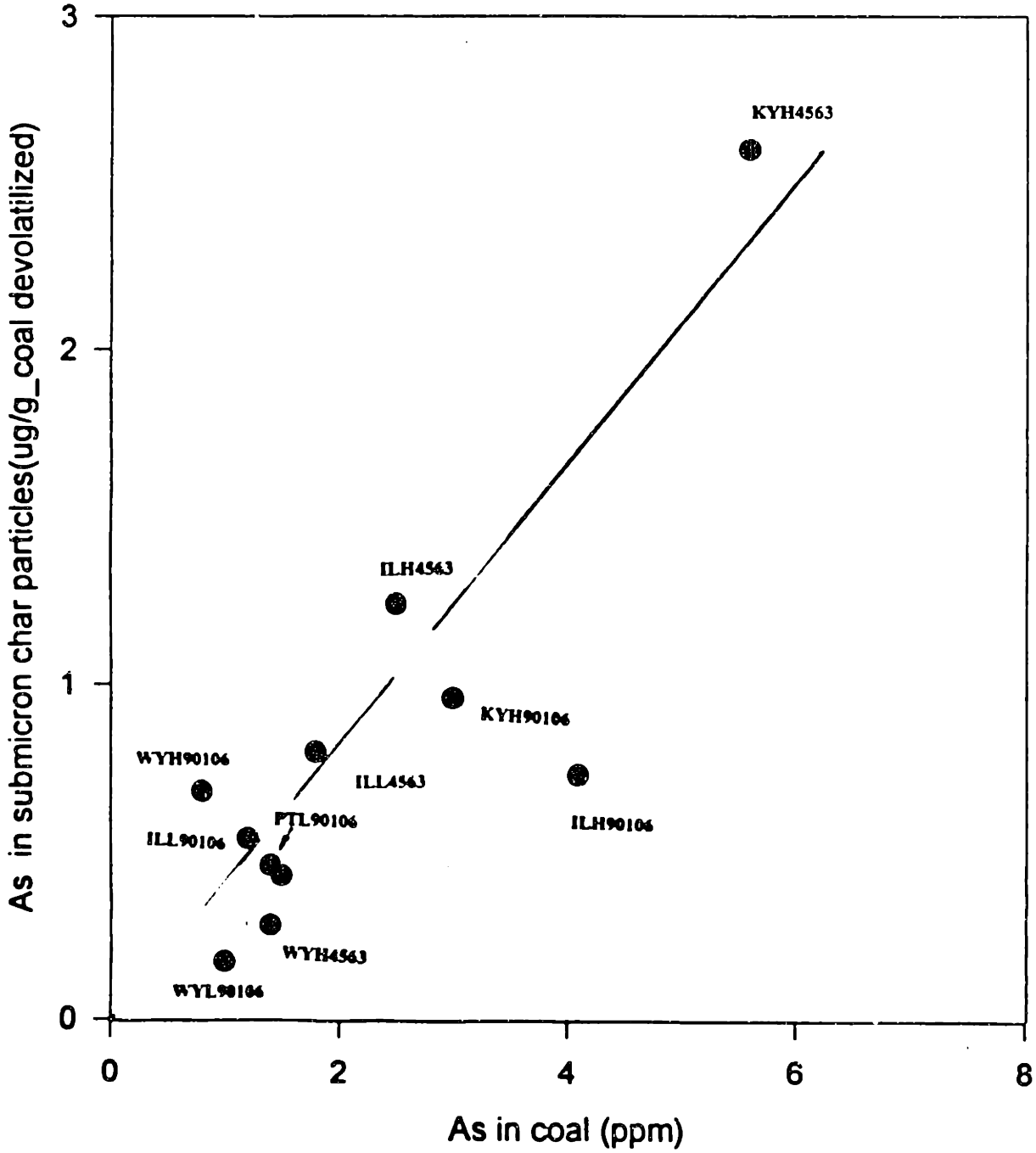

Figure 5-6 Effects of Se concentration in the coal on the total Se collected on submicron char particles

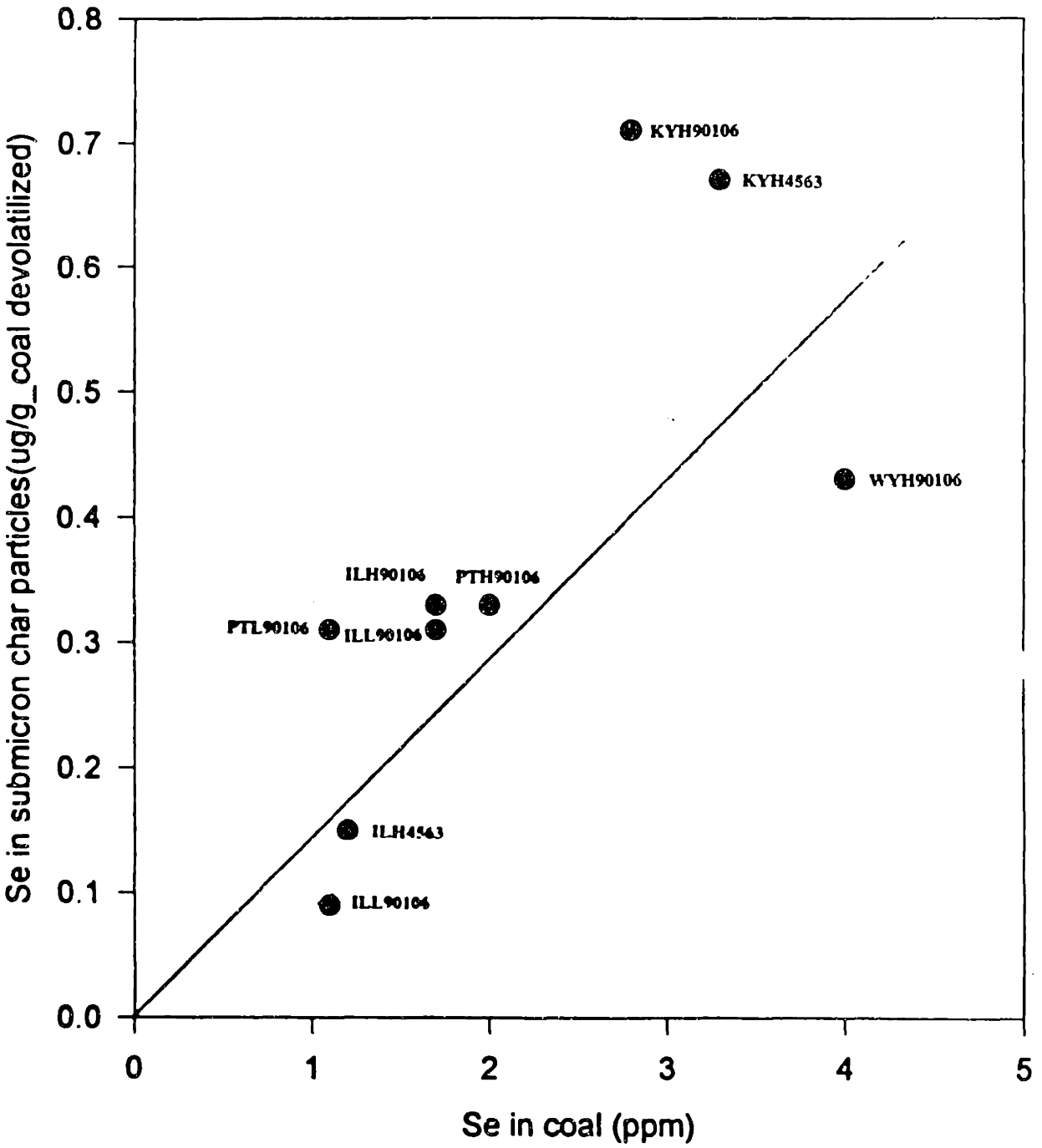

Figure 5-7 Effects of As concentration in the coal on the total As collected in submicron ash particles

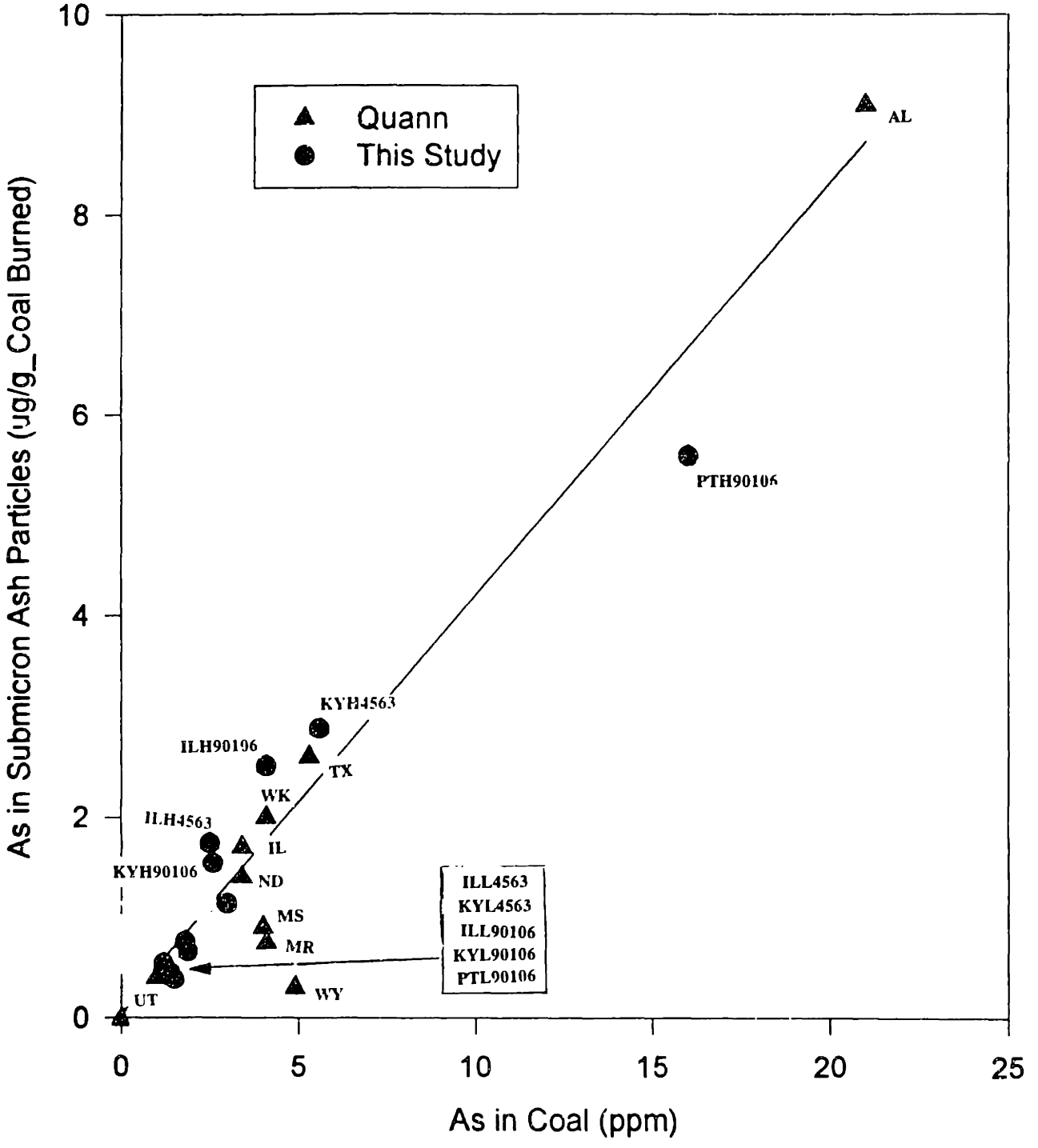

Figure 5-8 Effects of Zn concentration in the coal on the total Zn collected with submicron ash particles

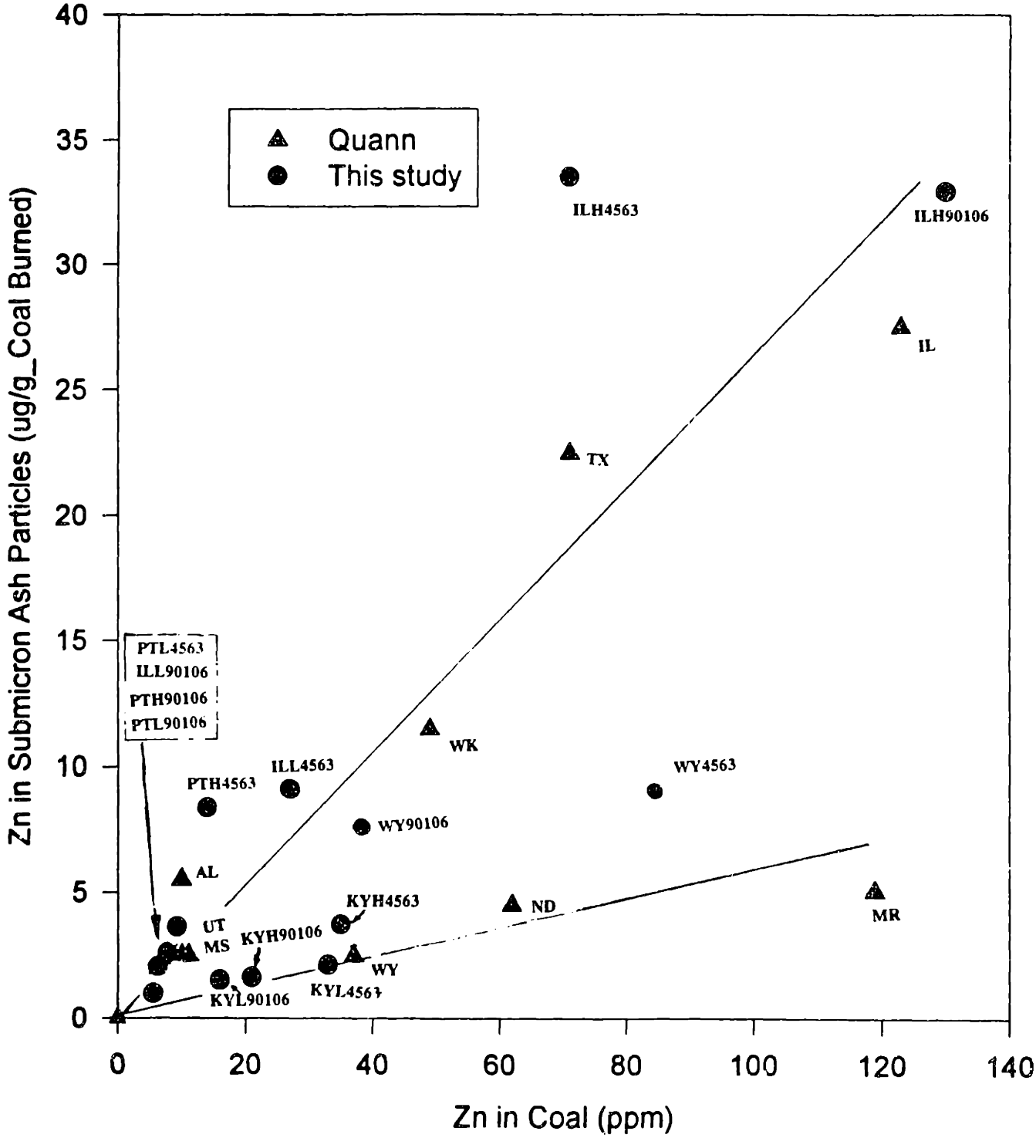

Figure 5-9 Effects of Fe concentration in the coal on the total Fe collected with submicron ash particles

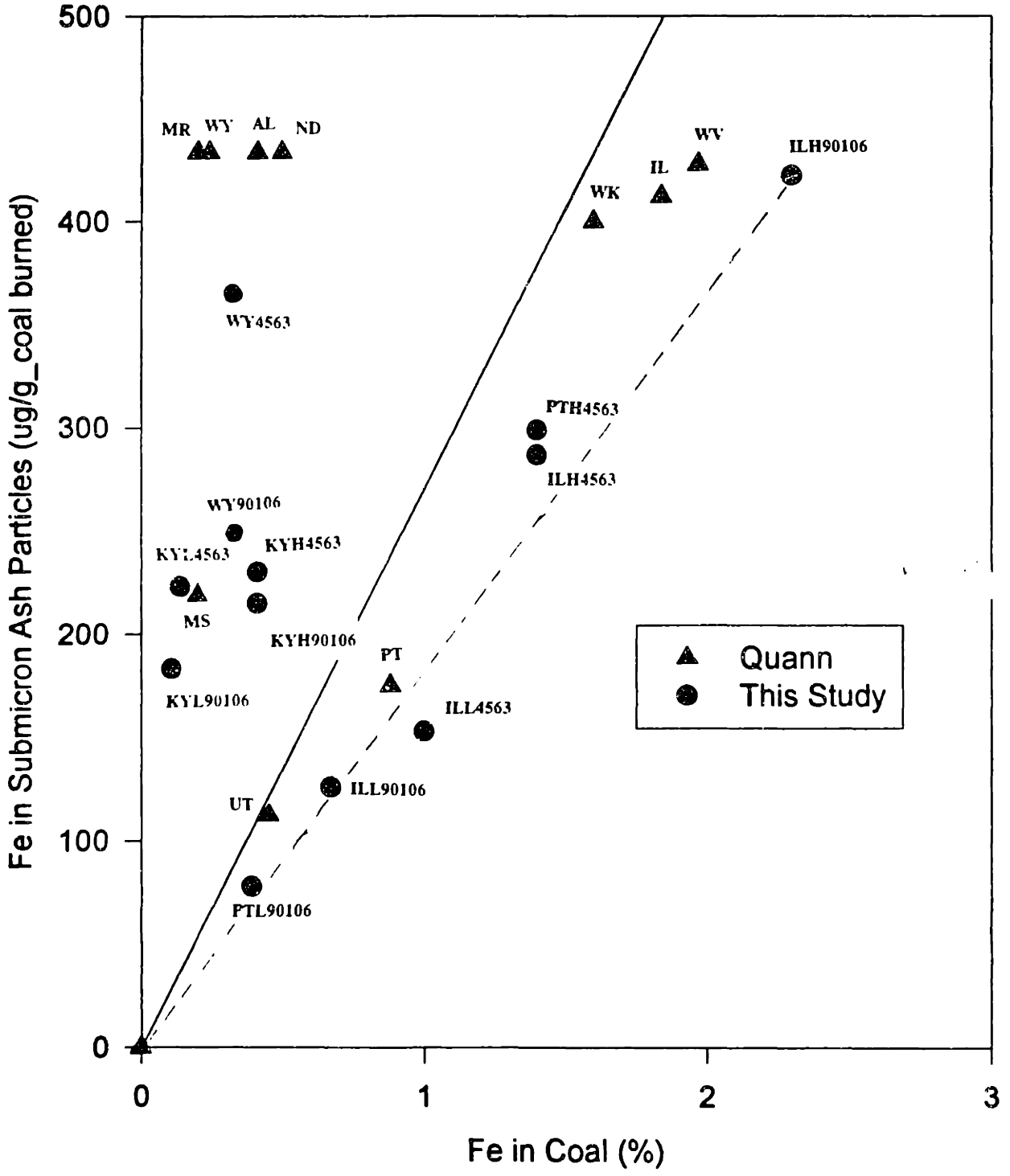

Figure 5-10 Effects of Cr concentration in the coal on the total Cr collected with submicron ash particles

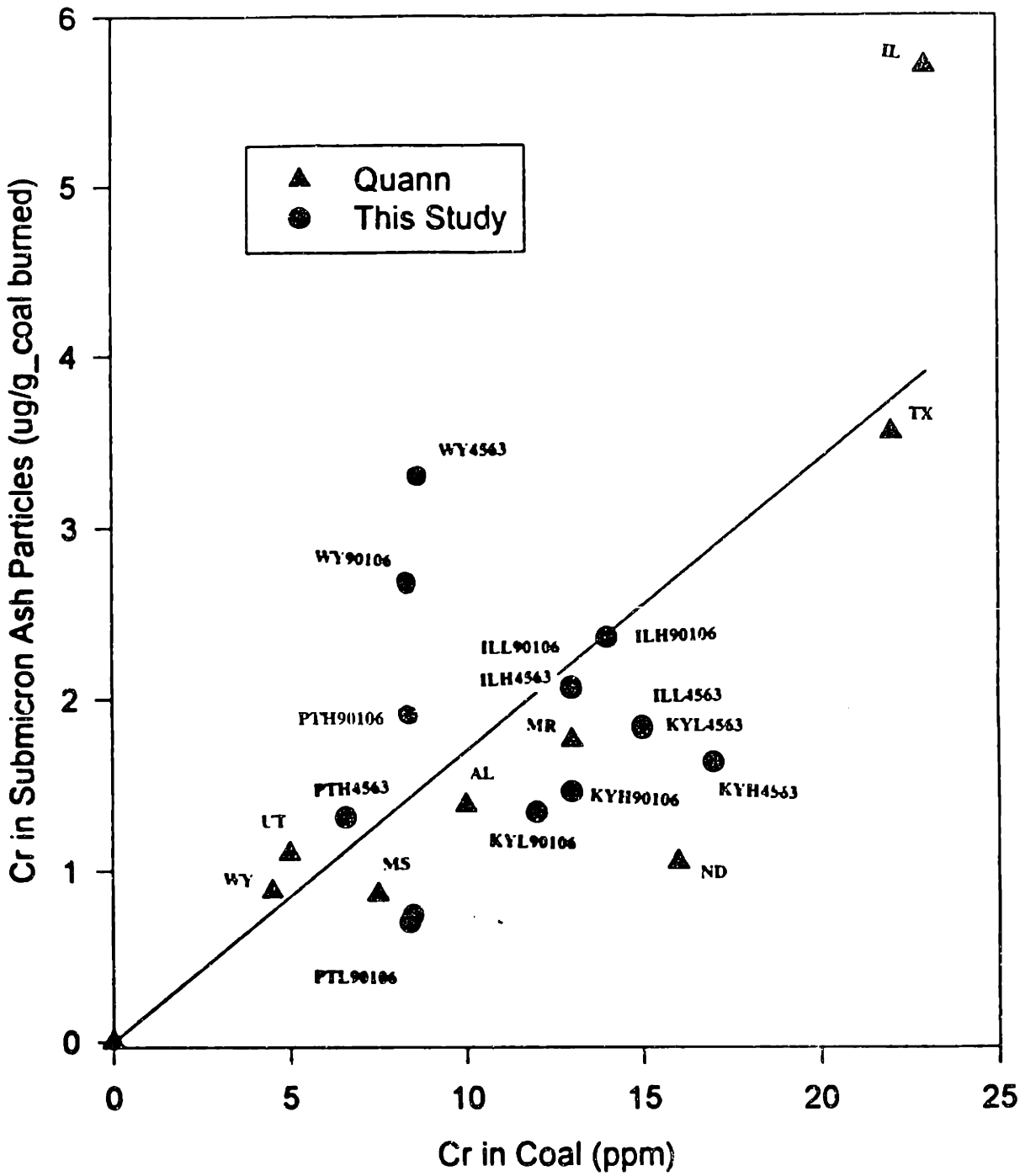

Figure 5-11 Effects of Na concentration in the coal on the total Na collected with submicron ash particles

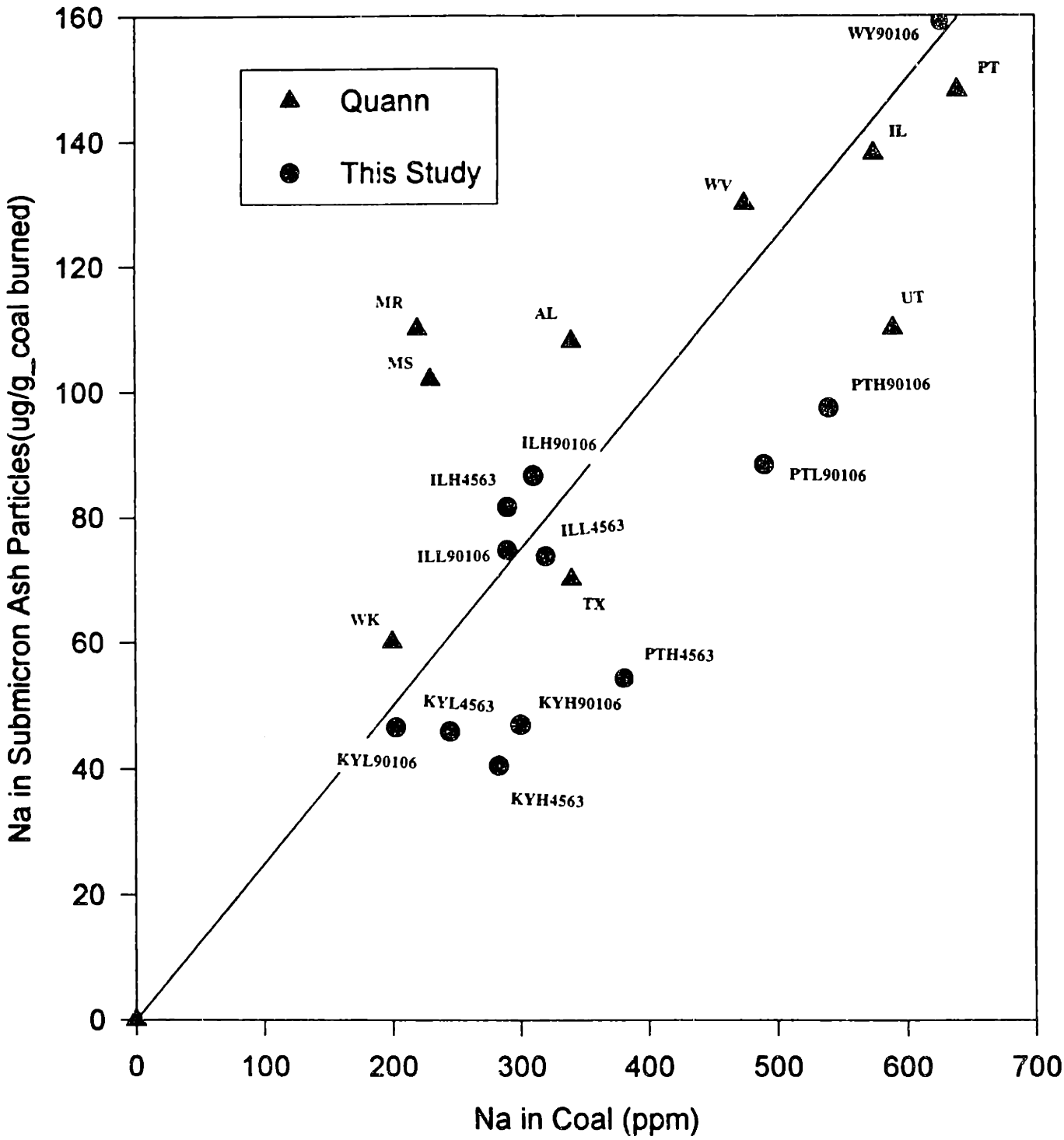

Figure 5-12 Effects of V concentration in the coal on the total V collected with submicron ash particles

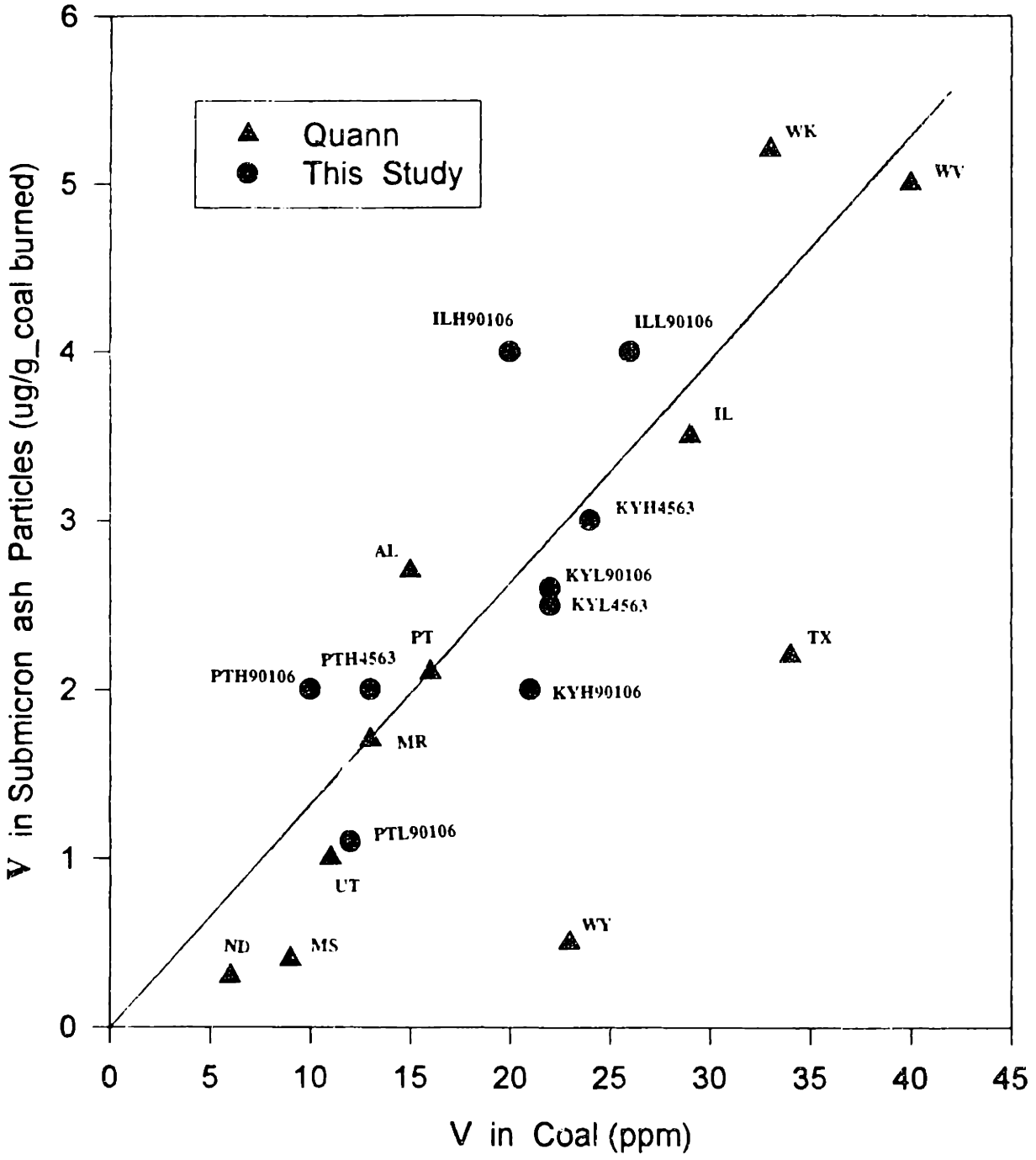

Figure 5-13(a) Effects of pyrolysis temperature and O2 concentration on the fractions of As retained in the coarse particles (%)

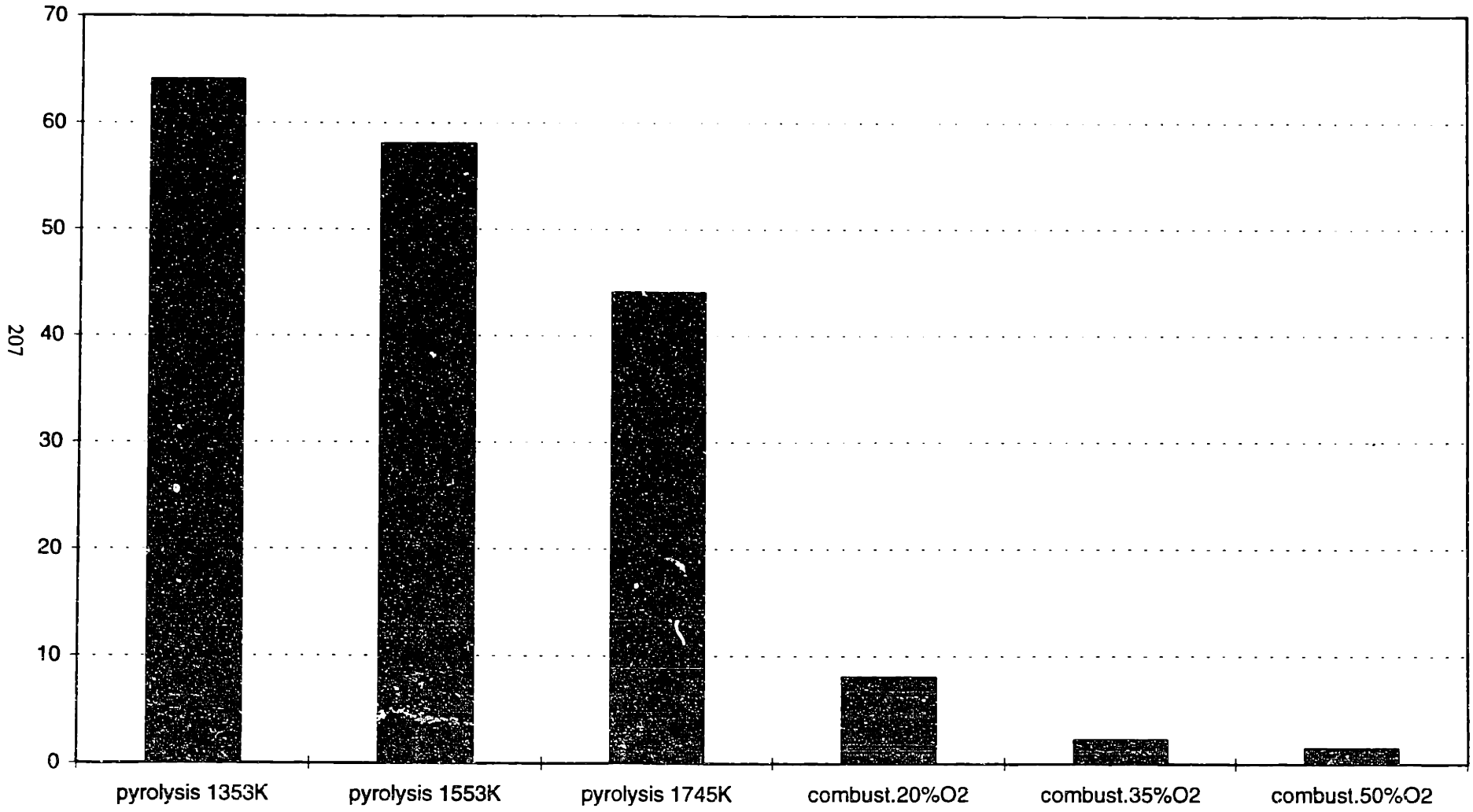

Figure 5-13(b) Effects of pyrolysis temperature and O2 concentration on the fraction of Se retained in the coarse particles (%)

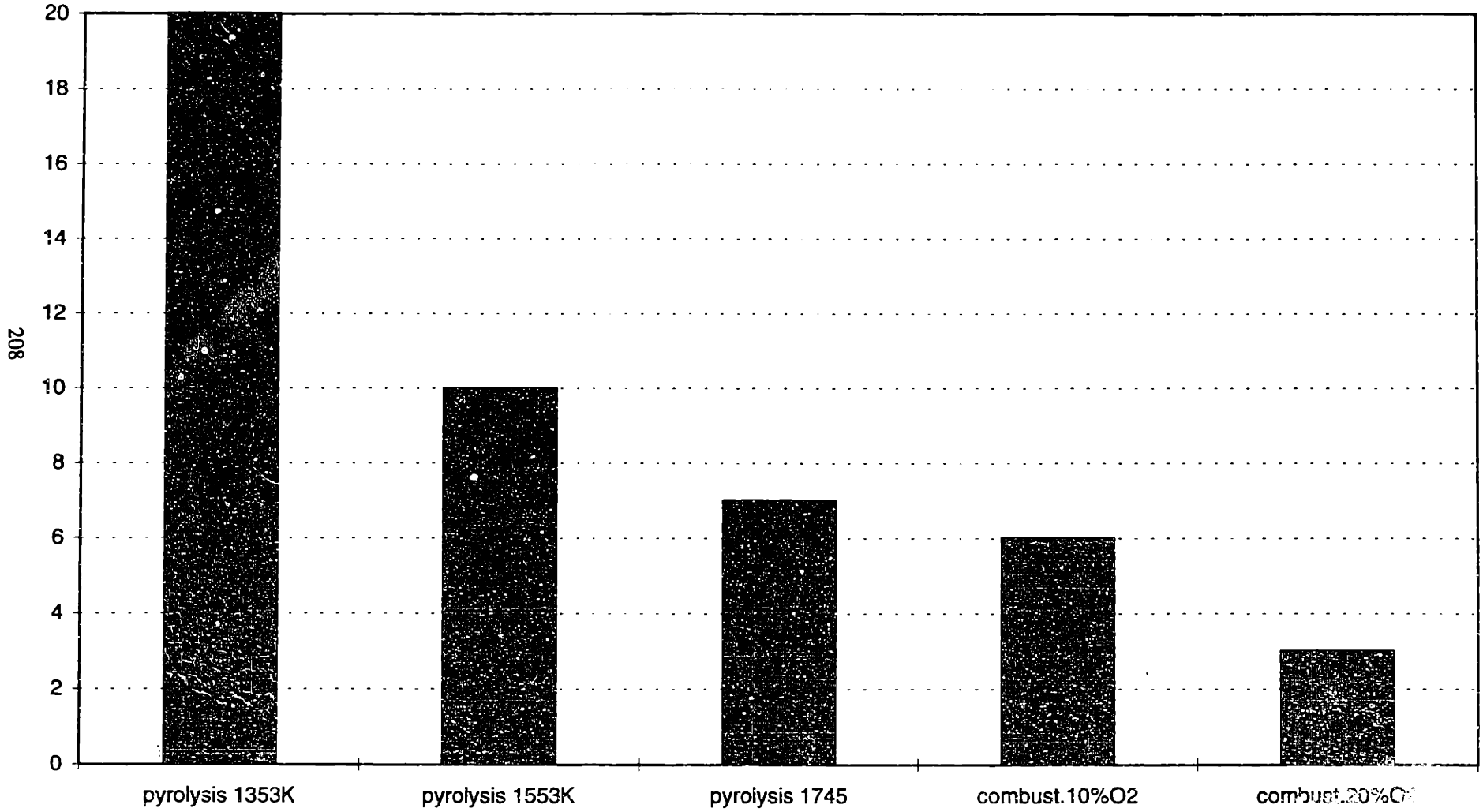

Figure 5-13(C) Effects of oxygen concentration on the fraction of Fe collected in submicron particles

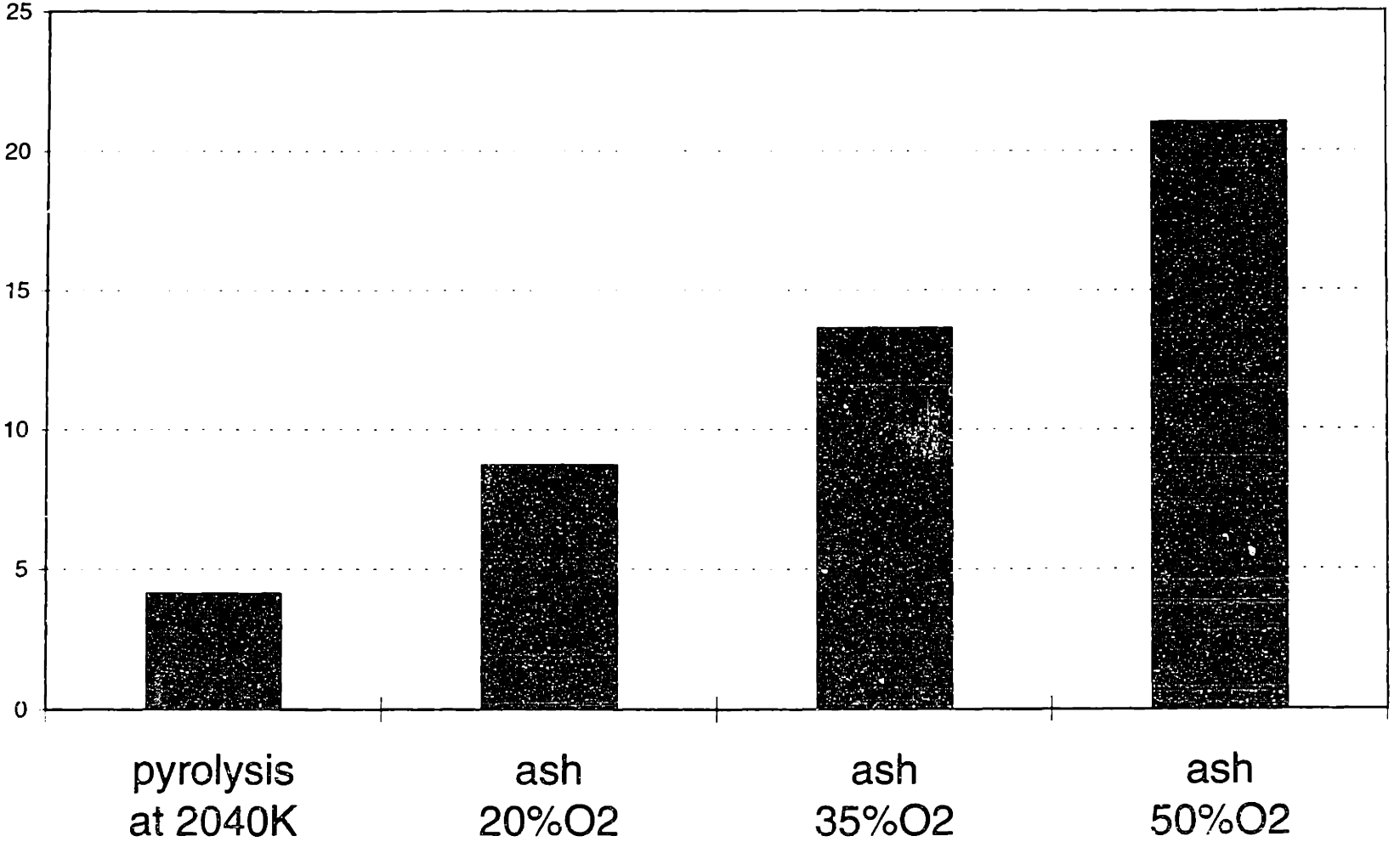

Figure 5-13(d) Effects of oxygen concentration on the fraction of Zn collected on submicron particles

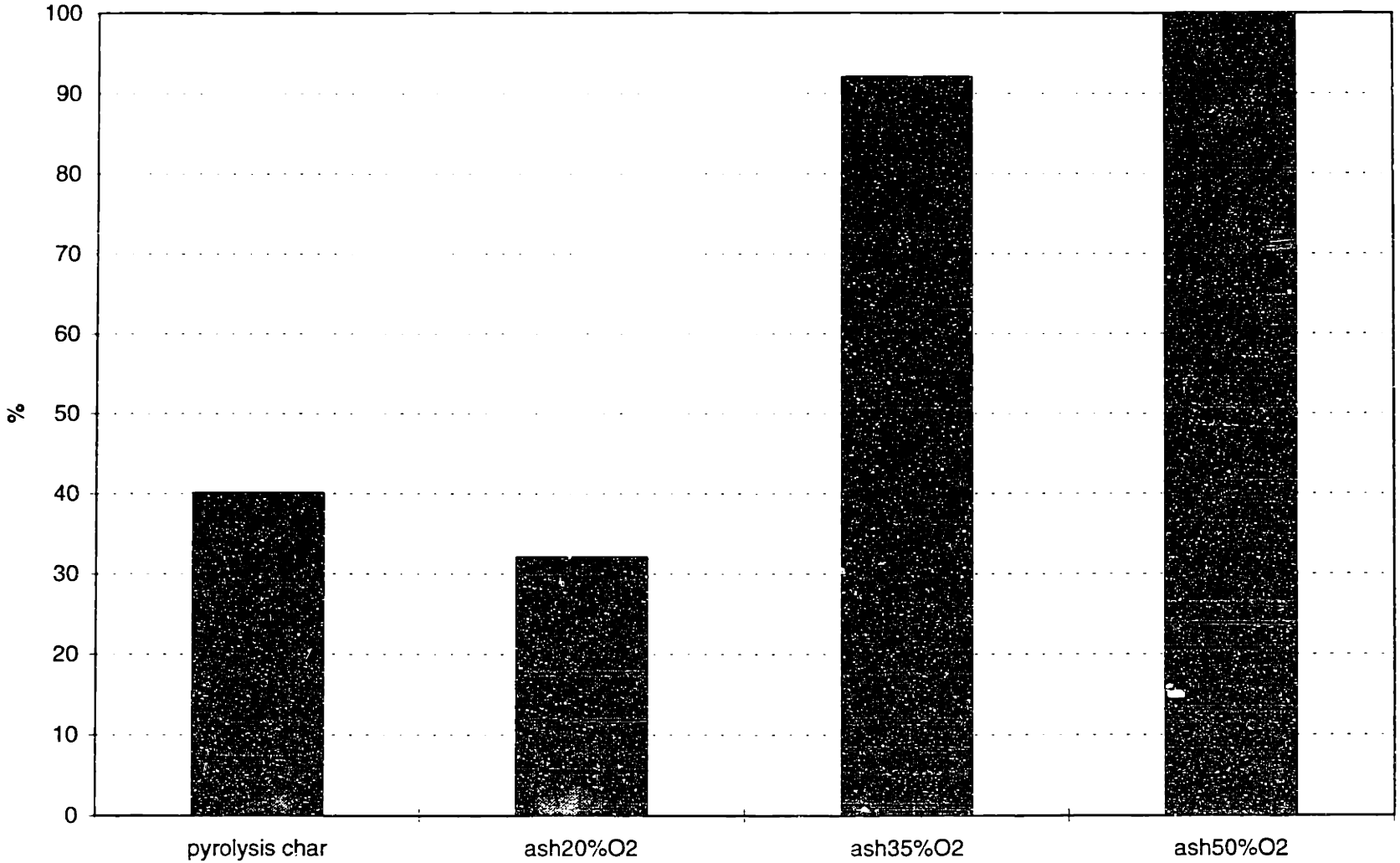

Figure 5-13(e) Effects of pyrolysis temperature and O2 concentration on the fractions of Cr retained in the coarse particles (%)

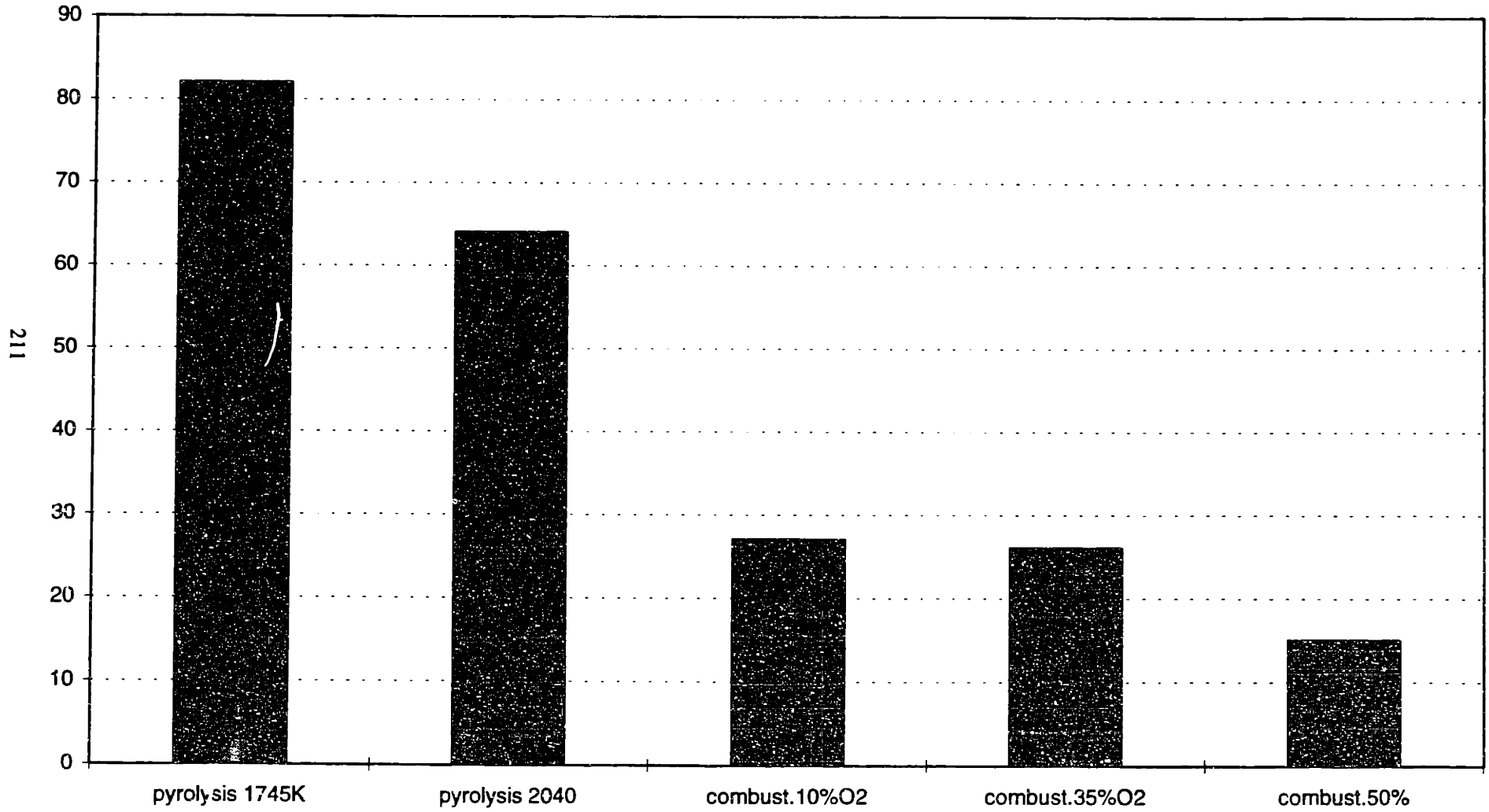

Figure 5-13(f) Effects of pyrolysis temperature and oxygen concentration on the fraction of Co retained in the coarse particles (%)

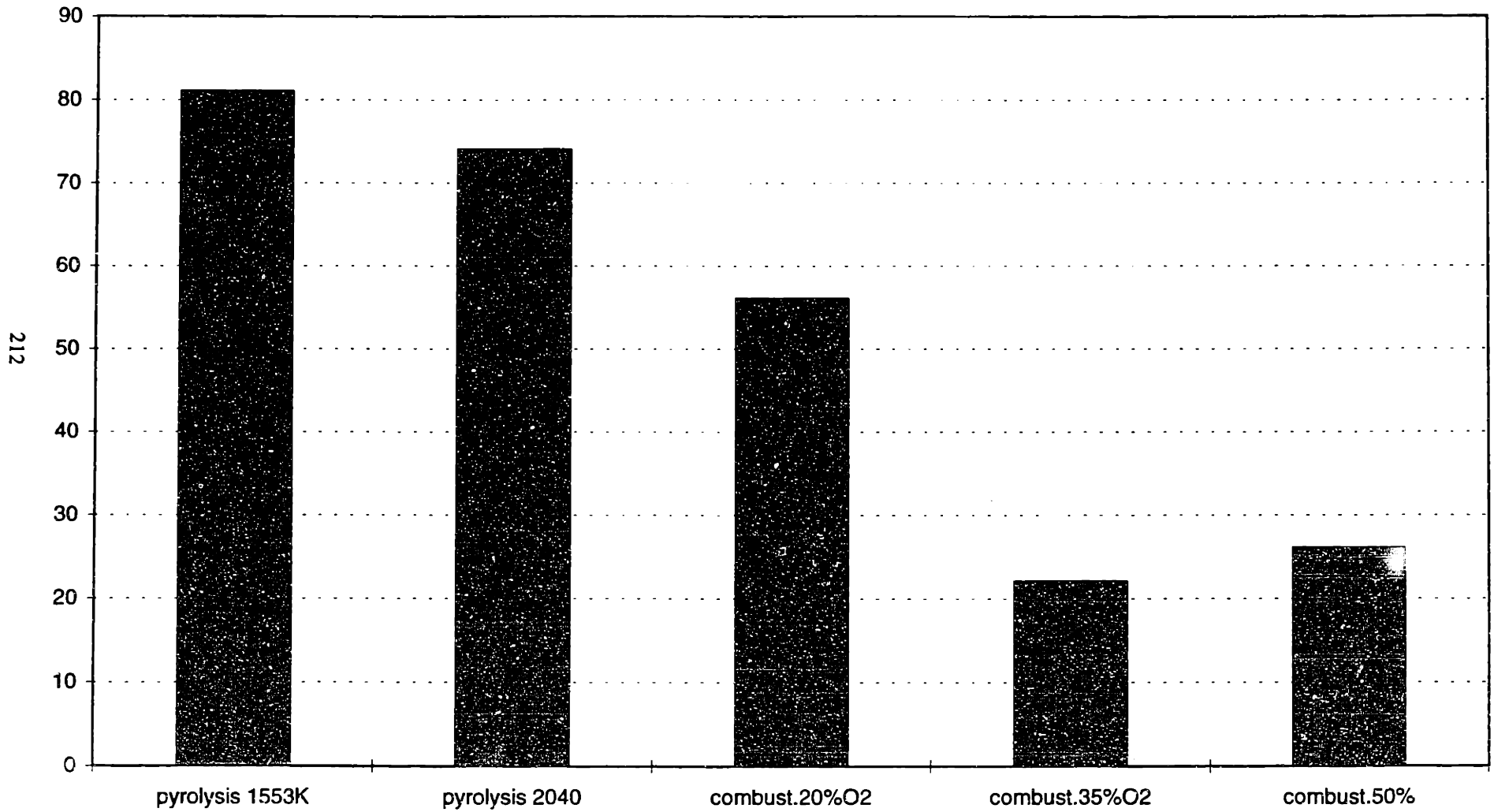

Figure 5-13(g) Effects of oxygen concentration on the fraction of Na collected on submicron particles

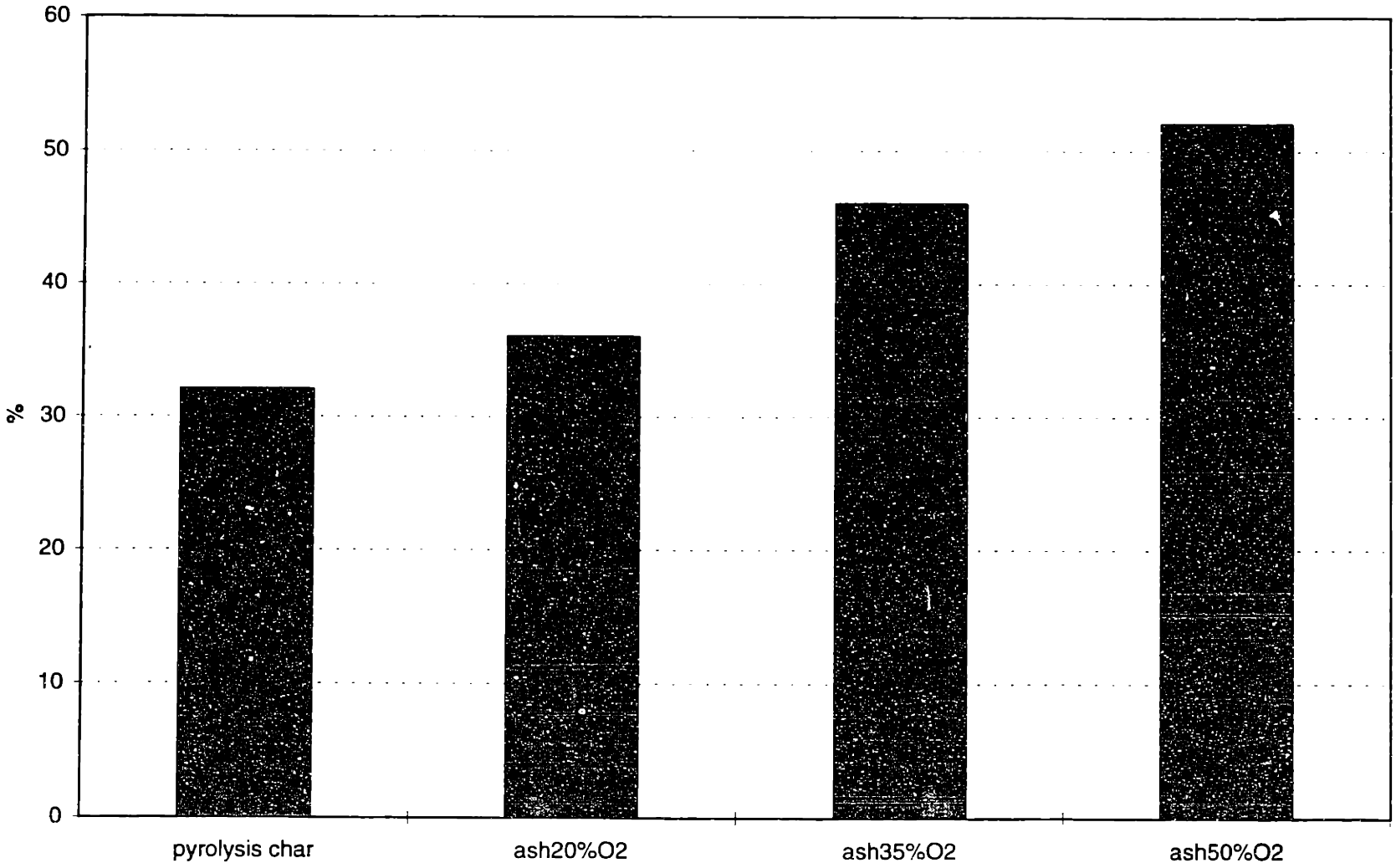

Figure 5-14 Temperature history for IL coal,d = 54microns

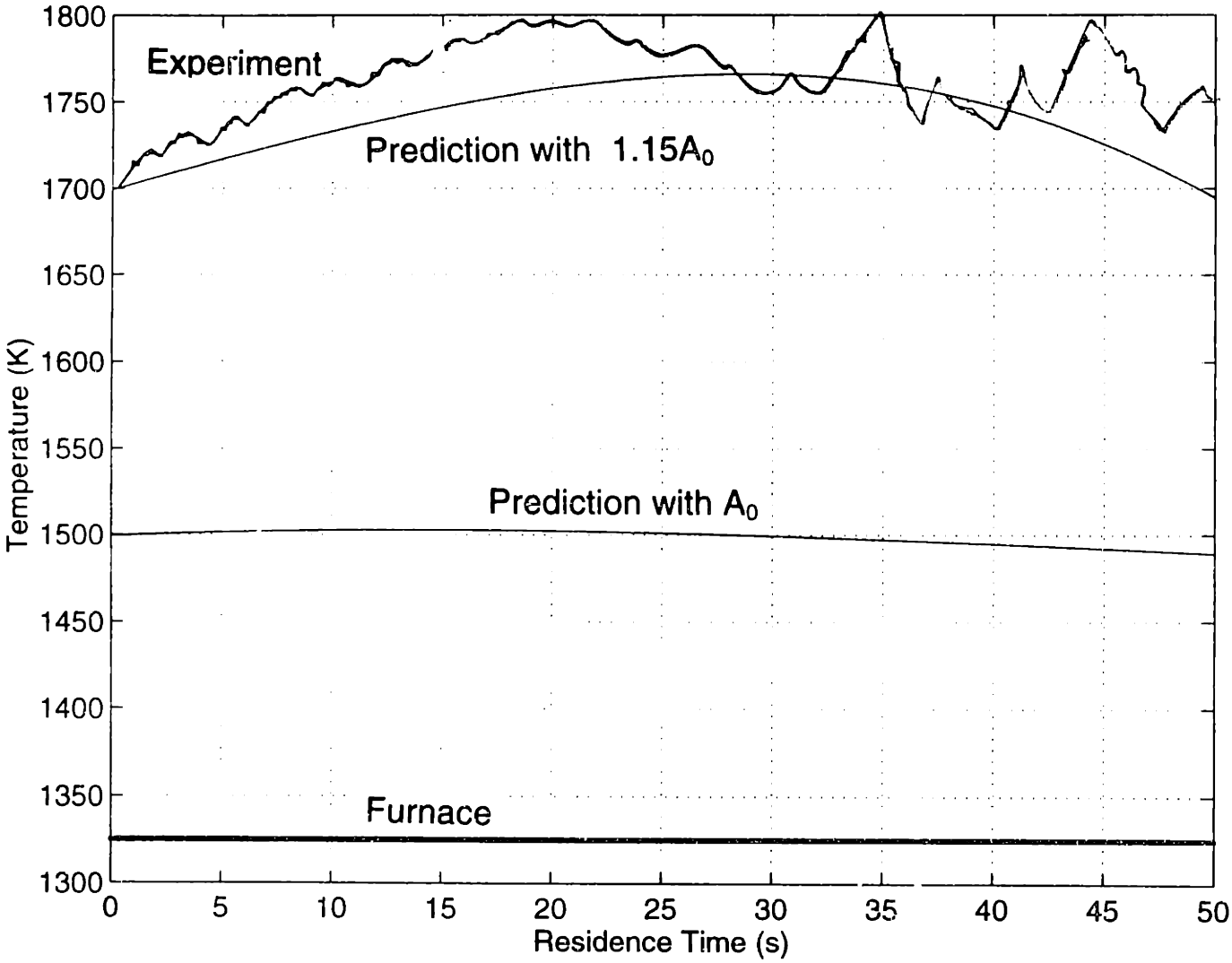

Figure 5–15 Temperature history for PTH90106 coal at a furnace temperature of 1500K

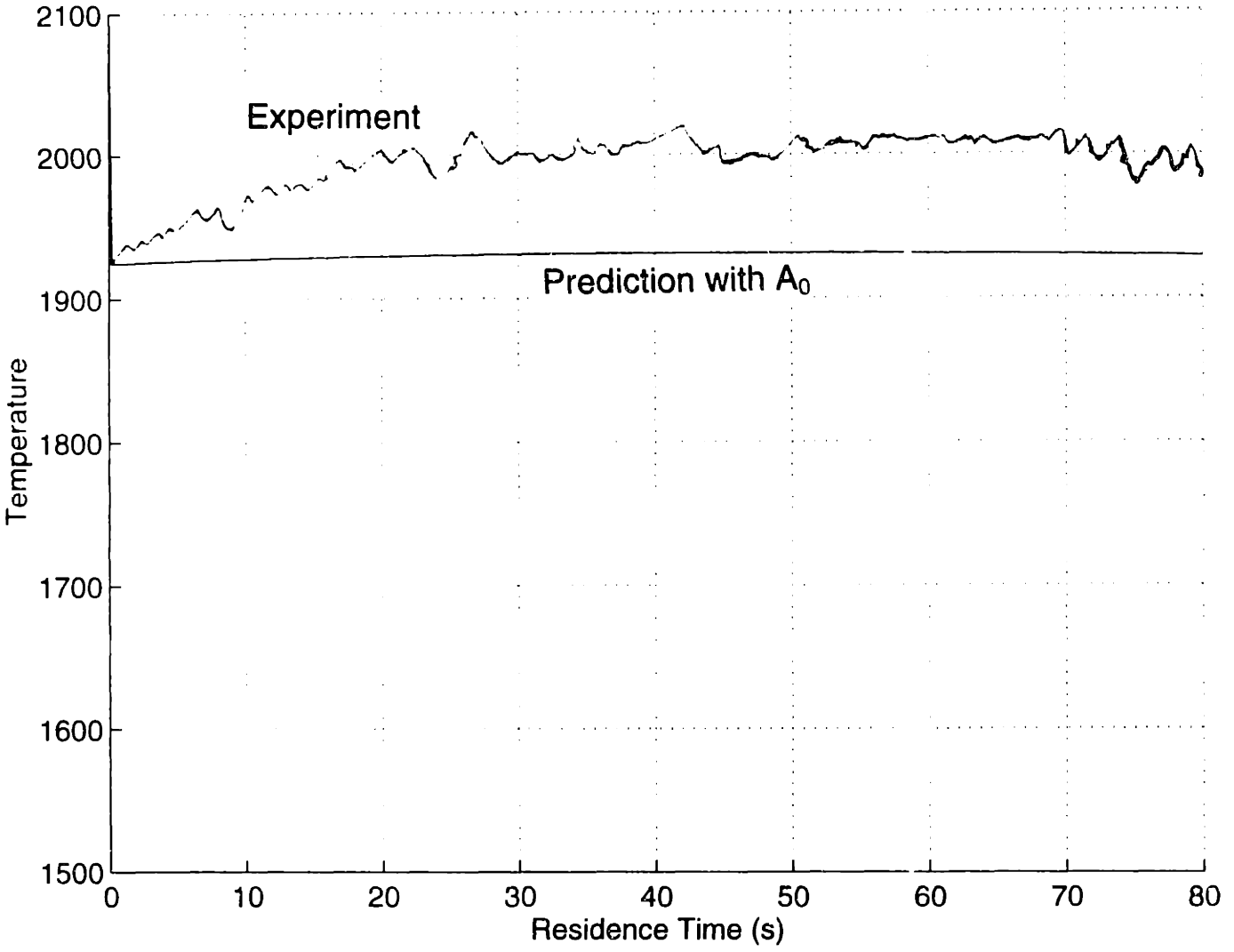

Figure 5-16 Temperature history for PTH90106 coal in furnace

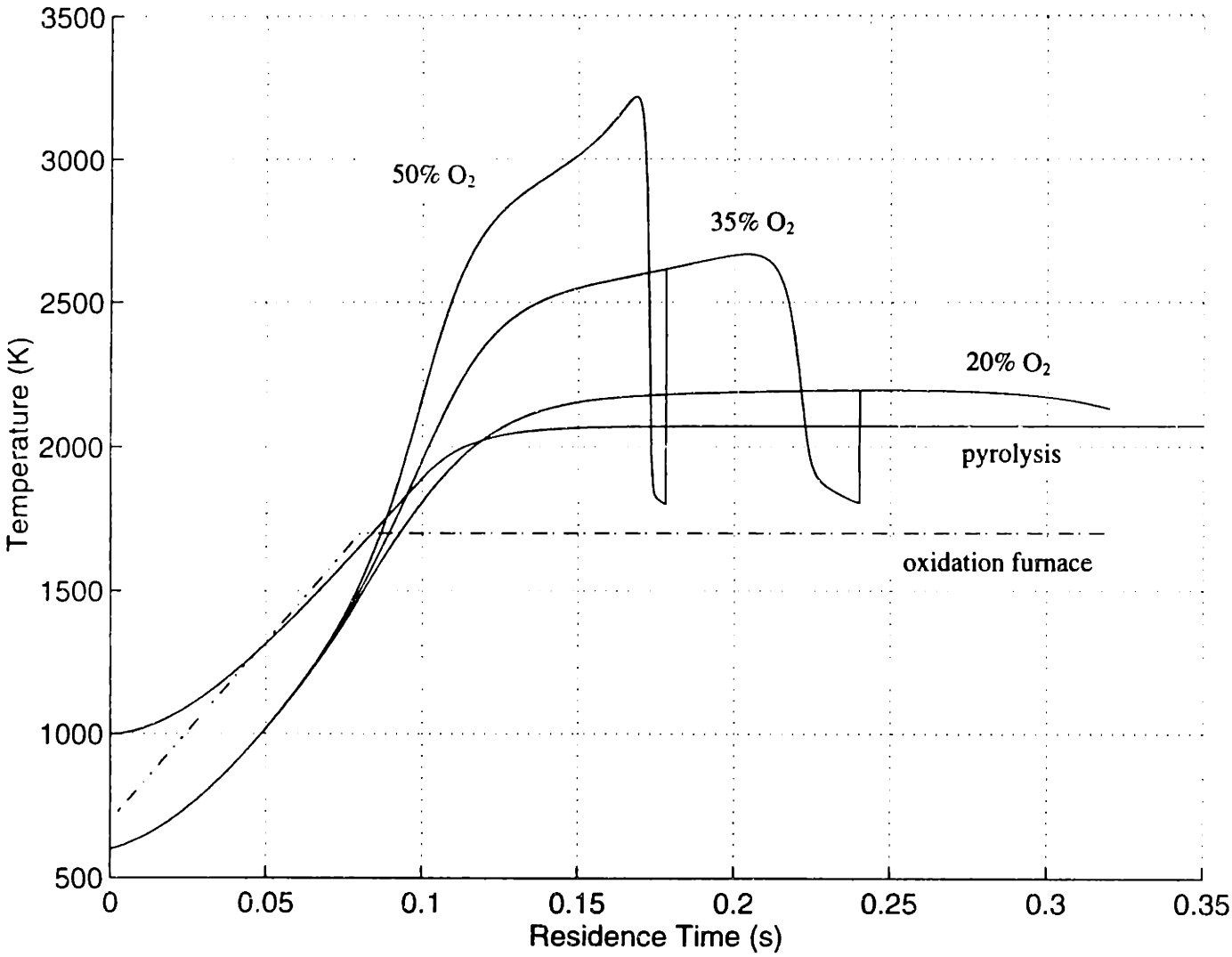

Figure 5-17 Processes for As vaporization

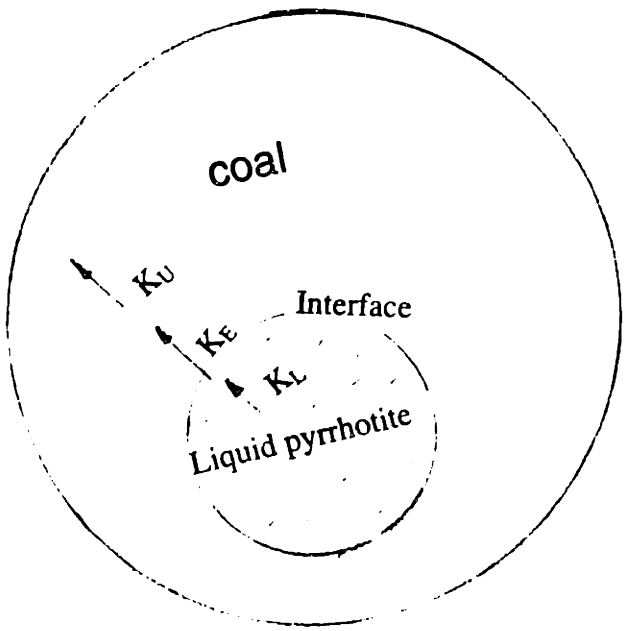

Figure 5-18 Fitting for constants in K_L of As

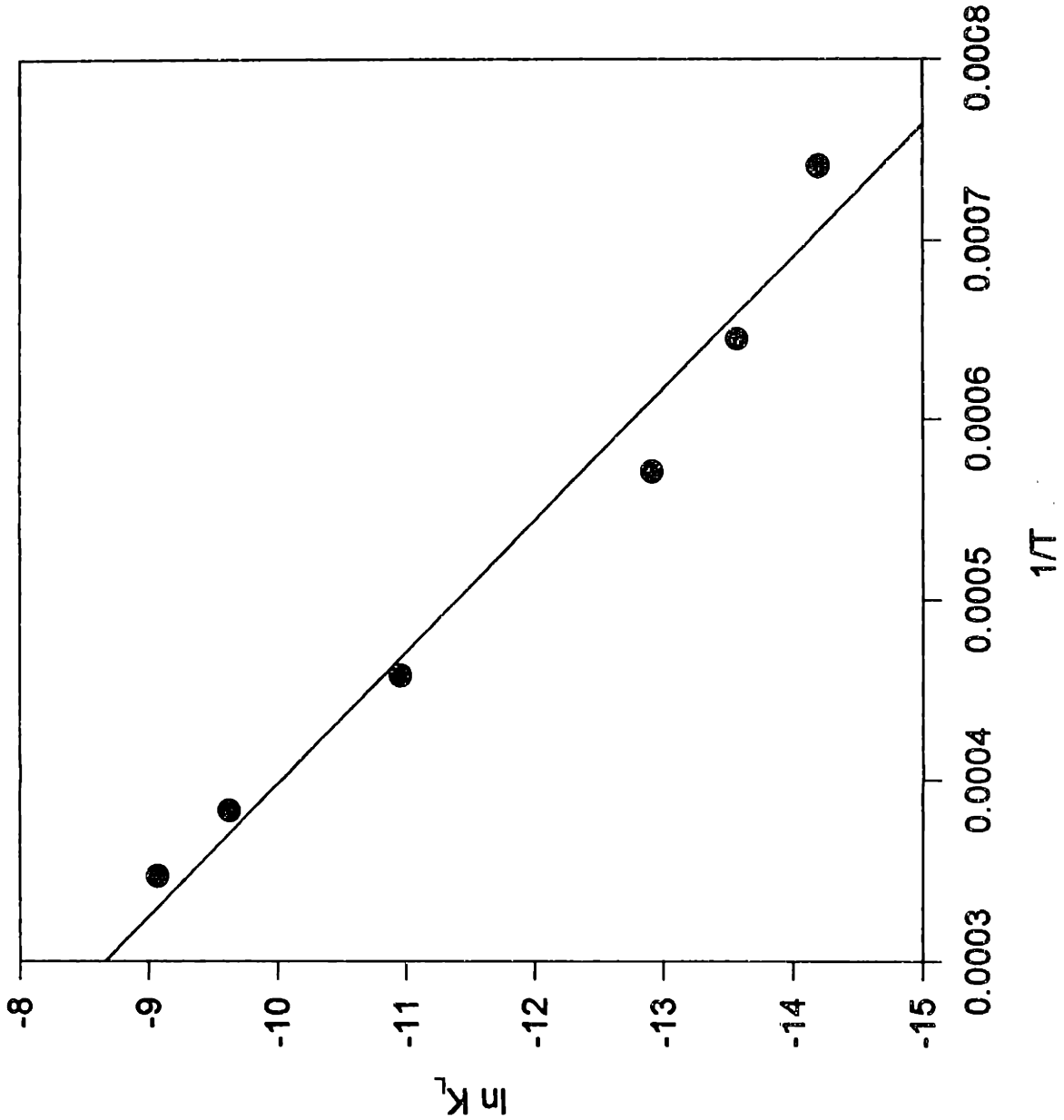

Figure 5-19 Comparison between prediction and experiment values of As retained in coarse ash particles

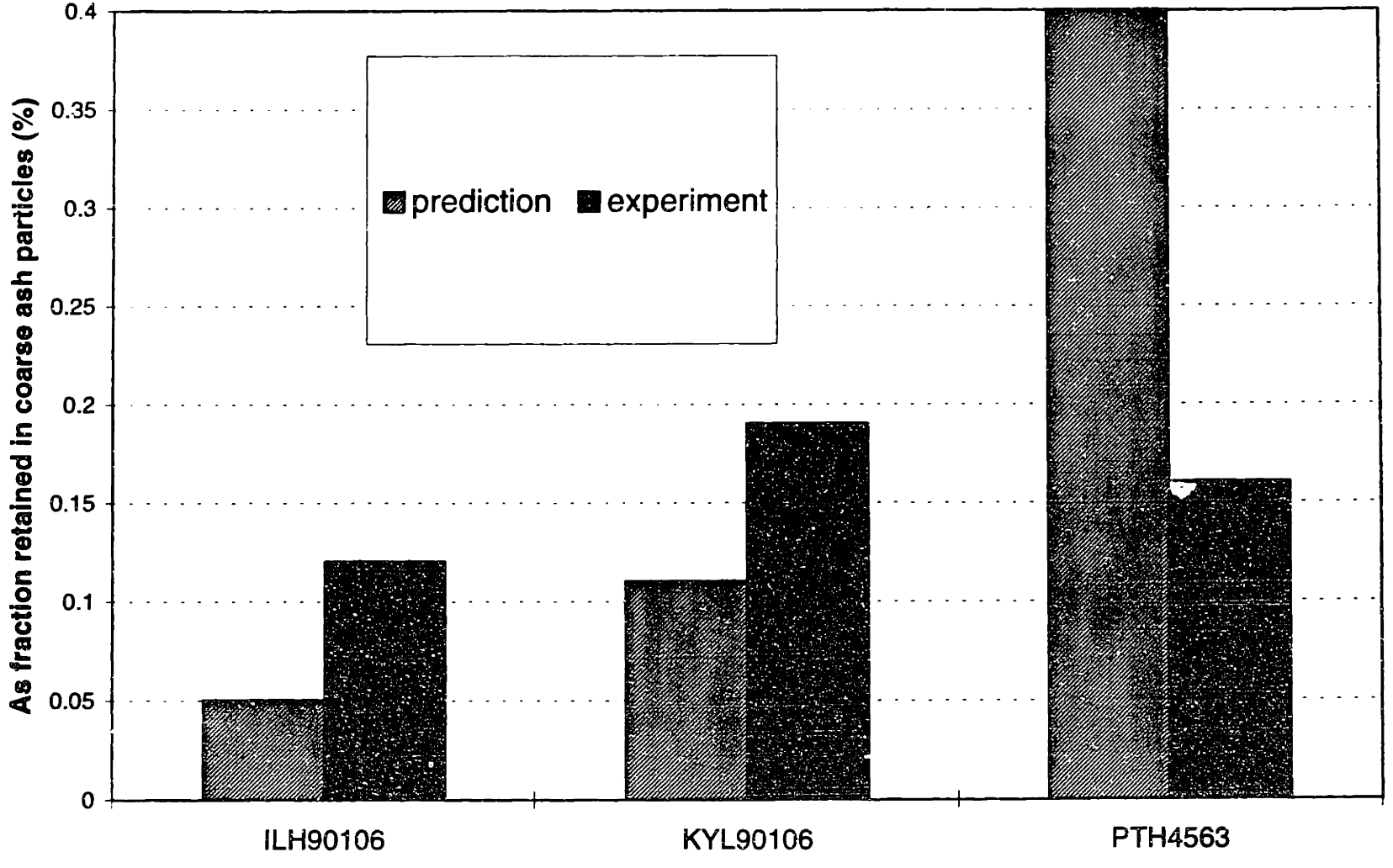

Figure 5-20 Comparison between prediction and experiment of Co retained in coase ash particles

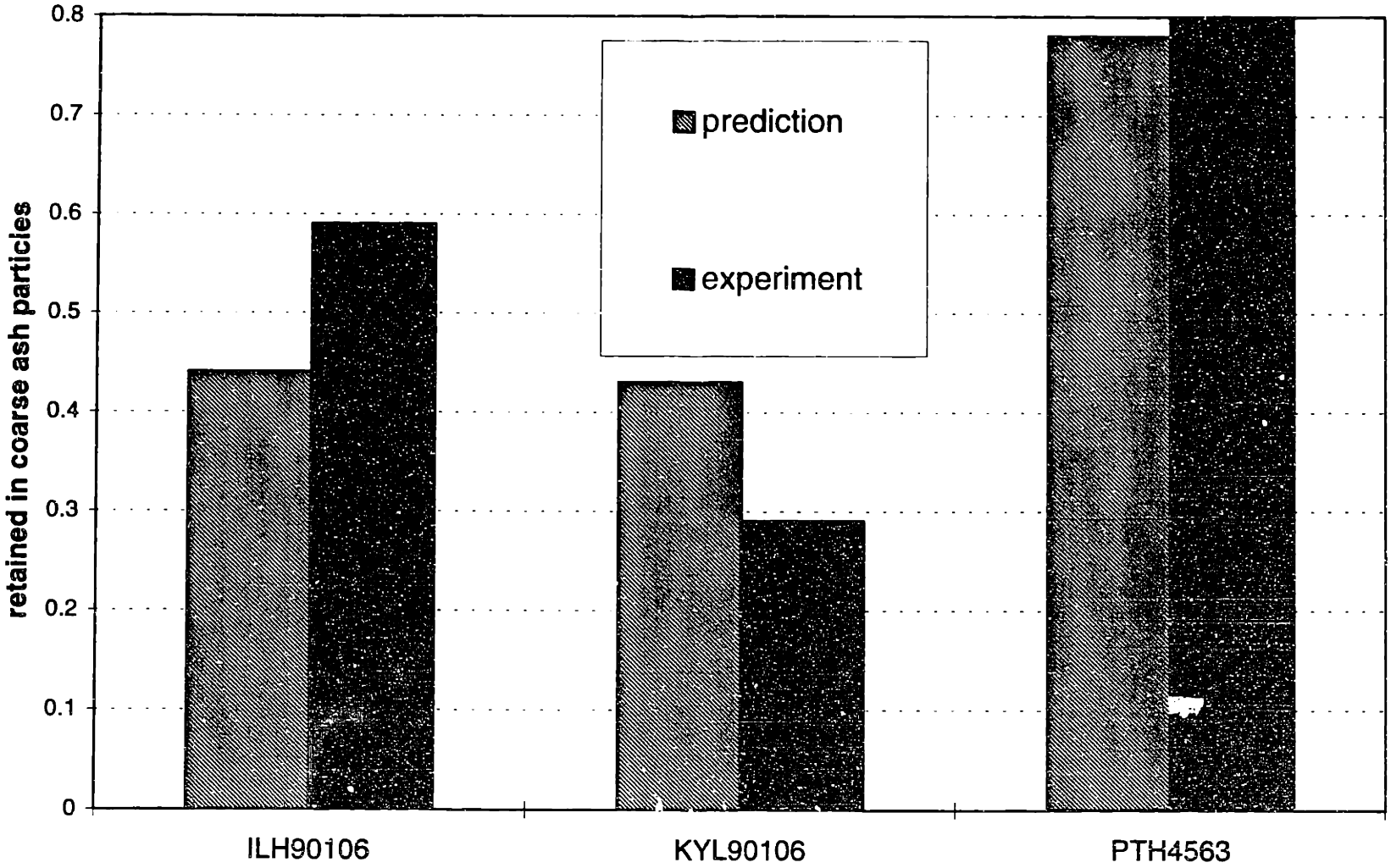

Chapter 6 CONCLUSIONS

Coal Characterization

Coal can be classified into size and density segregated fractions using the small fluidized-bed separator. The effect of density segregation is mainly due to the concentration of pyrites in the denser and large coal particle fraction. For Pittsburgh, Elkhorn/Hazard, and Illinois coals, arsenic, sodium, cerium, molybdenum, selenium, and antimony are also enriched in the higher density coal, since they are associated with pyrite in the coal. For Wyodak coal, about half of selenium and arsenic is associated with iron, which may be in the oxide state or clay, and the other half is organically bounded to the coal. Selective leaching experiment using different acids further justified those associations.

By using XAFS, the occurrences of elements were determined directly. It was found that: nearly all arsenic is associated with pyrite except for Wyodak coal; selenium is mainly associated with pyrite; chromium is probably presented in the form of -COOCr; zinc is mostly in the form of ZnS in Illinois coal, while Zn may be associated with other minerals in other coals; and iron is mostly in the form of pyrites, except for Elkhorn/Hazard coal which has a significant amount of jarosite.

Transformation of Iron during Combustion

Iron cannot be devolatilized like other trace elements using the ASTM standard pyrolysis procedure. But iron can be found in submicron char particles under very high heating up in the drop tube furnace, which is due to the fragmentation of pyrrhotite. During coal combustion, a small part of pyrrhotite was fragmented into fine particles (iron fume), which was testified by direct characterizing the iron state of submicron ash particles. Most of iron is in glassy state in the submicron ash particles, which shows that most iron was from vaporization, and the vaporized iron reacted with the vaporized

silicates to produce glassy iron. Most iron in coarse ash particle is with Fe^{3+} states. Therefore shedding/fragmentation of pyrrhotite and glassy iron from burning occurs during combustion, which was inferred from the thermodynamic properties.

Vaporization was enhanced by char combustion, thus controlled by the reducing reaction with CO, which is the primary product of char combustion: $FeX + CO \leftrightarrow Fe + COX$. The vaporization rate can be estimated using a modified Quann/Sarofim equilibrium-diffusion model.

Transformation of Trace Elements during Combustion

Experimental results show that vaporization rate is proportional to its concentration. More elements were vaporized at higher pyrolysis temperature and at higher oxygen concentration. Thus the vaporization rate is also determined by reaction temperature. Calculation shows that the thermodynamic properties for the elements concerned are very different, while the fraction vaporized is the same order of magnitude. Therefore vaporization rate is determined not only by combustion condition, but also by the occurrences of the elements.

For those elements(As, Se, Sb) associated with pyrite in coal, the release processes are composed by three series steps: diffusion through the pyrrhotite melt, vaporization at the interface of melt and gas, and transport through the pores of the char. The kinetics by vaporization at the interface and through the pores were calculated using results from previous researchers, and the diffusion through the melt was estimated using the experimental data of this study. For the elements organically bounded to the coal, they can be devolatilized during pyrolysis, and the release rate is approximated using the semi-empirical Arrhenius law for volatile devolatilization.

Appendix A CCSEM Results for Selected Coals

SAMPLE PSI PITT#8 COAL 3 2
RUN 1 DATE 25-JUN-96 SUMMARY 104 TOTAL 1199

AVERAGE SPECIES COMPOSITION

#	MINERAL SPECIES	Na	Mg	Al	Si	P	S	Cl	K	Ca	Ti	Fe	Weight %
142	Quartz	0.	0.	0.	98.	0.	1.	0.	1.	0.	0.	0.	11.1
133	Kaolinite	0.	0.	46.	53.	0.	1.	0.	1.	0.	0.	0.	9.2
122	Illite	0.	0.	30.	53.	0.	4.	0.	11.	0.	1.	1.	12.8
7	K-Feldspar	0.	0.	20.	52.	0.	2.	0.	23.	0.	1.	2.	1.4
1	Chlorite	0.	9.	20.	32.	0.	0.	0.	0.	3.	0.	36.	0.0
8	Montmorillonite	10.	0.	19.	67.	0.	0.	1.	0.	2.	0.	0.	0.4
291	Misc. Silicates	0.	0.	30.	58.	0.	5.	0.	4.	1.	0.	0.	28.8
152	Pyrite	0.	0.	0.	0.	0.	64.	0.	0.	0.	0.	36.	18.0
11	Misc. sulf.	0.	0.	1.	4.	0.	50.	0.	0.	22.	0.	23.	0.2
1	Apatite	0.	0.	0.	0.	26.	5.	3.	0.	61.	5.	0.	0.1
1	Misc. Phosphate	0.	0.	44.	0.	37.	5.	0.	0.	14.	0.	0.	0.0
2	Fe-rich	0.	0.	0.	0.	0.	0.	0.	0.	0.	0.	100.	0.6
51	Calcite	0.	1.	0.	0.	0.	0.	0.	0.	98.	0.	0.	6.0
28	Mixed Carbonate	0.	4.	0.	2.	17.	2.	0.	0.	72.	0.	2.	2.3
3	Ti oxide	0.	0.	0.	0.	1.	0.	0.	0.	2.	97.	0.	0.1
1	Ti-rich	0.	0.	0.	11.	0.	0.	0.	3.	0.	86.	0.	0.0
1	Trace-comp	10.	0.	0.	8.	0.	22.	0.	0.	33.	0.	0.	0.1
9	Quartz-Sulfate	0.	0.	4.	56.	0.	32.	2.	5.	0.	0.	0.	0.2
3	Quartz-Pyrite	0.	0.	0.	47.	0.	36.	0.	0.	0.	0.	17.	0.0
62	Sil-sulf	0.	0.	26.	41.	0.	26.	1.	3.	1.	1.	0.	2.2
4	Silicate-Pyrite	0.	0.	16.	28.	0.	32.	0.	5.	1.	0.	16.	0.3
1	Alumina-rich	0.	0.	100.	0.	0.	0.	0.	0.	0.	0.	0.	0.1
127	Misc. Mixed	1.	0.	18.	35.	2.	17.	2.	5.	17.	1.	2.	5.9
1161	GRAND TOTALS	0.	0.	19.	44.	1.	16.	0.	3.	9.	0.	8.	100.0

WEIGHT DISTRIBUTION

0 MINERAL SPECIES	WT. %	Size Ranges (Microns) 0.1 2.5	2.5 5.0	5.0 10.0	10. 20.	20. 40.	40. 80.	80. 500.
Quartz	11.1	10.	38.	21.	19.	3.	3.	7.
Kaolinite	9.2	3.	38.	23.	30.	5.	1.	0.
Illite	12.8	30.	51.	10.	6.	1.	1.	0.
Misc. Silicates	28.8	28.	53.	10.	5.	2.	1.	0.
Pyrite	18.0	3.	0.	14.	10.	16.	34.	23.
Calcite	6.0	2.	65.	13.	8.	5.	8.	0.
Misc. Mixed	5.9	62.	29.	5.	1.	2.	0.	0.
MINOR MINERALS	8.1	47.	34.	9.	6.	2.	1.	0.
GRAND TOTALS	100.0	21.	38.	13.	10.	5.	8.	5.

APPENDIX CCSEM RESULTS FOR SECLECTED COALS

SAMPLE MIT PT H 90106 COALM 3 2
RUN 1 DATE 05-MAY-97 SUMMARY 120 TOTAL 1199

AVERAGE SPECIES COMPOSITION

#	MINERAL SPECIES	Na	Mg	Al	Si	P	S	Cl	K	Ca	Ti	Fe	Weight %
106	Quartz	0.	0.	1.	96.	0.	2.	0.	0.	0.	0.	0.	7.1
175	Kaolinite	0.	0.	46.	51.	0.	1.	0.	1.	0.	0.	0.	7.0
100	Illite	0.	0.	30.	52.	0.	6.	0.	11.	0.	0.	0.	13.0
1	K-Feldspar	0.	0.	16.	57.	0.	4.	0.	18.	0.	0.	5.	.0
5	Montmorillonite	13.	0.	17.	66.	0.	0.	0.	3.	1.	0.	0.	.2
182	Misc. Silicates	0.	0.	18.	66.	0.	10.	0.	4.	0.	0.	1.	18.2
429	Pyrite	0.	0.	0.	0.	0.	65.	0.	0.	0.	0.	35.	36.9
2	Ferrous Sulfate	0.	0.	0.	0.	0.	52.	0.	0.	0.	0.	48.	.1
29	Misc. sulf.	0.	0.	2.	6.	0.	64.	0.	0.	0.	0.	29.	4.0
2	Misc. chloride	0.	0.	0.	13.	0.	5.	59.	5.	0.	7.	11.	.0
1	Apatite	0.	0.	0.	0.	29.	0.	0.	0.	71.	0.	0.	.0
5	Fe-rich	0.	0.	0.	0.	0.	1.	0.	0.	0.	0.	99.	.2
41	Calcite	0.	1.	0.	0.	0.	0.	0.	0.	99.	0.	0.	1.7
7	Mixed Carbonate	0.	0.	3.	9.	6.	0.	0.	0.	64.	0.	18.	.3
15	Quartz-Sulfate	0.	0.	3.	65.	0.	26.	0.	2.	0.	0.	4.	.4
5	Quartz-Pyrite	0.	0.	10.	54.	0.	26.	0.	0.	0.	0.	11.	2.0
33	Sil-sulf	0.	0.	17.	41.	0.	27.	0.	10.	0.	0.	4.	4.4
5	Silicate-Pyrite	0.	0.	15.	39.	0.	30.	1.	2.	1.	0.	12.	1.8
39	Misc. Mixed	0.	0.	15.	46.	1.	15.	1.	4.	7.	2.	4.	2.9
1182	GRAND TOTALS	0.	0.	12.	35.	0.	32.	0.	3.	2.	0.	15.	100.0

WEIGHT DISTRIBUTION

0 MINERAL SPECIES	WT. %	Size Ranges (Microns) .1 2.5	2.5 5.0	5.0 10.0	10. 20.	20. 40.	40. 80.	80. 500.
Quartz	7.1	8.	59.	17.	7.	2.	5.	2.
Kaolinite	7.0	4.	25.	24.	38.	4.	5.	0.
Illite	13.0	30.	59.	6.	4.	1.	1.	0.
Misc. Silicates	18.2	38.	48.	7.	2.	2.	3.	1.
Pyrite	36.9	2.	0.	3.	7.	5.	37.	46.
MINOR MINERALS	17.8	30.	48.	3.	2.	2.	7.	7.
GRAND TOTALS	100.0	18.	31.	6.	7.	3.	16.	18.

APPENDIX CCSEM RESULTS FOR SECLECTED COALS

SAMPLE MIT PT L 90106 COAL 3 2
RUN 1 DATE 28-MAY-97 SUMMARY 104 TOTAL 1199

AVERAGE SPECIES COMPOSITION

#	MINERAL SPECIES	Na	Mg	Al	Si	P	S	Cl	K	Ca	Ti	Fe	Weight %
186	Quartz	0.	0.	0.	98.	0.	1.	0.	0.	0.	0.	0.	17.4
129	Kaolinite	0.	0.	46.	54.	0.	0.	0.	0.	0.	0.	0.	6.9
139	Illit	0.	0.	29.	54.	0.	4.	0.	12.	0.	0.	0.	13.9
3	K-Feldspar	0.	0.	18.	60.	0.	0.	0.	19.	0.	0.	3.	.1
3	Montmorillonite	5.	0.	20.	75.	0.	0.	0.	0.	0.	0.	0.	.0
403	Misc. Silicates	0.	0.	25.	65.	0.	4.	0.	3.	1.	1.	1.	34.3
171	Pyrite	0.	0.	0.	0.	0.	66.	0.	0.	0.	0.	34.	17.5
2	Ferrous Sulfate	0.	0.	0.	0.	0.	51.	0.	0.	0.	0.	49.	.2
28	Misc. sulf.	0.	0.	0.	2.	0.	66.	0.	0.	4.	0.	27.	1.7
3	Apatite	0.	0.	0.	0.	31.	0.	0.	0.	66.	3.	0.	.1
4	Misc. Phosphate	0.	0.	19.	12.	36.	0.	0.	0.	34.	0.	0.	.8
2	Fe-rich	0.	0.	0.	0.	0.	0.	0.	0.	0.	0.	100.	.3
17	Calcite	0.	0.	0.	0.	0.	0.	0.	0.	99.	0.	0.	1.0
7	Mixed Carbonate	0.	0.	1.	15.	1.	1.	0.	0.	82.	0.	0.	.5
6	Ti-rich	0.	0.	4.	8.	0.	5.	0.	0.	1.	82.	0.	2.0
9	Quartz-Sulfate	0.	0.	10.	64.	0.	25.	0.	1.	0.	0.	0.	.1
1	Quartz-Pyrite	0.	0.	0.	39.	0.	41.	0.	1.	0.	0.	19.	.0
35	Sil-sulf	0.	0.	23.	46.	0.	25.	0.	3.	1.	0.	0.	1.0
1	Silicate-Pyrite	0.	0.	14.	27.	0.	31.	0.	0.	0.	0.	29.	.0
1	Alumina-rich	0.	0.	100.	0.	0.	0.	0.	0.	0.	0.	0.	.0
49	Misc. Mixed	0.	0.	16.	40.	5.	12.	1.	2.	21.	2.	1.	2.1
1199	GRAND TOTALS	0.	0.	17.	52.	0.	15.	0.	3.	3.	2.	7.	100.0

WEIGHT DISTRIBUTION

MINERAL SPECIES	WT. %	Size Ranges (Microns) .2 2.5	2.5 5.0	5.0 10.0	10. 20.	20. 40.	40. 80.	80. 500.
Quartz	17.4	12.	53.	20.	13.	0.	1.	1.
Kaolinite	6.9	6.	16.	25.	37.	10.	4.	2.
Illite	13.9	18.	61.	14.	3.	1.	2.	0.
Misc. Silicates	34.3	28.	46.	13.	10.	1.	1.	0.
Pyrite	17.5	1.	14.	14.	39.	13.	17.	1.
MINOR MINERALS	10.0	31.	25.	10.	18.	4.	8.	4.
GRAND TOTALS	100.0	18.	40.	15.	17.	4.	5.	1.

APPENDIX · CCSEM RESULTS FOR SECLECTED COALS

SAMPLE PSI ELKHORN/HAZARD 3 2
RUN 1 DATE 26-JUN-96 SUMMARY 108 TOTAL 1199

AVERAGE SPECIES COMPOSITION

#	MINERAL SPECIES	Na	Mg	Al	Si	P	S	Cl	K	Ca	Ti	Fe	Weight %
122	Quartz	0.	0.	0.	99.	0.	1.	0.	0.	0.	0.	0.	12.0
281	Kaolinite	0.	0.	45.	52.	0.	1.	0.	1.	0.	0.	0.	25.8
195	Illite	0.	0.	31.	52.	0.	2.	0.	11.	0.	1.	2.	14.5
3	K-Feldspar	0.	0.	17.	58.	0.	1.	0.	18.	0.	2.	5.	0.3
1	Montmorillonite	0.	0.	27.	61.	0.	8.	0.	0.	4.	0.	0.	0.0
383	Misc. Silicates	0.	0.	34.	55.	0.	4.	0.	4.	1.	1.	1.	29.2
31	Pyrite	0.	0.	1.	1.	0.	64.	0.	0.	0.	0.	35.	6.1
2	Chalcopyrite	0.	0.	0.	0.	0.	52.	0.	0.	0.	0.	25.	0.5
8	Misc. sulf.	0.	0.	4.	8.	1.	50.	0.	3.	6.	0.	28.	0.4
2	Apatite	0.	0.	2.	0.	27.	0.	1.	0.	70.	0.	0.	0.3
7	Misc. Phosphate	0.	1.	1.	46.	30.	0.	3.	0.	17.	2.	0.	1.5
7	Fe-rich	0.	0.	0.	0.	0.	0.	0.	0.	4.	0.	96.	1.1
4	Calcite	0.	0.	0.	3.	0.	0.	0.	0.	97.	0.	0.	0.8
9	Mixed Carbonate	0.	0.	0.	0.	16.	4.	0.	0.	55.	0.	24.	1.6
1	Ti oxide	0.	0.	0.	0.	0.	0.	0.	0.	0.	100.	0.	0.2
7	Ti-rich	0.	0.	1.	9.	0.	7.	0.	0.	0.	67.	13.	0.9
3	Quartz-Sulfate	0.	0.	0.	39.	0.	31.	19.	11.	0.	0.	0.	0.1
1	Quartz-Pyrite	0.	0.	7.	24.	0.	45.	0.	0.	0.	0.	23.	0.6
29	Sil-sulf	0.	0.	26.	40.	0.	26.	4.	1.	0.	1.	0.	0.5
6	Silicate-Pyrite	0.	0.	16.	23.	0.	28.	1.	4.	1.	0.	26.	0.2
1	Alumina-rich	0.	0.	93.	0.	0.	5.	0.	0.	0.	0.	0.	0.1
81	Misc. Mixed	0.	0.	24.	34.	2.	13.	3.	2.	9.	1.	10.	3.4
1184	GRAND TOTALS	0.	0.	27.	51.	1.	7.	0.	3.	3.	1.	5.	100.0

WEIGHT DISTRIBUTION

0 MINERAL SPECIES	WT. %	Size Ranges (Microns) 0.1 2.5	2.5 5.0	5.0 10.0	10. 20.	20. 40.	40. 80.	80. 500.
Quartz	12.0	10.	24.	16.	12.	10.	5.	24.
Kaolinite	25.8	6.	30.	15.	29.	10.	7.	1.
Illite	14.5	16.	24.	28.	14.	8.	10.	0.
Misc. Silicates	29.2	31.	26.	20.	15.	3.	4.	0.
Pyrite	6.1	8.	22.	15.	41.	7.	7.	0.
MINOR MINERALS	12.4	31.	39.	12.	6.	4.	2.	5.
GRAND TOTALS	100.0	19.	28.	18.	19.	7.	6.	4.

APPENDIX CCSEM RESULTS FOR SECLECTED COALS

SAMPLE MIT KY H 90106 COAL 3 2
RUN 1 DATE 06-MAY-97 SUMMARY 104 TOTAL 1199

AVERAGE SPECIES COMPOSITION

#	MINERAL SPECIES	Na	Mg	Al	Si	P	S	Cl	K	Ca	Ti	Fe	Weight %
111	Quartz	0.	0.	0.	99.	0.	1.	0.	0.	0.	0.	0.	10.9
378	Kaolinite	0.	0.	46.	50.	0.	1.	0.	1.	0.	0.	1.	21.0
197	Illite	0.	0.	32.	[illegible].	0.	3.	0.	10.	0.	1.	1.	12.8
2	K-Feldspar	0.	0.	16.	51.	0.	0.	0.	22.	0.	9.	2.	.1
1	Chlorite	0.	0.	16.	33.	0.	7.	0.	0.	0.	0.	44.	.0
3	Montmorillonite	10.	0.	19.	67.	0.	1.	0.	0.	4.	0.	0.	.2
380	Misc. Silicates	0.	0.	30.	58.	0.	4.	0.	2.	0.	4.	1.	41.0
31	Pyrite	0.	0.	0.	0.	0.	65.	0.	0.	0.	0.	35.	5.1
7	Gypsum	0.	0.	0.	0.	0.	47.	0.	0.	52.	0.	0.	.4
2	Misc. sulf.	0.	0.	0.	0.	0.	52.	0.	9.	0.	0.	39.	.2
2	Misc. Phosphate	0.	0.	12.	45.	35.	0.	0.	0.	7.	0.	0.	1.1
10	Fe-rich	0.	0.	0.	0.	0.	1.	0.	0.	1.	0.	98.	1.8
1	Calcite	0.	0.	0.	0.	0.	0.	0.	0.	100.	0.	0.	.2
8	Mixed Carbonate	0.	1.	0.	5.	1.	7.	0.	0.	60.	0.	25.	.9
9	Ti-rich	0.	0.	1.	9.	0.	2.	0.	0.	0.	88.	0.	2.1
7	Sil-sulf	0.	0.	22.	44.	0.	23.	3.	2.	0.	2.	0.	.2
5	Alumina-rich	0.	0.	76.	11.	5.	5.	0.	0.	0.	0.	2.	.2
27	Misc. Mixed	0.	0.	19.	35.	1.	8.	1.	2.	26.	3.	5.	1.8
1181	GRAND TOTALS	0.	0.	27.	54.	0.	6.	0.	2.	2.	4.	4.	100.0

WEIGHT DISTRIBUTION

0 MINERAL SPECIES	WT. %	Size Ranges (Microns) .2 2.5	2.5 5.0	5.0 10.0	10. 20.	20. 40.	40. 80.	80. 500.
Quartz	10.9	5.	38.	14.	15.	2.	6.	19.
Kaolinite	21.0	1.	25.	17.	16.	12.	20.	10.
Illite	12.8	15.	49.	12.	2.	10.	12.	0.
Misc. Silicates	41.0	16.	52.	11.	7.	3.	5.	5.
Pyrite	5.1	0.	0.	4.	33.	3.	22.	37.
MINOR MINERALS	9.2	15.	31.	8.	7.	2.	7.	31.
GRAND TOTALS	100.0	10.	40.	12.	10.	5.	10.	11.

APPENDIX . CCSEM RESULTS FOR SECLECTED COALS

SAMPLE MIT KY L 90106 COAL 3 2
RUN 1 DATE 29-MAY-97 SUMMARY 108 TOTAL 1199

AVERAGE SPECIES COMPOSITION

#	MINERAL SPECIES	Na	Mg	Al	Si	P	S	Cl	K	Ca	Ti	Fe	Weight %
103	Quartz	0.	0.	0.	98.	0.	1.	0.	0.	0.	0.	0.	7.1
190	Kaolinite	0.	0.	45.	53.	0.	1.	0.	0.	0.	0.	0.	12.7
230	Illite	0.	0.	31.	54.	0.	3.	0	9.	0.	1.	1.	15.1
1	K-Feldspar	0.	0.	15.	44.	0.	9.	0.	19.	0.	0.	14.	.1
2	Chlorite	0.	0.	21.	25.	0.	2.	0.	0.	0.	0.	52.	.0
3	Montmorillonite	0.	0.	25.	55.	0.	0.	0.	0.	19.	0.	0.	.2
547	Misc. Silicates	0.	0.	33.	57.	0.	6.	0.	1.	0.	1.	1.	54.0
10	Pyrite	0.	0.	0.	0.	0.	66.	0.	0.	0.	0.	33.	1.6
9	Misc. sulf.	0.	0.	0.	5.	0.	56.	0.	0.	23.	2.	12.	.3
1	Apatite	0.	0.	1.	2.	29.	0.	2.	0.	65.	0.	0.	.0
2	Misc. Phosphate	0.	0.	17.	5.	30.	11.	0.	0.	31.	7.	0.	.1
2	Fe-rich	0.	0.	0.	0.	0.	0.	0.	0.	0.	0.	100.	.3
1	Calcite	0.	0.	0.	0.	0.	0.	0.	0.	100.	0.	0.	.0
5	Mixed Carbonate	0.	0.	1.	0.	12.	3.	1.	0.	83.	0.	0.	.5
3	Ti oxide	0.	0.	0.	0.	0.	0.	0.	0.	0.	100.	0.	.9
9	Ti-rich	0.	0.	2.	4.	0.	5.	0.	0.	0.	86.	0.	1.0
1	Trace-comp	0.	0.	0.	0.	0.	0.	0.	1.	0.	0.	64.	.4
2	Quartz-Sulfate	0.	0.	6.	70.	0.	25.	0.	0.	0.	0.	0.	.1
20	Sil-sulf	0.	0.	28.	46.	0.	25.	0.	0.	0.	0.	0.	1.0
1	Silicate-Pyrite	0.	0.	21.	37.	0.	24.	0.	0.	0.	0.	18.	.1
2	Alumina-rich	0.	0.	95.	0.	0.	2.	0.	0.	0.	3.	0.	.8
55	Misc. Mixed	0.	0.	24.	36.	1.	16.	1.	0.	15.	1.	3.	3.8
1199	GRAND TOTALS	0.	0.	30.	54.	0.	6.	0.	2.	1.	3.	2.	100.0

WEIGHT DISTRIBUTION

MINERAL SPECIES	WT. %	Size Ranges (Microns) .2 2.5	2.5 5.0	5.0 10.0	10. 20.	20. 40.	40. 80.	80. 500.
Quartz	7.1	6.	36.	34.	17.	3.	1.	3.
Kaolinite	12.7	7.	35.	7.	18.	11.	18.	5.
Illite	15.1	19.	27.	19.	20.	7.	7.	1.
Misc. Silicates	54.0	25.	53.	10.	7.	3.	1.	1.
MINOR MINERALS	11.1	33.	39.	9.	11.	4.	2.	1.
GRAND TOTALS	100.0	22.	44.	13.	12.	5.	4.	1.

APPENDIX CCSEM RESULTS FOR SECLECTED COALS

SAMPLE PSI ILLINOIS #6 COAL 3 2
RUN 1 DATE 28-JUN-96 SUMMARY 112 TOTAL 1199

AVERAGE SPECIES COMPOSITION

#	MINERAL SPECIES	Na	Mg	Al	Si	P	S	Cl	K	Ca	Ti	Fe	Weight %
144	Quartz	0.	0.	0.	99.	0.	1.	0.	0.	0.	0.	0.	12.8
68	Kaolinite	0.	0.	46.	53.	0.	1.	0.	0.	0.	0.	0.	5.4
97	Illite	0.	0.	27.	53.	0.	5.	0.	11.	0.	0.	2.	11.1
4	K-Feldspar	0.	0.	16.	51.	0.	12.	2.	17.	2.	0.	0.	0.1
2	Chlorite	0.	0.	19.	30.	0.	5.	0.	1.	0.	0.	45.	0.2
1	Montmorillonite	0.	0.	20.	77.	0.	0.	0.	0.	3.	0.	0.	0.0
273	Misc. Silicates	0.	0.	19.	64.	0.	9.	0.	6.	0.	0.	1.	22.9
3	Elem. Sulfur	0.	0.	0.	0.	0.	73.	10.	8.	0.	0.	0.	0.0
260	Pyrite	0.	0.	0.	0.	0.	65.	0.	0.	0.	0.	35.	29.8
2	Ferrous Sulfate	0.	0.	0.	0.	0.	49.	0.	0.	0.	0.	51.	0.2
1	Gypsum	0.	0.	0.	0.	0.	47.	0.	0.	53.	0.	0.	0.0
24	Misc. sulf.	0.	0.	1.	8.	0.	67.	0.	1.	0.	0.	24.	1.5
3	Fe-rich	0.	0.	0.	0.	0.	0.	0.	0.	0.	0.	100.	0.3
53	Calcite	0.	0.	0.	0.	0.	0.	0.	0.	100.	0.	0.	3.2
7	Mixed Carbonate	0.	0.	0.	5.	7.	5.	0.	0.	68.	0.	14.	0.7
1	Ti oxide	0.	0.	0.	0.	0.	0.	0.	0.	0.	100.	0.	0.1
1	Ti-rich	0.	0.	0.	0.	0.	36.	0.	0.	0.	64.	0.	0.1
73	Quartz-Sulfate	0.	0.	4.	58.	0.	33.	0.	3.	1.	1.	0.	3.7
4	Quartz-Pyrite	0.	0.	0.	39.	0.	39.	0.	0.	2.	0.	20.	0.7
109	Sil-sulf	0.	0.	18.	40.	0.	30.	0.	8.	1.	1.	2.	4.1
4	Silicate-Pyrite	0.	0.	16.	44.	0.	21.	0.	9.	0.	0.	9.	0.3
56	Misc. Mixed	0.	0.	18.	38.	2.	23.	1.	8.	4.	0.	5.	2.7
1190	GRAND TOTALS	0.	0.	11.	42.	0.	27.	0.	3.	4.	0.	12.	100.0

WEIGHT DISTRIBUTION

Size Ranges (Microns)

0 MINERAL SPECIES	WT. %	0.1 2.5	2.5 5.0	5.0 10.0	10. 20.	20. 40.	40. 80.	80. 500.
Quartz	12.8	3.	29.	34.	24.	1.	0.	7.
Kaolinite	5.4	2.	15.	31.	43.	6.	3.	0.
Illite	11.1	8.	48.	19.	21.	1.	2.	0.
Misc. Silicates	22.9	18.	41.	26.	13.	2.	0.	0.
Pyrite	29.8	2.	17.	20.	40.	13.	4.	3.
MINOR MINERALS	18.0	38.	23.	14.	14.	5.	4.	1.
GRAND TOTALS	100.0	13.	29.	23.	25.	6.	2.	2.

APPENDIX CCSEM RESULTS FOR SECLECTED COALS

SAMPLE MIT IL H 4563 COAL 3 2
RUN 1 DATE 2-APR-97 SUMMARY 116 TOTAL 1199

AVERAGE SPECIES COMPOSITION

#	MINERAL SPECIES	Na	Mg	Al	Si	P	S	Cl	K	Ca	Ti	Fe	Weight %
126	Quartz	0.	0.	0.	98.	0.	2.	0.	0.	0.	0.	0.	12.1
46	Kaolinite	0.	0.	47.	50.	0.	2.	0.	1.	0.	0.	0.	3.7
90	Illite	0.	0.	27.	55.	0.	4.	0.	12.	0.	0.	1.	7.9
4	K-Feldspar	0.	0.	18.	48.	0.	7.	0.	20.	0.	0.	6.	.5
1	Montmorillonite	0.	0.	29.	59.	0.	10.	0.	0.	2.	0.	0.	.0
229	Misc. Silicates	0.	0.	22.	64.	0.	9.	0.	4.	0.	0.	1.	19.9
426	Pyrite	0.	0.	0.	0.	0.	65.	0.	0.	0.	0.	35.	42.5
6	Ferrous Sulfate	0.	0.	0.	1.	0.	49.	0.	0.	0.	0.	50.	1.1
2	Gypsum	0.	0.	0.	0.	0.	48.	0.	0.	52.	0.	0.	.1
32	Misc. sulf.	0.	0.	2.	5.	0.	66.	0.	0.	0.	0.	27.	2.0
1	Misc. chloride	0.	0.	0.	13.	0.	21.	66.	0.	0.	0.	0.	.1
4	Fe-rich	0.	0.	0.	0.	0.	1.	0.	0.	0.	0.	99.	.4
61	Calcite	0.	0.	0.	0.	0.	0.	0.	0.	100.	0.	0.	3.4
8	Mixed Carbonate	0.	2.	1.	6.	4.	7.	0.	0.	80.	0.	0.	.5
1	Trace-comp	24.	0.	13.	11.	0.	21.	0.	0.	0.	0.	0.	.0
19	Quartz-Sulfate	0.	1.	8.	52.	0.	34.	0.	4.	0.	0.	0.	.6
1	Quartz-Pyrite	0.	0.	0.	29.	0.	49.	0.	0.	0.	0.	21.	.0
46	Sil-sulf	0.	0.	25.	40.	0.	30.	0.	3.	0.	0.	0.	2.8
6	Silicate-Pyrite	0.	0.	16.	39.	0.	23.	0.	8.	0.	0.	13.	1.0
23	Misc. Mixed	0.	0.	19.	33.	0.	31.	1.	4.	2.	0.	6.	1.3
1132	GRAND TOTALS	0.	0.	10.	34.	0.	34.	0.	2.	4.	0.	17.	100.0

WEIGHT DISTRIBUTION

0 MINERAL SPECIES	WT. %	Size Ranges (Microns) .1 2.5	2.5 5.0	5.0 10.0	10. 20.	20. 40.	40. 80.	80. 500.
Quartz	12.1	3.	39.	30.	24.	2.	3.	0.
Illite	7.9	1.	31.	26.	35.	7.	2.	0.
Misc. Silicates	19.9	22.	32.	23.	11.	6.	5.	1.
Pyrite	42.5	1.	0.	8.	18.	27.	44.	2.
MINOR MINERALS	17.6	19.	19.	13.	15.	9.	24.	1.
GRAND TOTALS	100.0	8.	17.	16.	18.	15.	24.	1.

Appendix B Elements Balances

Table B-1† Coal and ash mass collected (g) under $T_{furnace}$ = 1700K, 20% O_2

coal type	coal used	ash on preseparator d>10 μm	ash on stage 1-5 1.1 μm<d<10 μm	ash on filter d<1.1 μm
PTH4563	1.912	0.071	0.1064	0.01
PTL4563	1.7182	0.031	0.0543	0.009
PTH90106	2.1625	0.0829	0.12594	0.01
PTL90106	1.9318	0.0531	0.05594	0.009
KYH4563	1.9866	0.0148	0.0942	0.008
KYL4563	1.0397	0.0075	0.0398	0.005
KYH90106	2.0386	0.0378	0.1162	0.017
KYL90106	1.2554	0.0104	0.0571	0.006
ILH4563	2.049	0.0345	0.0916	0.008
ILL4563	1.7226	0.031	0.0629	0.005
ILH90106	1.1751	0.0231	0.0798	0.009
ILL90106	1.9998	0.0287	0.0731	0.007

† Note: Table B-1, B-2 and B-3 are for ash samples generated under $T_{furnace}$=1700K, 20% O_2 in 1996. The elemental concentrations in coals are in Tables 3-3 to 3-6.

Table B-2 Concentrations of elements in ash particles(ppm)

	Fe*	As	Na	Zn	Cr	Sc	Co	Se	Sb	La	Sm
PTH4563 $d_{ash}>10\mu$	25	9	3974	84	93	19	32	2	1.9	53	9
$1.1<d_{ash}<10\mu$	26	12	3340	85	85	17	31	2	1.8	46	8
PTL4563 $d_{ash}>10\mu$	10	5	4527	66	106	22	23	1	1.1	63	9
$1.1<d_{ash}<10\mu$	12	5	4728	79	145	26	28	3	1.5	69	11
PTH90106 $d_{ash}>10\mu$	27	12	2743	90	81	13	26	2	0.8	38	7
$1.1<d_{ash}<10\mu$	18	12	3000	110	66	12	20	2	0.8	37	6
PTL90106 $d_{ash}>10\mu$	6	4	4792	210	112	23	20	8	0.5	66	10
$1.1<d_{ash}<10\mu$	4	6	4552	79	124	21	16	1	0.6	62	10
KYH4563 $d_{ash}>10\mu$	10	8	1876	90	217	307	31	3	8.8	116	21
$1.1<d_{ash}<10\mu$	8	10	1833	61	147	321	31	12	3.8	126	22
KYL4563 $d_{ash}>10\mu$	10	15	7393	1045	217	760	68	20	11	354	58
$1.1<d_{ash}<10\mu$	2.3	5	2058	73	146	355	24	10	2.6	145	26
KYH90106 $d_{ash}>10\mu$	9	11	2670	108	200	265	24	2	1.4	98	17
$1.1<d_{ash}<10\mu$	3.3	8	1900	90	99	263	19	8	1.5	112	19
KYL90106 $d_{ash}>10\mu$	1.8	4	1430	109	160	506	29	5	1.6	180	33
$1.1<d_{ash}<10\mu$	1.7	5	1414	74	183	468	30	4	1.9	180	30
ILH4563 $d_{ash}>10\mu$	22	5	2172	1015	141	24	31	4	0.9	41	9
$1.1<d_{ash}<10\mu$	20	3	1914	544	134	21	29	3	0.7	38	8
ILL563 $d_{ash}>10\mu$	12	3.5	2581	214	178	29	30	7	0.8	55	11
$1.1<d_{ash}<10\mu$	12	3.5	2479	163	176	28	27	5	1	52	11
ILH90106 $d_{ash}>10\mu$	22	6	1389	1209	137	15	25	5	0.8	28	6
$1.1<d_{ash}<10\mu$	18	5	1577	817	112	17	25	4	0.7	33	6.5
ILL90106 $d_{ash}>10\mu$	11	3	2248	46	202	28	28	4	0.8	52	9
$1.1<d_{ash}<10\mu$	10	4	2434	91	175	28	28	4	0.8	51	10

* %

Table B-3 Percentages of elements collected in ash particles(%)

	Fe	As	Na	Zn	Cr	Sc	Co	Sb	La	Sm	Se
PTH4563 coarse	80	16	88	56	125	80	80	57	123	110	21
submicron	2	34	12	26	18	2	17	34	2	2	1
total	82	50	100	82	141	82	97	91	125	112	22
PTL4563 coarse	86	8	51	40	77	73	85	25	78	77	25
submicron	1	38	16	39	18	3	9	39	2	18	2
total	87	46	67	79	95	76	93	64	80	95	27
PTH90106 coarse	70	8	88	153	74	68	56	16	69	74	9
submicron	1	35	18	32	16	3	16	36	2	16	1
total	71	43	106	185	90	71	72	52	71	90	10
PTL90106 coarse	74	28	54	144	80	78	48	16	81	80	23
submicron	2	26	18	17	16	4	13	31	4	16	1
total	76	54	72	161	96	82	61	47	85	96	24
KYH4563 coarse	110	21	34	17	66	43	26	29	47	66	20
submicron	6	52	14	11	10	9	31	32	5	10	3
total	116	73	48	28	76	52	57	61	52	76	23
KYL4563 coarse	97	13	46	29	43	40	19	16	56	45	13
submicron	6	34	26	8	5	7	36	28	5	5	4
total	103	47	72	37	48	47	55	44	61	48	17
KYH90106 coarse	88	25	53	36	72	50	25	13	60	72	18
submicron	6	59	32	8	13	10	36	39	8	13	2
total	94	74	85	44	85	60	61	51	69	85	20
KYL90106 coarse	90	19	38	27	81	77	29	13	88	81	9
submicron	17	32	23	9	10	9	45	39	8	10	1
total	107	51	61	36	91	86	74	52	96	91	10
ILL4563 coarse	66	11	43	38	65	78	60	14	56	65	18
submicron	2	33	23	33	12	3	12	45	3	12	1
total	68	44	66	71	77	81	72	59	59	77	19
ILL90106 coarse	80	23	42	52	76	75	53	12	82	76	9
submicron	2	33	29	33	16	4	11	42	3	16	1
total	82	56	71	85	92	79	64	54	85	92	10

Table B-4 elemental balances under pyrolysis conditions (%)

	Na	Sc	Cr	Fe	Co	As	Se	Sb
PTH90106[a] coarse	41	53	79	86	77	64	20	68
submicron	14	7	24	7	14	40	14	40
total	55	60	103	93	91	104	34	108
WYH90106[a] coarse	12	73	48	117	47	54	6	76
submicron	35	6	8	11	20	51	38	33
total	47	79	56	128	67	105	44	109

pyrolysis temperature 1745K

Table B-5 Elemental balances for PTH90106 coal burned at $T_{furnace}$=1700K with different O_2 concentrations (%)

	Na	Cr	Fe	Co	As	Sb
50%O_2[(3)] coarse	12	15	78	26	1.4	4
submicron	53	33	21	34	82	50
35%O_2[(2)] coarse	18	26	48	22	2.6	9
submicron	45	35	14	29	54	43
20%O_2[(3)] coarse	16	55	85	20	14	20
submicron	47	13	9	13	92	35
10%O_2[(3)] coarse	34	27	228	113	20	378
submicron	29	6	5	2	117	83

Note : (#) Number of parent PTH90106 coal, which has the following elemental concentrations

Table B-6 Elemental concentrations for different PTH90106 coals (ppm)

	Na	Cr	Fe	Co	As	Sb	Se
(1)	540	9.4	30000	3.8	16	0.47	2.1
(2)	540	18	21000	3.7	13	0.4	2
(3)	620	11	14000	3.2	9	0.4	2.8

THESIS PROCESSING SLIP

FIXED FIELD: ill. _____ name _____

index _____ biblio _____

▶ COPIES (Archives) Aero Dewey (Eng) Hum

Lindgren Music Rotch Science

TITLE VARIES: ▶☐ _____

_____

_____

NAME VARIES: ▶☐ _____

_____

IMPRINT: (COPYRIGHT) _____

▶COLLATION: 235l

_____

▶ADD. DEGREE: _____ ▶ DEPT.: _____

SUPERVISORS: _____

_____

NOTES:

cat'r: date:

page: J167

▶DEPT: M.E.

▶YEAR: 1998 ▶DEGREE: Sc.D.

▶NAME: ZENG, Taofang